The John von Neumann Institute for Computing (NIC) was established in 1998 by Forschungszentrum Jülich and Deutsches Elektronen-Synchrotron DESY to support the supercomputer-oriented simulation sciences. In 2006, GSI Helmholtzzentrum für Schwerionenforschung joined NIC as a contract partner.

The core task of NIC is the peer-reviewed allocation of supercomputing resources to computational science projects in Germany and Europe. The NIC partners also support supercomputer-aided research in science and engineering through a three-way strategy:

- Provision of supercomputing resources for projects in science, research, and industry.
- Supercomputer-oriented research and development by research groups in selected fields of physics and natural sciences.
- Education and training in all areas of supercomputing by symposia, workshops, summer schools, seminars, courses, and guest programmes for scientists and students.

The research groups of the John von Neumann Institute for Computing (NIC) regularly conduct workshops on leading-edge subjects in computational physics. In this tradition, the Computational Materials Physics Group organized a workshop on Hybrid Particle-Continuum Methods jointly with the Institute of Advanced Simulation on March 4 - 7, 2013 at the Forschungszentrum Jülich. The goal of the workshop was to foster the exchange of ideas between the communities working on complex fluids and complex solids. Particular emphasis was placed on continuum-mediated interactions between particles as well as on the adaptive and non-adaptive coupling between particle-based and continuum-based descriptions of materials.

JÜLICH FORSCHUNGSZENTRUM

GSI

Deutsches Elektronen-Synchrotron DESY

HYBRID 2013

M. H. Müser, G. Sutmann, R. G. Winkler (Editors)

Hybrid Particle-Continuum Methods in Computational Materials Physics

4 - 7 March 2013 | Jülich, Germany

Martin H. Müser, Godehard Sutmann, Roland G. Winkler (Editors)

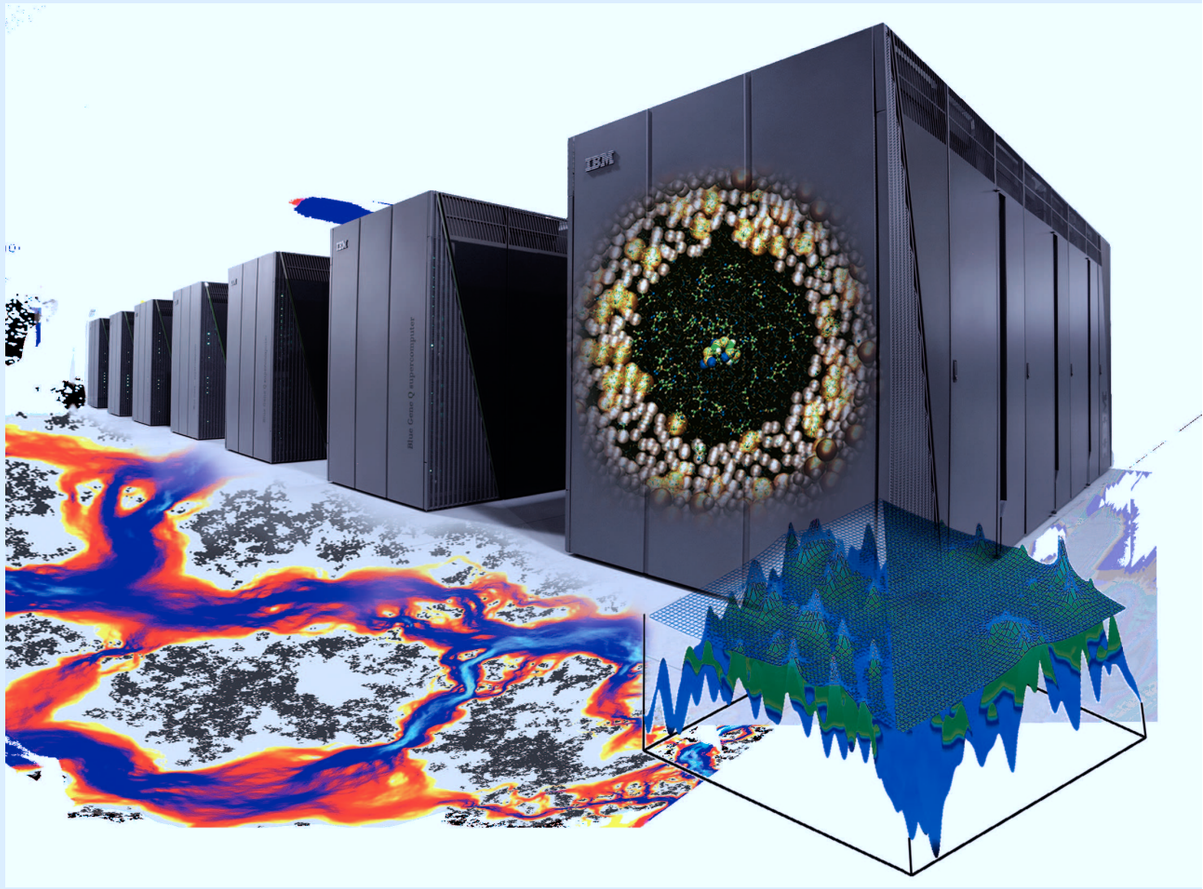

NIC Series Volume 46

ISBN 978-3-89336-849-5

Publication Series of the John von Neumann Institute for Computing (NIC)
NIC Series Volume 46

Forschungszentrum Jülich GmbH
John von Neumann Institute for Computing (NIC)

Hybrid Particle-Continuum Methods in Computational Materials Physics

4 - 7 March 2013 | Jülich, Germany

Proceedings

Martin H. Müser, Godehard Sutmann, Roland G. Winkler (Editors)

Publication Series of the John von Neumann Institute for Computing (NIC)

NIC Series Volume 46

ISBN 978-3-89336-849-5

Bibliographic information published by the Deutsche Nationalbibliothek.
The Deutsche Nationalbibliothek lists this publication in the Deutsche
Nationalbibliografie; detailed bibliographic data are available in the
Internet at http://dnb.d-nb.de.

Publisher and Distributor:	Forschungszentrum Jülich GmbH Zentralbibliothek 52425 Jülich Phone +49 (0) 24 61 61-53 68 · Fax +49 (0) 24 61 61-61 03 e-mail: zb-publikation@fz-juelich.de Internet: http://www.fz-juelich.de/zb
Cover Design:	Jülich Supercomputing Centre, Forschungszentrum Jülich GmbH
Printer:	Grafische Medien, Forschungszentrum Jülich GmbH
Copyright:	Forschungszentrum Jülich 2013

Publication Series of the John von Neumann Institute for Computing (NIC)
NIC Series Volume 46

ISBN 978-3-89336-849-5

The complete volume is freely available on the Internet on the Jülicher Open Access Server (JUWEL) at
http://www.fz-juelich.de/zb/juwel

Preface

Martin H. Müser
Jülich Supercomputing Centre, Forschungszentrum Jülich, 52425 Jülich, Germany
E-mail: m.mueser@fz-juelich.de

Godehard Sutmann
Jülich Supercomputing Centre, Forschungszentrum Jülich, 52425 Jülich, Germany
E-mail: g.sutmann@fz-juelich.de

Roland G. Winkler
Institute of Complex Systems and Institute for Advanced Simulation,
Forschungszentrum Jülich, 52425 Jülich, Germany
E-mail: r.winkler@fz-juelich.de

The research groups of the John von Neumann Institute for Computing (NIC) regularly conduct workshops on leading-edge subjects in computational physics. In this tradition, the Computational Materials Physics Group organized a workshop on Hybrid Particle-Continuum Methods jointly with the Institute of Advanced Simulation on March 4–7, 2013 at the Forschungszentrum Jülich. The goal of the workshop was to foster the exchange of ideas between the communities working on complex fluids and complex solids. Particular emphasis was placed on continuum-mediated interactions between particles as well as on the adaptive and non-adaptive coupling between particle-based and continuum-based descriptions of materials.

This proceedings volume collects selected invited and contributed presentations of the workshop. It covers subjects from modelling of hydrodynamic interactions between particles in complex fluids or environments, through coarse-grained descriptions of biological systems, to the coupling of atomically represented regions with various continuum-based theories for fluids and solids. Special aspects are long-time-scale properties of systems with slow collective dynamics, the development of efficient adaptive resolution algorithms, and the coupling of quantum-mechanically treated regions with continuum descriptions.

In the preparation of the workshop, the editors stimulated the authors of the proceedings to provide a pedagogical introduction to their field of expertise and to the methods used in addition to the overview of their results. We hope that readers of this volume agree that this goal has been achieved.

Besides the editors, Martina Kamps, Britta Hoßfeld, and Elke Bielitza at Forschungszentrum Jülich as well as Erik Luijten (Northwestern University) helped in organizing the workshop.

Jülich, March 2013

Martin H. Müser Godehard Sutmann Roland G. Winkler

Contents

Coupling Molecular Dynamics to a "Continuum" Mesh Background

Colin Denniston[1], **Frances E. Mackay**[1], **and Santtu T. T. Ollila**[1,2]

[1] Department of Applied Mathematics, University of Western Ontario,
London, ON, N6A 5B7, Canada
E-mail: {*cdennist, fmackay*}*@uwo.ca*

[2] Department of Applied Physics, Aalto University School of Science and Technology,
P.O. Box 11000, FIN-00076 Aalto, Espoo, Finland
E-mail: santtu.ollila@aalto.fi

We review different schemes to couple molecular dynamics simulations to a continuum fluid solvent represented on a discrete regular mesh. In particular, we look at stress coupling and velocity-dependent force coupling methods.

1 Introduction

Traditional modelling techniques fall into two broad classes: particle-based methods and continuum models. The prototypical particle method, molecular dynamics (MD), solves Newton's equations of motion for each particle, typically an atom or molecule. The particles interact with each other using forces derived from either *ab initio* techniques (using quantum mechanics) or phenomenological principles (force fields chosen so that they reproduce known behaviour). In order to use MD for simulating colloidal particles immersed in a solvent, for every colloidal particle one would need at least 100-1000 solvent molecules depending on how tightly packed the particles are (a large distance between colloids means that space needs to be filled with solvent molecules). Hence, to simulate several thousand colloids in solution, still a tiny block of material, one would need to track more than a million entities (colloids plus solvent molecules) in the molecular dynamics simulations. Using large-scale parallel computer computations, it is possible to do such a simulation, but only for time scales up to one nano-second (in real-time, the actual simulation would take days to run). The problem is that if hydrodynamic effects are fundamental to the problem one wishes to study, the dynamics are expected to occur on time scales of microseconds to milliseconds, thousands of times longer than the longest molecular dynamics simulation possible.

Continuum hydrodynamic models also have difficulty with this type of problem. In the continuum description, we average over large regions of solvent, allowing modelling on much larger length and time scales. However, if we wish to model a colloidal particle in a solvent, we must treat the particle surface as a moving boundary and must be able to resolve the particle shape with the mesh used for the continuum model. While we can coarse grain the mesh somewhat between the colloids, we still end up with millions of mesh nodes. Further, these nodes must be constantly rearranged because the boundaries (the particles) are moving. This limits a typical simulation to small numbers of colloids; however, one can typically simulate their dynamics on hydrodynamic time scales.

Attempts have been made to merge aspects of molecular dynamics and continuum models. In the simplest of these types of models, the solvent is present only in an effective interaction between the colloids, which are usually modelled as point particles[1]. However, these implicit solvent models still rely on Brownian dynamics, not hydrodynamics. Other than a Stokes drag force, hydrodynamics are not present in these models. Such models are incapable of reproducing many effects seen in experiments. This is most likely due to their inability to capture the local pressure gradients changes that result from colloids displacing the fluid solvent under confinement. For this, the hydrodynamic effects of the solvent must be present in the model.

In this paper we review methods for simulating discrete particles, or extended objects, interacting with a fluid that is simulated on a mesh. In Sec. 2, we look at how forces are transmitted from a fluid to a solid immersed in the fluid both in the continuum case and in a discretized representation of the continuum. An examination of how a velocity-based force coupling between the particles and fluid can be used to generate consistent and conservative forces in a discrete-time simulation is done in Sec. 3. Finally in Sec. 4, we discuss how the volume of an object can be kept fixed during the course of such a simulation.

2 Forces on Objects in a Fluid

At the continuum level, the fluid motion is governed by the continuity and Navier-Stokes equations,

$$\partial_t \rho + \partial_\beta (\rho u_\beta) = 0$$
$$\partial_t (\rho u_\alpha) + \partial_\beta (\rho u_\alpha u_\beta) = \partial_\beta \sigma_{\alpha\beta} + F_\alpha, \tag{1}$$

where ρ is the fluid density, u_α is the velocity, F_α is a local external force, and the total stress tensor $\sigma_{\alpha\beta}$ is

$$\sigma_{\alpha\beta} = -P_{\alpha\beta} + \eta_{\alpha\beta\gamma\nu}\partial_\gamma u_\nu, \tag{2}$$

where the viscosity tensor is typically of the form

$$\eta_{\alpha\beta\gamma\nu} = \eta\left[\delta_{\alpha\gamma}\delta_{\beta\nu} + \delta_{\alpha\nu}\delta_{\beta\gamma} - \frac{2}{3}\delta_{\alpha\beta}\delta_{\gamma\nu}\right] + \Lambda\delta_{\alpha\beta}\delta_{\gamma\nu}. \tag{3}$$

Here, η represents the shear viscosity, and Λ, the bulk viscosity. For simple fluids, $P_{\alpha\beta} = -\rho a_0 \delta_{\alpha\beta}$, where a_0 represents the square of the isothermal speed of sound in the fluid.

The boundary conditions for a fluid are commonly specified as a "no-slip" condition for the velocity at the bounding surface, in addition to the obvious "no-flow" through the surface. While this is almost always a very good assumption at the macroscopic scale, there is often some microscopic slip and possibly even some driving if there is a gradient of the surface energy. At the microscopic scale, the velocity normal to the surface is indeed always zero assuming it is an impenetrable surface. However, the tangential velocity will typically only relax to the value specified by the macroscopic boundary condition in a steady-state situation (which normally still occurs very quickly in the vicinity of the boundary). The boundary condition at a fluid boundary may also be specified by a condition on the stress, which may be more general than a condition on the velocity. In the next subsection we discuss the usual conditions used for sharp interfaces in a continuum

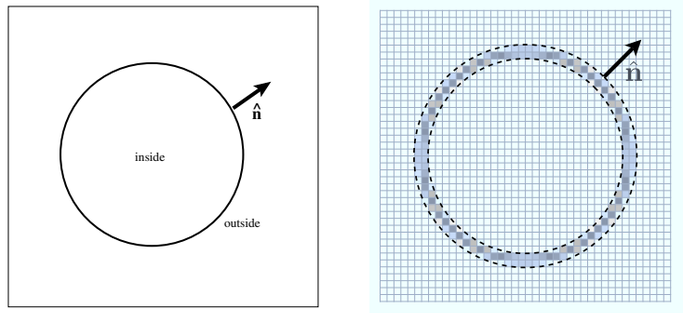

Figure 1. Left: Sharp interface in a continuum fluid. Right: Grid representation from a stencil used to interpolate a set of surface nodes on a circle. The result is a fuzzy interface interpolated onto a fluid mesh.

fluid and then go on to discuss how this translates to a more diffuse interface on a fluid simulation mesh.

2.1 Sharp Interface in a Continuum Fluid

Consider a particle in a fluid like the one in Fig. 1 (left). If the interface between the fluid and particle is sharp, the local force that the fluid outside exerts on the particle is

$$dF_\alpha = n_\beta \sigma_{\alpha\beta} dS, \tag{4}$$

where $\mathbf{n}$ is a unit normal pointing out, $\sigma_{\alpha\beta}$ is the total stress tensor in the fluid (including hydrostatic pressure and viscous stresses) and is measured just outside the surface, and dS is a surface element. If we neglect elastic forces at the interface (such as surface tension) then force balance at the interface would dictate that $n_\beta(\sigma_{\mathrm{o},\alpha\beta} - \sigma_{\mathrm{i},\alpha\beta}) = 0$, where o and i indicate the outside and inside respectively. If we account for elastic properties of the interface in terms of a surface tension s, then we have the more general expression[2]

$$n_\beta(\sigma_{\mathrm{o},\alpha\beta} - \sigma_{\mathrm{i},\alpha\beta}) = s\left(\frac{1}{R_1} + \frac{1}{R_2}\right) + \partial_\alpha s, \tag{5}$$

where R_1 and R_2 are the local principal radii of curvature of the surface. The first term on the right-hand side is the Laplace pressure term and the second term is the Marangoni force. We see that generally this means that the *total stress is not necessarily continuous across a sharp interface*. In the most common situation, the Laplace term results in a jump in the pressure from inside to outside and the Marangoni force results in a jump in the shear stress at the interface (assuming $\sigma_{\alpha\beta} = -p\delta_{\alpha\beta} + \sigma'_{\alpha\beta}$, where p is the pressure and σ' is the viscous stress).

Sometimes it is useful to have the interface represented as a set of boundary conditions for the fluid velocity instead of as a force at the interface. This is typically the case for a solid-fluid interface, rather than an interface between two fluids. In this case, one can

obtain the boundary condition for tangential flow[3]

$$(u_\alpha - v_\alpha)t_\alpha = \frac{L_s}{\eta}\sigma_{\alpha\beta}n_\beta t_\alpha + \frac{L_M}{\eta}t_\alpha \partial_\alpha s, \tag{6}$$

where $\mathbf{u}$ is the fluid velocity at the interface, $\mathbf{v}$ is the velocity of the solid, and t_α is any vector normal to n. The slip length L_s and Marangoni length L_M are material parameters that characterize the interface. They are typically microscopic length scales (thus the conventional approximation of no-slip, or $L_s = 0$). Note that inherent in the sharp interface model is that the boundary conditions depend only on the instantaneous values of the continuum solution extrapolated to the boundary. The relaxation time for the velocity to attain these values can be characterized by an interfacial Reynolds number $Re_i \equiv \rho\xi\delta u/\eta$ where ξ is the true microscopic interface width and δu is the difference in the velocity at the wall and just outside the interfacial region. As ξ is microscopic, Re_i is typically extremely and hence the "steady-state" assumption at the interface is reasonably justified.

2.2 Fuzzy Interface on a Mesh

Consider now a fluid simulated on a discrete mesh. The fluid could be simulated by any of a number of methods, such as a finite-difference scheme, a spectral scheme, or a lattice Boltzmann scheme. We will assume that the mesh on which the fluid is simulated has cells of equal sizes, all of which are cubes, similar to the grid in the right hand side of Fig. 1, pictured in two-dimensions for clarity.

The object immersed in the fluid is also discretized and is represented by a series of nodes on its surface (surface *nodes*, fluid *mesh*). The surface nodes typically do not coincide with the fluid mesh and are commonly arranged as a triangulation of the surface. The surface nodes need to be spaced at distances closer than the spacing of the fluid mesh Δx in order to be able to construct an "impenetrable" surface, although spacings much less than Δx would be inefficient and should be avoided.

In order to interact with the fluid, we need to interpolate quantities such as the density ρ, velocity $\mathbf{u}_i$, and/or the stress $\sigma_{\alpha\beta}$ to the surface, and the surface location and local velocity $\mathbf{v}$ onto the fluid mesh. This is accomplished for each node, labelled by the index i and located at (x_i, y_i, z_i), by assigning weights $\xi_{\alpha i} = \phi_i(x_\alpha)\phi_i(y_\alpha)\phi_i(z_\alpha)$, which satisfy $\Sigma_i \xi_{\alpha i} = 1$, to the nearby fluid mesh sites, labelled α and located at $(x_\alpha, y_\alpha, z_\alpha)$, based on the distance between the site and the particle node. These weights can then be used to perform a weighted sum of, say, the fluid velocity at the nearby sites, to obtain an interpolated fluid velocity at the surface node. Conversely, any force we apply to the surface node due to its interaction with the fluid can, using Newton's third law dictating equal and opposite forces, be transmitted back onto the fluid weighted by $\xi_{\alpha i}$. We describe two such interpolation schemes. The first, which we refer to as the trilinear stencil, assigns weights to each of the 8 nearest grid points according to

$$\phi_j(r_\alpha) = 1 - |\Delta r|, \tag{7}$$

where $|\Delta r|$ corresponds to the scalar absolute value of $\Delta r = (r_\alpha - r_j)/\Delta x$. Here, r_α gives the position of the grid point, r_i is the position of the particle node, and Δx is the lattice spacing. The second method we have implemented is based on the immersed boundary method[4,5]. Here, a smoothing kernel is used to spread the influence of a point

particle to a compact support. For this, we use a 4-point approximation to the Dirac delta function, providing a support of 64 grid points, with grid weights given by[6]

$$\phi_j(r_\alpha) = \begin{cases} \frac{1}{8}(3 - 2\Delta r + \sqrt{1 + 4\Delta r - 4\Delta r^2}), & 0 < \Delta r < 1; \\ \frac{1}{8}(5 - 2\Delta r - \sqrt{-7 + 12\Delta r - 4\Delta r^2}), & 1 < \Delta r < 2; \\ 0, & 2 < \Delta r. \end{cases} \tag{8}$$

The inevitable result of the interpolation stencil is that the interface is spread out onto the fluid mesh (see right-side of Fig. 1). As a result, any force transmitted from the surface to the fluid will also be spread out over a similar area. This broadening of the interface results in the discontinuities in the stress expected from Eq. 5 also becoming diffuse. As a result, if we want to use Eq. 4 to compute the force on the surface from the fluid we need to be at the outer edge of the surface, so step out one mesh unit, Δx, along the surface normal, to the outer dashed line shown in Fig. 1. While this can be done[7], it is a bit cumbersome and worthwhile only if there are forces associated with other degrees of freedom such as those associated with a structured fluid. In a simple fluid it is usually easier to use a force coupling associated with an effective boundary condition for the fluid velocity, something we discuss in detail in the next section.

3 Velocity Coupling

3.1 Continuous Time

A concrete example for which analytic results are available is the case of the objects in the fluid being spheres. If an impenetrable sphere of radius a is moving at a constant speed $\mathbf{v}$ relative to the background fluid (or, more precisely, relative to a fluid that is at rest an infinite distance from the particle) and has no-slip boundary conditions it experiences a drag force of

$$\mathbf{F}_S = -6\pi\eta a\mathbf{v}, \tag{9}$$

as long as $v \equiv |\mathbf{v}|$ is relatively small. If the sphere is in a shear flow, but kept from rotating, it experiences a drag torque of

$$\mathbf{T}_S = 4\pi\eta a^3 s_0 \hat{\mathbf{w}}, \tag{10}$$

where s_0 is the shear rate and $\hat{\mathbf{w}}$ is a unit vector normal to the shear plane. These expressions give us the "Stokes" drag that can be used to verify the accuracy of numerical implementations.

Based on the idea that the total drag force on a sphere is proportional to its velocity relative to the fluid background, people have tried[8] a local force coupling between the surface and fluid of the form

$$\mathbf{F} = \pm\lambda\gamma(\mathbf{v} - \mathbf{u}) \tag{11}$$

where instead of the far-field velocity, the local velocity of the fluid $\mathbf{u}$ is substituted ($+$ sign for force of particle on fluid and $-$ for force of fluid on particle), and λ is the density of nodes on the surface of the sphere. The result is that in this case γ bears little relation to the Stokes drag. In fact, Navier-Stokes equations with this sort of coupling, called the

Brinkman equations, have been studied in detail[8] and it is possible to show[9], that the drag force and torque felt by such a particle, for large γ, is

$$\frac{F}{F_S} = \frac{2\beta^2}{2\beta^2 + 9}, \tag{12}$$

$$\frac{T}{T_S} = \frac{\beta^2}{\beta^2 + 9}, \tag{13}$$

where $\beta = a\sqrt{\frac{\gamma\lambda}{\eta}}$. We can then see that as $\gamma \to \infty$, $F/F_S \to 1 - 9/(2\beta^2)$ so that the approach to Stokes drag (and torque) go like $1/\gamma$ for large γ. As a result, if we want to use Eq. 11 as a force coupling for no-slip particles, we will need to use a large value of γ. Thus, the main disadvantage to using Eq. 11 in a simulation is that it can effectively introduce stiff terms that are likely to cause numerical instabilities. This leads to the temptation to use a small value of γ for ease of computation, and make the particle's "hydrodynamic" radius an effective derived quantity. Unfortunately, this will lead to numerous inconsistencies[10]. For example, the drag force and torque depend on the particle radius in *very* different ways (cf. Eq. 11 and 10) so using these expressions, along with Eq. 13 give very different predictions for an effective hydrodynamic radius at finite γ. For very small particles where thermal fluctuations are important, there will also be a different prediction for the hydrodynamic radius from the diffusion coefficient. However, small γ also causes problems in the regime where there are thermal fluctuations due to dissipation.

As we noted above, the approach to Stokes drag, and hence $v - u \propto 1/\gamma$ for large γ. To see how much dissipation this causes, consider the power output from this force alone (i.e. not counting any dissipation in the fluid):

$$P \sim \mathbf{F} \cdot \mathbf{v} - \mathbf{F} \cdot \mathbf{u} \sim \gamma(\mathbf{v} - \mathbf{u})^2 \propto 1/\gamma, \tag{14}$$

where the last relation is valid in the large γ limit. As a result we see that this coupling results in no dissipation for $\gamma = 0$ (no coupling) and for $\gamma = \infty$, but finite dissipation otherwise. In a fluid with thermal fluctuations, the first case clearly corresponds to the particle velocity and the fluid velocity to be statistically independent variables with both u, v, and $v - u$ being Gaussian random variables with variance $\sim k_B T$. The other extreme, $\gamma \to \infty$ corresponds to a constraint that v and u are identical and $v - u = 0$ so that some degrees of freedom have been removed from the system. It is clear that $\gamma = \infty$ is not practical for a simulation. For finite γ there is dissipation so that, in principle, one might think you should add fluctuations to satisfy the fluctuation-dissipation theorem. However, doing this will keep v and u statistically independent and $\langle (v-u)^2 \rangle \sim k_B T$. If you are modelling a point particle, this may be a reasonable assumption. However, if you are trying to model an impenetrable surface, this is not at all what you want. This brings up the question of whether you can make γ "big enough" so that the dissipation is minimized and is small compared to the typical thermal fluctuations in the fluid. To consider how large γ needs to be, first note that it has units of mass per time. So, given an appropriate mass scale, γ gives us a time scale over which $v - u \to 0$. As most of the dissipation will also occur during this same time scale, this suggests that if this time scale is comparable to the time step of the simulation, the dissipation occurs in a shorter time scale than resolved in the simulation. In fact, as we will see next, it is actually possible to eliminate the dissipation entirely in a discrete time simulation.

3.2 Discrete Time

If we consider the simulation process as a sequence of discrete events, separated in time by Δt, then we can view the interaction of the nodes making up a particle and the fluid mesh as an instantaneous collision[11]. A node has an assigned mass m_v and moves with velocity $\mathbf{v}$. Each tile of the fluid mesh has a mass $\rho\Delta x^3$ and we can use the same stencil weights to determine the total mass of fluid interacting with each surface node, m_u and the velocity of the fluid interpolated at the site of the surface node $\mathbf{u}$. Then, conservation of momentum requires that

$$m_u\mathbf{u}_i + m_v\mathbf{v}_i = m_u\mathbf{u}_f + m_v\mathbf{v}_f, \tag{15}$$

where i and f indicate the initial and final states (before/after collision). This, combined with the conservation of kinetic energy, then requires that

$$|\mathbf{v}_i - \mathbf{u}_i| = |\mathbf{v}_f - \mathbf{u}_f|. \tag{16}$$

We require two more conditions to determine all components of $\mathbf{v}_f$ and $\mathbf{u}_f$. If we are modelling an impenetrable surface, it makes sense to add the bounce condition that

$$\hat{\mathbf{n}} \cdot (\mathbf{v}_i - \mathbf{u}_i) = -\hat{\mathbf{n}} \cdot (\mathbf{v}_f - \mathbf{u}_f). \tag{17}$$

Similarly, no-slip can be imposed via

$$[(\mathbf{v}_i - \mathbf{u}_i) - \hat{\mathbf{n}} \cdot (\mathbf{v}_i - \mathbf{u}_i)] = -\left[(\mathbf{v}_f - \mathbf{u}_f) - \hat{\mathbf{n}} \cdot (\mathbf{v}_f - \mathbf{u}_f)\right]. \tag{18}$$

Complete slip ($L_s \to \infty$) can also be easily implemented by changing the sign on the right-hand side. A finite slip length would be harder to implement and would probably require a stochastic rotation of the tangential relative velocity (the magnitude of the tangential relative velocity is fixed by the conservation of energy and impenetrability constraints above).

For the no-slip case, the resulting change in momentum for the collision can be written as

$$\Delta p_{node} = m_v(\mathbf{v}_f - \mathbf{v}_i) = -\frac{2m_u m_v}{m_u + m_v}(\mathbf{v}_i - \mathbf{u}_i), \tag{19}$$

$$\Delta p_{fluid} = m_u(\mathbf{u}_f - \mathbf{u}_i) = \frac{2m_u m_v}{m_u + m_v}(\mathbf{v}_i - \mathbf{u}_i). \tag{20}$$

Note that in a discrete time simulation, there is no difference between imparting this change in momentum instantaneously or via a force of the form $\mathbf{F} = \Delta\mathbf{p}/\Delta t$ as the momentum transferred over the time Δt will be just $\mathbf{F}\Delta t$. Thus in a discrete time simulation, having a force of the form in Eq. 11 with

$$\gamma = \frac{2m_u m_v}{m_u + m_v}\frac{1}{\Delta t_{collision}}, \tag{21}$$

will result in energy conservation (at least no dissipation from the force coupling although there may still be dissipation within the fluid itself).

There are various tests that can be performed to verify that these conditions result in the desired behaviour. The most obvious are tests of relations Eq. 10 and 11. There are also several other tests that have been used[11] involving hydrodynamic interactions with walls, with other particles, and tests of the fluctuation-dissipation theorem for small particles undergoing Brownian motion in a fluid with thermal fluctuations.

4 Constant Volume

In addition, if the surface is deformable, by connecting the nodes with springs, one often requires that the nodes maintain a constant particle volume, V, (the area enclosed by the node-spring surface) throughout the simulations. While a numerically exact no-flow boundary condition would make the surface impenetrable and thus conserve volume automatically, the conditions above are not numerically exact and so the volume can drift slowly over time. To fix this, a volume constraint force can be introduced, corresponding to the energy,

$$E_{\text{volume}} = \frac{1}{2}(V - V_0)^2, \tag{22}$$

where V_0 is the starting volume of the colloidal particles. Since at each timestep only information about the locations of the surface nodes is available, we employ the method of Hong *et al.*[12] in order to calculate the volume of these particles. This method utilizes the divergence theorem to express the volume of a particle in terms of an integration over its surface,

$$\begin{aligned} \int\int \bigtriangledown \cdot \mathbf{r}\, dV &= \int \mathbf{r} \cdot \hat{\mathbf{n}}\, dS, \\ 2V &= \int \mathbf{r} \cdot \hat{\mathbf{n}}\, dS. \end{aligned} \tag{23}$$

Here, $\mathbf{r}$ is the position vector, and $\hat{\mathbf{n}}$ is the surface normal. If we calculate the surface normal at the midpoint locations between the nodes in 2D, or the centre of a triangle for a triangulated surface in 3D, and convert this integral to a sum at those locations, the volume can be expressed (in 2D) as

$$V = \sum_i \frac{1}{4}\left[(y_{i+1} - y_i)(x_{i+1} + x_i) - (x_{i+1} - x_i)(y_{i+1} + y_i)\right]. \tag{24}$$

Then the corresponding forces, $\partial E_{\text{volume}}/\partial x_{i,\alpha}$ that keep the volume constant are local and easily computed.

5 Concluding Remarks

Long-range hydrodynamic interactions, as described above, have been implemented into the open-source molecular dynamics package, LAMMPS[13], through the creation of a fix, `lb_fluid`. These interactions are treated by interpolating the MD particle density onto a discrete lattice, which is then coupled to the fluid. A thermal lattice-Boltzmann algorithm is used to model the fluid, which includes mass and momentum conserving noise, providing a thermostat for both the particles and the fluid[14].

Acknowledgements

We would like to thank the Natural Science and Engineering Research Council of Canada (NSERC) and the Ontario Ministry of Research and Innovation (ERA award) for financial support, as well as the Shared Hierarchical Academic Research Computing Network (SHARCNet), and the Western Canada Research Grid (WestGrid) for use of their computing facilities.

References

1. W. C. Still, A. Tempczyk, R. C. Hawley, and T. Hendrickson, *Semianalytical Treatment of Solvation for Molecular Mechanics and Dynamics*, J. Am. Chem. Soc. **112**, 6127, 1990.
2. L. D. Landau and E. M. Lifshitz, *Fluid Mechanics, 2nd edition* (Pergamon Press, Oxford, 1987).
3. C. Denniston and M. O. Robbins, *General continuum boundary conditions for miscible binary fluids from molecular dynamics simulations*, J. Chem. Phys. **125**, 214102, 2006.
4. A. M. Roma, C. S. Peskin, M. J. Berger, *An adaptive version of the immersed boundary method*, J. Comput. Phys. **153**, 509-534, 1999.
5. M. C. Lai, C. S. Peskin, *An immersed boundary method with formal second-order accuracy and reduced numerical viscosity*, J. Comput. Phys. **160**, 705-719, 2000.
6. C. S. Peskin, *The immersed boundary method*, Acta Numerica **11**, 479-517, 2002.
7. F. E. Mackay and C. Denniston, *Deformable particles interacting in a nematic liquid crystal*, submitted to Soft Matter.
8. S. T. T. Ollila, T. Ala-Nissila, and C. Denniston, *Hydrodynamic forces on steady and oscillating porous particles*, J. Fluid Mech. **709**, 123, 2012.
9. J. M. Deutch and B. U. Felderhof, *Frictional properties of dilute polymer solutions II. The effect of preaveraging*, J. Chem. Phys. **62**, 2398, 1975;
   B. U. Felderhof, *Frictional properties of dilute polymer solutions III. Translational friction coefficient*, Physica A **80**, 63-75, 1975.
10. S. T. T. Ollila, C. J. Smith, T. Ala-Nissila, and C. Denniston, *The hydrodynamic radius of particles in the hybrid lattice Boltzmann-molecular dynamics method*, Multiscale Model. Simul., in press.
11. F. E. Mackay and C. Denniston, *Coupling MD particles to a lattice-Boltzmann fluid through the use of conservative forces*, J. Comp. Phys., in press.
12. M. Hong, S. Jung, M. Choi and S. Welch, *Fast Volume Preservation for a Mass-Spring System*, IEEE Comput. Graph. **26**, 83-91, 2006.
13. S. J. Plimpton, *Fast parallel algorithms for -range molecular dynamics*, J. Comp. Phys. **117**, 1–19, 1995.
14. F. E. Mackay, S. T. T. Ollila, and C. Denniston, *Hydrodynamic forces implemented into LAMMPS through a lattice-Boltzmann fluid*, submitted to Comp. Phys. Commun.

Simulating Colloids and Self-Propelled Particles with Fully Resolved Hydrodynamics Using the Smoothed Profile Method (SPM)

Ryoichi Yamamoto, John J. Molina, and Rei Tatsumi

Department of Chemical Engineering, Kyoto University, Kyoto 615-8510, Japan
E-mail: {*ryoichi, john, tatsumi*}*@cheme.kyoto-u.ac.jp*

The smoothed profile method (SPM) provides an efficient numerical scheme for coupling continuum fluid dynamics with moving dispersed particles using a smeared interface between the fluids and the particles. The SPM has been successfully applied to directly simulate several dynamical problems of colloidal dispersions in incompressible fluids, including those involving sedimentation, diffusion, coagulation, rheology, and tumbling motion in shear flow as well as electrophoresis in external electric fields. More recently, the SPM was extended to two important problems. The first extension simulates colloidal particles in compressible host fluids, whereas the second extension simulates self-propelled swimming particles. A comprehensive summary of SPM is provided in this paper.

1 Introduction

Interparticle interactions in colloidal dispersions mainly consist of thermodynamic potential interactions as well as hydrodynamic interactions. Whereas the former applies to both static and dynamic situations, the latter only applies to dynamic situations. Although thermodynamic interactions in static situations have been studied extensively and are treated as effective interactions, the nature of dynamic interactions is poorly understood. Because hydrodynamic interactions are essentially long-range, many-body effects, they are extremely difficult to study using analytical means alone. Numerical simulations can be used to investigate the role of hydrodynamic interactions in colloidal dynamics.

Several numerical methods have been developed to simulate the dynamics of colloidal dispersions. Two of the most well-known methods include Stokesian dynamics[1] and the Eulerian–Lagrangian method[2]. The former is the most widely used method because of its proper treatment of hydrodynamic interactions between spherical particles in a Newtonian fluid at zero Reynolds number. Furthermore, it can be implemented as a $O(N)$ scheme for N particles by utilizing the fast multi-pole method[3]. However, it is not easy to address dense dispersions and dispersions consisting of non-spherical particles by means of Stokesian dynamics due to the complicated mathematical structures used in Stokesian dynamics. In contrast, the Eulerian–Lagrangian method is a very natural and sensible approach for stimulating solid particles. It is possible to apply this method to dispersions consisting of many particles with different shapes. However, numerical efficiencies arise from the following concerns: i) the re-construction of irregular meshes according to the temporal particle position is necessary for every simulation step, and ii) the Navier–Stokes equation must be solved with boundary conditions imposed on the surfaces of all colloidal particles. Thus, these computational demands are particularly cumbersome for systems involving many particles, even if the shapes are all spherical.

To overcome problems arising from the particle-fluid interface in the Eulerian–Lagrangian method, we have developed an efficient direct numerical simulation (DNS) method for colloidal dispersions. This method was named the "smoothed profile method (SPM)" because the original sharp interface between the colloids and solvent is replaced by a smeared out, smoothed interface with a finite thickness[4–20]. This simple modification greatly improves the resulting quality of the of numerical computations in comparison with the original Eulerian–Lagrangian method for the following reasons:

1. Regular fixed Cartesian coordinates can be used for many particle systems by defining a particle shape instead of providing boundary-fitted coordinates. The particle-fluid interface has a finite volume ($\propto \pi a^{d-1}\xi$, with a and d as the particle radius and system dimension) supported by multiple grid points. Thus, the round particles can be treated in a fixed Cartesian coordinates without any difficulties. The simulation scheme is thus free from the mesh re-construction problem that significantly suppresses the computational efficiency of the Eulerian–Lagrangian method. In addition, the simple Cartesian coordinate enables the use of periodic boundary conditions as well as fast Fourier transformations (FFT).

2. At the particle-fluid interfaces, the velocity component in the direction normal to the interface of the host fluid must be equal to that of the particle. In the Eulerian–Lagrangian method, this non-penetration condition is imposed by the Navier–Stokes equation as the boundary condition defined for the particle-fluid interface. In the SPM, however, this condition is automatically satisfied by an incompressibility condition on the entire domain.

3. The computational demands for this method include sensitivity to the number of grid points (volume of the total system). Nevertheless, because the method is insensitive to the number of particles, it is suitable for simulating dense colloidal dispersions.

The SPM has been successfully used to directly simulate various dynamical problems of colloidal dispersion in incompressible fluids, including sedimentation[20], diffusion[9,12,13], coagulation[8,19], rheology[11,14,17], tumbling motion in shear flow[15], and electrophoresis in external electric fields[7,10]. Several simulation methods similar in spirit to the SPM have also been proposed in recent publications[22–25]. A comprehensive summary of SPM is provided in this study including the recent key extensions for stimulating colloidal particles in compressible host fluids[18] and also for stimulating the self-propelled swimming of particles[21].

2 Colloids in Incompressible Fluids

2.1 Working Equations

The motion of the host fluid is determined by the Navier-Stokes equation with the following incompressibility condition:

$$\nabla \cdot \boldsymbol{u}_f = 0 \tag{1}$$

$$\rho \left(\partial_t + \boldsymbol{u}_f \cdot \nabla\right) \boldsymbol{u}_f = \nabla \cdot \boldsymbol{\sigma} \tag{2}$$

where ρ is the total mass density of the fluid, $\boldsymbol{u}_f$ is the host fluid velocity field, $\boldsymbol{\sigma}$ is the stress tensor

$$\boldsymbol{\sigma} = -p\boldsymbol{I} + \boldsymbol{\sigma}' \tag{3}$$

$$\boldsymbol{\sigma}' = \eta\left[\nabla\boldsymbol{u}_f + (\nabla\boldsymbol{u}_f)^{\mathrm{t}}\right] \tag{4}$$

and η is the shear viscosity of the fluid. Consider a mono-disperse system containing N-spherical particles with a radius a, mass M_p, and moment of inertia $\boldsymbol{I}_p = 2/5M_pa^2\boldsymbol{I}$ (with $\boldsymbol{I}$ the unit tensor). The evolution of colloids is described by the Newton-Euler equations[28],

$$\begin{aligned} \dot{\boldsymbol{R}}_i &= \boldsymbol{V}_i & \dot{\boldsymbol{Q}}_i &= \boldsymbol{Q}_i\,\mathrm{skew}\,(\boldsymbol{\Omega}_i) \\ M_p\dot{\boldsymbol{V}}_i &= \boldsymbol{F}_i^{\mathrm{H}} + \boldsymbol{F}_i^{\mathrm{C}} + \boldsymbol{F}_i^{\mathrm{ext}} & \boldsymbol{I}_p\cdot\dot{\boldsymbol{\Omega}}_i &= \boldsymbol{N}_i^{\mathrm{H}} + \boldsymbol{N}^{\mathrm{ext}} \end{aligned} \tag{5}$$

where $\boldsymbol{R}_i$ and $\boldsymbol{V}_i$ denote the centre of mass positions and the velocity of the particle i, respectively, and $\boldsymbol{Q}_i$ is the orientation matrix[b]. Hence, $\boldsymbol{\Omega}_i$ the angular velocity and skew $(\boldsymbol{\Omega}_i)$ is the skew-symmetric angular velocity matrix:

$$\mathrm{skew}(\boldsymbol{\Omega}_i) = \begin{pmatrix} 0 & -\Omega_i^z & \Omega_i^y \\ \Omega_i^z & 0 & -\Omega_i^x \\ -\Omega_i^y & \Omega_i^x & 0 \end{pmatrix} \tag{6}$$

The forces on the particles are comprised of hydrodynamic contributions arising from fluid-particle interactions $\boldsymbol{F}^{\mathrm{H}}$, colloid-colloid interactions due to the core particle potential $\boldsymbol{F}^{\mathrm{C}}$ (which prevents particle overlap), and a possible external field contribution $\boldsymbol{F}^{\mathrm{ext}}$ (such as gravity). Likewise, the torques on the particles can be divided into a hydrodynamic $\boldsymbol{N}^{\mathrm{H}}$ and an external contribution $\boldsymbol{N}^{\mathrm{ext}}$ (for simplicity, the particle-particle interactions are assumed to be described by a radial potential). Subsequently, we consider buoyancy-neutral particles, for which $\boldsymbol{F}^{\mathrm{ext}} = \boldsymbol{N}^{\mathrm{ext}} = 0$. Finally, the conservation of momentum between the fluid and the particles implies the following hydrodynamic force and torque on the i-th particle:

$$\boldsymbol{F}_i^{\mathrm{H}} = \int \mathrm{d}\boldsymbol{S}_i\cdot\boldsymbol{\sigma} \tag{7}$$

$$\boldsymbol{N}_i^{\mathrm{H}} = \int (\boldsymbol{x} - \boldsymbol{R}_i)\times(\mathrm{d}\boldsymbol{S}_i\cdot\boldsymbol{\sigma}) \tag{8}$$

where $\int \mathrm{d}\boldsymbol{S}_i$ indicates an integral over the surface of the particle. In addition, thermal fluctuations can be introduced by adding a random stress tensor $\boldsymbol{s}$in Eq. 3, that satisfies the fluctuation-dissipation relation:[26]

$$\langle s_{ik}(\boldsymbol{x},t)s_{jl}(\boldsymbol{x}',t')\rangle = 2k_BT\eta(\delta_{ij}\delta_{kl} + \delta_{il}\delta_{kj})\delta(\boldsymbol{x}-\boldsymbol{x}')\delta(t-t'), \tag{9}$$

where k_B is the Boltzmann constant, T is the temperature. Alternatively, it is also possible to introduce thermal fluctuations by adding Langevin random forces and torque to Eq. 5[9,11–13].

[b]For numerical stability, we use quaternion instead of rotation matrices to represent the rigid body dynamics of the particles.

2.2 Simulation Procedure for Incompressible Fluids

We now present the computational algorithm used to simulate the motion of spherical particles using the SPM. We require that all field variables are defined over the entire computational domain (fluid + particle). The concentration field for the colloids is described as follows:

$$\phi(\boldsymbol{x},t) = \sum_{i=1}^{N} \phi_i(\boldsymbol{x},t), \tag{10}$$

where $\phi_i \in [0,1]$ is the smooth profile field of particle i. This field is defined as unity within the particle domain, as zero in the fluid domain, and as a smooth interpolation between the two extremes within the interface region. Several possible mathematical forms exist for $\phi_i(\boldsymbol{x})$, however, we adopted the following definition of ϕ_i:

$$\phi_i(\boldsymbol{x}) = g(|\boldsymbol{x} - \boldsymbol{R}_i|), \tag{11}$$

$$g(x) = \frac{h((a+\xi/2)-x)}{h((a+\xi/2)-x) + h(x-(a-\xi/2))}, \tag{12}$$

$$h(x) = \begin{cases} \exp\left(-\Delta^2/x^2\right) & x \geq 0, \\ 0 & x < 0. \end{cases} \tag{13}$$

where a, ξ, and Δ are the radius of the particle, the interfacial thickness, and lattice spacing, respectively. The particle velocity field is defined in a similar fashion:

$$\phi \boldsymbol{u}_p(\boldsymbol{x},t) = \sum_{i=1}^{N} \left\{\boldsymbol{V}_i(t) + \boldsymbol{\Omega}_i(t) \times \boldsymbol{r}_i(t)\right\} \phi_i(\boldsymbol{x},t) \tag{14}$$

with $\boldsymbol{r}_i = \boldsymbol{x} - \boldsymbol{R}_i$, which allows one to define the total fluid velocity field using the following expression:

$$\boldsymbol{u}(\boldsymbol{x},t) \equiv (1-\phi)\boldsymbol{u}_f + \phi \boldsymbol{u}_p \tag{15}$$

where the incompressibility condition is satisfied over the entire domain $\nabla \cdot \boldsymbol{u} = 0$. The evolution equation for $\boldsymbol{u}$ is then derived assuming momentum-conservation between fluid and particles[6,10]

$$\rho\left(\partial_t + \boldsymbol{u}\cdot\nabla\right)\boldsymbol{u} = \nabla\cdot\boldsymbol{\sigma} + \rho\phi\boldsymbol{f}_p \tag{16}$$

where $\phi\boldsymbol{f}_p$ represents the force density field needed to maintain rigidity constraints on the particle velocity field.

We use a fractional step approach to update the total velocity field. Let $\boldsymbol{u}^n$ be the field at time $t_n = nh$ (h is the time interval).

i) We first solve for advection and hydrodynamic viscous stress terms, and we then propagate the particle positions (orientations) using the current particle velocities,

which affords the following relation:

$$\boldsymbol{u}^* = \boldsymbol{u}^n + \int_{t_n}^{t_n+h} \mathrm{d}s\, \nabla \cdot \left[\frac{1}{\rho}\left(-p^*\boldsymbol{I} + \boldsymbol{\sigma}'\right) - \boldsymbol{u}\boldsymbol{u}\right] \tag{17}$$

$$\boldsymbol{R}_i^{n+1} = \boldsymbol{R}_i^n + \int_{t_n}^{t_n+h} \mathrm{d}s\, \boldsymbol{V}_i \tag{18}$$

$$\boldsymbol{Q}_i^{n+1} = \boldsymbol{Q}_i^n + \int_{t_n}^{t_n+h} \mathrm{d}s\, \boldsymbol{Q}_i \mathrm{skew}\left(\boldsymbol{\Omega}_i\right) \tag{19}$$

where the pressure term p^* in Eq. 17 is determined by the incompressibility condition $\nabla \cdot \boldsymbol{u}^* = 0$. The remaining updating procedure imposes a rigidity constraint on the velocity field.

ii) The hydrodynamic force and torque exerted by the fluid on the colloids is determined by assuming momentum conservation. The time integrated hydrodynamic force and torque over a period h are equal to the momentum exchange over the particle domain

$$\left[\int_{t_n}^{t_n+h} \mathrm{d}s\, \boldsymbol{F}_i^{\mathrm{H}}\right] = \int \mathrm{d}\boldsymbol{x}\, \rho\phi_i^{n+1}\left(\boldsymbol{u}^* - \boldsymbol{u}_p^n\right) \tag{20}$$

$$\left[\int_{t_n}^{t_n+h} \mathrm{d}s\, \boldsymbol{N}_i^{\mathrm{H}}\right] = \int \mathrm{d}\boldsymbol{x}\, \left[\boldsymbol{r}_i^{n+1} \times \rho\phi_i^{n+1}\left(\boldsymbol{u}^* - \boldsymbol{u}_p^n\right)\right] \tag{21}$$

Based on this and other forces acting on the colloids, the particles velocities are updated as follows:

$$\boldsymbol{V}_i^{n+1} = \boldsymbol{V}_i^n + M_p^{-1}\left[\int_{t_n}^{t_n+h} \mathrm{d}s\, \boldsymbol{F}_i^{\mathrm{H}}\right] + M_p^{-1}\left[\int_{t_n}^{t_n+h} \mathrm{d}s\, \left(\boldsymbol{F}_i^{\mathrm{C}} + \boldsymbol{F}_i^{\mathrm{ext}}\right)\right] \tag{22}$$

$$\boldsymbol{\Omega}_i^{n+1} = \boldsymbol{\Omega}_i^n + \boldsymbol{I}_p^{-1} \cdot \left[\int_{t_n}^{t_n+h} \mathrm{d}s\, \boldsymbol{N}_i^{\mathrm{H}}\right] + \boldsymbol{I}_p^{-1} \cdot \left[\int_{t_n}^{t_n+h} \mathrm{d}s\, \boldsymbol{N}_i^{\mathrm{ext}}\right] \tag{23}$$

iii) Finally, the resulting particle velocity field $\phi^{n+1}\boldsymbol{u}_p^{n+1}$ is enforced on the total velocity field as follows:

$$\boldsymbol{u}^{n+1} = \boldsymbol{u}^* + \left[\int_{t_n}^{t_n+h} \mathrm{d}s\, \phi \boldsymbol{f}_p\right] \tag{24}$$

$$\left[\int_{t_n}^{t_n+h} \mathrm{d}s\, \phi \boldsymbol{f}_p\right] = \phi^{n+1}\left(\boldsymbol{u}_p^{n+1} - \boldsymbol{u}^*\right) - \frac{h}{\rho}\nabla p_{\mathrm{p}} \tag{25}$$

wherein the pressure is due to the rigidity constraint obtained from the incompressibility condition $\nabla \cdot \boldsymbol{u}^{n+1} = 0$. The total pressure field is thus obtained as $p = p^* + p_{\mathrm{p}}$.

The above procedure defines the consistent time-propagation, $\{\boldsymbol{u}^n; \boldsymbol{R}_i^n, \boldsymbol{Q}_i^n, \boldsymbol{\Omega}_i^n\} \rightarrow \{\boldsymbol{u}^{n+1}; \boldsymbol{R}_i^{n+1}, \boldsymbol{Q}_i^{n+1}, \boldsymbol{\Omega}_i^{n+1}\}$, to simulate colloidal particles in incompressible fluids.

3 Colloids in Compressible Fluids

3.1 Working Equations

The hydrodynamic equations consist of three conservation laws concerning mass, momentum, and energy. The conservation equations of mass and momentum for incompressible fluids are described by the following:

$$\frac{\partial \rho}{\partial t} + \nabla \cdot \boldsymbol{m} = 0, \tag{26}$$

$$\frac{\partial \boldsymbol{m}}{\partial t} + \nabla \cdot (\boldsymbol{m}\boldsymbol{u}) = \nabla \cdot \boldsymbol{\sigma} + \rho\phi \boldsymbol{f}_p, \tag{27}$$

where $\boldsymbol{m}(\boldsymbol{r}, t) = \rho(\boldsymbol{r}, t)\boldsymbol{u}(\boldsymbol{x}, t)$ is the momentum density field. We consider a compressible Newtonian fluid, and the stress tensor is described as follows:

$$\boldsymbol{\sigma} = -p\boldsymbol{I} + \eta[\nabla \boldsymbol{u} + (\nabla \boldsymbol{u})^{\mathrm{t}}] + \left(\eta_v - \frac{2}{3}\eta\right)(\nabla \cdot \boldsymbol{u})\boldsymbol{I}, \tag{28}$$

where $p(\boldsymbol{r}, t)$ is the pressure, η is the shear viscosity, and η_v is the bulk viscosity. A body force $\rho\phi\boldsymbol{f}_p$ is also added to satisfy the rigidity of the particles. Additionally, we assume a barotropic fluid described by $p = p(\rho)$, with a pressure gradient that is proportional to the density:

$$\nabla p = c^2 \nabla \rho, \tag{29}$$

where c is the speed of sound in the fluid. Eqs. 26-29 are closed to variables ρ, $\boldsymbol{m}$, and p; therefore, energy conservation does not need to be considered for barotropic fluids.

The motion of the dispersed particles is governed by Newton-Euler equations of motion Eq. 5. The effect of thermal fluctuations on the particles dynamics is important when the particle size is on the order of a micrometer or smaller. Fluctuations were introduced using a random stress tensor $\boldsymbol{s}$, which is added to the stress tensor Eq. 28. The random stress is a stochastic variable satisfying the fluctuation-dissipation relation[26]:

$$\langle s_{ij}(\boldsymbol{r}, t) s_{kl}(\boldsymbol{r}', t')\rangle = 2k_B T \eta_{ijkl} \delta(\boldsymbol{r}' - \boldsymbol{r})\delta(t' - t), \tag{30}$$

and

$$\eta_{ijkl} = \eta(\delta_{ik}\delta_{jl} + \delta_{il}\delta_{jk}) + \left(\eta_v - \frac{2}{3}\eta\right)\delta_{ij}\delta_{kl}. \tag{31}$$

Brownian motion of the dispersed particles is induced by the random stresses acting on the fluid. Thermal fluctuations can be introduced using the Langevin approach, wherein random forces are exerted on the particles[9,11–13]. However, this approach does not accurately represent the short-time dynamics of the system because the autocorrelation time of the hydrodynamic force acting on the particles is neglected. Therefore, the fluctuating hydrodynamics approach is more appropriate for investigating dynamics at a time scale of sound propagation.

3.2 Simulation Procedure for Compressible Fluids

In this section, the time-discretized evolution of the equations is derived for colloidal dispersions in compressible fluids. The time evolution of the fluid is determined using the following steps:

i) The mass and momentum density changes associated with sound propagation are calculated using the following equations:

$$\rho^{n+1} = \rho^n - \int_{t_n}^{t_n+h} \mathrm{d}s\, \nabla \cdot \boldsymbol{m}, \tag{32}$$

$$\boldsymbol{m}^* = \boldsymbol{m}^n - c^2 \int_{t_n}^{t_n+h} \mathrm{d}s\, \nabla \rho. \tag{33}$$

When we assume a periodic boundary condition and use the Fourier spectral method, a semi-implicit scheme becomes feasible[27]. This situation eliminates restrictions on time increments with a small compressibility factor ε.

ii) The time evolution of the advection and viscous diffusion terms are calculated using the following equations:

$$\boldsymbol{m}^{**} = \boldsymbol{m}^* + \int_{t_n}^{t_n+h} \mathrm{d}s\, \nabla \cdot (\boldsymbol{\sigma}' - \boldsymbol{m}\boldsymbol{u}), \tag{34}$$

where $\boldsymbol{\sigma}'$ is the dissipative stress defined in Eq. 3.

iii) In concert with the advection of the particle domain, the position (orientation) of each dispersed particle evolves according to the following equations:

$$\boldsymbol{R}_i^{n+1} = \boldsymbol{R}_i^n + \int_{t_n}^{t_n+h} \mathrm{d}s\, \boldsymbol{V}_i \tag{35}$$

$$\boldsymbol{Q}_i^{n+1} = \boldsymbol{Q}_i^n + \int_{t_n}^{t_n+h} \mathrm{d}s\, \boldsymbol{Q}_i \mathrm{skew}\left(\boldsymbol{\Omega}_i\right). \tag{36}$$

iv) The hydrodynamic force and torque are derived by considering the conservation of momentum. The time-integrated hydrodynamic force and torque are computed using the following equations:

$$\int_{t_n}^{t_n+h} \mathrm{d}s\, \boldsymbol{F}_i^H = \int \mathrm{d}\boldsymbol{x}\, \phi_i^{n+1}(\boldsymbol{m}^{**} - \rho^{n+1}\boldsymbol{u}_p^n), \tag{37}$$

$$\int_{t_n}^{t_n+h} \mathrm{d}s\, \boldsymbol{N}_i^H = \int \mathrm{d}\boldsymbol{x}\, [(\boldsymbol{r} - \boldsymbol{R}_i^{n+1}) \times \phi_i^{n+1}(\boldsymbol{m}^{**} - \rho^{n+1}\boldsymbol{s}_p^n)]. \tag{38}$$

With these and other forces acting on the particles, the translational and rotational velocities of each dispersed particle evolve according to the following equations:

$$\boldsymbol{V}_i^{n+1} = \boldsymbol{V}_i^n + M_p^{-1} \int_{t_n}^{t_n+h} \mathrm{d}s\, (\boldsymbol{F}_i^H + \boldsymbol{F}_i^C), \tag{39}$$

$$\boldsymbol{\Omega}_i^{n+1} = \boldsymbol{\Omega}_i^n + \boldsymbol{I}_p^{-1} \cdot \int_{t_n}^{t_n+h} \mathrm{d}s\, \boldsymbol{N}_i^H. \tag{40}$$

v) The updated velocity of the particle region is imposed on the velocity field as the volume force $\rho\phi\boldsymbol{f}_p$.

$$\boldsymbol{m}^{n+1} = \boldsymbol{m}^{**} + \int_{t_n}^{t_n+h} \mathrm{d}s\, \rho\phi\boldsymbol{f}_p, \tag{41}$$

$$\int_{t_n}^{t_n+h} \mathrm{d}s\, \rho\phi\boldsymbol{f}_p = \phi^{n+1}(\rho^{n+1}\boldsymbol{u}_p^{n+1} - \boldsymbol{m}^{**}). \tag{42}$$

In the case of an incompressible fluid, the pressure is spontaneously determined by the solenoid condition of the velocity field. In contrast, in this case, the pressure and mass density variations are independent of the velocity field.

The above procedure defines the consistent time-propagation, $\{\rho^n, \boldsymbol{m}^n; \boldsymbol{R}_i^n, \boldsymbol{Q}_i^n, \boldsymbol{\Omega}_i^n\} \to \{\rho^{n+1}, \boldsymbol{m}^{n+1}; \boldsymbol{R}_i^{n+1}, \boldsymbol{Q}_i^{n+1}, \boldsymbol{\Omega}_i^{n+1}\}$, to simulate colloidal particles in compressible fluids.

4 Self-Propelled Particles

4.1 Squirmer Model

We consider a simple model of self-propelled spherical swimmers, originally introduced by Lighthill[29] and later extended by Blake[30], which move due to a self-generated surface-tangential velocity $\boldsymbol{u}^s$. This specific mechanism was proposed as a model for an ideal ciliate particle, in which the synchronized beating of the cilia at the surface gives rise to net motion in the absence of any external fields. If one assumes that the displacements of this cilia envelope are purely tangential, then the effective (time-averaged) slip velocity for these *squirmers* is described by the following equation[30]:

$$\boldsymbol{u}^s(\hat{\boldsymbol{r}}) = \sum_{n=1}^{\infty} \frac{2}{n\,(n+1)} B_n\,(\hat{\boldsymbol{e}}\cdot\hat{\boldsymbol{r}}\hat{\boldsymbol{r}} - \hat{\boldsymbol{e}})\,P_n'\,(\hat{\boldsymbol{e}}\cdot\hat{\boldsymbol{r}}) \tag{43}$$

where $\hat{\boldsymbol{e}}$ is the squirmer's fixed swimming axis (*i.e.*, we consider that each squirmer carries with it a fixed coordinate system that determines its preferred swimming direction at each instant), $\hat{\boldsymbol{r}}$ is a unit vector from the particle centre to a point on the surface, P_n' is the derivative of the n-th order Legendre polynomial, and B_n is the amplitude of the corresponding mode.

When all squirming modes higher than three are neglected, $B_n = 0\,(n \geq 3)$, the following simple expression for the surface tangential velocity as a function of polar angle $\theta = \cos^{-1}(\hat{\boldsymbol{r}}\cdot\hat{\boldsymbol{e}})$, is obtained:

$$\boldsymbol{u}^s(\theta) = B_1\left(\sin\theta + \frac{\alpha}{2}\sin 2\theta\right) \tag{44}$$

where $\alpha = B_2/B_1$ determines whether the swimmer is a pusher ($\alpha < 0$) or a puller ($\alpha > 0$). A schematic representation of the flow profile generated by these two types of swimmers is provided in Fig. 1. An example of the former include spermatozoa and most bacteria, whereas the latter includes unicellular algae *Chlamydomonas*. Although the squirmer model we adopt does not include a detailed propulsion mechanism, it is capable of distinguishing between pushers/pullers and provides an adequate approximation for the far-field flow profile generated by these swimmers.

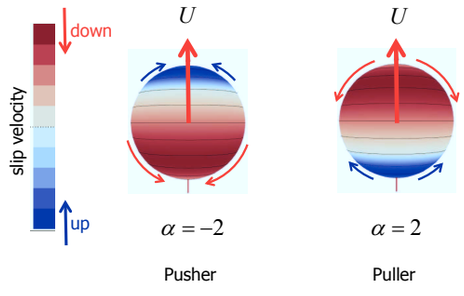

Figure 1. Schematic representation of the flow profiles generated by a pusher (left) and a puller (right). In both cases, the particle's swimming direction is towards the top of the page.

For Newtonian fluids, which is the only case considered here, the swimming speed U of the squirmer is determined uniquely by the first mode B_1, irrespective of the size of the particle, as $U = 2/3B_1$, while the second mode gives the strength of the stresslet[31,32]. In the Stokes regime, the velocity field generated by a single such squirmer was solved analytically by Ishikawa et al.[31], providing the following expression in the laboratory frame (fluid at rest far away from the particle):

$$\boldsymbol{u}(\boldsymbol{r}) = B_1 \frac{a^2}{r^2}\left[\frac{a}{r}\left(\frac{2}{3}\hat{\boldsymbol{e}} + \sin\theta\,\hat{\boldsymbol{\theta}}\right) + \frac{\alpha}{2}\left\{\left(\frac{a^2}{r^2} - 1\right)\left(3\cos^2\theta - 1\right)\hat{\boldsymbol{r}} + \frac{a^2}{r^2}\sin 2\theta\,\hat{\boldsymbol{\theta}}\right\}\right] \tag{45}$$

where a is the radius of the particle. Notice that for neutral swimmers ($\alpha = 0$), the velocity field decays as r^{-3}, whereas for pushers/pullers ($\alpha \neq 0$), the velocity field decays as r^{-2}. In contrast, the velocity field for a sedimenting particle (or a particle experiencing a net body force) decays as r^{-1} [33]. This observation will have important consequences on the hydrodynamic interactions describing suspensions of swimmers.

4.2 Simulation Procedure for Squirmers

We now present the computational algorithm used to simulate the motion of spherical particles, with a given surface tangential slip velocity $\boldsymbol{u}^s$ using the SPM. The evolution equation for $\boldsymbol{u}$ is then derived by assuming momentum-conservation between the fluid and particles[6,10]

$$\rho\left(\partial_t + \boldsymbol{u}\cdot\nabla\right)\boldsymbol{u} = \nabla\cdot\boldsymbol{\sigma} + \rho\phi\boldsymbol{f}_p + \rho\boldsymbol{f}_{sq} \tag{46}$$

where $\phi\boldsymbol{f}_p$ represents the force density field needed to maintain the rigidity constraint on the particle velocity field and $\boldsymbol{f}_{sq}$ is the force density field generated by the squirming motion of the particles. The motion of the dispersed particles is governed by Newton-Euler equations of motion Eq. 5.

We use the fractional step approach to update the total velocity field.

i) We first solve for the advection and hydrodynamic viscous stress terms, and we then propagate the particle positions (orientations) using the current particle velocities. This operation yields the following results:

$$\boldsymbol{u}^* = \boldsymbol{u}^n + \int_{t_n}^{t_n+h} \mathrm{d}s\, \nabla \cdot \left[\frac{1}{\rho}\left(-p^*\boldsymbol{I} + \boldsymbol{\sigma}'\right) - \boldsymbol{u}\boldsymbol{u}\right] \tag{47}$$

$$\boldsymbol{R}_i^{n+1} = \boldsymbol{R}_i^n + \int_{t_n}^{t_n+h} \mathrm{d}s\, \boldsymbol{V}_i \tag{48}$$

$$\boldsymbol{Q}_i^{n+1} = \boldsymbol{Q}_i^n + \int_{t_n}^{t_n+h} \mathrm{d}s\, \boldsymbol{Q}_i \mathrm{skew}\left(\boldsymbol{\Omega}_i\right) \tag{49}$$

where the pressure term p^* in Eq. 47 is determined by the incompressibility condition $\nabla \cdot \boldsymbol{u}^* = 0$. The remaining updating procedure applies to the slip condition at the particle boundary as well as the rigidity constraint on the velocity field.

ii) We now consider the momentum change needed to maintain the slip velocity at the surface of each of the squirmers, where the slip profile $\boldsymbol{u}^s$ is imposed with respect to the particle velocities $\{\boldsymbol{V}_i'; \boldsymbol{\Omega}_i'\}$, using the previously updated positions and orientations orientations $\{\boldsymbol{R}_i^{n+1}; \boldsymbol{Q}_i^{n+1}\}$. We note that at this point we do not yet know the correct updated particle velocities $\{\boldsymbol{V}_i^{n+1}; \boldsymbol{\Omega}_i^{n+1}\}$, which are the values that should be used when enforcing the surface slip profile $\boldsymbol{V}_i' = \boldsymbol{V}_i^{n+1}$ ($\boldsymbol{\Omega}_i' = \boldsymbol{\Omega}_i^{n+1}$). Therefore, we adopt an iterative solution, and as an initial guess, we use the particle velocities at the previous time step, i.e., $\boldsymbol{V}_i' = \boldsymbol{V}_i^n$ ($\boldsymbol{\Omega}_i' = \boldsymbol{\Omega}_i^n$). The updated total velocity field is now obtained using the following:

$$\boldsymbol{u}^{**} = \boldsymbol{u}^* + \left[\int_{t_n}^{t_n+h} \mathrm{d}s\, \boldsymbol{f}_{\mathrm{sq}}\right] \tag{50}$$

$$\begin{aligned}\left[\int_{t_n}^{t_n+h} \mathrm{d}s\, \boldsymbol{f}_{\mathrm{sq}}\right] = \boldsymbol{u}^* &+ \sum_{i=1}^{N} \varphi_i \left(\boldsymbol{V}_i' + \boldsymbol{\Omega}_i' \times \boldsymbol{r}_i + \boldsymbol{u}_i^s - \boldsymbol{u}^*\right) \\ &+ \sum_{i=1}^{N} \phi_i \left(\delta\boldsymbol{V}_i + \delta\boldsymbol{\Omega}_i \times \boldsymbol{r}_i\right) - \frac{h}{\rho}\nabla p_{sq}\end{aligned} \tag{51}$$

The second term on the right hand side of Eq. 51 imposes a slip velocity profile $\boldsymbol{u}^s$ at the surface of each of the squirmers where $\varphi_i \propto (1-\phi_i)\,|\nabla\phi_i|$ is a smooth surface profile function that is non-zero only within the interface domain of the squirmer (normalized to have a maximum value of one), and zero everywhere else (the red arrows in Fig. 2). The third term adds a counter-flow entirely within the particle domain, such that local momentum conservation is preserved (the blue arrows in Fig. 2). Assuming rigid-body motion, with velocities $\delta\boldsymbol{V}_i$ and $\delta\boldsymbol{\Omega}_i$, this requires

$$\int \mathrm{d}\boldsymbol{x}\, \phi_i \left(\delta\boldsymbol{V}_i + \delta\boldsymbol{\Omega}_i \times \boldsymbol{r}_i\right) = -\int \mathrm{d}\boldsymbol{x}\, \varphi_i \left(\boldsymbol{V}_i' + \boldsymbol{\Omega}_i' \times \boldsymbol{r}_i + \boldsymbol{u}_i^s - \boldsymbol{u}^*\right) \tag{52}$$

$$\int \mathrm{d}\boldsymbol{x}\, \boldsymbol{r}_i \times \phi_i \left(\delta\boldsymbol{V}_i + \delta\boldsymbol{\Omega}_i \times \boldsymbol{r}_i\right) = -\int \mathrm{d}\boldsymbol{x}\, \boldsymbol{r}_i \times \varphi_i \left(\boldsymbol{V}_i' + \boldsymbol{\Omega}_i' \times \boldsymbol{r}_i + \boldsymbol{u}_i^s - \boldsymbol{u}^*\right) \tag{53}$$

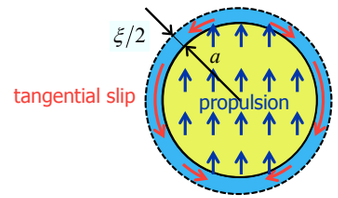

Figure 2. Schematic representation of the updating scheme used to enforce the slip boundary condition at the surface of the squirmers. Each particle is considered to exert a force on the fluid at the surface, in order to maintain the specified flow profile $\boldsymbol{u}^s$ (red arrows) for the squirming motion. To ensure local momentum conservation, a counter-flow is added within the particle domain (blue arrows).

from which we can easily obtain the counter-flow terms $\delta \boldsymbol{V}_i$ ($\delta \boldsymbol{\Omega}_i$) from the particle velocities $\boldsymbol{V}_i'$ ($\boldsymbol{\Omega}_i'$). A schematic representation of the procedure used to enforce the specific slip-boundary conditions for our model squirmers is shown in Fig. 2. Finally, the pressure term due to the squirming motion p_{sq} is obtained from the incompressibility condition $\nabla \cdot \boldsymbol{u}^{**} = 0$. At this point, the momentum conservation relation is solved for the total velocity field.

iii) The hydrodynamic force and torque exerted by the fluid on the colloids (which includes all contributions to the squirming motion) is again derived by assuming momentum conservation. The time integrated hydrodynamic force and torque for a period h are equal to the momentum exchange over the particle domain:

$$\left[\int_{t_n}^{t_n+h} \mathrm{d}s \, \left(\boldsymbol{F}_i^{\mathrm{H}} + \boldsymbol{F}_i^{\mathrm{sq}}\right)\right] = \int \mathrm{d}\boldsymbol{x} \, \rho \phi_i^{n+1} \left(\boldsymbol{u}^{**} - \boldsymbol{u}_p^n\right) \tag{54}$$

$$\left[\int_{t_n}^{t_n+h} \mathrm{d}s \, \left(\boldsymbol{N}_i^{\mathrm{H}} + \boldsymbol{N}_i^{\mathrm{sq}}\right)\right] = \int \mathrm{d}\boldsymbol{x} \, \left[\boldsymbol{r}_i^{n+1} \times \rho \phi_i^{n+1} \left(\boldsymbol{u}^{**} - \boldsymbol{u}_p^n\right)\right] \tag{55}$$

From this and any other forces on the colloids, the particles velocities are updated according to the following equations:

$$\boldsymbol{V}_i^{n+1} = \boldsymbol{V}_i^n + M_p^{-1} \left[\int_{t_n}^{t_n+h} \mathrm{d}s \, \left(\boldsymbol{F}_i^{\mathrm{H}} + \boldsymbol{F}_i^{\mathrm{sq}}\right)\right] + M_p^{-1} \left[\int_{t_n}^{t_n+h} \mathrm{d}s \, \left(\boldsymbol{F}_i^{\mathrm{C}} + \boldsymbol{F}_i^{\mathrm{ext}}\right)\right] \tag{56}$$

$$\boldsymbol{\Omega}_i^{n+1} = \boldsymbol{\Omega}_i^n + \boldsymbol{I}_p^{-1} \cdot \left[\int_{t_n}^{t_n+h} \mathrm{d}s \, \left(\boldsymbol{N}_i^{\mathrm{H}} + \boldsymbol{N}_i^{\mathrm{sq}}\right)\right] + \boldsymbol{I}_p^{-1} \cdot \left[\int_{t_n}^{t_n+h} \mathrm{d}s \, \boldsymbol{N}_i^{\mathrm{ext}}\right] \tag{57}$$

We recall that we have imposed the slip profile $\boldsymbol{u}^s$ with respect to the primed velocities $\{\boldsymbol{V}_i'; \boldsymbol{\Omega}_i'\}$, which need not be equal to the final velocities of the particle at step $n+1$. To maintain consistency, we iterate over Eqs. 50-57 until a convergence of velocities is achieved.

iv) Finally, the resulting particle velocity field $\phi^{n+1}\boldsymbol{u}_p^{n+1}$ is enforced over the total velocity field using the following relations:

$$\boldsymbol{u}^{n+1} = \boldsymbol{u}^{**} + \left[\int_{t_n}^{t_n+h} \mathrm{d}s\, \phi \boldsymbol{f}_p\right] \tag{58}$$

$$\left[\int_{t_n}^{t_n+h} \mathrm{d}s\, \phi \boldsymbol{f}_p\right] = \phi^{n+1}\left(\boldsymbol{u}_p^{n+1} - \boldsymbol{u}^{**}\right) - \frac{h}{\rho}\nabla p_{\mathrm{p}} \tag{59}$$

wherein the pressure due to the rigidity constraint obtained from the incompressibility condition $\nabla \cdot \boldsymbol{u}^{n+1} = 0$. The total pressure field is then given by $p = p^* + p_{\mathrm{p}} + p_{\mathrm{sq}}$.

The above procedure defines the consistent time-propagation, $\{\boldsymbol{u}^n; \boldsymbol{R}_i^n, \boldsymbol{Q}_i^n, \boldsymbol{\Omega}_i^n\} \rightarrow \{\boldsymbol{u}^{n+1}; \boldsymbol{R}_i^{n+1}, \boldsymbol{Q}_i^{n+1}, \boldsymbol{\Omega}_i^{n+1}\}$, to simulate self-propelled squirmers in incompressible fluids.

We are aware of two alternative simulation methods that aim to describe these squirmer suspensions at the same level of description, the first was developed by Ramachandran et al.[35] using a Lattice Boltzmann model, and the second was originally introduced by Downton and Stark[36] within a multi-particle collision dynamics framework, and later extended by Götze and Gompper[37] to recover the correct rotational dynamics. For the moment though, these DNS approaches have not been extensively used to study these types of swimming systems; the most popular methods, which still account for the hydrodynamic interactions, have usually been based on Stokesian Dynamics[31,34], and are thus limited to Newtonian fluids in the Stokes regime.

5 Concluding Remarks

A new computational method named the SPM has been developed to simulate particle dispersion in fluids[4–21]. Utilizing a smoothed profile for particle-fluid boundaries, hydrodynamic interactions in many particle dispersions can be fully taken into account, yielding both accurate and efficient results. In principle, the SPM can be easily applied to systems consisting of many particles with different shapes. The reliability and the performance of the method was confirmed to be satisfactory by several critical tests[4–22].

Recently, we extended the SPM to particle dispersions in compressible fluids[18]. The validity of the method was confirmed by calculating the velocity relaxation function of a single spherical particle in a compressible fluid[21]. The effect of compressibility on the velocity relaxation was also observed, revealing a two-stage relaxation process for low-compressibility fluids and a backtracking motion for high-compressibility fluids. A simulation of the motion of a single spherical particle in a fluctuating fluid was also performed. The calculated velocity autocorrelation function of the particle showed good agreement with the analytical solution of the relaxation function, thereby confirming the validity of the fluctuation-dissipation theorem without any fitting parameters.

We have also shown that SPM can be extended to systems with self-propelled swimming particles, making it possible to describe the actions of squirmers (active swimmers that move due to self-generated surface tangential velocities)[21]. The validity of the method was confirmed by comparing the simulation data with the exact results for the case of a

single swimmer, wherein the correct swimming speed is recovered and it is possible to accurately reproduce the fluid flow generated by the squirming motion. The advantage of the SPM for swimming particles in comparison with Stokesian Dynamics (which have been successfully and extensively used to study these systems)[31,34] is its applicability to particle dispersions in complex fluids. This is relevant in the case of swimming micro-organisms as the role of nutrients and the presence of a non-Newtonian host fluid must be considered when making comparisons with experimental data.

Acknowledgements

The authors would like to express their gratitude to Dr. K. Kim, Dr. Y. Nakayama, Dr. T. Iwashita, and Dr. H. Kobayashi for their contributions to the development of the SPM. This work was supported by Grant No. KAKENHI 23244087.

References

1. J. F. Brady and G. Bossis, Ann. Rev. Fluid Mech., **20**, 111 (1988).
2. H. H. Hu, N. A. Patankar, M. Y. Zhu, J. Comput. Phys., **169**, 427 (2001).
3. K. Ichiki, J. Fluid Mech., **452**, 231 (2002).
4. `http://www-tph.cheme.kyoto-u.ac.jp/kapsel/`
5. R. Yamamoto, Phys. Rev. Lett., **87**, 075502 (2001).
6. Y. Nakayama and R. Yamamoto, Phys. Rev. E, **71**, 036707 (2005).
7. K. Kim, Y. Nakayama, and R. Yamamoto, Phys. Rev. Lett., **96**, 208302 (2006).
8. R. Yamamoto, K. Kim, Y. Nakayama, K. Miyazaki, and D. R. Reichman, J. Phys. Soc. Japan, **77**, 084804 (2008).
9. T. Iwashita, Y. Nakayama, and R. Yamamoto, J. Phys. Soc. Japan, **77**, 074007 (2008).
10. Y. Nakayama, K. Kim, and R. Yamamoto, Eur. Phys. J. E, **26**, 361–368 (2008).
11. T. Iwashita and R. Yamamoto, Phys. Rev. E, **80**, 061402 (2009).
12. T. Iwashita and R. Yamamoto, Phys. Rev. E, **79**, 031401 (2009).
13. T. Iwashita, Y. Nakayama, and R. Yamamoto, Progress of Theoretical Physics, **11**, 86–91 (2009).
14. T. Iwashita, T. Kumagai, and R. Yamamoto, Eur. Phys. J. E, **32**, 357–363 (2010).
15. H. Kobayashi and R. Yamamoto, Phys. Rev. E, **81**, 041807 (2010).
16. S. Jafari, R. Yamamoto, and M. Rahnama, Phys. Rev. E, **83**, 026702 (2011).
17. H. Kobayashi and R. Yamamoto, Phys. Rev. E, **84**, 051404 (2011).
18. R. Tatsumi and R. Yamamoto, Phys. Rev. E, **85**, 066704 (2012).
19. Y. Matsuoka, T. Fukasawa, K. Higashitani, and R. Yamamoto, Phys. Rev. E, **86**, 051403 (2012).
20. A. Hamid and R. Yamamoto, J. Phys. Soc. Japan, in print.
21. J. J. Molina, Y. Nakayama, and R. Yamamoto, arXiv:1212.6133.
22. X. Luo, M. R. Maxey, and G. E. Karniadakis, J. Comp. Phys., **228**, 1750 (2009).
23. M. Fujita and Y. Yamaguchi, Phys. Rev. E, **77**, 026706 (2008).
24. F. B. Usabiaga, I. Pagonabarraga, and R. Delgado-Buscalioni, J. Comp. Phys., **235**, 701–722 (2012).
25. F. B. Usabiaga, R. Delgado-Buscalioni, B. E. Griffith, A. Donev, arXiv:1212.6427.

26. L. D. Landau and E. M. Lifshitz, *Fluid Mechanics*, (Pergamon Press, London, 1959).
27. G. Erlebacher, M. Y. Hussaini, H. O. Kreiss, and S. Sarkar, Theor. Comput. Fluid. Dyn., **2**, 73 (1990).
28. J. V. José and E. J. Saletan, *Classical Dynamics: A Contemporary Approach*, (Cambridge University Press, New York, 1998).
29. M. J. Lighthill, Ann. Rev. Fluid Mech., **1**, 413–446 (1969).
30. J. R. Blake, J. Fluid Mech., **46**, 199–208 (1971).
31. T. Ishikawa, M. P. Simmonds, and T. J. Pedley, J. Fluid Mech., **568**, 119–160 (2006).
32. L. Zhu, E. Lauga, and L. Brandt, Phys. Fluids, **24**, 051902 (2012).
33. W. B. Russel, D. A. Saville, and W. R. Schowalter, *Colloidal Dispersions*, (Cambridge University Press, Cambridge, 1992).
34. J. W. Swan, J. F. Brady, R. S. Moore, and ChE 174, Phys. Fluids, **23**, 071901 (2011).
35. S. Ramachandran, P. B. Sunil Kumar, and I. Pagonabarraga, Eur. Phys. J. E, **20**, 151 (2006).
36. M. T. Downton and H. Stark, J. Phys.: Condens. Matt., **21**, 204101 (2009).
37. I. Götze and G. Gompper, Phys. Rev. E, **82**, 041921 (2010).

Parallel Brownian Dynamics Simulation with MPI, OpenMP and UPC

Carlos Teijeiro[1], Godehard Sutmann[2,3], Guillermo L. Taboada[1], and Juan Touriño[1]

[1] Computer Architecture Group, Department of Electronics and Systems,
University of A Coruña, 15071 A Coruña, Spain
E-mail: {cteijeiro, taboada, juan}@udc.es

[2] Institute for Advanced Simulation, Jülich Supercomputing Centre,
Forschungszentrum Jülich, 52425 Jülich, Germany
E-mail: {g.sutmann}@fz-juelich.de

[3] ICAMS, Ruhr-University Bochum, 44801 Bochum, Germany

This work presents the design and implementation of a parallel simulation code for the Brownian motion of particles in a fluid. Three different parallelization approaches have been followed: (1) traditional distributed memory message-passing programming with MPI, (2) a directive-based approach on shared memory with OpenMP, and (3) the Partitioned Global Address Space (PGAS) programming model, oriented towards hybrid shared/distributed memory systems, with the Unified Parallel C (UPC) language. According to the selected environment, different domain decompositions and work distributions are studied in terms of efficiency and programmability in order to select the most suitable strategy. Performance results on different testbeds and using a large number of threads are presented in order to assess the performance and scalability of the parallel solutions.

1 Introduction

Particle simulation methods aim at exploring the configuration- or phase-space of a system in order to gather statistics for approximating expectation values of structural and dynamical quantities. Simulation methods thereby strongly depend on the level of resolution of the underlying system and the physical mechanisms under study, including *ab initio* methods[1,2], force field[3–5] or effective medium[6] descriptions. In principle, these methods allow for molecular dynamics approaches, where the equations of motion are solved via finite difference schemes and provide information about coordinates and momenta of particles, i.e. generating trajectories in phase space.

For large systems, e.g. diluted or semi-diluted systems of particles in a solvent, the number of degrees of freedom gets very large, if all system components are described on an atomistic level. This imposes limits due to both the available memory on a computer architecture and the complexity of the underlying algorithm. For particle systems, the time for computing interactions and integrating system trajectories is most often the main bottleneck, compared to memory constraints. Therefore, coarse grain and stochastic approaches are often used to describe the surrounding or environment effects in the system, thereby neglecting the explicit description of a solvent. This benefits two aspects of the simulation: (i) the number of degrees of freedom and therefore the CPU-time/step is dramatically reduced and as a consequence (ii) the accessible time scale is strongly increased. The latter one is the result from both the increase in performance of the simulation method and of the coarse grain or stochastic description of the environment effects, including averaging of

effects on the smallest time scales and therefore allowing for larger time steps in the simulation. Care has to be taken, when considering coarse grain potentials between particles, without including environment effects. Since coarse graining tends to flatten potential energy surfaces, larger time steps might be applied, but in that way also transport coefficients are modified due to faster dynamics, i.e. less friction, on larger time scales[7]. This effect is avoided when considering an environment which imposes correct transport properties, e.g. diffusion coefficient or conductivity, for the solutes.

In recent years the simulation of the dynamics of particles coupled to an environment has strongly profited from advances in mesoscopic solvent methods, which include lattice Boltzmann calculations[8] as a grid based method or dissipative particle dynamics[9] or multi-particle collision dynamics[10] as particle simulation methods. These models take into account the collective properties of the solvent and provide hydrodynamic interactions between solutes. The models conserve energy, momentum and (in most cases) angular momentum. As a limiting case the models have the Navier-Stokes equations and can therefore be considered as a discretization of Navier-Stokes within an Euler- or Lagrange description. These methods provide a strong reduction of degrees of freedom of the solvent, but still a large number of degrees-of-freedom is necessary to properly account for momentum and energy transport in the system.

In coarse grain simulations of solvated particles the mobility of particles is often taken into account via the solvent viscosity or more generally the mobility- or diffusivity-tensor of the solvent. As a zero order approximation, viscosity is taken into account as a constant, averaging out all non-local effects and not considering collective effects like hydrodynamic interactions. Hydrodynamic effects play an important effect for the transport properties of particles on a mesoscopic scale. A proper description of the hydrodynamic interactions have to take into account their collective nature, i.e. considering multi-particle contributions up to high order. A full account of high order multi-particle contributions puts not only limitations to the computability but also to the modelling. In Ref. 11 multi-particle contributions were taken into account up to order 4, which already strongly increases the complexity of the analytical expressions and the computational load. For diluted systems, many-body effects are reduced and therefore the approximation of pair-wise interactions is often made on the basis of the Oseen-tensor[12], which is the Green's function of linearized Stokes equation, or on the basis of the Rotne-Prager-tensor[13] (sometimes also called Rotne-Prager-Yamakawa tensor[14]), which takes into account the finite size of particles in solution. By definition, the Oseen-tensor is the response function of the solvent due to point like force-sources. From a physical point of view, point-like sources do not have a surface and therefore do not reflect a velocity field, which leads to the linear superposition of velocity fields in such a description. For finite sized particles the Oseen-tensor is not positive definite, which would lead to the unphysical picture of negative diffusivities of particles. Therefore, the use of the Rotne-Prager tensor is more save for stability considerations of the simulation. Nevertheless, if particles approach too close, i.e. $r_{ij} < 2a$, where $r_{ij} = \|\mathbf{r}_i - \mathbf{r}_j\|$ is the mutual distance between particles i and j and a the radius of the particles, also the Rotne-Prager-tensor looses positive definiteness which makes it necessary to regularize the tensor for small distances[13]. The Rotne-Prager-tensor can be considered as a second order approximation of an expansion of the velocity field at a distance a from the expansion point. Formally, this expansion can be carried out to arbitrary order[15]. As a demonstration, the expansion was carried out explicitly up to order 20 in Ref. 15. For

larger distances the expansion converges very well and for dilute systems the results will be improved. However, for small distances of the order of $r \approx 2a$, convergence is not yet reached and there will be a truncation error left.

For more dense systems, the second order (or higher order) approximation of the mobility tensor might not be sufficient for reproducing correct physical behaviour, like collective behaviour in sedimentation processes. An alternative scheme was proposed by considering not the mobility tensor, but the friction tensor, which relates the forces on a particle to the velocity field. Inverting the friction tensor gives formally a mobility tensor. Taking into account only pair contributions between particles to the friction tensor will lead to a collective contribution in the mobility tensor due to the inversion procedure and which seems to provide more consistent results[16]. However, for applications in Brownian dynamics simulations which need the mobility tensor, this implies the necessity of inverting a $3N \times 3N$-dimensional matrix which i.g. implies an $\mathcal{O}(N^3)$ operation in the simulation.

As will be more detailed in the next section, the computationally most intensive parts in the Brownian dynamics simulation are the construction of the mobility tensor, computation of forces and the calculation of correlated random variates. To construct sequences of correlated random numbers a Cholesky decomposition of the mobility matrix is often applied. This technique also requires an $\mathcal{O}(N^3)$ operation. Alternatives to this approach make use of approximations. In the approach of Fixman[17] a truncated series of Chebyshev polynomials is used, where the accuracy of correlation coefficients depend on the number of terms in the series. Another approach was proposed in Ref. 18 which reduces the problem of correlated random forces to a complexity of $\mathcal{O}(N^2)$. In this approach, called the *truncated expansion ansatz*, the contribution to the displacements due to stochastic forces is formally written in the same way as the one of systematic forces. This contribution can then be expressed as a weighted sum of partial force contributions, which multiply unconditional random variates to each term in the sum. The weight factors are determined in such a way that the moments of random displacement vectors are correctly reproduced. The approximation which enters into this approach is the fact that off-diagonal terms in the mobility-tensor are considered small with respect to diagonal terms, i.e. that hydrodynamic coupling is weak and that the square root is linearly expanded. Although the field of application might be restricted due to these approximations, it is a very interesting approach, which brings the whole method of Brownian dynamics simulations to higher efficiency.

Although there are several algorithmic improvements to speed up the simulation procedure of Brownian dynamics, the size of particle systems is still rather limited. The reason for this is (i) the numerical complexity of (at least) $\mathcal{O}(N^2)$ which implies a quadratic increase in CPU time when enlarging the number of degrees of freedom and (ii) the memory needs also increase quadratically due to the necessity of constructing the mobility-matrix of size $3N \times 3N$. For $N = 10^4$, the memory needs for 8 Byte number representation would be about 7 GBytes, being close to or even beyond of sizes of current workstations or desktop systems. Therefore there is a strong need to work on efficient parallel implementations, which cope with these limitations. The present article gives an overview on recent work devoted to scalable implementations of Brownian dynamics of solvated particles, including hydrodynamic interactions. Different parallelization strategies and implementations are presented and discussed which pave the way for large scale Brownian dynamics simulations on massively parallel architectures.

2 Brownian Dynamics Simulation

In Brownian dynamics a time scale separation between configurational and momentum relaxation is considered, i.e. an assumption is that the average velocity between two successive moves corresponds to the thermal velocity $\langle v_{\alpha,i} \rangle = k_B T / m_i, \ \alpha = x, y, z$. Based on a Chapman-Enskog type method, the corresponding Fokker-Planck equation, which describes the change of the configuration-space distribution function $P(\mathbf{r})$ is given by[19]

$$\frac{\partial}{\partial t} P(\mathbf{r}) = \sum_{i,j} \frac{\partial}{\partial \mathbf{r}_j} \mathbf{D}_{ij}(\mathbf{r}) \left(\frac{\partial}{\partial \mathbf{r}_j} P(\mathbf{r}) - \frac{1}{k_B T} \mathbf{F}_j P(\mathbf{r}) \right) \tag{1}$$

where $\mathbf{D} \in \mathbb{R}^{3N \times 3N}$ is the diffusion tensor of the system and $\mathbf{D}_{ij} \in \mathbb{R}^{3 \times 3}$ a sub-matrix, corresponding to the pair-contribution of particles i and j to the diffusion tensor and $k_B T$ the thermal energy of the system, where T is the temperature and k_B the Boltzmann constant.

The solution of Eq. 1 is obtained in first order in Δt as a multi-variate Gaussian distribution, which is uniquely defined by its first two moments

$$\langle \Delta \mathbf{r}_i \rangle = \sum_j \left(\frac{\partial \mathbf{D}_{ij}}{\partial \mathbf{r}_j} + \frac{1}{k_B T} \mathbf{D}_{ij} \mathbf{F}_j \right) \Delta t \tag{2}$$

$$\langle \Delta \mathbf{r}_i \Delta \mathbf{r}_j^T \rangle = 2 \, \mathbf{D}_{ij} \, \Delta t \tag{3}$$

It should be noted that although the inclusion of hydrodynamics will have an effect on cross-correlations between particles in the system, i.e. an influence on mutual diffusion, it has no effect on self-diffusion, i.e. it does not change the mean square displacement $\langle \Delta \mathbf{r}_i^2 \rangle$ of a particle[20].

A procedure which provides a description for particle displacements in a Brownian dynamics simulation is based on the Langevin dynamics, which describes the momentum change of a particle i in a system of N interacting particles, solvated in a fluid which is characterized by its friction. The momentum change of such a particle is described by three contributions, i.e. (i) friction, (ii) a systematic interaction between the particles and (iii) a random contribution, containing thermal effects

$$m_i \frac{\partial^2 \mathbf{r}_i}{\partial t^2} = \sum_{j=1}^{N} \boldsymbol{\zeta}_{ij} \frac{\partial \mathbf{r}_j}{\partial t} + \sum_{j=1}^{N} \mathbf{c}_{ij} \mathbf{F}_j^r \tag{4}$$

where $\boldsymbol{\zeta}_{ij}$ is the friction tensor, c_{ij} correlation coefficients and $\mathbf{F}_j^r$ a random force contribution. The friction tensor is thereby related to the diffusion tensor via $\sum_k \boldsymbol{\zeta}_{ik} \mathbf{D}_{kj} = \mathbf{I} \delta_{ij}$, where δ_{ij} is the Kronecker-δ and $\mathbf{I}$ is the identity-matrix. The correlation coefficients are related to the friction coefficient via $\boldsymbol{\zeta}_{ij} = \sum_k \mathbf{c}_{ik} \mathbf{c}_{kj}$. The random forces are Gaussian distributed and defined by their moments

$$\langle \mathbf{F}_i^r \rangle = 0 \qquad , \qquad \langle \mathbf{F}_i^r(t) (\mathbf{F}_j^r(t'))^T \rangle = 2 \mathbf{I} \delta_{ij} \delta(t - t') \tag{5}$$

Note that this is a special choice for the random correlations, which are δ-correlated in time and space. In fact, a spatial correlation is obtained via the correlation coefficients $\mathbf{c}_{ij}$.

Also a temporal correlation is possible, which then leads to the generalized Langevin equation, which then takes into account the history of the trajectory via the so called memory function[21,22].

The formal derivation of the equation for the displacement of the particle proceeds then by multiplying Eq. 4 with $\mathbf{D}_{ij}$ and summing over j, Taylor expanding $\mathbf{D}_{ij}$ and $\mathbf{F}_j$ and performing a double integral over time, which finally leads to

$$\mathbf{r}_i(t+\Delta t) = \mathbf{r}_i(t) + \sum_{j=1}^{N} \frac{\partial \mathbf{D}_{ij}(t)}{\partial \mathbf{r}_j}\Delta t + \sum_{j=1}^{N} \frac{1}{k_B T}\mathbf{D}_{ij}(t)\mathbf{F}_j(t)\Delta t + \mathbf{R}_i(t+\Delta t) \quad (6)$$

Details of the derivation of Eq. 6 can be found in Ref. 23.

This one-step propagation scheme takes into account the coupling of the particles to the flow field via the diffusion tensor $\mathbf{D}$ and the systematic forces $\mathbf{F}$, acting onto the particles with the global property $\sum_j \mathbf{F}_j = 0$. The vector $\mathbf{R} \in \mathbb{R}^{3N}$ contains correlated Gaussian random numbers with zero mean, which are constructed according to the fluctuation-dissipation theorem, with $\mathbf{R}_i \in \mathbb{R}^3$ being a sub-vector corresponding to particle i.

In the present work we restrict ourselves to the application of the Rotne-Prager-tensor, which is given in its regularized form as

$$\mathbf{D}_{ii} = \frac{k_B T}{6\pi\eta a}\,\mathbf{I} \quad (7a)$$

$$\mathbf{D}_{ij} = \begin{cases} \dfrac{k_B T}{8\pi\eta r_{ij}}\left[\left(\mathbf{I} + \hat{\mathbf{r}}_{ij}\hat{\mathbf{r}}_{ij}^T\right) + \left(\dfrac{2}{3}\dfrac{a^2}{r_{ij}^2}\mathbf{I} - 3\hat{\mathbf{r}}_{ij}\hat{\mathbf{r}}_{ij}^T\right)\right] & : r_{ij} > 2a \\ \dfrac{k_B T}{6\pi\eta a}\left[\left(1 - \dfrac{9}{32}\dfrac{r_{ij}}{a}\right)\mathbf{I} + \dfrac{3}{32}\dfrac{r_{ij}}{a}\hat{\mathbf{r}}_{ij}\hat{\mathbf{r}}_{ij}^T\right] & : r_{ij} \leq 2a \end{cases} \quad (7b)$$

where η is the viscosity of the fluid and $\hat{\mathbf{r}}_{ij} = (\mathbf{r}_i - \mathbf{r}_j)/r_{ij}$. Note that the $\mathbf{D}$ has a leading term of $1/r$, which implies a long-range contribution to the diffusion tensor. Algorithmically, this is the same problem as it appears in electrostatic calculations, when considering the total energy in the system, subject to periodic boundary conditions. Therefore, for a simulation protocol the expression has to be extended in order to take into account proper boundary conditions in the system. In the so-called *minimum image convention*, contributions to $\mathbf{D}$ between nearest particles i and j are considered, where particle i is located in the central box and particle j might be located in the central or one of its periodic image boxes. A more consistent picture is obtained by an analog to electrostatics, where a lattice sum (e.g. Ewald sum) over all periodic images in the system is performed. An expression for the Ewald sum of the regularized version of the Rotne-Prager tensor is given in the Appendix A. This formulation is also followed in the code which is considered in this report. Note, however, that other forms of the diffusion tensor might be applied within the same formalism of Eq. 6. The Rotne-Prager-tensor has the nice property that the partial derivative on the right-hand side of Eq. 6 drops out and therefore the equation the displacement vector of the Brownian particles, $\Delta\mathbf{r} = \mathbf{r}(t+\Delta t) - \mathbf{r}(t)$, can be rewritten as

$$\Delta\mathbf{r} = \frac{1}{kT}\mathbf{D}\mathbf{F}\Delta t + \sqrt{2\Delta t}\,\mathbf{Z}\boldsymbol{\xi} \quad (8)$$

where $\boldsymbol{\xi}$ is a vector of independent Gaussian random numbers. According to the previous simplifications, $\mathbf{Z}$ may be calculated via a Cholesky decomposition or via the square root of $\mathbf{D}$. Both approaches are very CPU-time consuming with a computational complexity of $\mathcal{O}(N^3)$ and impose a large computational load. Therefore the development of faster and more efficient and scalable methods with smaller complexity is an important task, and here Fixman[17] applied an expansion of the random displacement vector $\mathbf{R}$ in terms of Chebyshev polynomials, approximating its values without constructing $\mathbf{Z}$ explicitly.

The systematic interactions between particles are modelled by a Lennard-Jones-type potential, from which the forces are obtained via the negative gradient:

$$V(r_{ij}) = 4\varepsilon \left[\left(\frac{\sigma}{r_{ij}} \right)^{12} - \left(\frac{\sigma}{r_{ij}} \right)^{6} \right] \tag{9a}$$

$$\mathbf{F}_{ij} = -\nabla_{\mathbf{r}_{ij}} V(r_{ij}) = 24\varepsilon \left[2 \left(\frac{\sigma}{r_{ij}} \right)^{12} - \left(\frac{\sigma}{r_{ij}} \right)^{6} \right] \frac{\hat{\mathbf{r}}_{ij}}{r_{ij}^2} \tag{9b}$$

where σ is the diameter of the particles and ϵ is the depth of the potential minimum. This potential has a short range character and practically interactions between particles are neglected for mutual distances $r_{ij} > R_c$, where R_c is the radius of a so called cutoff sphere, which is chosen as $R_c = 2.5\,\sigma$. The distance r_{ij} is chosen according to the minimum image convention, i.e. the shortest distance between particle i (located in the central simulation box) and particle j or one of its periodic images is taken into account. Several software tools focus on the simulation of these systems, such as BrownDye[24]. There is some relevant work parallelizations of these simulations[25], including a simulation suite called BD_BOX[26], but little information is given about the actual implementation and the performance and scalability on large supercomputers. Therefore, the next sections provide a description of the parallelization of a Brownian dynamics simulation, presenting different workload distributions and a performance analysis of the most relevant cases.

3 Analysis of the Sequential Simulation Code

The parallel implementations are based on an existing optimized sequential code, which defines the system as a cubic box for which periodic boundary conditions are applied. The time integration of trajectories of Brownian particles is performed according to Eq. 8. The main component of the code is the `for` loop that includes the function calls, necessary to propagate the particles in configuration space. The most time consuming functions include `calc_force()` and `covar()`, which are the main targets for parallelization. Function `calc_force()` includes: (1) the computation of systematic forces (Eq. 9), for which a linked-cell technique[27] is used ($\mathcal{O}(N)$), and (2) the setup of the diffusion tensor ($\mathcal{O}(N^2)$), which needs the explicit calculation of $N(N-1)/2$ particle pair-contributions. The correlated random displacements are calculated in function `covar()` using the approximation method according to Fixman, with complexity $\mathcal{O}(N^{2.25})$ [17]. Tab. 1 presents the breakdown of the execution time of the sequential program in the testbed used in the performance evaluation (see Sec. 5) in terms of the previously discussed functions, using 256 and 1024 input

particles for 50 time steps of simulation. The diffusion tensor, which is defined in the code as a matrix called `D`, has $(3 \times N)^2$ elements (i.e. the information between all pairs of N particles on 3 dimensions), thus its construction takes at least a complexity of $\mathcal{O}(N^2)$. This is true for the real space contributions of the Ewald sum as the cutoff radius is of the order of half the system size (or even larger), in order to keep the reciprocal space contribution, i.e. the number of k-values, small for a given error tolerance. Since the mutual distances between particles are calculated in the real space contribution, it is natural to integrate the construction of matrix `D` in the calculation of short range direct interactions between particles (whose complexity is $\mathcal{O}(N)$), thus giving out the $\mathcal{O}(N^2)$ complexity stated in row "short range contributions" of Tab. 1. The long range contribution to the diffusion tensor also has to be calculated for every matrix element, i.e. for each particle pair, which also imposes a computational complexity of $\mathcal{O}(N^2)$. However, there is an additional contribution to the long range part, giving rise to a larger complexity, since a set of reciprocal vectors has to be considered to fulfill a prescribed error tolerance in the Ewald sum, increasing the complexity to approximately $\mathcal{O}(N^{2.5})$.

Code Part	**Complexity**	**N = 256**	**N = 1024**
`calc_force()` - `D` & short range contributions	$\mathcal{O}(N^2)$	4.733 s	75.966 s
`calc_force()` - Ewald long range contributions	$\mathcal{O}(N^{2.5})$	7.095 s	181.103 s
`covar()` - Fixman	$\mathcal{O}(N^{2.25})$	0.762 s	17.735 s
`move()`	$\mathcal{O}(N^2)$	0.019 s	0.341 s
Total time	$\mathcal{O}(N^{2.5})$	12.609 s	275.145 s

Table 1. Breakdown of the execution time of the sequential code.

4 Development of the Parallel Implementation

The iterations of the main simulation loop define a sequence of time steps, where the information for time step $(n+1)$ is dependent on positions and mutual interactions between particles in time step n and therefore these iterations cannot be executed concurrently, and a work distribution is only possible within each iteration. At this point, the main parallelization efforts are focused on the workload decomposition of `calc_force()`, according to Tab. 1, but considering the performance bottlenecks that might arise when performing communications, especially at the `covar()` function.

In order to allow for parallel computations needed to update the diffusion tensor values and random displacements, all processes (for clarity purposes, the term "processes" will be used when considering processes in MPI and threads in OpenMP or UPC) require to have access to the coordinates for every particle in the system. Thus, all processes store all the initial coordinates of the particles to avoid continuous remote calls to obtain the necessary coordinate values when using MPI and UPC. After each iteration, all coordinates are updated for every process by means of function `move()`, thus minimizing communications. The calculation of each random displacement in `covar()` depends on the diffusion tensor matrix `D`, whose computation has been previously performed by different processes in `calc_force()`, and consequently communications are unavoidable here. Therefore, it is necessary to find a suitable workload distribution of diffusion tensor values in matrix `D`

to favour the scalability of the code by minimizing the amount of communications required by `covar()`.

4.1 Shared Memory Parallelization (UPC & OpenMP)

The use of the shared memory space in UPC to store matrix `D` allows a straightforward shared memory parallelization: all threads are able to access all the data stored in the shared memory region, so this parallelization only requires changes in the matrix indexing to support the access in parallel by UPC threads. However, there are two drawbacks in this parallelization. The first one is its poor load balancing: thread 0 performs much more work than the last thread (`THREADS`-1) because of the distribution in rows of the triangular matrix `D`, either with a block or a cyclic distribution. The second issue is the inefficiency of single-valued remote memory copies in UPC[28], which is due to the use of virtual memory addresses to map the shared variables in UPC. As a result, the computational cost of handling these shared address translations is not acceptable when simulating large systems for a long period of time.

Regarding the OpenMP code, the parallelization of `calc_force()` and `covar()` can be performed by introducing `for` directives in the code, which are all fully parallelizable, in order to compute concurrently the interaction values and displacements associated to each particle. For the two iterative methods required for Fixman's algorithm (the calculation of the minimum and maximum eigenvalues of matrix `D`, which uses a variant of the power method; and the computation of coefficients using the Chebyshev polynomial expansion), the `for` loops use a `critical` directive and a `reduction` clause, respectively, to compute the total error value for the final approximated coefficients.

The efficiency of the OpenMP code is significantly better than the most simple approach presented for UPC, even though the differences in programmability are small. However, in both cases the implemented codes cannot obtain reasonable performance when distributed memory communications are involved. The shared address translations and implicit remote data movements are not able to provide scalability for more than 2 nodes in any of these cases, because of the data dependencies in the random displacement calculation. Therefore, a different approach is required for executions on more than one node.

4.2 Distributed Memory Parallelization (UPC & MPI)

An initial approach to the distribution of the diffusion tensor matrix `D` and its associated computations is the force-stripped row decomposition scheme proposed by Murty and Okunbor[29], which has the goal of achieving a more balanced number of computations and remote copies. This workload/domain decomposition consists in distributing the number of elements in the upper triangular part of matrix `D` between the number of processes in the program by assigning consecutive blocks of 3 rows (associated to a particle) to process `i` until the total number of assigned diffusion tensor values is equal to or higher than `nlocal*(i+1)`, where `nlocal` is $3 * N$ divided by the number of processes. Despite the relatively good balancing of this distribution, Fixman's algorithm requires to fill the lower triangular part of matrix `D` in order to avoid element-by-element data movements in `covar()`, and the communication time becomes too high.

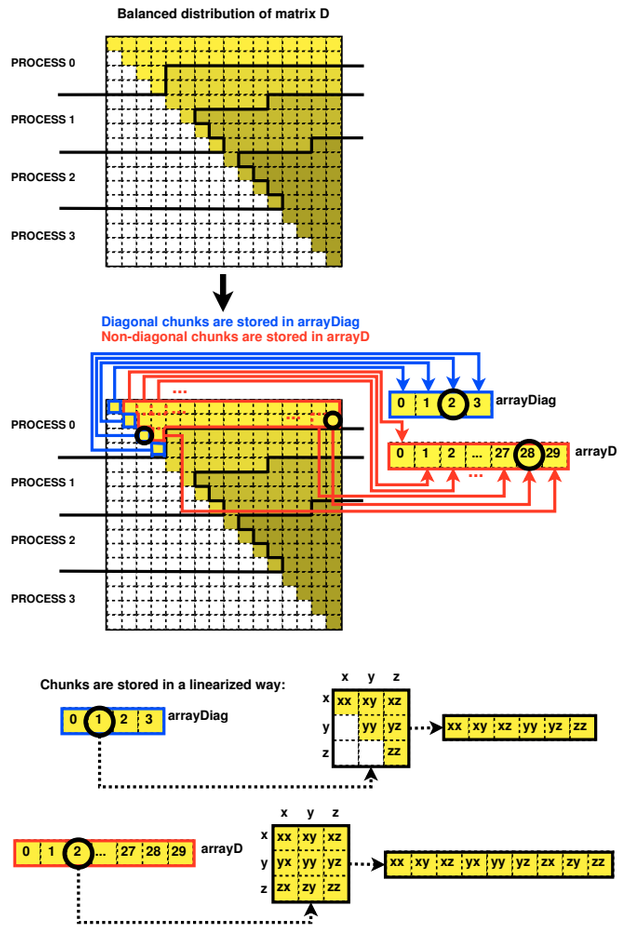

Figure 1. Balanced distribution of matrix D for Fixman's algorithm (detailed data structures for process 0).

Fig. 1 presents a more suitable domain decomposition for Fixman's algorithm, where each square in matrix D represents the diffusion tensor values associated to a pair of particles in every combination of their dimensions, i.e. a 3×3 submatrix. These squares are defined as diagonal and non-diagonal elements, and this distribution assigns to each pro-

cess a balanced number of consecutive elements of each type, regardless of the particles to which they are associated. In this example, the 16 diagonal elements are distributed among the 4 processes (each one receives 4 diagonal elements), and the 120 remaining elements are scattered (30 elements per process). Finally, every chunk is linearized in `arrayDiag` (diagonal chunks) and `arrayD` (non-diagonal chunks) following the flattening process shown at the bottom of the figure for every 3×3 submatrix. This distribution favours local processing for diagonal values, as well as the balanced distribution of data and communications for non-diagonal values.

According to this, the approximation methods for Fixman's algorithm are parallelized by having each process to calculate locally a partial result for an approximated value using its assigned elements in `D`. Then, an all-to-all collective communication is invoked by every process to get all the partial results of its assigned rows (defined by non-diagonal elements) and compute its associated displacements. Additional collective communications are used in order to start a new iteration of the method.

However, this method presents a limit to its scalability because of the overhead derived from the communications required at each iteration. Therefore, a new approach is proposed considering matrix `D` as being non-triangular: the particles in the system are all evenly distributed by rows between processes and all elements of `D` are computed by the corresponding process. This distribution uses a minimum number of communications, because the approximations in `covar()` are always computed locally by the corresponding process, and only an allgather collective operation is necessary to prepare a new iteration. The main drawback of this implementation is its higher computational cost, because it computes double the number of elements in `D`. However, the scalability of this approach is significantly higher than that of the previous algorithms because of the reduced number of communications required, which allows to outperform previous approaches as the number of processes increases.

5 Performance Evaluation

The evaluation of the developed parallel Brownian dynamics codes has been accomplished mainly on the JuRoPa supercomputer (JRP) at Jülich Supercomputing Centre. Additionally, a second system has been used for shared memory executions: an HP ProLiant SL165z G7 node with 2 dodeca-core AMD Opteron processors 6174 (Magny-Cours) at 2.2 GHz with 32 GB of memory, and from now on is referred as "MGC". The Intel C Compiler (icc) v12.1 and the Open64 Compiler Suite (opencc) v4.2.5.2 have been used as OpenMP compilers in JRP and MGC, respectively. The UPC compiler used in both systems was Berkeley UPC v2.14.2 (released in May 2012) with the Intel C Compiler v12.1 as back-end C compiler. ParaStation MPI 5.0.27.1 has been used by the MPI code in JRP. All the executions in this evaluation were compiled with the optimization flag `-O3`. In order to perform a fair comparison, all speedup results have been calculated taking the execution times of the original sequential C code as baseline, as it represents the fastest approach.

Fig. 2 shows the simulation on shared memory for 4096 particles and 50 time steps. The algorithmic complexity of calculating the diffusion tensor $\mathbf{D}$ is $\mathcal{O}(N^2)$, whereas Fixman's algorithm is $\mathcal{O}(N^{2.25})$; thus, when the problem size increases, the generation of random displacements represents a larger percentage of the total simulation time. As a result of this, and also given the parallelization issues mentioned in Sec. 4, the speedup

is slightly limited for 16 or more threads, mainly for OpenMP (also because of the use of Simultaneous Multithreading in JRP). However, considering the distance to the ideal speedup, both systems present reasonably good speedups for this code.

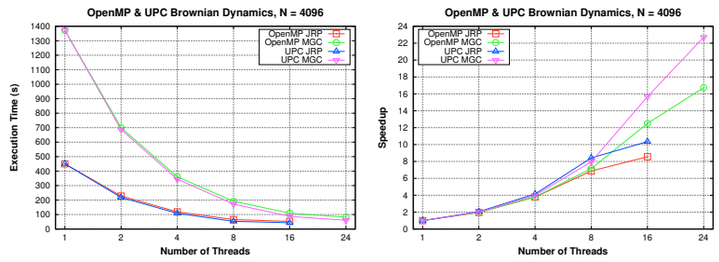

Figure 2. Performance results with 4096 particles (shared memory on MGC and JRP).

Fig. 3 presents the performance results on distributed memory using 4096 particles and 50 time steps. Here *bal-comms* and *min-comms* refers to the mentioned distribution with balanced and minimum communications, respectively. The *bal-comms* version obtains an almost linear speedup up to 64 cores, and also the best results up to the number of cores for which the computation time is still higher than the communication time (i.e., up to 64 cores with MPI and 128 cores with UPC for 4096 particles), and UPC all-to-all communications represent a better choice than MPI in the simulation. The *min-comms* code shows the highest scalability, both for MPI and UPC, achieving in general a speedup of about half of the number of cores being used. Taking into account that this implementation requires almost double the number of computations of the original sequential code (hence its speedup with one core is around 0.6), this represents a significant scalability.

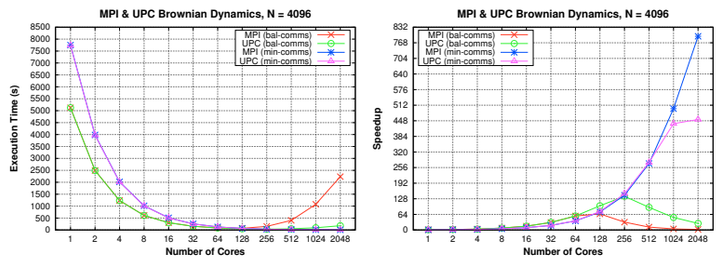

Figure 3. Performance results with 4096 particles (distributed memory on JRP).

6 Conclusions

Brownian dynamics simulations which take into account hydrodynamic interactions between particle pairs are computationally expensive with respect to other classical particle simulation protocols, e.g. MD. The computational bottleneck lies in constructing the complete diffusion matrix $\mathbf{D}$ in periodic boundary conditions and based on this the construction of correlated random variates, which induces a computational complexity of $\mathcal{O}(N^3)$ in the case of Cholesky decomposition (exact representation) or $\mathcal{O}(N^{2.25})$ in the case of the Fixman method (approximation). For $N > 1000$ the computational effort is significant and limits long time simulations if the simulation is not performed on a parallel architecture. Therefore, several approaches were conducted to compare the performance of various parallel implementations. The main contributions of this parallelization are: (1) the analysis of data dependencies in the simulation codes and the domain decompositions for different environments, (2) the assessment of the alternatives in the work distributions to maximize performance and manage memory requirements efficiently, and (3) the performance evaluation of different versions of the parallel code with a large number of cores. The experimental results have shown there is no single optimal approach on distributed memory communications, but the parallel simulation can scale performance up to thousands of cores with minimum communications (*min-comms*) while providing an alternative implementation with less memory requirements for a reduced number of cores with balanced communications (*bal-comms*). Regarding the programming models considered, significant differences have been found: the higher maturity of MPI routines has provided high performance and stability at the cost of a higher programming effort, OpenMP has provided the lowest time to solution with good performance only on intra-node communications, and UPC exploits the PGAS model to obtain an efficient code for all testbed environments.

Acknowledgements

This work has been developed using two previous works published in the Journal of Supercomputing[30] and Computer Physics Communications[31] as main basis. We acknowledge the Jülich Supercomputing Centre for providing access to the JUROPA supercomputer.

Appendix

A Rotne-Prager Tensor in Periodic Boundary Conditions

In this Appendix the expression for the regularized version of the Rotne-Prager tensor in periodic boundary conditions is given. The expression follows closely the one derived by Beenaker[32] with the extension of the regularization for distances $r < 2a$.

The tensor $\mathbf{D}$ is split into four parts:

$$\begin{aligned}\mathbf{D}(\mathbf{r}_{ij}) = \sum_{\boldsymbol{\ell}} \theta(r_{ij(0)} - 2a) \left[\mathbf{D}^{(1)}(\mathbf{r}_{ij(\ell)}) + \mathbf{D}^{(2)}(\mathbf{r}_{ij(\ell)}) + \mathbf{D}^{(3)}(\mathbf{r}_{ij(\ell)})\right] \\ +(1 - \theta(r_{ij(0)} - 2a))\, \mathbf{D}^{(4)}(\mathbf{r}_{ij(\ell)})\,,\end{aligned} \tag{10}$$

where

$$\theta(x) = \begin{cases} 0 : x < 0 \\ 1 : x \geq 0 \end{cases} \tag{11}$$

is the step function and $\mathbf{r}_{ij(\ell)} = \mathbf{r}_i - \mathbf{r}_j + \boldsymbol{\ell} L$, with L the simulation box length and $\boldsymbol{\ell} = (\ell_x, \ell_y, \ell_z)^T \in \mathbb{Z}^3$, i.e. the resulting tensor contains all contributions between particle i and j plus all periodic images of particle j. The individual terms of the tensor are given by:

$$\mathbf{D}^{(1)}(\mathbf{r}_{ij}) = \frac{k_B T}{6\pi\eta a} \left(1 - \frac{6}{\sqrt{\pi}}\kappa a \left(1 + \frac{20}{9}\kappa^2 a^2\right)\right) \mathbf{I}\, \delta_{ij}\delta_{\alpha\beta} \tag{12a}$$

$$\begin{aligned} \mathbf{D}^{(2)}(\mathbf{r}_{ij}) = \frac{k_B T}{6\pi\eta a}\, \theta(r_{ij} - R_{c,D}) \Bigg\{ & \mathbf{I} \left(\frac{3}{4}\frac{a}{r_{ij}} + \frac{1}{2}\frac{a^3}{r_{ij}^3}\right) \operatorname{erfc}(\kappa r_{ij}) \\ & + \mathbf{I}\, \frac{1}{\sqrt{\pi}} \left(4\kappa^7 a^3 r_{ij}^4 + 3\kappa^3 a r_{ij}^2 - 20\kappa^5 a^3 r_{ij}^2 - \frac{9}{2}\kappa a + 14\kappa^3 a^3 + \kappa\frac{a^3}{r_{ij}^2}\right) \\ & \times \exp(-\kappa^2 r_{ij}^2) + \hat{\mathbf{r}}\hat{\mathbf{r}} \left(\frac{3}{4}\frac{a}{r_{ij}} - \frac{3}{2}\frac{a^3}{r_{ij}^3}\right) \operatorname{erfc}(\kappa r_{ij}) \\ & - \hat{\mathbf{r}}\hat{\mathbf{r}} \left(4\kappa^7 a^3 r_{ij}^4 + 3\kappa^3 a r_{ij}^2 - 16\kappa^5 a^3 r_{ij}^2 - \frac{3}{2}\kappa a + 2\kappa^3 a^3 + 3\kappa\frac{a^3}{r_{ij}^2}\right) \\ & \times \frac{\exp\left(-\kappa^2 r_{ij}^2\right)}{\sqrt{\pi}} \Bigg\} \end{aligned} \tag{12b}$$

$$\mathbf{D}^{(3)}(\mathbf{r}_{ij}) = \frac{k_B T}{6\pi\eta a}\, \frac{1}{V} \sum_{|\mathbf{k}|<k_{max}} (\mathbf{I} - \hat{\mathbf{k}}\hat{\mathbf{k}}) \left(a - \frac{1}{3}a^3 k^2\right) \left(1 + \frac{1}{4}\frac{k^2}{\kappa^2} + \frac{1}{8}\frac{k^4}{\kappa^4}\frac{6\pi}{k^2}\right) \times \exp\left(-\frac{1}{4}\frac{k^2}{\kappa^2}\right) \cos(\mathbf{k}\mathbf{r}_{ij(\ell)}) \tag{12c}$$

$$\mathbf{D}^{(4)}(\mathbf{r}_{ij}) = \frac{k_B T}{6\pi\eta a} \left(1 - \frac{9}{32}\frac{r_{ij}}{a}\right) \mathbf{I} + \sum_{\substack{\ell \\ r_{ij(\ell)}>2a}} \mathbf{D}^{(2)}(\mathbf{r}_{ij(\ell)}) + \mathbf{D}^{(3)}(\mathbf{r}_{ij(\ell)}) \tag{12d}$$

with

$$\delta_{ij} = \begin{cases} 0 : i \neq j \\ 1 : i = j \end{cases} \tag{13}$$

the Kronecker-δ and $\alpha, \beta = x, y, z$ being cartesian indices of the position vectors. Since these expressions are approximations to the evaluation of an infinite sum, parameters which control the limits in the sums are introduced, i.e. Eq. 12b is evaluated only for particle pairs within a cutoff radius $R_{c,D}$ and Eq. 12c is limited to wavenumbers $|\mathbf{k}| < k_{max}$, where $\mathbf{k} = 2\pi/L\mathbf{n},\ \mathbf{n} \in \mathbb{Z}^3$. The parameters $R_{c,D}, k_{max}, \kappa$ of the periodic version of the Rotne-Prager tensor have to be determined according to an error threshold ϵ. There is no unique set of parameters fulfilling this requirement, but one may obtain an optimal set of parameters which, for a given ϵ, minimizes the runtime.

References

1. D. Marx and J. Hutter. *Ab Initio Molecular Dynamics: Basic Theory and Advanced Methods*. Cambridge University Press, Cambridge, 2009.
2. B. Kirchner, P. J. di Dio, and J. Hutter. Real-world predictions from ab initio molecular dynamics simulations. *Top Curr Chem.*, 307:109–153, 2012.
3. D. Frenkel and B. Smit. *Understanding molecular simulation. From algorithms to applications.* Academic Press, San Diego, 1996.
4. G. Sutmann. Molecular Dynamics - Vision and Reality. In S. Blügel J. Grotendorst and D. Marx, editors, *Computational Nanoscience - Do it yourself*, volume 31, pages 159–194, Jülich, 2006. John von Neumann Institute for Computing.
5. G. Sutmann. Molecular Dynamics - Extending the Scale from Microscopic to Mesoscopic. In S. Blügel J. Grotendorst, N. Attig and D. Marx, editors, *Multiscale Simulations Methods in Molecular Sciences*, volume 42, pages 1–50, Jülich, 2009. John von Neumann Institute for Computing.
6. U. Haberthuer and A. Caflisch. FACTS Fast analytical continuum treatment of solvation. 701-715 . *J. Comput. Chem.*, 29:701–715, 2008.
7. Chr. Peter and K. Kremer. Soft Matter, Fundamentals and Coarse Graining Strategies. In S. Blügel J. Grotendorst, N. Attig and D. Marx, editors, *Multiscale Simulations Methods in Molecular Sciences*, volume 42, pages 1–50, Jülich, 2009. John von Neumann Institute for Computing.
8. S. Succi. *The Lattice Boltzmann Equation: For Fluid Dynamics and Beyond*. Oxfor University Press, Oxford, 2001.
9. P. Espanol. Hydrodynamics from dissipative particle dynamics. *Phys. Rev. E*, 52:1734–1732, 1995.
10. G. Gompper, T. Ihle, D. M. Kroll, and R. G. Winkler. Multi-Particle Collision Dynamics: A Particle-Based Mesoscale Simulation Approach to the Hydrodynamics of Complex Fluids. *Adv. Polym. Sci.*, 221:1–87, 2009.
11. P. Mazur and W. van Saarloos. *Physica A*, 115:21, 1982.
12. S. Kim and S. J. Karrila. *Microhydrodynamics; Principles and Selected Applications*. Butterworth-Heinemann, Boston, 1991.
13. J. Rotne and S. Prager. Variational treatment of hydrodynamic interaction on polymers. *J. Chem. Phys.*, 50:4831–4837, 1969.
14. H. Yamakawa. Transport Properties of Polymer Chains in Dilute Solution: Hydrodynamic Interaction. *J. Chem. Phys.*, 53:436–443, 1970.
15. R. B. Jones and R. Schmitz. Mobility matrix for arbitrary spherical particles in solution. *Physica A*, 149:373, 1988.
16. H. A. Knudsen, J. H. Werth, and D. E. Wolf. Failure and success of hydrodynamic interaction models. *Eur. Phys. J. E*, 27:161–170, 2008.
17. M. Fixman. Construction of Langevin Forces in the Simulation of Hydrodynamic Interaction. *Macromol.*, 19:1204–1207, 1986.
18. T. Geyer and U. Winter. An O(N2) approximation for hydrodynamic interactions in Brownian dynamics simulations. *J. Chem. Phys.*, 130:114905, 2009.
19. T. J. Murphy and J. L. Aguirre. Brownian Motion of N interacting particles. I. Extension of the Einstein diffusion relation to the N-particle case. *J. Chem. Phys.*, 57:2098, 1972.

20. J. M. Deutsch and I. Oppenheim. Molecular Theory of Brownian Motion for Several Particles. *J. Chem. Phys.*, 54:3547–3555, 1971.
21. J. P. Boon and S. Yip. *Molecular Hydrodynamics*. Dover Publications, New York, 1980.
22. U. Balucani and M. Zoppi. *Dynamics of the Liquid State*. Clarendon Press, Oxford, 1994.
23. D. L. Ermak and J. A. McCammon. Brownian dynamics with hydrodynamic interactions. *J. Chem. Phys.*, 69:1352–1360, 1987.
24. G. A. Huber and J. A. McCammon. Browndye: A Software Package for Brownian Dynamics. *Comp. Phys. Comm.*, 181:1896–1905, 2010.
25. S. Dematte. Smoldyn on Graphics Processing Units: Massively Parallel Brownian Dynamics Simulations. *IEEE/ACM Trans. Comput. Biol. Bioinf.*, 9:655–667, 2012.
26. J. Trylska, M. Długosz, P. Zieliński. Brownian Dynamics Simulations on CPU and GPU with BD_BOX. *J. Comp. Chem.*, 32:2734–2744, 2011.
27. M. P. Allen and D. J. Tildesley. *Computer simulation of liquids*. Oxford Science Publications, Oxford, 1987.
28. T. A. El-Ghazawi and S. Chauvin. UPC Benchmarking Issues. In *Proceedings of the 2001 International Conference on Parallel Processing*, ICPP '02, pages 365–372, Washington, DC, USA, 2001. IEEE Computer Society.
29. R. Murty and D. Okunbor. Efficient parallel algorithms for molecular dynamics simulations. *Parall. Comp.*, 25:217–230, 1999.
30. C. Teijeiro, G. Sutmann, G. L. Taboada, and J. Touriño. Parallel Simulation of Brownian Dynamics on Shared Memory Systems with OpenMP and Unified Parallel C. J. Supercomp. (in press), 2012.
31. C. Teijeiro, G. Sutmann, G. L. Taboada, and J. Touriño. Parallel Brownian Dynamics Simulations with the Message-Passing and PGAS Programming Models. Comp. Phys. Commun. (in press), 2012.
32. C. W. J. Beenakker. Ewald sum of the Rotne-Prager tensor. *J. Chem. Phys.*, 85:1581–1582, 1986.

Hydrodynamic Correlations in Multiparticle Dynamics Fluids and their Effect on the Dynamics of Polymers in Solutions

Chien-Cheng Huang and Roland G. Winkler

Institute of Complex Systems and Institute for Advanced Simulation,
Forschungszentrum Jülich, 52425 Jülich, Germany
E-mail: r.winkler@fz-juelich.de

1 Introduction

During the last few decades, soft matter has developed into an interdisciplinary research field combining physics, chemistry, chemical engineering, biology, and materials science[1]. This is driven by the specificities of soft matter, which consists of large structural units in the nano- to micrometer range and is sensitive to thermal fluctuations and weak external perturbations[2–4]. Soft matter comprises traditional complex fluids such as amphiphilic mixtures, colloidal suspensions, and polymer solutions, as well as a wide range of phenomena including self-organization, transport in microfluidic devices and biological capillaries, chemically reactive flows, the fluid dynamics of self-propelled objects, and the viscoelastic behaviour of networks in cells[3].

The presence of disparate time, length, and energy scales poses particular challenges for conventional simulation techniques[1]. Biological systems present additional problems, because they are often far from equilibrium and are driven by strong spatially and temporally varying forces. The modelling of these systems often requires the use of coarse-grained or mesoscopic approaches that mimic the behaviour of atomistic systems on the length scales of interest. The goal is to incorporate the essential features of the microscopic physics in models which are computationally efficient and are easily implemented in complex geometries and on parallel computers, and can be used to predict emergent properties, test physical theories, and provide feedback for the design and analysis of experiments and industrial applications[3]. In many situations, a simple continuum description, e.g., based on the Navier-Stokes equation is not sufficient, since molecular-level details play a central role in determining the dynamic behaviour. A key issue is to resolve the interplay between thermal fluctuations, hydrodynamic interactions (HI), and spatiotemporally varying forces.

The desire to bridge the length- and time-scale gap has stimulated the development of mesoscale simulation methods such as Dissipative Particle Dynamics (DPD)[5–7], Lattice-Boltzmann (LB)[8–10], Direct Simulation Monte Carlo (DSMC)[11–13], and Multiparticle Collision dynamics (MPC)[14,15]. Common to these approaches is a simplified, coarse-grained description of the solvent degrees of freedom. Embedded solute particles, such as polymers or colloids, are often treated by conventional molecular dynamics simulations. All these approaches are essentially alternative ways of solving the Navier-Stokes equation for the fluid dynamics.

In this contribution, the basic properties of the MPC approach are presented and its emergent hydrodynamic behaviour is discussed. Thereby, we focus on the stochastic ro-

tation dynamics (SRD) version of MPC[3,14–18]. In MPC, the fluid is represented by point particles and their dynamics proceeds in two steps: A streaming and a collision step. Collisions occur at fixed discrete time intervals, and although space is discretized into cells to define the multiparticle collision environment, both the spatial coordinates and the velocities of the particles are continuous variables. To illuminate the effects of hydrodynamic correlations on the dynamics of embedded particles, we consider centre-of-mass velocity correlation functions of polymers in dilute solution. The fluctuating hydrodynamics approach based on the linearized Landau-Lifshitz Navier-Stokes equation is adopted to derive corresponding theoretical expressions[19]. This approach has been shown to describe the emergent fluctuating hydrodynamics of the MPC fluid very well[18].

2 Multiparticle Collision Dynamics

In MPC, the solvent is represented by N pointlike particles of mass m. The algorithm consists of individual streaming and collision steps. In the streaming step, the particles move independent of each other and experience only possibly present external forces[1]. Without such forces, they move ballistically and their positions $\boldsymbol{r}_i$ are updated according to

$$\boldsymbol{r}_i(t+h) = \boldsymbol{r}_i(t) + h\boldsymbol{v}_i(t), \tag{1}$$

$i = 1, \ldots, N$, $\boldsymbol{v}_i$ is the velocity of particle i, and h is the time interval between collisions, which will be denoted as collision time. In the collision step, a coarse-grained interaction between the fluid particles is imposed by a stochastic process. For this purpose, the system is divided in cubic collision cells of side length a. An elementary requirement is that the stochastic process conserves momentum on the collision-cell level, only then HI are present in the system. There are various possibilities for such a process. Originally, the rotation of the relative velocities, with respect to the centre-of-mass velocity of the cell, around a randomly orientated axis by a fixed angle α has been suggested[14,15], i.e,

$$\boldsymbol{v}_i(t+h) = \boldsymbol{v}_i(t) + (\mathcal{D}(\alpha) - \mathcal{E})\left(\boldsymbol{v}_i(t) - \boldsymbol{v}_{cm}(t)\right), \tag{2}$$

where $\mathcal{D}(\alpha)$ is the rotation matrix, $\mathcal{E}$ is the unit matrix, and

$$\boldsymbol{v}_{cm} = \frac{1}{N_c}\sum_{i=1}^{N_c}\boldsymbol{v}_i \tag{3}$$

is the centre-of-mass velocity of the N_c particles contained in the cell of particle i. The orientation of the rotation axis is chosen randomly for every collision cell and time step. As is easily shown, the algorithm conserves mass, momentum, and energy in every collision cell, which leads to long-range correlations between particles.

The rotations can be realized in different ways. On the one hand, the rotation matrix

$$\mathcal{D}(\alpha) = \begin{pmatrix} \mathcal{R}_x^2 + (1-\mathcal{R}_x^2)c & \mathcal{R}_x\mathcal{R}_y(1-c) - \mathcal{R}_z s & \mathcal{R}_x\mathcal{R}_z(1-c) + \mathcal{R}_y s \\ \mathcal{R}_x\mathcal{R}_y(1-c) + \mathcal{R}_z s & \mathcal{R}_y^2 + (1-\mathcal{R}_y^2)c & \mathcal{R}_y\mathcal{R}_z(1-c) - \mathcal{R}_x s \\ \mathcal{R}_x\mathcal{R}_z(1-c) - \mathcal{R}_y s & \mathcal{R}_y\mathcal{R}_z(1-c) + \mathcal{R}_x s & \mathcal{R}_z^2 + (1-\mathcal{R}_z^2)c \end{pmatrix} \tag{4}$$

can be used, with the unit vector $\boldsymbol{\mathcal{R}} = (\mathcal{R}_x, \mathcal{R}_y, \mathcal{R}_z)^T$, $c = \cos\alpha$, and $s = \sin\alpha$. The Cartesian components of $\boldsymbol{\mathcal{R}}$ are defined as

$$\mathcal{R}_x = \sqrt{1-\theta^2}\cos\varphi\ ,\ \mathcal{R}_y\sqrt{1-\theta^2}\sin\varphi\ ,\ \mathcal{R}_z = \theta, \tag{5}$$

where φ and θ are uncorrelated random numbers, which are taken from uniform distributions in the intervals $[0, 2\pi]$ and $[-1, 1]$, respectively. On the other hand, a vector rotation can be performed[20]. The vector $\Delta\boldsymbol{v}_i = \boldsymbol{v}_i - \boldsymbol{v}_{cm} = \Delta\boldsymbol{v}_{i,\parallel} + \Delta\boldsymbol{v}_{i,\perp}$ is given by the component $\Delta\boldsymbol{v}_{i,\parallel} = (\Delta\boldsymbol{v}_i\boldsymbol{\mathcal{R}})\boldsymbol{\mathcal{R}}$ parallel to $\boldsymbol{\mathcal{R}}$ and $\Delta\boldsymbol{v}_{i,\perp} = \Delta\boldsymbol{v}_i - \Delta\boldsymbol{v}_{i,\parallel}$ perpendicular to $\boldsymbol{\mathcal{R}}$. Rotation by an angle α transforms $\Delta\boldsymbol{v}_i$ into $\Delta\boldsymbol{v}_i' = \Delta\boldsymbol{v}_{i,\parallel} + \Delta\boldsymbol{v}_{i,\perp}'$. $\Delta\boldsymbol{v}_{i,\perp}'$ can be expressed by the vector $\Delta\boldsymbol{v}_{i,\perp}$ and the vector $\boldsymbol{\mathcal{R}} \times \Delta\boldsymbol{v}_{i,\perp}$, which yields

$$\begin{aligned}\boldsymbol{v}_i(t+h) &= \boldsymbol{v}_{cm}(t) + \cos\alpha\Delta\boldsymbol{v}_{i,\perp} + \sin\alpha\,(\boldsymbol{\mathcal{R}} \times \Delta\boldsymbol{v}_{i,\perp}) + \Delta\boldsymbol{v}_{i,\parallel} \\ &= \boldsymbol{v}_{cm}(t) + \cos\alpha\,[\Delta\boldsymbol{v}_i - (\Delta\boldsymbol{v}_i\boldsymbol{\mathcal{R}})\boldsymbol{\mathcal{R}}] \\ &\quad + \sin\alpha\,\boldsymbol{\mathcal{R}} \times [\Delta\boldsymbol{v}_i - (\Delta\boldsymbol{v}_i\boldsymbol{\mathcal{R}})\boldsymbol{\mathcal{R}}] + (\Delta\boldsymbol{v}_i\boldsymbol{\mathcal{R}})\boldsymbol{\mathcal{R}}\ ,\end{aligned} \tag{6}$$

since the vector $\boldsymbol{\mathcal{R}} \times \Delta\boldsymbol{v}_{i,\perp}$ is perpendicular to $\boldsymbol{\mathcal{R}}$ and $\Delta\boldsymbol{v}_{i,\perp}$.

In its original form[3, 14, 15, 17], the MPC algorithm violates Galilean invariance. This is most pronounced at low temperatures or small time steps, where the mean free path $\lambda = h\sqrt{k_BT/m}$ of a particle is smaller than the cell size a. Then, the same particles repeatedly interact with each other in the same cell and thereby build up correlations. In a collision lattice moving with a constant velocity, other particles interact with each other, creating less correlations, which implies breakdown of Galilean invariance. In Refs. 16,21, a random shift of the entire computational grid is introduced to restore Galilean invariance. In practice, all particles are shifted by the same random vector with components uniformly distributed in the interval $[-a/2, a/2]$ before the collision step. After the collision, particles are shifted back to their original positions. As a consequence, no reference frame is preferred.

The velocity distribution is given by the Maxwell-Boltzmann distribution in the limit $N \to \infty$, and the probability to find N_c particles in a cell is given by the Poisson distribution

$$P(N_c) = e^{-\langle N_c\rangle}\langle N_c\rangle^{N_c}/N_c!\ , \tag{7}$$

where $\langle N_c\rangle$ is the average number of the particles in a cell.

As an alternative collision rule, Maxwell-Boltzmann, i.e., Gaussian distributed relative velocities $\boldsymbol{v}_i^{\mathrm{ran}}$ of variance $\sqrt{k_BT/m}$ can be used to create new velocities according to Refs. 20, 22, 23.

$$\boldsymbol{v}_i(t+h) = \boldsymbol{v}_{cm}(t) + \boldsymbol{v}_i^{\mathrm{ran}} - \frac{1}{N_c}\sum_{j=1}^{N_c}\boldsymbol{v}_i^{\mathrm{ran}}\ . \tag{8}$$

Here, a canonical ensemble is simulated and no further thermalization is needed in non-equilibrium simulations, where there is viscose heating. From a numerical point of view, however, the calculation of the Gaussian random numbers is somewhat more time consuming, hence the performance is slower compared to SRD[3]. In Refs. 22–24 algorithms are presented, which additionally preserve angular momentum.

3 Embedded Objects and Boundary Conditions

A very simple procedure for coupling embedded objects such as colloids or polymers to a MPC solvent has been proposed in Refs. 25–28. In this approach, every colloidal particle or monomer in a polymer is taken to be a point particle which participates in the MPC collision. If monomer μ has mass M and velocity $\boldsymbol{v}_\mu$ the centre-of-mass velocity of all particles (MPC and monomers) in a collision cell is

$$\boldsymbol{v}_{cm} = \frac{\sum_{i=1}^{N_c} m\boldsymbol{v}_i + \sum_{\mu=1}^{N_m^c} M\boldsymbol{v}_\mu}{mN_c + MN_m^c}, \tag{9}$$

where N_m^c is the number of monomers in the collision cell. A stochastic collision of the relative velocities of both the solvent particles and embedded monomers is then performed in the collision step, which leads to an exchange of momentum between them. The dynamics of the monomers is typically treated by molecular dynamics simulations (MD), applying the velocity Verlet integration scheme[29,30]. Hence, the new monomer momenta (velocities) are used as initial conditions for the subsequent streaming step (MD) of duration h. In this approach, the average mass of solvent particles per cell $m\langle N_c\rangle$, should be of the order of the monomer or colloid mass M (assuming one embedded particle per cell). This corresponds to a neutrally buoyant object. It is also important to note that the average number of monomers per cell $\langle N_m^c\rangle$ should be on the order of unity or smaller in order to properly resolve HI between them. On the other hand, the average bond length in a semiflexible polymer or rodlike colloid should not far exceed the cell size a, in order to capture the anisotropic friction of rodlike molecules due to HI (which leads to a twice as large perpendicular than parallel friction coefficient for long stiff rods[31,32]), and to avoid an unnecessarily large ratio of the number of solvent to solute particles. Hence, the average bond length should be of order a.

To accurately resolve the local flow field around a colloid, methods have been proposed which exclude fluid-particles from the interior of the colloid and mimic slip[15,33] or no-slip[3,34,35,24] boundary conditions. No-slip boundary conditions are modelled by the bounce-back rule. Here, the velocity of a particle is inverted from $\boldsymbol{v}_i$ to $-\boldsymbol{v}_i$ when it intersects the surface of an impenetrable particle, e.g., colloid or blood cell, or wall. Since walls or surfaces will generally not coincide with the collision cell boundaries, in particular due to random shifts, the simple bounce-back rule fails to guarantee no-slip boundary conditions. The following generalization of the bounce-back rule has therefore been suggested[34]: For all cells that are intersected by walls, fill the wall part of the cell with a sufficient number of virtual particles in order to make the total number of particles equal to $\langle N_c\rangle$. The velocities of the wall particles are taken from a Maxwell-Boltzmann distribution with zero mean and variance k_BT/m. Since the sum of Gaussian random numbers is also Gaussian distributed, the velocities of the individual virtual particles need not be determined explicitly, it suffices to determine a momentum $\boldsymbol{p}$ from a Maxwell-Boltzmann distribution with zero mean and variance mN_pk_BT, where $N_p = \langle N_c\rangle - N_c$ is the number of virtual particles corresponding to the partially filled cell of N_c particles. The centre-of-

mass velocity of the cell is then

$$\boldsymbol{v}_{cm} = \frac{1}{m\,\langle N_c\rangle}\left(\sum_{i=1}^{N_c} m\boldsymbol{v}_i + \boldsymbol{p}\right). \tag{10}$$

Results for a Poiseuille flow obtained by this procedure, both with and without cell shifting, are in good agreement with the correct parabolic flow profile[34].

However, this does not completely prevent slip, because the average centre-of-mass position of all particles in a collision cell – including the virtual particle – does not coincide with the wall. In order to further reduce slip, the following modification of the original approach has been proposed[36]. To treat a surface cell on the same basis as a cell in the bulk, i.e., the number of particles satisfies the Poisson distribution with the average $\langle N_c\rangle$, we take fluctuations in the particle number into account by adding N_p virtual particles to every cell intersected by a wall such that $\langle N_p + N_c\rangle = \langle N_c\rangle$. There are various ways to determine the number N_p. For a system with parallel walls, we suggest to use the number of fluid particles in the opposite surface cell, i.e., the surface cell cut by the opposing wall. The average of the two numbers is equal to $\langle N_c\rangle$. Alternatively, N_p can be taken from a Poisson distribution with average $\langle N_c\rangle$ accounting for the fact that there are already N_c particles in the cell. Now, the centre-of-mass velocity of the particles in a boundary cell is

$$\boldsymbol{v}_{cm} = \frac{1}{m(N_c + N_p)}\left(\sum_{i=1}^{N_c} m\boldsymbol{v}_i + \boldsymbol{p}\right). \tag{11}$$

The momentum $\boldsymbol{p}$ of the effective virtual particle is obtained as described above.

4 Simulation Parameters

The linear size of the cubic simulation box is typically chosen in the range $L/a = 20 - 120$, where a is length of the cubic collision cell. The transport properties of the solvent depend on h, α, and N_c[3,17,37]. Tuning these parameters allows us to attain solvents with a high Schmidt number Sc and a low Reynolds number Re. The choice $\langle N_c\rangle = 10$, $\alpha = 130°$, and $h/\sqrt{ma^2/(k_BT)} = 0.1$, where T is the temperature and k_B is the Boltzmann constant, yields the solvent viscosity $\eta = m\,\langle N_c\rangle\,\nu = 8.7\sqrt{mk_BT/a^4}$, where ν is the kinematic viscosity, and the Schmidt number $Sc = 17$, which ensures that momentum transport dominates over mass transport[38].

5 Cell-Level Canonical Thermostat

In any nonequilibrium situation, the presence of external fields destroys energy conservation and a control mechanism has to be implemented to maintain temperature (a brief review on existing thermostats is presented in Ref. 39). A basic requirement of any thermostat is that it does not violate local momentum conservation, smear out local flow profiles, or distort the velocity distribution significantly. A simple and efficient way to maintain a constant temperature is velocity scaling. For a homogeneous system, a single global scaling factor is sufficient. For an inhomogeneous system, such as shear flow or Poiseuille flow, a local, profile-unbiased thermostat is required. Here, the relative velocities

$\Delta \boldsymbol{v}_i = \boldsymbol{v}_i - \boldsymbol{v}_{cm}$ (Eq. 2) are scaled, before or after the rotation (velocity scaling exchanges with the rotation), i.e., new velocities $\Delta \boldsymbol{v}_i'$ are obtained according to $\Delta \boldsymbol{v}_i' = \kappa \Delta \boldsymbol{v}_i$, where κ is the scale factor.

In its simplest form, velocity scaling keeps the kinetic energy at the desired value. For a profile-unbiased *global scaling* scheme, the scale factor is give by

$$\kappa = \left(\frac{3(N - N_{cl}) k_B T}{2 E_k} \right)^{1/2} \tag{12}$$

in three-dimensional space, where N_{cl} is the number of collision cells and $E_k = \sum_{i=1}^{N} m \Delta \boldsymbol{v}_i^2 / 2$ the kinetic energy of all particles with respect to their cells' centre-of-mass velocities. The corresponding expression for *cell-level* scaling is

$$\kappa = \left(\frac{3(N_c - 1) k_B T}{2 E_k} \right)^{1/2}, \tag{13}$$

where now $E_k = \sum_{i=1}^{N_c} m \Delta \boldsymbol{v}_i^2 / 2$ is the kinetic energy of the particles within the particular cell. Note that the scale factor is different for every cell.

This kind of temperature control corresponds to an isokinetic rather than isothermal, i.e., canonical ensemble, and may have sever consequences on certain properties such as local temperature or particle number[39]. Such artifacts are avoided by a cell-level canonical thermostat. Instead of using the thermal energy as reference, an kinetic energy is determined from its distribution function in a canonical ensemble[39]

$$P(E_k) = \frac{1}{E_k \Gamma(f/2)} \left(\frac{E_k}{k_B T} \right)^{f/2} \exp\left(-\frac{E_k}{k_B T} \right). \tag{14}$$

Here, $f = 3(N_c - 1)$ denotes the degrees of freedom of the considered system and $\Gamma(x)$ is the gamma function. The distribution function $P(E_k)$ itself is denoted as gamma distribution. In the limit $f \to \infty$, the gamma distribution turns into a Gaussian function with the mean $\langle E_k \rangle = f k_B T / 2$ and variance $f (k_B T)^2 / 2$.

To thermalize the velocities of the MPC fluid on the cell level, a different energy E_k is taken from the distribution function (Eq. 14) for every cell and time step and the velocities are scaled by the factor

$$\kappa = \left(\frac{2 E_k}{\sum_{i=1}^{N_c} m \Delta \boldsymbol{v}_i^2} \right)^{1/2}. \tag{15}$$

For a fixed N_c, we then obtain the following distribution function for the relative velocity of a particle in a cell in the limit of a large number of MPC steps

$$P(\Delta \boldsymbol{v}, N_c) = \left(\frac{m}{2\pi k_B T (1 - 1/N_c)} \right)^{3/2} \exp\left(-\frac{m}{2 k_B T (1 - 1/N_c)} \Delta \boldsymbol{v}^2 \right). \tag{16}$$

However, the number of fluid particles in a cell is fluctuating in time. Thus, the actual distribution function is obtained by averaging Eq. 16 over the Poisson distribution Eq. 7

$$P(\Delta \boldsymbol{v}) = \sum_{N_c=2}^{\infty} e^{-\langle N_c \rangle} \frac{\langle N_c \rangle^{N_c}}{N_c!} P(\Delta \boldsymbol{v}, N_c) / \left(1 - (\langle N_c \rangle + 1) e^{-\langle N_c \rangle} \right). \tag{17}$$

Results for various examples are provided in Ref. 39.

6 Transport Coefficients

A major advantage of the MPC dynamics is that the transport properties may be computed and analytical expressions be derived[17]. In the following, the self-diffusion coefficient and the viscosity of the MPC solvent will be discussed. Other aspects are presented in Refs. 3, 17, 40.

6.1 Diffusion Coefficient

The diffusion coefficient D of a particle i can be obtained from the Green-Kubo relation[3, 17, 21, 41]

$$D = \frac{h}{6}\left\langle \boldsymbol{v}_i(0)^2 \right\rangle + \frac{h}{3}\sum_{n=1}^{\infty}\left\langle \boldsymbol{v}_i(nh)\boldsymbol{v}_i(0)\right\rangle \tag{18}$$

for a discrete-time random system in three-dimensional space. $t_n = nh$ denotes the discrete time of the nth collision. The average $\langle \ldots \rangle$ comprises both, averaging over the orientation of the rotation axis ($\boldsymbol{\mathcal{R}}$) and the distribution of velocities. The two are independent. To evaluate the expression, the velocity auto-correlation function is required. An exact evaluation of the correlation function is difficult or even impossible, because it would imply that the full correlated dynamics of the particles can analytically be calculated. However, an approximate expression can be derived.

In a first step, the average over the random orientation of the rotation axis is performed. Since the orientation is isotropic in space, all odd moments of the Cartesian components of $\boldsymbol{\mathcal{R}}$ vanish and the second moments are given by $\langle \mathcal{R}_\beta \mathcal{R}_{\beta'}\rangle = \delta_{\beta\beta'}/3$. Thus,

$$\left\langle \boldsymbol{v}_i(t+h)\boldsymbol{v}_i(t)\right\rangle = \left\langle \boldsymbol{v}_{cm}(t)\boldsymbol{v}_i(t)\right\rangle + \frac{1}{3}\left(1+2\cos\alpha\right)\left\langle \Delta\boldsymbol{v}_i(t)\boldsymbol{v}_i(t)\right\rangle . \tag{19}$$

To evaluate the correlation function with the centre-of-mass velocity, we apply the molecular chaos assumption, which assumes that different particles are independent, i.e., $\langle \boldsymbol{v}_j(t)\boldsymbol{v}_i(t')\rangle = \delta_{ij}\left\langle \boldsymbol{v}_i(t)\boldsymbol{v}_i(t')\right\rangle$. Hence,

$$\left\langle \boldsymbol{v}_i(t+h)\boldsymbol{v}_i(t)\right\rangle = (1-\gamma)\left\langle \boldsymbol{v}_i(t)^2\right\rangle, \text{ with } \gamma = \frac{2}{3}(1-\cos\alpha)\left(1-\frac{1}{\langle N_c\rangle}\right). \tag{20}$$

Since we typically consider $\langle N_c\rangle \geq 10$, number fluctuations in a collision cell can be neglected[1]. More generally, iteration yields

$$\left\langle \boldsymbol{v}_i(nh)\boldsymbol{v}_i(0)\right\rangle = (1-\gamma)^n\left\langle \boldsymbol{v}_i(0)^2\right\rangle . \tag{21}$$

With Eq. 21, the diffusion coefficient follows as[40, 41]

$$D = \frac{h\left\langle \boldsymbol{v}_i(0)^2\right\rangle}{3}\left(\frac{1}{\gamma}-\frac{1}{2}\right) = \frac{hk_BT}{m}\left(\frac{1}{\gamma}-\frac{1}{2}\right) \tag{22}$$

within the molecular chaos assumption[42, 27].

6.2 Viscosity

The shear viscosity is one of the most important properties of complex fluids. In particular, it characterizes their non-equilibrium behaviour, e.g., in rheology. Various ways have been suggested to obtain an analytical expression for the viscosity of a MPC fluid. In Refs. 3, 21, 41, 43, 44, linear hydrodynamic equations (Navier-Stokes equation) and Green-Kubo relations are exploited. Alternatively, non-equilibrium simulations can be performed and transport coefficients are obtained from the linear response to an imposed gradient. The two approaches are related by the fluctuation-dissipation theorem.

In simple shear flow, with the velocity field $v_x = \dot{\gamma} y$, where v_x is the fluid flow field along the x-direction (flow direction), y the gradient direction, and $\dot{\gamma}$ the shear rate, the viscosity η is related to the stress tensor σ_{xy} via

$$\sigma_{xy} = \eta \dot{\gamma}. \tag{23}$$

Hence, an expression is required for the stress tensor to either derive η analytically and/or to determine it in simulations. In Refs. 45, 46, the kinetic theory moment method has been applied to derive an analytical expression.

6.2.1 Stress Tensor

An expression for the stress tensor can be determined by the virial theorem[36, 47, 1]. Starting from the equation of motion of a particle, the following expressions are obtained

$$\sigma^e_{xy} = \frac{1}{Vh} \sum_{i=1}^{N} \Delta p_{ix} R_{iy} - \frac{\dot{\gamma}}{2V} \sum_{i=1}^{N} m(v_{iy} + \hat{v}_{iy}) R_{iy}, \tag{24}$$

$$\sigma^i_{xy} = -\frac{1}{V} \sum_{i=1}^{N} m \hat{v}'_{ix} \hat{v}_{iy} - \frac{\dot{\gamma} h}{2V} \sum_{i=1}^{N} m v^2_{iy} - \frac{1}{Vh} \sum_{i=1}^{N} \Delta p_{ix} r'_{iy} \tag{25}$$

for the internal σ^i_{xy} and external σ^e_{xy} stress tensor in the presence of shear flow.

6.2.2 Viscosity of MPC Fluid: Analytical Expressions

The derived expressions for the stress tensors are independent of any particular collision rule. The viscosity of a system, however, depends on the applied collision procedure. Analytical expressions for the viscosity of an MPC fluid have been derived by various approaches[3, 15, 17, 16, 23, 45, 36, 44, 46].

In simple shear flow, the viscosity η is given by Eq. 23, where the (macroscopic) stress tensor follows from $\sigma_{xy} = \langle \sigma^i_{xy} \rangle = \langle \sigma^e_{xy} \rangle$ [1, 36]. For a MPC fluid, the stress tensor is composed of a kinetic and collisional contribution[3, 15, 17, 16, 23, 45, 36], i.e, $\sigma_{xy} = \sigma^{\mathrm{kin}}_{xy} + \sigma^{\mathrm{col}}_{xy}$, which implies that the viscosity $\eta = \eta_{\mathrm{kin}} + \eta_{\mathrm{col}}$ consists of a kinetic η_{kin} and collisional η_{col} part too. For a system with periodic boundary conditions, the two contributions are conveniently obtained from the internal stress tensor (Eq. 25). The kinetic contribution η_{kin} is determined by streaming, i.e., the velocity dependent terms in Eq. 25. Evaluation of the expressions, employing the molecular chaos assumption, yields

$$\eta_{\mathrm{kin}} = \frac{N k_B T h}{V} \left[\frac{5 \langle N_c \rangle}{(\langle N_c \rangle - 1)(4 - 2\cos\alpha - 2\cos(2\alpha))} - \frac{1}{2} \right], \tag{26}$$

with the equipartition of energy $\left\langle v_{iy}^2 \right\rangle_{N_s} = k_B T/m$.

The collisional viscosity $\eta_{\rm col}$ is determine by the momentum change of the particles during the collision step. Since the collisions in the various cells are independent, it is sufficient to consider one cell only. Evaluation of the averages then yields

$$\eta_{\rm col} = \frac{Nma^2}{18Vh}\left(1-\cos\alpha\right)\left(1-\frac{1}{\langle N_c\rangle}\right). \tag{27}$$

7 Fluctuating Hydrodynamics

The hydrodynamic properties of the MPC fluid are described by the linearized Navier-Stokes on sufficiently large length and long time scales[14,17,3,46,40,18]. A recent detailed study of the emergent fluctuating hydrodynamics of the SRD-MPC fluid even demonstrated that the linearized Landau-Lifshitz Navier-Stokes equation provides a excellent description on length scales above a collision cells[18].

For a compressible isothermal SRD fluid, the corresponding linearized continuity and Landau-Lifshitz Navier-Stokes equations are

$$\frac{\partial}{\partial t}\rho + \rho\nabla\cdot\boldsymbol{v} = 0, \tag{28}$$

$$\rho\frac{\partial}{\partial t}\boldsymbol{v} = -\nabla p + \eta\Delta\boldsymbol{v} + \frac{1}{3}\eta^{\rm kin}\nabla(\nabla\cdot\boldsymbol{v}) + \boldsymbol{f} + \boldsymbol{f}^R \tag{29}$$

in three dimensions[18,19]. Here, $\rho = \rho(\boldsymbol{r},t)$ denotes the mass density of the fluid, $\boldsymbol{v} = \boldsymbol{v}(\boldsymbol{r},t)$ the fluid velocity field at the position $\boldsymbol{r}$ in space at the time t, $\boldsymbol{f}(\boldsymbol{r},t)$ is a volume force density, and $\boldsymbol{f}^R(\boldsymbol{r},t) = \nabla\cdot\boldsymbol{\sigma}^R$ the random force density due to the thermal fluctuations of the fluid, with $\boldsymbol{\sigma}^R$ the corresponding stress tensor. $\eta = \eta^{\rm kin} + \eta^{\rm col}$ is the MPC fluid viscosity[40,18,36].

The stochastic process for $\boldsymbol{\sigma}^R$ is assumed to be Gaussian and Markovian with the moments

$$\left\langle \boldsymbol{\sigma}^R \right\rangle = 0 \tag{30}$$

$$\left\langle \sigma^R_{\alpha\beta}(\boldsymbol{r},t)\sigma^R_{\alpha'\beta'}(\boldsymbol{r},t)\right\rangle = 2k_BT\eta_{\alpha\beta\alpha'\beta'}\delta(\boldsymbol{r}-\boldsymbol{r}')\delta(t-t'),$$

$\alpha,\,\alpha',\,\beta,\,\beta' \in \{x,y,x\}$, and

$$\eta_{\alpha\beta\alpha'\beta'} = \eta\delta_{\alpha\beta'}\delta_{\beta\alpha'} + \frac{1}{2}\left[\eta+\eta^{\rm kin}\right]\delta_{\alpha\alpha'}\delta_{\beta\beta'} - \frac{1}{2}\left[\eta+\frac{1}{3}\eta^{\rm kin}\right]\delta_{\alpha\beta}\delta_{\alpha'\beta'}\,. \tag{31}$$

Since SRD is not conserving angular momentum in the MPC collision step, the fluid stress tensor is non-symmetric, which is also accounted for in the correlations (Eq. 30).

The linear Eqs. 28 and 29 are solved by Fourier transformation. Since we want to compare the analytical results with computer simulation results, we adopt a discrete Fourier transformation for a spatial periodic system, i.e., we use[18]

$$\boldsymbol{v}(\boldsymbol{r},t) = \frac{1}{2\pi}\sum_{\boldsymbol{k}}\int \boldsymbol{v}(\boldsymbol{k},\omega)e^{-i\boldsymbol{k}\cdot\boldsymbol{r}}e^{i\omega t}d\omega, \tag{32}$$

$$\boldsymbol{v}(\boldsymbol{k},\omega) = \frac{1}{V}\int \boldsymbol{v}(\boldsymbol{r},t)e^{i\boldsymbol{k}\cdot\boldsymbol{r}}e^{-i\omega t}d^3r dt, \tag{33}$$

with $k_\alpha = 2\pi n_\alpha/L$ and $n_\alpha \in \mathbb{Z}\backslash\{0\}$. This yields the flow field

$$\boldsymbol{v}(\boldsymbol{k},\omega) = \mathbf{Q}(\boldsymbol{k},\omega)\left[\boldsymbol{f}^R(\boldsymbol{k},\omega) + \boldsymbol{f}(\boldsymbol{k},\omega)\right], \tag{34}$$

with the tensor $\mathbf{Q}(\boldsymbol{k},\omega) = \mathbf{Q}^L(\boldsymbol{k},\omega) + \mathbf{Q}^T(\boldsymbol{k},\omega)$ and

$$\mathbf{Q}^L = \left(\tilde{\eta}k^2 + \frac{i\rho}{\omega}[\omega^2 - c^2k^2]\right)^{-1}\mathbf{P} = Q^L\mathbf{P}, \tag{35}$$

$$\mathbf{Q}^T = \left(\eta k^2 + i\rho\omega\right)^{-1}(\mathbf{E}-\mathbf{P}) = Q^T(\mathbf{E}-\mathbf{P}), \tag{36}$$

and $\tilde{\eta} = \eta + \eta^{\mathrm{kin}}/3$. Note that for angular-momentum conserving fluids $\tilde{\eta} = 4\eta/3$. Otherwise the same expressions 35 and 36 are obtained. $\mathbf{P}$ is a projection operator with the components $P_{\alpha\beta} = k_\alpha k_\beta/k^2$, and projects a vector along the direction of $\boldsymbol{k}$; $k = |\boldsymbol{k}|$. Hence, $\boldsymbol{v}(\boldsymbol{k},\omega) = \boldsymbol{v}^L(\boldsymbol{k},\omega) + \boldsymbol{v}^T(\boldsymbol{k},\omega)$ consists of a longitudinal part $\boldsymbol{v}^L$ and transverse part $\boldsymbol{v}^T$ with respect to $\boldsymbol{k}$, i.e., $\boldsymbol{v}\cdot\boldsymbol{k} = v^L k$ and $\boldsymbol{v}^T\cdot\boldsymbol{k} = 0$. Fourier transformation with respect to ω yields

$$Q^T(\boldsymbol{k},t) = \frac{1}{\rho}e^{-\nu k^2 t}\Theta(t) \tag{37}$$

for the transverse part, where $\Theta(t)$ is Heaviside's function and $\nu = \eta/\rho$ the kinematic viscosity. For the longitudinal contribution, we obtain the expression[18]

$$Q^L(\boldsymbol{k},t) = \frac{1}{\rho}e^{-k^2\tilde{\nu}t/2}\left[\cos(\Omega t) - \sqrt{\frac{k^2\tilde{\nu}^2}{4c^2 - k^2\tilde{\nu}^2}}\sin(\Omega t)\right]\Theta(t) \tag{38}$$

for $4c^2/(k^2\tilde{\nu}^2) > 1$, where $\Omega = k^2\tilde{\nu}\sqrt{4c^2/(k^2\tilde{\nu}^2) - 1}/2$, and

$$Q^L(\boldsymbol{k},t) = \frac{1}{\rho}e^{-k^2\tilde{\nu}t/2}\left[\cosh(\Lambda t) - \sqrt{\frac{k^2\tilde{\nu}^2}{k^2\tilde{\nu}^2 - 4c^2}}\sinh(\Lambda t)\right]\Theta(t) \tag{39}$$

for $4c^2/(k^2\tilde{\nu}^2) < 1$, with $\Lambda = k^2\tilde{\nu}\sqrt{1 - 4c^2/(k^2\tilde{\nu}^2)}/2$.

7.1 Velocity Correlation Functions

Insight into the fluid dynamics is obtained by the velocity correlation functions $\langle\boldsymbol{v}(\boldsymbol{k},t)\cdot\boldsymbol{v}(\boldsymbol{k}',0)\rangle$ and $\langle\boldsymbol{v}(t)\cdot\boldsymbol{v}(0)\rangle$ in Fourier and real space, respectively. By convolution, we obtain the expression[18]

$$\langle\boldsymbol{v}(\boldsymbol{k},t)\cdot\boldsymbol{v}(\boldsymbol{k}',0)\rangle = \frac{2k_BTk^2}{V}\delta_{\boldsymbol{k},-\boldsymbol{k}'}\int\left[2\eta Q^T(\boldsymbol{k},t-t')Q^T(\boldsymbol{k}',-t') + \tilde{\eta}Q^L(\boldsymbol{k},t-t')Q^L(\boldsymbol{k}',-t')\right]dt'. \tag{40}$$

7.1.1 Transverse Velocity Correlation Function

With Eq. 37, the transverse velocity correlation becomes

$$\left\langle\boldsymbol{v}^T(\boldsymbol{k},t)\cdot\boldsymbol{v}^T(-\boldsymbol{k},0)\right\rangle = \frac{2k_BT}{\rho V}e^{-\nu k^2|t|} \tag{41}$$

in the stationary state[18]. Hence, the correlation function decays exponentially for all k values. The time integral of the normalized correlation function $\left\langle \boldsymbol{v}^T(\boldsymbol{k},t)\cdot\boldsymbol{v}^T(-\boldsymbol{k},0)\right\rangle / \left\langle \boldsymbol{v}^T(\boldsymbol{k},0)\cdot\boldsymbol{v}^T(-\boldsymbol{k},0)\right\rangle$ yields

$$T(\boldsymbol{k},t) = \int_0^t e^{-\nu k^2 t'} dt' = \frac{1}{\nu k^2}\left(1 - e^{-\nu k^2 t}\right). \tag{42}$$

Thus, in the limit $t \to \infty$, $T(\boldsymbol{k})$ is proportional to the Oseen tensor[31,32]

$$\mathbf{O} = \frac{1}{\eta k^2}(\mathbf{E} - \mathbf{P}) \tag{43}$$

in $\boldsymbol{k}$-space.

Fig. 1 depicts simulation results for the k dependence of $T(\boldsymbol{k}) = \lim_{t\to\infty} T(\boldsymbol{k},t)$ for various collision time steps h. For sufficiently small k values, $T(\boldsymbol{k})$ follows the prediction of the Stokes equation and hence shows the same dependence as the Oseen tensor. Above a certain value, which depends on the collision time step, $T(\boldsymbol{k})$ itself approaches a plateau. Hence, below a certain length scale no hydrodynamic interactions are present anymore. The asymptotic behaviour can be calculated by applying the molecular chaos assumption. As shown in Fig. 1, the theoretical expression captures the small scale behaviour[18].

An characteristic length scale λ_c, which separates the hydrodynamic from the non-hydrodynamic regime, is obtained by the intercept of the Oseen-type dependence $T(\boldsymbol{k}) = 1/(\nu k^2)$ with the asymptotic dependence $T(\boldsymbol{k}) = T_{\mathrm{mc}}(\boldsymbol{k}) = h/2$, which yields $\lambda_c = \pi\sqrt{2\nu h}$. As shown by the inset of Fig. 1, the theoretical expression describes the experimental data very well[18].

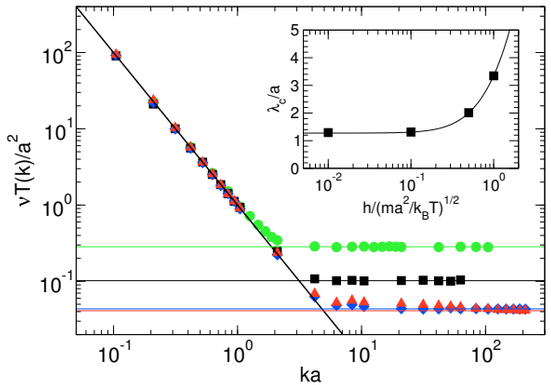

Figure 1. Dependence of $T(k) = \lim_{t\to\infty} T(k,t)$ (Eq. 42) on the wave number for the collision times $h/\sqrt{ma^2/(k_BT)} = 0.01$ (▲), 0.1 (◆), 0.5 (■), and 1.0 (●). The thick solid line indicates the dependence $1/k^2$, corresponding to the Oseen tensor. The horizontal lines are the theoretical predictions for the plateau values[18] of $\nu T(k)$. The inset shows the theoretical prediction for the characteristic length scale λ_c (solid line) and the values extracted from the simulations (squares).

7.1.2 Longitudinal Velocity Correlation Function

The longitudinal velocity correlation function reads as

$$\left\langle v^L(\boldsymbol{k},t)v^L(-\boldsymbol{k},0)\right\rangle = \frac{k_BT}{\rho V}e^{-\tilde{\nu}k^2|t|/2}\left[\cos(\Omega|t|) - \sqrt{\frac{k^2\tilde{\nu}^2}{4c^2-k^2\tilde{\nu}^2}}\sin(\Omega|t|)\right], \quad (44)$$

with Eq. 38. For $4c^2/(k^2\tilde{\nu}) < 1$, the hyperbolic functions with the argument Λ has to be used, as in Eq. 39. Thus, the correlation functions for the various k values decay exponentially and oscillate for small k values. For large k values, the decay is more complex[18].

7.1.3 Velocity Correlation Function in Real Space

The velocity correlation function $\langle \boldsymbol{v}(\boldsymbol{r},t)\cdot\boldsymbol{v}(\boldsymbol{r}',0)\rangle$ of the fluid at a point $\boldsymbol{r}$ at time t and $\boldsymbol{r}'$ at $t'=0$ follows by Fourier transformation

$$\langle \boldsymbol{v}(\boldsymbol{r},t)\cdot\boldsymbol{v}(\boldsymbol{r}',0)\rangle = \sum_{\boldsymbol{k}}\langle \boldsymbol{v}(\boldsymbol{k},t)\cdot\boldsymbol{v}(-\boldsymbol{k},0)\rangle\, e^{-i\boldsymbol{k}\cdot(\boldsymbol{r}-\boldsymbol{r}')}, \quad (45)$$

with $\langle \boldsymbol{v}(\boldsymbol{k},t)\cdot\boldsymbol{v}(-\boldsymbol{k},0)\rangle$ the sum of the transverse (Eq. 41) and longitudinal (Eq. 44) correlation functions.

Adopting the Lagrangian description of the fluid, where a fluid element is followed as it moves through space and time, we additionally average the correlation function over the distribution of displacements $\boldsymbol{r}-\boldsymbol{r}'$. Hence, Eq. 45 turns into

$$\langle \boldsymbol{v}(t)\cdot\boldsymbol{v}(0)\rangle = \sum_{\boldsymbol{k}}\langle \boldsymbol{v}(\boldsymbol{k},t)\cdot\boldsymbol{v}(-\boldsymbol{k},0)\rangle\left\langle e^{-i\boldsymbol{k}\cdot(\boldsymbol{r}-\boldsymbol{r}')}\right\rangle. \quad (46)$$

Assuming a diffusive motion of the fluid element, with Gaussian distributed displacements, we find

$$\langle \boldsymbol{v}(t)\cdot\boldsymbol{v}(0)\rangle = \sum_{\boldsymbol{k}}\langle \boldsymbol{v}(\boldsymbol{k},t)\cdot\boldsymbol{v}(-\boldsymbol{k},0)\rangle\exp\left(-k^2\left\langle(\boldsymbol{r}(t)-\boldsymbol{r}(0))^2\right\rangle/6\right). \quad (47)$$

Here, $\left\langle(\boldsymbol{r}(t)-\boldsymbol{r}(0))^2\right\rangle$ indicates the mean square displacement, which, in the simplest case, reduces to $\left\langle(\boldsymbol{r}(t)-\boldsymbol{r}(0))^2\right\rangle = 6Dt$, with D the diffusion coefficient of a MPC particle.

In general, the sum over $\boldsymbol{k}$ in Eq. 47 cannot be evaluated analytically. For the transverse velocity correlation function, however, we obtain the expression

$$\left\langle \boldsymbol{v}^T(t)\cdot\boldsymbol{v}^T(0)\right\rangle = \frac{2k_BT}{\rho(2\pi)^3}\int e^{-\nu k^2t}e^{-Dk^2t}d^3k = \frac{k_BT}{4\rho}\frac{1}{[\pi(\nu+D)t]^{3/2}} \quad (48)$$

in the limit of an infinitely large system ($L\to\infty$). Hence, we find the well-known long-time tail of the transverse velocity correlation function[48–54].

Velocity correlation functions of a MPC fluid in real space are presented in Fig. 2. The simulation data are well described by the theoretical expression Eq. 47, with Eqs. 41 and 44, over several decades in time. We like to emphasize that we include the full mean square displacement of a MPC particle (Eq. 47) and not simply the linear dependence on time. The latter yields a slightly different theoretical curve, in particular in the vicinity of the minimum at $t/\sqrt{ma^2/(k_BT)} \approx 2$. The theoretical approach even reproduces the

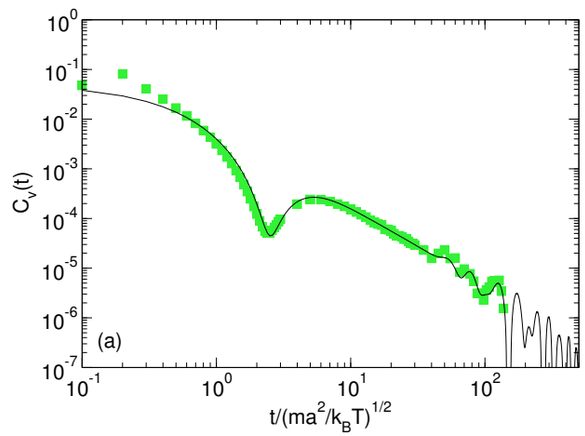

Figure 2. Magnitude of the normalized velocity autocorrelation function (Eq. 47) of a MPC fluid (symbols) for the collision times $h/\sqrt{ma^2/(k_BT)} = 0.1$. The theoretical results (solid lines) are obtained from Eq. 47 with Eqs. 41 and 44[18].

oscillations at large time. They are caused by sound and the finite system size. More details are discussed in Ref. 18. However, we have to introduce an upper cut-off for the k values. As discussed, the hydrodynamic description of the MPC fluid breaks down below a certain length scale. To achieve a good fit over a large time range, the maximum k value is $k_n = 2\pi n/60$ with $n = 16$. This corresponds to the lower length scales $\approx 3.8a$. This value is somewhat above the theoretically estimated critical length scale $\lambda_c \approx a$.

The deviation between the theoretical expression and the simulation results at short times is also related to the cut-off in k values. The correlation function is determined by large k values at short times. Here, however, the theoretical and simulation results deviate, because the MPC solvent does not exhibit hydrodynamic behaviour anymore for $2\pi/\lambda_c < k < \infty$.

8 Dynamics of Polymers in Dilute Solution

As an example for the effect of hydrodynamic correlations on the dynamics of objects embedded in a MPC solvent, we will briefly discuss the (short) time dynamics of polymers in dilute solution.

8.1 Model

We consider a single flexible Gaussian polymer embedded in the MPC fluid[31,56]. The polymer is composed of mass points of Mass M, which are linear connected by harmonic

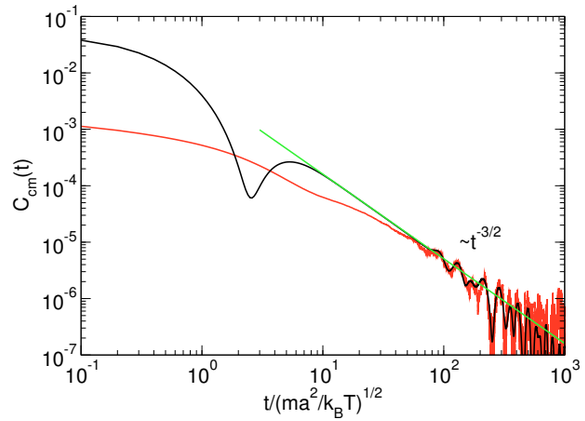

Figure 3. Polymer centre-of-mass velocity correlation function $C_{cm}(t) = \langle \boldsymbol{v}_{cm}(t) \cdot \boldsymbol{v}_{cm}(0) \rangle / (k_B T/m)$ for a polymer of length $N_m = 160$ (red)[55]. For comparison, the fluid velocity correlation function is presented as well (black line). The green line indicates the long-time tail according to Eq. 48[18].

springs with the potential

$$U_G = \frac{3k_BT}{2l^2} \sum_{\mu=1}^{N_m-1} (\boldsymbol{r}_{\mu+1} - \boldsymbol{r}_\mu)^2, \tag{49}$$

where $\boldsymbol{r}_\mu(t)$ is the position of the bead μ ($\mu = 1, \ldots, N_m$), l is the root-mean-square bond length, and N_m is the number of beads. In the following we will use $l = a$. The dynamics of the beats is described by Newton's equations of motion, which are solved by the Velocity Verlet algorithm[30,29].

8.2 Velocity Correlation Function

Fig. 3 shows the polymer centre-of-mass velocity correlation function for a polymer of length $N_m = 160$. Evidently, its correlation function is significantly different from that of the fluid itself at short times. At longer times, however, the polymer aspects vanish and the correlation function is solely determined by the fluid correlations. In that regime, the correlation function exhibits the fluid-velocity long-time tail. The oscillations at longer times are caused by finite-size effects, as discussed already for the bare fluid.

There is a polymer-length dependent time regime, where the correlation function is governed by polymer properties. For the transverse part of the correlation function, analytical calculations yield[57]

$$\left\langle \boldsymbol{v}_{cm}^T(t) \cdot \boldsymbol{v}_{cm}^T(0) \right\rangle = \frac{k_BT}{\rho\sqrt{\pi^3}R_g^2} \left[\frac{1}{\sqrt{\nu t}} + \frac{2}{R_g^2} \left(\sqrt{\nu t} - \sqrt{\nu t + R_g^2} \right) \right], \tag{50}$$

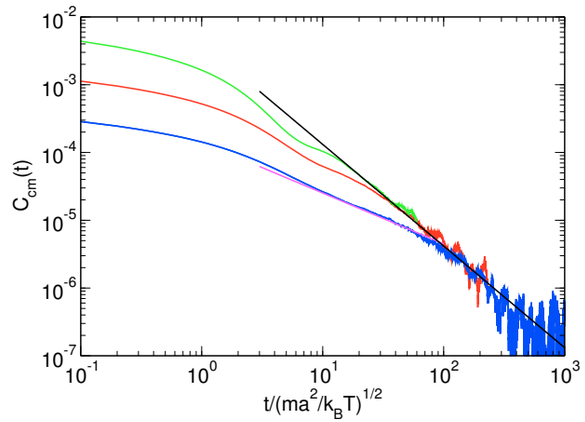

Figure 4. Polymer centre-of-mass velocity correlation functions for polymers of lengths $N_m = 40$ (green), 160 (red), and 640 (blue)[55]. The black line indicates the long-time tail. The magenta line shows the dependence $C_{cm}(t) \sim t^{-3/4}$.

where $R_g^2 = l^2 N_m/6$ is radius of gyration, in the limit of an infinitely large system[55,57]. This expression yields the fluid long-time tail $t^{-3/2}$ for $\nu t \gg R_g^2$. In the opposite limit $\nu t \ll R_g^2$, the expression predicts the dependence

$$\left\langle \boldsymbol{v}_{cm}^T(t) \cdot \boldsymbol{v}_{cm}^T(0) \right\rangle \sim \left(R_g^2\right)^{-1} (\nu t)^{-1/2} \tag{51}$$

on the radius of gyration and time. For sufficiently long times, the theoretical expression describes the simulation results very well, as shown in Fig. 4. As predicted, the crossover to the fluid-dominated correlation function shifts to longer times with increasing polymer length. However, the considered polymers are too short to exhibit the $t^{-1/2}$ dependence. We rather find a dependence closer to $t^{-3/4}$. The $t^{-1/2}$ dependence should follow for much longer polymers. At short times, sound plays a certain role – an aspect more pronounced for short polymers. This is reflected by the non-monotonous behaviour of the correlation functions in the vicinity of $t/\sqrt{ma^2/(k_BT)} \approx 10$.

The correlation functions clearly reveal the strong impact of fluid hydrodynamic correlations on the dynamics of polymers, at least for short times. For the centre-of-mass diffusion coefficient, sound does not play any role, as pointed out for colloids already[58]. The calculation of the diffusion coefficient, however, requires inclusion of the long-time tail. As is well known, for any finite system, the diffusion coefficient underestimates the asymptotic infinite-system value. This simply reflects the fact that the long-time tail is not fully accounted for.

9 Conclusions

In the short time since Malevanets and Kapral[14,15] introduced the MPC dynamics approach as a particle-based mesoscale simulation technique, the method developed into a versatile tool to study hydrodynamic properties of complex fluids[1]. By now, several collision algorithms have been proposed and employed, and the method has been generalized to describe multi-phase flows and viscoelastic fluids[3]. A major advantage of the algorithm is the simplicity by which the fluid can be coupled to the dynamics of embedded particles using a hybrid MPC-MD simulations approach. Results of such studies are in excellent quantitative agreement with both theoretical predictions and results obtained using other simulation techniques. Here, we have demonstrated that the emergent hydrodynamic correlations of the MPC fluid can well be described by fluctuating hydrodynamic Landau-Lifshitz Navier-Stokes equation, or, vice versa, the MPC approach provides a solution of this equation, at least at low Reynolds numbers[18]. Naturally, fluid correlations also influence the dynamical behaviour of embedded objects, as we demonstrated for polymer centre-of-mass velocity-correlation functions. In the future, we will see more applications of the method in non-equilibrium and driven soft-matter systems. Specifically, systems where thermal fluctuations play a major role. Here, the full advantage of the method can be exploited, because the interactions of colloids, polymers, and membranes with the mesoscale solvent can be treated on the same basis.

References

1. R. G. Winkler, “Flow simulations with multiparticle collision dynamics”, in: Hierarchical Methods for Dynamics in Complex Molecular Systems, J. Grotendorst, G. Sutmann, G. Gompper, and D. Marx, (Eds.). Forschungszentrum Jülich, Jülich, 2012.
2. H. Löwen, *Colloidal soft matter under external control*, J. Phys.: Condens. Matter, **13**, R415, 2001.
3. G. Gompper, T. Ihle, D. M. Kroll, and R. G. Winkler, *Multi-Particle Collision Dynamics: A particle-based mesoscale simulation approach to the hydrodynamics of complex Fluids*, Adv. Polym. Sci., **221**, 1, 2009.
4. M. Doi, *Onsager’s variational principle in soft matter*, J. Phys.: Condens. Matter, **23**, 284118, 2011.
5. P. J. Hoogerbrugge and J. M. V. A. Koelman, *Simulating microscopic hydrodynamics phenomena with Dissipative Particle Dynamics*, Europhys. Lett., **19**, 155, 1992.
6. P. Espanol, *Hydrodynamics from Dissipative Particle Dynamics*, Phys. Rev. E, **52**, 1734, 1995.
7. P. Espanol and P. B. Warren, *Statistical mechanics of Dissipative Particle Dynamics*, Europhys. Lett., **30**, 191, 1995.
8. G. McNamara and G. Zanetti, *Use of the Boltzmann equation to simulate lattice-gas automata*, Phys. Rev. Lett., **61**, 2332, 1988.
9. X. Shan and H. Chen, *Lattice Boltzmann model for simulating flows with multiple phases and components*, Phys. Rev. E, **47**, 1815, 1993.
10. X. He and L.-S. Luo, *Theory of the lattice Boltzmann method: From the Boltzmann equation to the lattice Boltzmann equation*, Phys. Rev. E, **56**, 6811, 1997.

11. G. A. Bird, *Molecular Gas Dynamics and the Direct Simulation of Gas Flows*, Oxford University Press, Oxford, 1994.
12. F. J. Alexander and A. L. Garcia, *The Direct Simulation Monte Carlo Method*, Comp. in Phys., **11**, 588, 1997.
13. A. L. Garcia, *Numerical Methods for Physics*, Prentice Hall, 2000.
14. A. Malevanets and R. Kapral, *Mesoscopic model for solvent dynamics*, J. Chem. Phys., **110**, 8605, 1999.
15. A. Malevanets and R. Kapral, *Solute molecular dynamics in a mesoscopic solvent*, J. Chem. Phys., **112**, 7260–7269, 2000.
16. T. Ihle and D. M. Kroll, *Stochastic rotation dynamics: A Galilean-invariant mesoscopic model for fluid flow*, Phys. Rev. E, **63**, 020201(R), 2001.
17. R. Kapral, *Multiparticle Collision Dynamics: Simulations of complex systems on mesoscale*, Adv. Chem. Phys., **140**, 89, 2008.
18. C.-C. Huang, G. Gompper, and R. G. Winkler, *Hydrodynamic correlations in multiparticle collision dynamics fluids*, Phs. Rev. E, **86**, 056711, 2012.
19. L. D. Landau and E. M. Lifshitz, *Fluid Mechanics*, Pergamon Press, London, 1960.
20. E. Allahyarov and G. Gompper, *Mesoscopic solvent simulations: Multiparticle-collision dynamics of three-dimensional flows*, Phys. Rev. E, **66**, 036702, 2002.
21. T. Ihle and D. M. Kroll, *Stochastic rotation dynamics I: Formalism, Galilean invariance, Green-Kubo relations*, Phys. Rev. E, **67**, 066705, 2003.
22. H. Noguchi, N. Kikuchi, and G. Gompper, *Particle-based mesoscale hydrodynamic techniques*, EPL, **78**, 10005, 2007.
23. H. Noguchi and G. Gompper, *Transport coefficients of off-lattice mesoscale-hydrodynamics simulation techniques*, Phys. Rev. E, **78**, 016706, 2008.
24. I. O. Götze, H. Noguchi, and G. Gompper, *Relevance of angular momentum conservation in mesoscale hydrodynamics simulations*, Phys. Rev. E, **76**, 046705, 2007.
25. A. Malevanets and J. M. Yeomans, *Dynamics of short polymer chains in solution*, Europhys. Lett., **52**, 231–237, 2000.
26. M. Ripoll, K. Mussawisade, R. G. Winkler, and G. Gompper, *Low-Reynolds-number hydrodynamics of complex fluids by Multi-Particle-Collision dynamics*, Europhys. Lett., **68**, 106, 2004.
27. K. Mussawisade, M. Ripoll, R. G. Winkler, and G. Gompper, *Dynamics of polymers in a particle based mesoscopic solvent*, J. Chem. Phys., **123**, 144905, 2005.
28. R. G. Winkler, M. Ripoll, K. Sawisade, and G. Gompper, *Simulation of complex fluids by multi-particle-collision dynamics*, Comput. Phys. Commun., **169**, 326, 2005.
29. M. P. Allen and D. J. Tildesley, *Computer Simulation of Liquids*, Clarendon Press, Oxford, 1987.
30. W. C. Swope, H. C. Andersen, P. H. Berens, and K. R. Wilson, *A computer simulation method for the calculation of equilibrium constants for the formation of physical clusters of molecules: Application to small water clusters*, J. Chem. Phys., **76**, 637, 1982.
31. M. Doi and S. F. Edwards, *The Theory of Polymer Dynamics*, Clarendon Press, Oxford, 1986.
32. J. K. G. Dhont, *An Introduction to Dynamics of Colloids*, Elsevier, Amsterdam, 1996.
33. S. H. Lee and R. Kapral, *Friction and diffusion of a Brownian particle in a mesoscopic solvent*, J. Chem. Phys., **121**, 11163, 2004.

34. A. Lamura, G. Gompper, T. Ihle, and D. M. Kroll, *Multiparticle collision dynamics: Flow around a circular and a square cylinder*, Europhys. Lett., **56**, 319, 2001.
35. Y. Inoue, Y. Chen, and H. Ohashi, *Development of a simulation model for solid objects suspended in a fluctuating fluid*, J. Stat. Phys., **107**, 85, 2002.
36. R. G. Winkler and C.-C. Huang, *Stress tensors of multiparticle collision dynamics fluids*, J. Chem. Phys., **130**, 074907, 2009.
37. C.-C. Huang, R. G. Winkler, G. Sutmann, and G. Gompper, *Semidilute polymer solutions at equilibrium and under shear flow*, Macromolecules, **43**, 10107, 2010.
38. M. Ripoll, K. Mussawisade, R. G. Winkler, and G. Gompper, *Dynamic regimes of fluids simulated by Multi-Particle-Collision dynamics*, Phys. Rev. E, **72**, 016701, 2005.
39. C.-C. Huang, A. Chatterji, G. Sutmann, G. Gompper, and R. G. Winkler, *Cell-level canonical sampling by velocity scaling for multiparticle collision dynamics simulations*, J. Comput. Phys., **229**, 168, 2010.
40. E. Tüzel, T. Ihle, and D. M. Kroll, *Dynamic correlations in stochastic rotation dynamics*, Phys. Rev. E, **74**, 056702, 2006.
41. T. Ihle and D. M. Kroll, *Stochastic rotation dynamics II: Transport coefficients, numerics, long time tails*, Phys. Rev. E, **67**, 066706, 2003.
42. M. Ripoll, R. G. Winkler, and G. Gompper, *Star polymers in shear flow*, Phys. Rev. Lett., **96**, 188302, 2006.
43. T. Ihle, E. Tüzel, and D. M. Kroll, *Resummed Green-Kubo relations for a fluctuating fluid-particle model*, Phys. Rev. E, **70**, 035701, 2004.
44. T. Ihle, E. Tüzel, and D. M. Kroll, *Equilibrium calculation of transport coefficients for a fluid-particle model*, Phys. Rev. E, **72**, 046707, 2005.
45. N. Kikuchi, C. M. Pooley, J. F. Ryder, and J. M. Yeomans, *Transport coefficients of a mesoscopic fluid dynamics model*, J. Chem. Phys., **119**, 6388–6395, 2003.
46. C. M. Pooley and J. M. Yeomans, *Kinetic theory derivation of the transport coefficients of stochastic rotation dynamics*, J. Phys. Chem. B, **109**, 6505, 2005.
47. R. Becker, *Theory of Heat*, Springer Verlag, Berlin, 1967.
48. B. J. Alder and T. E. Wainwright, *Decay of the velocity autocorrelation function*, Phy. Rev. A, **1**, 18, 1970.
49. R. Zwanzig and M. Bixon, *Hydrodynamic theory of the velocity correlation function*, Phys. Rev. A, **2**, 2005, 1970.
50. M. H. Ernst, E. H. Hauge, and J. M. J. van Leeuwen, *Asymptotic time behavior of correlation functions. I. Kinetic terms*, Phys. Rev. A, **4**, 2055, 1971.
51. E. H. Hauge and A. Martin-Löf, *Fluctuating hydrodynamics and Brownian motion*, J. Stat. Phys., **7**, 259, 1973.
52. E. J. Hinch, *Application of the Langevin equation to fluid suspensions*, J. Fluid Mech., **72**, 499, 1975.
53. G. L. Paul and P. N. Pusey, *Observation of a long-time tail in Brownian motion*, J. Phys. A, **14**, 3301, 1981.
54. B. U. Felderhof, *Backtracking of a sphere slowing down in a viscous compressible fluid*, J. Chem. Phys., **123**, 044902, 2005.
55. C.-C. Huang, G. Gompper, and R. G. Winkler, *Effect of hydrodynamic correlations on the dynamics of polymers in dilute solution*, submitted for publication, 2013.

56. R. G. Winkler, S. Keller, and J. O. Rädler, *Intramolecular dynamics of linear macromolecules by Fluorescence Correlation Spectroscopy*, Phys. Rev. E, **73**, 041919, 2006.
57. V. Lisy, J. Tothova, and A. V. Zatovsky, *The effects of hydrodynamic noise on the diffusion of polymers in dilute solutions*, J. Stat. Mech.: Theory Exp., **(2008)**, P01024.
58. M. Belushkin, R. G. Winkler, and G. Foffi, *Backtracking of colloids: A multiparticle collision dynamics simulation study*, J. Phys. Chem. B., **115**, 14263, 2011.

Inertial Coupling Method for Blob-Model Particle Hydrodynamics: From Brownian Motion to Inertial Effects

Florencio Balboa Usabiaga[1], **Aleksandar Donev**[2], **and Rafael Delgado-Buscalioni**[1]

[1] Departamento de Física Teórica de la Materia Condensada,
Univeridad Autónoma de Madrid, Madrid 28049, Spain
E-mail: rafael.delgado@uam.es

[2] Courant Institute of Mathematical Sciences,
New York University, New York, NY 10012
E-mail: donev@courant.nyu.edu

We present an overview of a novel method for hydrodynamics of small particles in a fluid solvent. The method consistently solves the fluid and particle inertia and accounts for thermal fluctuations in the fluid momentum equation. The coupling between the fluid and the blob is based on a no-slip constraint equating the particle velocity with the local average of the fluid velocity, and conserves momentum and energy. Owing to the non-dissipative nature of the no-slip coupling, the fluctuation-dissipation balance is possible without addition of extra particle noise. The local averaging and spreading operations are accomplished using compact kernels commonly used in immersed boundary methods. These kernels make the discrete blob a particle with surprisingly physically-consistent volume, mass, and hydrodynamic properties. The present inertial coupling method can model particulate flows in a wide range of time-scales ranging from Brownian to convection-driven motion, using a minimal cost. It can be naturally extended to polymeric fluids and other types of physico/chemical phenomena.

1 Introduction

Many natural phenomena and industrial process involve small particles immersed in a solvent fluid moving over disparate length and time scales[1]: from dust (10^{-3}m) in turbulent flow to colloidal molecules ($10^{-[5-8]}$) in quiescent, laminar[2,3] or turbulent regimes[4]. Quite often disparate dynamic regimes coexists within different subdomains of the same reaction chamber[5] thus posing a serious challenge for any computational approach. This type of scenario is paradigmatic of what one might call the *multi-regime* condition. At present, these type of processes demand efficient ways to resolve the motion of *many* colloidal particles $O(10^5)$ driven by either diffusion, friction or inertial forces.

Particle-particle methods (such as smoothed particle hydrodynamics (SPH)[6] and stochastic rotation dynamics (SRD)[3]) resolve both the particle and fluid phase using similar discrete Lagrangian descriptions. They all have important drawbacks when compared with standard solvers for discretized continuum fluid dynamics (CFD). They offer limited control over the fluid properties and/or require relatively small time steps compared with advanced time-stepping CFD techniques (e.g. semi-implicit schemes). More importantly, they cannot be adapted to efficiently treat the natural dynamical time scales, such as those governing the Brownian motion or the incompressible flow limit. These drawbacks also apply to the lattice Boltzmann (LB) method.

In the realm of CFD one can still distinguish methods in which the computational mesh self-adapts to follow the particle[7] from those using a fixed (Eulerian) grid which translate the particle boundary conditions into body forces (which also drive the particle)[8]. These second group of methods, sometimes called "mixed Eulerian-Lagrangian schemes"[2] are particularly suited to attack the "multiregime" problem because they are faster, more flexible and can work with minimal resolution models (pointwise particle descriptions). Precisely, for a minimal resolution methodology, we present here briefly a consistent description of inertial forces.

In their seminal work, Maxey and Riley[9] decomposed the fluid velocity as $\mathbf{v}(\mathbf{r},t) = \mathbf{v}_0(\mathbf{r},t) + \mathbf{v}_1(\mathbf{r},t)$, where $\mathbf{v}_0$ is the undisturbed flow (which would result if the boundary conditions at the particle surface were not applied), and $\mathbf{v}_1$ is the perturbative component created by the fluid-particle interaction. In the bulk flow, convection (advection) becomes relevant for $\mathrm{Re}_F = v_0 L\rho/\eta > 1$; where the *fluid* Reynolds number Re_F is defined in terms of the typical flow speed v_0, the fluid density ρ, the dynamic viscosity $\eta = \rho\nu$, and a characteristic length L for velocity variation in the flow. Maxey and Riley decompose the fluid force on the particle in the local fluid inertial force (proportional to the local material derivative of $\mathbf{v}_0$) and in a frictional contribution arising from the pressure created by the particle disturbance. From this analysis one can first distinguish a *relaxational* particle inertia (consequence of its mass resistance to follow the fluid) which manifests in a fluid drag (linear in velocity) which damps the particle velocity to the local fluid velocity. This relaxation process occurs in an inertial lag-time $\tau_P \sim (\rho_P - \rho)R^2/\eta$ which increases with the density contrast $\rho_P - \rho$ and with the particle radius R.

By contrast, *convective* inertia arises from non-linear interactions between the particle dynamics and perturbative flow[10]. The *particle* Reynolds number $\mathrm{Re}_P = 2wR/\nu$, defined with the particle-fluid relative speed w, determines the strength of perturbative flow advection relative to viscous dissipation. The importance of convective inertia is indicated by the ratio $\mathrm{Re}_F(R/L)^2$ between the characteristic times associated with Stokes drag and convection[9,10]. At finite values of the non-dimensional groups $\mathrm{Re}_P = 2wR/\nu$ and $\mathrm{Re}_F(R/L)^2$ inertia effects due to particle mass and particle size are not interchangeable anymore, leading to a relevant open problem in turbulence[4]. Interestingly, at small Re_P non-linear interaction between particle advection and thermal fluctuations are also possible. Some examples are the change in mobility of colloidal particles with respect the Stokes limit at low Schmidt numbers (typical of aerosol)[11] and inertial effects in directional locking (a process to to separate nanoparticles at very small Re_P)[12].

Computational approaches can be naturally classified according to the dynamical regime they can be safely applied to. In order to highlight the relevance of the present approach, we present an overview of the different methodologies designed to the dynamical regimes characterized by Re_F, Re_P and R/L.

1.1 Creeping Flow Limit, $\mathbf{Re_F \to 0}$ and $\mathbf{Re_P \to 0}$

In this case the perturbative flow $\mathbf{v}_1$ has a negligible effect on the unperturbed field, which is *a priori* fixed. The perturbative field created by a collection of particles is the linear superposition of the Stokes fields and it determines the multi-body hydrodynamic forces on the particle ensemble. Analytically expressions for these forces are embedded in the mobility matrix of Brownian hydrodynamics (BD)[13,14] and Stokesian dynamics (SD)[15] which

in addition to the stokeslet (monopole) term might include higher terms of the multipole expansion of the perturbative stress. The zero-Reynolds regime resolves the long-time diffusive limit of colloidal motion where fluctuations are important. A direct implementation of the fluctuation dissipation (FD) relation between the friction and noise matrices requires $O(N^3)$ operations (where N is the number of particles) although sophisticated and technically-complex techniques[15,14], reduce the cost to $O(N \ln N)$ operations, albeit with large multiplicative prefactors.

1.2 Finite $\mathbf{Re_F}$ and $\mathbf{Re_P} < 1$

As an alternative to BD and SD methods, two-way coupling algorithms using a Stokes frictional force were developed for mixed Eulerian-Lagrangian dynamics[2,16,17]. The idea is to deploy a relative simple and efficient fluid solver to explicitly resolve the perturbative flow responsible for the hydrodynamic coupling between particles. The total particle computational cost scales almost linearly as $O(N \log N)$ while the added fluid solver cost scales like the system volume. These schemes are based on the Stokes (i.e. frictional) coupling assumption so they are limited to $\mathrm{Re}_P < 1$ and far-field hydrodynamics ($R/L < 1$). Convective inertia is neglected and some form of particle relaxational inertia is introduced *a la Langevin*, via a *phenomenological* friction coefficient which provides a finite particle response time τ_P. Frictional coupling is obviously dissipative and requires introducing an additional noise term in the particle equation, different from that of the fluctuating fluid[2,17].

1.3 Finite $\mathbf{Re_F}$ and $\mathbf{Re_P} = 0$: Neutrally Buoyant Particles

For $\mathrm{Re}_P = 0$, particle inertia is absent, the relative fluid-particle acceleration is zero and the particle velocity just follows the local fluid velocity. The hydrodynamic force due to the particle-fluid interaction is then equal to the total force exerted on the particle by sources other than the fluid. This permits a fluid-only formulation whereby the net non-hydrodynamic particle force is *spread* from the particle to the surrounding fluid using some compact kernel. Two relevant methods working in this limit are the stochastic Immersed Boundary method (IBM)[17] commonly used for fluid-structure interaction $R/L = O(1)$, and the Force Coupling method (FCM)[18,10], where each particle is represented by a low-order expansion of force multipole ($R/L < 1$) and thermal fluctuations are not included.

1.4 Large $\mathbf{Re_F}$ and $\mathbf{Re_P} \ll 1$ for $\boldsymbol{R/L} \ll 1$: Point-Particle Models

In the point-particle limit $R/L \ll 1$ at small particle Reynolds, the advection of the perturbative flow can be neglected and the perturbative field can be analytically solvable (unsteady Stokes equation)[9]. The fluid-particle force is expressed as a rather complicated function of the relative velocity field $\mathbf{u} - \mathbf{v}_0$ *interpolated* at the particle site. This forms the basis of *one-way-coupling* schemes for point-particle dynamics frequently used in turbulent research[10] $\mathrm{Re}_F \gg 1$. Although the point-particle approach can probably describe the relaxational inertia of very small ($R/L \ll 1$) heavy particles in a light fluid (e.g. aerosol), it has the serious limitation of neglecting the convective inertia arising from the particle finite size[4] where energy dissipation and vorticity production in the particles wake become relevant[19].

1.5 Arbitrary Re_F and Re_P for $R/L \sim O(1)$: Fully Resolved Particles

Several Eulerian-Lagrangian methods have appeared in recent years to allow for a fully consistent treatment of the coupled particle and fluid inertia. A key issue is the spatial resolution of the particle. In the "direct forcing" method[20], and related extensions to fluctuating hydrodynamics[21,22], the fluid force on the particle is obtained by imposing the no-slip constraint on a well-resolved particle surface (and perhaps also the interior of the particle). High spatial resolution requires a substantial computational effort; the largest simulations so far reached $O(10^3)$ particles[20]. The smoothed particle method (SPM)[23,8] works with a mixed (particle-fluid) velocity field constructed with a smooth characteristic function which discriminates particle and fluid cells. This permits an intermediate resolution with a typical particle radius $R \simeq 5h$ (here h is the mesh size) requiring $O(10^3)$ fluid cells per particle.

1.6 Arbitrary Re_F and Re_P for $R/L < 1$: Pointwise Resolution

Fully or partially resolved methods are still far from a point-particle approach which can require as few as 13 cells to perform a fourth-order orthogonal Lagrangian interpolation. The present *Inertial Coupling method* (ICM) is a minimal resolution model which recovers finite particle effects at moderate computational cost (as an advantage, it just requires 27 fluid cells per particle[24]). The ICM is hereby applied to pointwise particle resolution or "blob" particle models, and it aims to to become a flexible coarse-grained model, which can capture hydrodynamics and other physico/chemical effects over a broad range of time scales and Re_P: from Brownian motion to convection-driven regimes. To that end, the "inertial coupling" between the particle and the fluid is not assumed to have any functional form (e.g. Stokes drag) but *naturally* arises from the no-slip constraint averaged over the particle (or "blob") domain. Results presented hereafter indicate that this type of (nonlinear) coupling permits to take into account both fluid *and* particle inertia beyond the Stokes limit, where advective interactions take place.

The present proceeding is an excerpt from our recent works[29,24,25]. In particular, in Ref. 24 we present a compressible finite-volume fluctuating hydrodynamic solver[26] which includes the effect of the particle and fluid inertia in the dynamics, while still consistently including thermal fluctuations even in non-trivial geometries. It was numerically demonstrated that the inertial coupling method can reproduce ultrasound forces on colloidal particles, taking place at much faster rates than viscous friction[27]. In a sequel we considered the *isothermal incompressible* fluctuating Navier-Stokes equations to allow for a significantly larger time step size in the fluid solver[25]. This second work also presents second-order accurate (both compressible and incompressible) solvers, which fully include particle and fluid inertia.

2 The *blob* Particle Model

Let us consider a particle of physical mass m and size (e.g., radius) a immersed in a fluid with density ρ. In real problems there will be many particles $i = 1, \ldots, N_p$ that interact with each other (an extension to bead-spring polymer models is indeed possible) but for simplicity of notation, we now focus on a single particle and omit the particle

index. The position of the particle is denoted with $\boldsymbol{q}(t)$ and its velocity with $\boldsymbol{u} = \dot{\boldsymbol{q}}$. The shape of the particle and its effective interaction with the fluid is captured through a smooth kernel function $\delta_a(\Delta\boldsymbol{r})$ that integrates to unity and whose support is localized in a region of size a. We use the immersed-boundary kernels[28] whose properties were designed to "hide" the underlying grid to the particle Lagrangian motion. Interestingly, these properties *also* provide a coherent physical dimension to the particle and are essential to ensure momentum, energy conservation and fluctuation-dissipation balance, as we have recently proved[25].

2.1 Average and Spreading Operations

The interaction between the fluid and particle is mediated via the kernel function through two crucial local operations. The *local averaging* linear operator $\boldsymbol{J}(\boldsymbol{q})$ averages the fluid velocity inside the particle to estimate a local fluid velocity

$$\boldsymbol{v_q}(t) = \boldsymbol{J}\boldsymbol{v}(\boldsymbol{r},t) = \int \delta_a(\boldsymbol{q}-\boldsymbol{r})\,\boldsymbol{v}(\boldsymbol{r},t)\,d\boldsymbol{r}.$$

The reverse of local averaging is accomplished using the *local spreading* linear operator $\boldsymbol{S}(\boldsymbol{q})$ which takes a force $\boldsymbol{F}$ applied to the particle and spreads it over the extent of the kernel function to return a smooth force density field,

$$\boldsymbol{f}(\boldsymbol{r},t) = \boldsymbol{S}\boldsymbol{F}(t) = \boldsymbol{F}(t)\,\delta_a(\boldsymbol{q}-\boldsymbol{r}).$$

2.1.1 Essential Properties

Note that the local spreading operator $\boldsymbol{S}$ has dimensions of inverse volume. Averaging and spreading operators are *adjoint* $\boldsymbol{S} = \boldsymbol{J}^\star$, i.e., the natural dot products in the particle (Lagrangian) and fluid (Eulerian) domains are related via[17]

$$(\boldsymbol{J}\boldsymbol{v})\cdot\boldsymbol{u} = \int \boldsymbol{v}\cdot(\boldsymbol{S}\boldsymbol{u})\,d\boldsymbol{r} = \int \delta_a(\boldsymbol{q}-\boldsymbol{r})\,(\boldsymbol{v}\cdot\boldsymbol{u})\,d\boldsymbol{r} \tag{1}$$

for any $\boldsymbol{u}$ and $\boldsymbol{v}$. This adjoint property is crucial in maintaining energy conservation and fluctuation-dissipation balance.

The physical volume of the particle ΔV is related to the shape and width of the kernel function via

$$\Delta V = (\boldsymbol{J}\boldsymbol{S})^{-1} = \left[\int \delta_a^2(\boldsymbol{r})\,d\boldsymbol{r}\right]^{-1}. \tag{2}$$

Therefore, even though the particle is represented only by the position of its centroid, it is not appropriate to consider it a "point" particle[9]. Rather, it might be thought of as a diffuse spherical particle which interacts with the fluid in the kernel interior. We have called this a "blob". Also, note that in fluctuating hydrodynamics the fluid velocity is a distribution and cannot be evaluated pointwise, therefore, to obtain well-defined fluctuating equations spatial averaging must be used and a physical volume associated to each blob.

In the present model, the fluid velocity field $\boldsymbol{v}(\boldsymbol{r},t)$ extends over the whole domain including the particle interior. Therefore the effective inertia of the particle is enlarged by $\rho\Delta V$ and the particle physical mass is

$$m = m_e + \rho\Delta V = m_e + m_f$$

where m_e is the *excess mass* of the particle over the mass of the entrained fluid $m_f = \rho \Delta V$. Indeed, a crucial property that should be preserved in the discrete mesh is that ΔV is a constant that only depends on the shape of the kernel function and *not* on the position of the particle. This ensures a well-defined (fixed) particle mass m and size.

2.1.2 Average and Spreading in a Regular Grid

We use a regular Eulerian grid with mesh size $h = \Delta x = \Delta y = \Delta z$ to solve the fluctuating Navier-Stokes equations using finite volumes[26]. In this discrete space, the local averaging operator $\boldsymbol{J}$ (a convolution operator in the continuum setting) becomes a discrete summation over the grid points that are near the particle,

$$\boldsymbol{J}\boldsymbol{v} \equiv \sum_{\boldsymbol{k} \in \text{grid}} \phi_a \left(\boldsymbol{q} - \boldsymbol{r}_k \right) \boldsymbol{v}_k,$$

where $\boldsymbol{r}_k$ denotes the centre of the control volume with which $\boldsymbol{v}_k$ is associated, and ϕ_a is a function that takes the role of the kernel function δ_a. We follow the traditional choice and do the local averaging independently along each direction α,

$$\phi_a \left(\boldsymbol{q} - \boldsymbol{r}_k \right) = \prod_{\alpha=1}^{d} \phi_a \left[q_\alpha - (r_k)_\alpha \right],$$

The discrete local spreading operator is

$$\left(\boldsymbol{S}\boldsymbol{F} \right)_k = \left(\Delta V_f \right)^{-1} \phi_a \left(\boldsymbol{q} - \boldsymbol{r}_k \right) \boldsymbol{F},$$

where $\Delta V_f = \Delta x \Delta y \Delta z$ is the volume of the hydrodynamic cell. The discrete kernel function ϕ_a was constructed by Peskin[28] to yield translationally-invariant zeroth, first moment and L^2-norm,

$$\begin{aligned} \sum_{\boldsymbol{k} \in \text{grid}} \phi_a \left(\boldsymbol{q} - \boldsymbol{r}_k \right) &= 1 \\ \sum_{\boldsymbol{k} \in \text{grid}} \left(\boldsymbol{q} - \boldsymbol{r}_k \right) \phi_a \left(\boldsymbol{q} - \boldsymbol{r}_k \right) &= 0 \\ \sum_{\boldsymbol{k} \in \text{grid}} \phi_a^2 \left(\boldsymbol{q} - \boldsymbol{r}_k \right) &= \Delta V^{-1} = \text{const.}, \end{aligned} \tag{3}$$

independent of the position of the particle $\boldsymbol{q}$ relative to the underlying (fixed) fluid grid. These properties require making $a \sim \Delta x$ meaning that the size and shape of the particles is directly tied to the discretization of the fluid equations, and the two cannot be varied independently. This is a shortcoming of the immersed boundary method, but, at the same time, it is physically unrealistic to resolve the fluid flow and, in particular, the fluctuations in fluid velocity, with different levels of resolution for different particles or dimensions. In the present work we have used the 3-point IBM kernel which yields[24], $\Delta V = 2^d \, h^3$ and in 3D space ($d = 3$) contains 27 fluid cells.

3 Inertial Coupling Method

3.1 No-Slip Condition

Coupling of a continuum (fluctuating) fluid with point-like (blob) particles has been considered by other researchers[2], who described the motion of the particle by a Langevin equation in which a phenomenological Stokes frictional force between the particle and the fluid is postulated, proportional to the difference $\boldsymbol{u} - \boldsymbol{J}\boldsymbol{v}$ between the particle and the locally-averaged fluid velocity.

An important downside of the inertial Stokes coupling is the imposition of an artificial friction parameter and an associated delay with the response of the particle to changes in the flow. Such a delay is often not physically acceptable unless a very large friction constant is imposed, leading to numerical stiffness. Instead we impose an *instantaneous* coupling[24] between the fluid and the particle in the form of a *no-slip constraint*,

$$\boldsymbol{u} = \dot{\boldsymbol{q}} = \boldsymbol{J}\boldsymbol{v}, \tag{4}$$

The no-slip condition simply states that the velocity of the particle is equal to a local average of the fluid velocity. The imposition of Eq. 4 leads to a physically-consistent and sensible coarse-grained model of the coupled fluid-particle system. Notably, our coupling conserves momentum, energy, and obeys a fluctuation-dissipation principle.

The particle acceleration is

$$\dot{\boldsymbol{u}} = \frac{d}{dt}\left[\boldsymbol{J}\left(\boldsymbol{q}\right)\boldsymbol{v}\right] = \boldsymbol{J}\left(\partial_t \boldsymbol{v}\right) + \left(\boldsymbol{u}\cdot\frac{\partial}{\partial \boldsymbol{q}}\boldsymbol{J}\right)\boldsymbol{v}, \tag{5}$$

where for our choice of interpolation operator we have the explicit form:

$$\left(\boldsymbol{u}\cdot\frac{\partial}{\partial \boldsymbol{q}}\boldsymbol{J}\right)\boldsymbol{v} = \int\left[\boldsymbol{u}\cdot\frac{\partial}{\partial \boldsymbol{q}}\delta_a\left(\boldsymbol{q}-\boldsymbol{r}\right)\right]\boldsymbol{v}\left(\boldsymbol{r},t\right)d\boldsymbol{r}.$$

Observe that in the limit of a "point particle", $a \to 0$, the kernel function approaches a Dirac delta function and one can identify Eq. 5 with the advective derivative, which is expected since in this limit the particle becomes a Lagrangian marker. For a blob particle, however, the relative fluid-particle acceleration is non-zero,

$$\boldsymbol{a}_{\boldsymbol{J}} = \frac{d}{dt}\left(\boldsymbol{J}\boldsymbol{v}\right) - \boldsymbol{J}\left(D_t\boldsymbol{v}\right) = \left(\boldsymbol{u}\cdot\frac{\partial}{\partial \boldsymbol{q}}\boldsymbol{J}\right)\boldsymbol{v} - \boldsymbol{J}\boldsymbol{v}\cdot\boldsymbol{\nabla}\boldsymbol{v} \neq \boldsymbol{0}. \tag{6}$$

3.2 Equations of Motion

Following the discussion in the Introduction and the derivation in Sec. 2 of Ref. 24 we take the equations of motion for a single particle coupled to a fluctuating fluid to be

$$\rho\left(\partial_t\boldsymbol{v} + \boldsymbol{v}\cdot\boldsymbol{\nabla}\boldsymbol{v}\right) = \rho D_t\boldsymbol{v} = -\boldsymbol{\nabla}\pi - \boldsymbol{\nabla}\cdot\boldsymbol{\sigma} - \boldsymbol{S}\left(\boldsymbol{q}\right)\boldsymbol{\lambda} \tag{7}$$

$$m_e\dot{\boldsymbol{u}} = \boldsymbol{F}\left(\boldsymbol{q}\right) + \boldsymbol{\lambda} \tag{8}$$

$$\text{s.t. } \boldsymbol{u} = \boldsymbol{J}\left(\boldsymbol{q}\right)\boldsymbol{v}, \tag{9}$$

where the fluid-particle force $\boldsymbol{\lambda}$ is a Lagrange multiplier that enforces the constraint (Eq. 9) and $\boldsymbol{F}\left(\boldsymbol{q}\right)$ is the external force applied to the particle. Observe that the total particle-fluid momentum $P = m_e\boldsymbol{u} + \int\rho\boldsymbol{v}\left(\boldsymbol{r},t\right)d\boldsymbol{r}$ is conserved because Newton's third law is

enforced. Similar equations apply for both compressible and incompressible fluids. In the compressible case[24], a density equation is added to the system (Eqs. 7,8,9) and the pressure $\pi(\rho)$ obtained from the equation of state. In the incompressible case[25] the divergence-free condition $\boldsymbol{\nabla}\cdot\boldsymbol{v}=0$ is used instead to determine the (non-thermodynamic) pressure as a Lagrange multiplier.

3.2.1 Fluid-Only Formulation and Particle Effective Equations

Using Eq. 8 to eliminate $\boldsymbol{\lambda}=m_e\dot{\boldsymbol{u}}-\boldsymbol{F}$ and Eq. 6 to eliminate $\dot{\boldsymbol{u}}$, the fluid equation Eq. 7 becomes,

$$\rho D_t\boldsymbol{v}=\rho\left(\partial_t\boldsymbol{v}+\boldsymbol{v}\cdot\boldsymbol{\nabla}\boldsymbol{v}\right)=-m_e\boldsymbol{S}\boldsymbol{J}\left(D_t\boldsymbol{v}\right)-\boldsymbol{\nabla}\pi-\boldsymbol{\nabla}\cdot\boldsymbol{\sigma}-m_e\boldsymbol{S}\boldsymbol{a}_{\boldsymbol{J}}+\boldsymbol{S}\boldsymbol{F}. \quad (10)$$

This gives the effective fluid equation

$$\left(\rho+m_e\boldsymbol{S}\boldsymbol{J}\right)\partial_t\boldsymbol{v}=-\left[\rho\left(\boldsymbol{v}\cdot\boldsymbol{\nabla}\right)+m_e\boldsymbol{S}\left(\boldsymbol{u}\cdot\frac{\partial}{\partial\boldsymbol{q}}\boldsymbol{J}\right)\right]\boldsymbol{v}-\boldsymbol{\nabla}\pi-\boldsymbol{\nabla}\cdot\boldsymbol{\sigma}+\boldsymbol{S}\boldsymbol{F}, \quad (11)$$

in which the effective fluid inertia is given by the operator $\rho+m_e\boldsymbol{S}\boldsymbol{J}$, and the kinetic stress term $\rho\boldsymbol{v}\cdot\boldsymbol{\nabla}\boldsymbol{v}$ includes an additional term due to the excess inertia of the particle. When there are many interacting particles one simply adds a summation over all particles in front of all terms involving particle quantities in Eq. 11. Note that for a neutrally-buoyant particle $m_e=0$ and one obtains the constant-density Navier-Stokes equation with external forcing $\boldsymbol{S}\boldsymbol{F}$.

The effective particle equation of motion can be obtained upon elimination of λ, from Eq. 8,

$$m\dot{\boldsymbol{u}}=-\Delta V\,\boldsymbol{J}\left(\boldsymbol{\nabla}\pi+\boldsymbol{\nabla}\cdot\boldsymbol{\sigma}\right)+\boldsymbol{F}+m_f\boldsymbol{a}_{\boldsymbol{J}}, \quad (12)$$

where the first term in the right hand side is the "blob" equivalent of the total fluid pressure force over a real particle's surface $-\oint(\pi\boldsymbol{I}+\boldsymbol{\sigma})\cdot\mathbf{n}dr^2=-\int_{\Delta V}\boldsymbol{\nabla}\cdot(\pi\boldsymbol{I}+\boldsymbol{\sigma})\,dr^3$. The last term $m_f\boldsymbol{a}_{\boldsymbol{J}}$ arises, because, in the present model, the fluid is allowed to permeate into the particle domain with a different local acceleration. At small Reynolds (Re) numbers the velocity field will be smooth at the scale of the particle size and thus $\boldsymbol{a}_{\boldsymbol{J}}\approx\mathbf{0}$[29]. However, we have not observed any significant effect of $\boldsymbol{a}_{\boldsymbol{J}}$ in simulations at large Re_P[25].

3.2.2 Momentum Conservation

A total *momentum field* can be obtained as the sum of the fluid momentum and the spreading of the particle momentum $\boldsymbol{p}(\boldsymbol{r},t)=\rho\boldsymbol{v}+m_e\boldsymbol{S}\boldsymbol{u}=\left(\rho+m_e\boldsymbol{S}\boldsymbol{J}\right)\boldsymbol{v}$ The total momentum is $\boldsymbol{P}(t)=\int\boldsymbol{p}(\boldsymbol{r},t)\,d\boldsymbol{r}$ and therefore a local conservation law for $\boldsymbol{p}(\boldsymbol{r},t)$ implies conservation of the total momentum. The dynamics of the momentum field is obtained by adding the fluid and particle equations 7,8 together. This leads to[25]

$$\partial_t\boldsymbol{p}=-\boldsymbol{\nabla}\cdot\left[\pi\boldsymbol{I}+\boldsymbol{\sigma}+\rho\boldsymbol{v}\boldsymbol{v}^T+m_e\boldsymbol{S}\left(\boldsymbol{u}\boldsymbol{u}^T\right)\right]+\boldsymbol{S}\boldsymbol{F}. \quad (13)$$

Thus, in the absence of applied external forces $\mathbf{F}=0$, the total momentum field has a local conservation equation, where the kinetic-stress tensor includes a contribution from the inertia of the particle $m_e\boldsymbol{S}\left(\boldsymbol{u}\boldsymbol{u}^T\right)$.

3.2.3 Energy Conservation

In the absence of viscous dissipation, the equations of motion Eqs. 7,8,9 conserve a coarse-grained Hamiltonian[30] given by the sum of potential energy and the kinetic energy of the particle and the fluid,

$$H(\boldsymbol{v},\boldsymbol{u},\boldsymbol{q}) = \rho\int \frac{v^2}{2}\,d\boldsymbol{r} + m_e\frac{u^2}{2} + U(\boldsymbol{q}), \tag{14}$$

where $U(\boldsymbol{q})$ is the interaction potential of the particle with external sources and other particles, with an associated conservative force $\boldsymbol{F}(\boldsymbol{q}) = -\partial U/\partial \boldsymbol{q} = -\partial H/\partial \boldsymbol{q}$. For compressible flow one needs to include the (density-dependent) internal energy of the fluid in the Hamiltonian as well[31].

It can be easily demonstrated[25] that in the absence of viscous dissipation,

$$\frac{dH}{dt} = -\boldsymbol{F}\cdot\boldsymbol{u} + m_e\boldsymbol{u}\cdot\dot{\boldsymbol{u}} + \int \rho\boldsymbol{v}\cdot(\partial_t\boldsymbol{v})\,d\boldsymbol{r} = 0,$$

that is, the non-dissipative terms in the equation strictly conserve the coarse-grained free energy. For this derivation to hold the adjoint property (Eq. 1) and second the no-slip constraint $\boldsymbol{u} = \boldsymbol{J}\boldsymbol{v}$ are essential.

3.2.4 Fluctuation-Dissipation Balance

The no-slip constraint ensures that the fluid-particle interaction is non-dissipative and conserves energy. As a consequence, the only dissipation comes from the fluid viscous terms. and it can be demonstrated[25] that in order to account for thermal fluctuations in a manner that preserves fluctuation-dissipation balance it is sufficient to add the usual Landau-Lifshitz stochastic stress $(k_BT\eta)^{1/2}\left(\boldsymbol{\mathcal{W}} + \boldsymbol{\mathcal{W}}^T\right)$ to the viscous stress tensor in $\boldsymbol{\sigma}$, without adding any extra stochastic forces to the particle.

The fluctuation-dissipation balance ensures that at thermodynamic equilibrium the particle-fluid system is ergodic and time-reversible with respect to the Gibbs-Boltzmann distribution $Z^{-1}\exp(-H/k_BT)$, where the "Hamiltonian" H given in Eq. 14 is to be interpreted as a coarse-grained free energy. It is not necessary here to include an entropic contribution to the coarse-grained free energy because our formulation is isothermal, and we assume that the particles do not have internal structure.

3.2.5 Equipartition of Energy

The fact that the Gibbs-Boltzmann distribution is separable in $\boldsymbol{v}$ and $\boldsymbol{q}$ and that the Hamiltonian Eq. 14 is quadratic in $\boldsymbol{v}$ means that the fluctuations of velocity are Gaussian with covariance $\langle \boldsymbol{v}\boldsymbol{v}^\star\rangle = (k_BT)\,\boldsymbol{\rho}_{\text{eff}}^{-1}$. It can be shown (see Ref. 25) that for a single particle immersed in a periodic incompressible fluid in d dimensions,

$$\langle u^2\rangle = d\frac{k_BT}{\tilde{m}}, \tag{15}$$

where $\tilde{m} = m_e + d\,m_f/(d-1)$. This result should be compared to the corresponding result for a compressible fluid[24], $\langle u^2\rangle = d(k_BT)/m$ following from the usual equipartition principle of statistical mechanics. When incompressibility is accounted for, a fraction of

the equilibrium kinetic energy is carried in the unresolved sound waves, and therefore the apparent mass of the particle is $\tilde{m}$ and not $m = m_e + m_f$. This difference leads to the *added mass effect* a well-known but surprising difference between the short-time motion of a particle immersed in a compressible versus an incompressible fluid[32]. It is reassuring that the incompressible formulation of the inertial coupling correctly captures the added mass effect, as discussed in detailed in Ref. 25.

4 Temporal Discretization

In Ref. 24 a first-order splitting algorithm was developed for the case of a compressible fluid. This type of algorithm is similar to the original projection algorithm of Chorin[33] for incompressible flow and can be summarized as follows. Update the fluid first without accounting for the force $\boldsymbol{\lambda}$ exerted by the particle. Then, solve for the value of $\boldsymbol{\lambda}$ that, when applied as a correction to the fluid update, exactly imposes the no-slip condition. Extending this type of approach to be higher than first order accurate is known to be difficult from the literature on incompressible flow[34], due to the fact that the splitting introduces a commutator error. In a recent work we have extended the previous compressible formulation to incompressible flow and developed a second order scheme. Details of the algorithm are given in Ref. 25; its general idea is based on the following considerations:

1. Estimate the position of the particle at the midpoint to leading order,

$$\boldsymbol{q}^{n+\frac{1}{2}} = \boldsymbol{q}^n + \frac{\Delta t}{2}\boldsymbol{J}^n\boldsymbol{v}^n. \tag{16}$$

2. Update the fluid velocity based on Eq. 11 using a second-order algorithm, while keeping the particle positions fixed at the midpoint estimates,

$$\left(\rho\boldsymbol{I} + m_e\boldsymbol{S}^{n+\frac{1}{2}}\boldsymbol{J}^{n+\frac{1}{2}}\right)\frac{\boldsymbol{v}^{n+1}-\boldsymbol{v}^n}{\Delta t} + \boldsymbol{\nabla}\pi^{n+\frac{1}{2}} =$$

$$-\boldsymbol{\nabla}\cdot\left(\rho\boldsymbol{v}\boldsymbol{v}^T + \boldsymbol{\sigma}\right)^{n+\frac{1}{2}} + \boldsymbol{S}^{n+\frac{1}{2}}\boldsymbol{F}^{n+\frac{1}{2}} - \left[m_e\boldsymbol{S}\boldsymbol{J}\left(\boldsymbol{v}\cdot\frac{\partial}{\partial\boldsymbol{q}}\boldsymbol{J}\right)\boldsymbol{v}\right]^{n+\frac{1}{2}} \tag{17}$$

   subject to $\boldsymbol{\nabla}\cdot\boldsymbol{v}^{n+1} = 0$. Here any higher order (e.g., a Runge-Kutta or Adams-Bashforth) scheme can be used to evaluate the fluid momentum fluxes to at least second-order accuracy, denoted generically here by superscript $n+\frac{1}{2}$.

3. Update the particle position using a second-order midpoint estimate of the velocity,

$$\boldsymbol{q}^{n+1} = \boldsymbol{q}^n + \frac{\Delta t}{2}\boldsymbol{J}^{n+\frac{1}{2}}\left(\boldsymbol{v}^{n+1}+\boldsymbol{v}^n\right). \tag{18}$$

Observe that the above scheme never actually uses the particle velocity $\boldsymbol{u}$, although one can and should keep track of the particle excess momentum $m_e\boldsymbol{u}$ and update it whenever the fluid momentum is updated, to ensure strict conservation of momentum. Also observe that during the fluid update we fix the particle at its midpoint position $\boldsymbol{q}^{n+\frac{1}{2}}$.

5 Results

The present implementation of the ICM is designed to work with periodic boundary conditions where the velocity and the pressure linear systems in the incompressible formulation decouple and Fast Fourier Transforms can be used to solve them efficiently[28]. At least for the case of neutrally buoyant particles, $m_e = 0$, the algorithm can be easily generalized to non-periodic systems by using the fluid solver employed in Ref. 26. Our algorithm has been parallelized to run efficiently on Graphics Processing Units (GPUs)[24]. The code is written in the CUDA programming environment and it is public domain.

The stability and accuracy of our spatio-temporal discretization is controlled by the dimensionless advective and viscous CFL numbers $\alpha = (V\Delta t)/h$ and $\beta = (\nu\Delta t)/h^2$ where V is a typical advection speed, which may be dominated by the thermal velocity fluctuations or by a deterministic background flow. Here we always use the same grid spacing along all dimensions, $h = \Delta x = \Delta y = \Delta z$. The strength of advection relative to dissipation is measured by the cell Reynolds number $r = \alpha/\beta = V\Delta x/\nu$. Note that for compressible flow (see Refs. 26, 25) there is a sonic CFL number $\alpha_s = c\Delta t/\Delta x$, where c is the speed of sound. The temporal integrator can be considered to be "good" as it produces reasonably-accurate results with a time step for which at least one of α or β is close to $1/2$. We now present some of the tests we have applied the present model against, either in compressible flow[24] or in the incompressible limit[25].

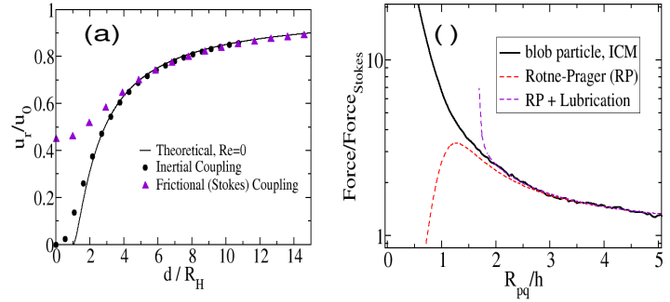

Figure 1. Radial velocity profile around one particle in a plug flow at low Reynolds number, Re$\ll 1$. Results corresponds to $\theta = 0$ (angle between the radial vector and far field flow-velocity) in a periodic box of size $L = 100\,h$. Comparison is made between the outcome of the ICM and the analytical Stokes flow (for infinite system) along with results from the frictional coupling method, using the same effective hydrodynamic radius. See Ref. 24 for further details. (b) Hydrodynamic forces between two slowly approaching particles (p and q) versus their distance $d = R_{pq}$. For $d > 3h$ simulation results (black line) agree with the theoretical Rotne-Prager force[35]. As particles come closer the ICM provides an increase in friction force up to $d > 1.9h$. For the sake of comparison, a lubrication force diverging $d = 2R_l = 1.84\,R_H = 1.66\,h$ is added to the RP (dashed line).

5.1 Deterministic Settings and Hydrodynamic Interactions

The first illustrative feature of the no-slip constraint is observed in the fluid velocity profile around one fixed particle in a Stokes flow (Re $\simeq 0$). Fig. 1a compares the radial component of the fluid velocity $u_r(r)$ along $\theta = 0$ (direction of motion of the incoming flow) and with the analytical Stokes flow for a solid sphere with no-slip surface in a infinite system, as a function of the distance from the particle r. Results for the ICM are compared with the Stokes (frictional) coupling. The frictional coupling induces a significant slip over the particle and only recovers the Stokes flow for $r > 5\,R_H$. By contrast, the ICM strictly imposes no-slip at the particle centre and recovers the Stokes flow for $r > 2\,R_H$. This difference is essential to recover near-flow effects. As an example in Fig. 1b we have computed the hydrodynamic forces between two slowly approaching particles as a function of their distance, d, at creeping flow, Re$\ll 1$. At large enough distances $d > 3R_H$ the IC force converges to the force derived from the Rotne-Prager expression for a hard sphere with stick surfaces and radius $R_H(L)$. As the two particles further approach and their separation becomes comparable to their hydrodynamic radius, the mutual force increases substantially above the Rotne-Prager prediction, indicating that the model grasp at least the essence of lubrication forces.

As the Reynolds number is increased, the drag force on one particle increases over the Stokes ($\mathrm{Re}_P = 0$) limit, $6\pi\eta R_H \boldsymbol{u}$. As shown in Fig. 2, the no-slip constraint used in the ICM correctly captures the increase in drag over a wide range of particle Reynolds (we have studied $\mathrm{Re}_P \leq 324$). Moreover, the blob particle produces wakes which are consistent with those observed for rigid spheres with no-slip surface, including the transition to oscillatory flow and vortex shedding[25]. This agreement is certainly remarkable, notably because in a real rigid sphere of radius R the viscous boundary layer formed around its surface (Oseen layer) decreases like R/Re_P [10] so for $\mathrm{Re}_P > 1$, it is unresolved by the ICM blob model. The "local" no-slip constraint grasps however the non-linear velocity-pressure coupling and produce physically sound wakes behind the blob.

5.2 Ultrasound Forces

To check the ability of the ICM to grasp acoustic forces, we have analyzed the effect of a stationary sound plane wave of frequency ω and wavelength $\lambda = 2\pi c_F/\omega$ on a suspended array of particles. The diffusive layer around the particle is characterized by an acoustic boundary layer of width $\delta = \sqrt{\nu/\omega}$. Typical experiments[38] performed in ambient temperature, manipulate colloids of size $R \sim 10\mu$m, with pressure waves of amplitude $\Delta p = c_F^2 \Delta\rho$ ∼MPa and frequencies ω ∼MHz which require resonant cavities of millimeter size in water $\rho \sim 10^3$kg/m^3 and $c_F \sim 10^3$m/s. This corresponds to the so-called non-viscous regime, studied by Gor'kov[39], where the acoustic boundary layer is small $\delta/R \sim 10^{-1}$ and the sonic time is much shorter than the friction time $\tau_\nu/\tau_s \sim 10^4$. These average colloids are much smaller than the wavelength $\lambda/R \sim 10^2$. They are quite insensitive to thermal forces (inducing dispersion), as the sound energy $\mathcal{U} \sim F_s\lambda$ is much larger than the thermal energy $\mathcal{U}/kT \sim 10^8$. Finally for a typical pressure input, the fluid is hardly compressed with $\Delta\rho/\rho \sim 10^{-2}$. The numerical simulations can be mapped to this experimental regime[38] (thermal fluctuations are switched off and the sound wavelength chosen to be $\lambda \simeq 20\,R_H$). We impose a relatively fast forcing, providing a small acoustic layer of $\delta/R_H \simeq 0.21$. The friction time $\tau_\nu = R_H^2/\nu$ is about 100 times larger than the

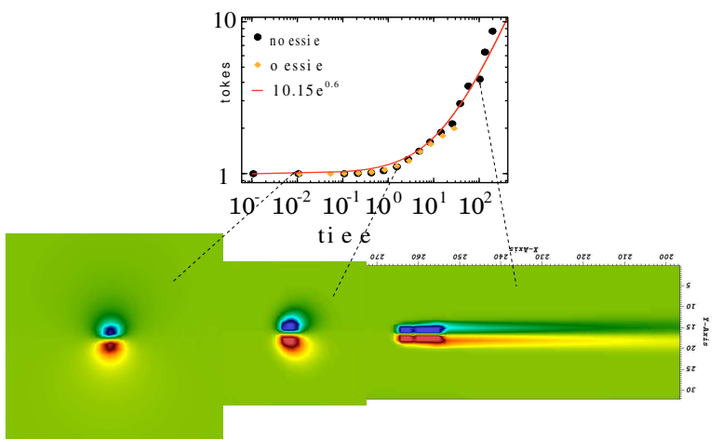

Figure 2. The drag force on the blob particle scaled with the Stokes (Re$=0$) limit, plotted against the Reynolds number. Results were obtained with either the compressible[24] and/or incompressible[25] formulations. The solid line is the empirical law for the drag on a rigid sphere with no-slip surface[36]. (Bottom) Snapshots of the in-plane-vorticity isocontours at three different regimes (Stokes flow $\mathrm{Re}_P \simeq 0$, Oseen flow $\mathrm{Re}_P = 1.5$ and stationary bifid vortex trail[37] $\mathrm{Re}_P = 137$.)

sonic time $\tau_s = R_H/c_F$ (the frictional coupling method cannot obviously capture such fast forcing). Finally, we choose sound amplitudes such that density variations are kept small $\Delta\rho/\rho \simeq 10^{-2}$. Again, although the sound viscous boundary layer around the blob is unresolved ($\delta < h$), simulations of ultrasound-matter interaction by the ICM[24] found to be in quantitative agreement with the inviscid theory, as illustrated in Fig. 3.

5.3 Velocity Autocorrelation and Diffusive Behaviour

The velocity autocorrelation function (VACF)

$$C(t) = \langle v_x(0) v_x(t) \rangle = \frac{1}{d} \langle \boldsymbol{v}\,(0) \cdot \boldsymbol{v}\,(t) \rangle\,, \tag{19}$$

of a single free Brownian particle diffusing through a periodic fluid is a non-trivial quantity that contains crucial information at both short and long times. The integral of the VACF determines the diffusion coefficient and gets contributions from three distinct stages. At molecular times, an important signature of fluctuation-dissipation balance is expressed in the equipartition which dictates $C(0) = k_B T/m$. Here, the effective particle mass of the

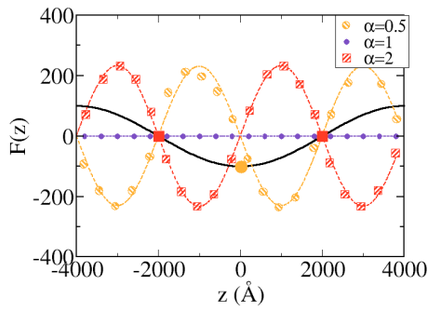

Figure 3. The acoustic force exerted to blob particles by a standing pressure wave along the z-axis. The pressure wave (twice wavelength) is indicated in the thick solid line. The force is measured at different phase locations and for different particle/fluid ratios $\alpha = m/m_f$. The average sound force can be related to the derivative of a potential energy $F_s(z) = -d\mathcal{U}(z)/dz$, so particle stable locations correspond to $F_s = 0$ and $dF_s/dz < 0$. For heavy particles, $\alpha > 1$ stable sites are located at pressure nodes (solid red squares), while light particles are driven to the pressure valleys (solid orange circle). Dashed lines corresponds to the theoretical result[39].

blob particle $m = m_e + m_f$ includes the mass of the fluid dragged with the particle m_f, as well as its excess mass m_e. The compressible inertial coupling method is able to reproduce the intercept $k_B T/m$ very accurately even for relatively large sound CFL numbers[24].

On the time scale of sound waves, $t < t_c = 2R_H/c$, the major effect of compressibility is that sound waves carry away a fraction of the particle momentum with the sound speed c. The VACF quickly decays from its initial value to $C(t_c) \approx k_B T/\tilde{m}$, where $\tilde{m} = m_e + d\, m_f/\,(d-1)$ includes an "added mass" $m_f/(d-1)$ that comes from the fluid around the particle that has to move with the particle[32]. In the incompressible limit (i.e. infinitely large speed of sound) the initial decay of the VACF due to sound waves thus appear to be instantaneous. The incompressible ICM correctly produces the intercept $C(0^+) = k_B T/\tilde{m}$ but without suffering from the severe time step limitation of compressible flow solvers. The asymptotic long time tail $(t/t_\nu)^{-3/2}$ beyond the viscous time scale, is also correctly captured. Further details in Refs. 24, 25.

5.4 Concluding Remarks

We have briefly presented a novel method for particle hydrodynamics based on an Eulerian-Lagrangian mixed approach. The particle resolution is based on a minimal (pointwise) model while the particle mass and hydrodynamic size are robustly introduced via the efficient IB kernels[28]. The present inertial coupling method (ICM)[24,25] does not assume any explicit form of particle-fluid force, but rather *directly couples both dynamics* using a non-linear constraint, which ensures no-slip of fluid over the particle domain. By construction, the no-slip coupling does not dissipate energy and leads to an instantaneous particle response to unsteady fluid forces of whatever type (from thermal fluctuations, transient,

frictional or convective ones). As a result, inertial forces coming from the particle or the fluid (and their interactions) are taken into account. This method, we have called "Inertial Coupling Method"[24], is able to solve dynamics ranging from Brownian motion to convective inertia to ultrasound forces in compressible flows. Quite importantly, a relevant part of the physics arising from the finite particle size is properly tackled with a minimal cost. The computational cost has been significantly reduced and its scope enlarged upon its promotion to second-order accurate versions to the incompressible limit[25]. The proposed model includes inertial and stochastic effects in a consistent manner, ensuring fluctuation-dissipation balance and independence of equilibrium thermodynamic properties on dynamical parameters. As such we believe that the method presented here can be applied to model the dynamics of dilute and semi-dilute colloidal suspensions and polymeric fluids over a broader range of conditions than existing methods[13–15,2,17]. We are now working on further generalizations of the ICM which we expect to present soon. To cite two relevant examples, it is not difficult to include the anti-symmetric component of the dipole (*rotlet*) stress[18] to describe the particle rotation. An additional (and more complicated) *rigidity constraint* would be required to also constrain the locally-averaged strain rate, and thus consistently include the symmetric components of the dipole (*stresslet*) force terms[18]. The scope of the method runs from colloidal to polymeric fluids. However, at molecular scales, the simple coupling used by the ICM can also be used to isolate hydrodynamic from non-hydrodynamic effects and study basic physics questions about the importance of inertia and fluctuations on Brownian motion, going beyond the uncontrolled approximations required by existing theoretical approaches. Notably, we have showed[25] that nonlinear effects becomes important at small Schmidt numbers leading to a non-trivial contribution of the thermal fluctuations to the mean fluid-particle force.

References

1. S. Kim and S. J. Karrila, *Microhydrodynamics:Principles and Selected Applications*, Butterworth Heinemann, Boston, 1991.
2. B. Dünweg and A. J. C. Ladd, *Lattice Boltzmann simulations of soft matter systems*, Adv. Comp. Sim. for Soft Matter Sciences III, pp. 89–166, 2009.
3. R. Kapral, *Multiparticle Collision Dynamics: Simulation of Complex Systems on Mesoscales*, Advances in Chemical Physics, **140**, 89, 2008.
4. J. K. Eaton, *Two-way coupled turbulence simulations of gas-particle flows using point-particle tracking*, International Journal of Multiphase Flow, **35**, no. 9, 792–800, Sept. 2009.
5. M. Rhodes, *Introduction to particle technology*, John Wiley and Sons, 2008.
6. X. Bian, S. Litvinov, R. Qian, M. Ellero, and N. A. Adams, *Multiscale modeling of particle in suspension with smoothed dissipative particle dynamics*, Physics of Fluids, **24**, no. 1, 012002, 2012.
7. H. H. Hu, N. A. Patankar, and M. Y. Zhu, *Direct numerical simulation of fluid-solid systems using the arbitrary Lagrangian-Eurlerian technique*, J. Comp. Phys., **169**, 427, 2001.
8. X. Luo, M. R. Maxey, and G. Karniadakis, *Smoothed profile method for particulate flows: Error analysis and simulations*, Journal of Computational Physics, **228**, 1750, 2009.

9. M. R. Maxey and J. J. Riley, *Equation of motion for a small rigid sphere in a nonuniform flow*, Physics of Fluids, **26**, no. May 2006, 883, 1983.
10. S. Lomholt, *Numerical Investigations of Macroscopic Particle Dynamics in Microflows*, PhD thesis, RisøNational Laboratory, Roskilde, Denmark, 2001.
11. M. Ripoll, K. Mussawisade, R. Winkler, and G. Gompper, *Dynamic regimes of fluids simulated by multiparticle-collision dynamics*, Physical Review E, **72**, no. 1, 016701, July 2005.
12. M. Balvin, E. Sohn, T. Iracki, G. Drazer, and J. Frechette, *Directional Locking and the Role of Irreversible Interactions in Deterministic Hydrodynamics Separations in Microfluidic Devices*, Phys. Rev. Lett., **103**, 078301, Aug. 2009.
13. D. L. Ermak and J. A. McCammon, *Brownian dynamics with hydrodynamic interactions*, The Journal of Chemical Physics, **69**, no. 4, 1352, 1978.
14. J. P. Hernandez-Ortiz, J. J. de Pablo, and M. D. Graham, *Fast Computation of Many-Particle Hydrodynamic and Electrostatic Interactions in a Confined Geometry*, Phys. Rev. Lett., **98**, no. 14, 140602, 2007.
15. A. Sierou and J. F. Brady, *Accelerated Stokesian Dynamics simulations*, J. Fluid Mech., **448**, 115–146, 2001.
16. G. Giupponi, G. De Fabritiis, and P. V. Coveney, *Hybrid method coupling fluctuating hydrodynamics and molecular dynamics for the simulation of macromolecules*, J. Chem. Phys., **126**, no. 15, 154903, 2007.
17. P. J. Atzberger, *Stochastic Eulerian-Lagrangian Methods for Fluid-Structure Interactions with Thermal Fluctuations*, J. Comp. Phys., **230**, 2821–2837, 2011.
18. S. Lomholt and M. R. Maxey, *Force-coupling method for particulate two-phase flow: Stokes flow*, J. Comp. Phys., **184**, no. 2, 381–405, 2003.
19. L. Botto and A. Prosperetti, *A fully resolved numerical simulation of turbulent flow past one or several spherical particles*, Physics of Fluids, **24**, no. 1, 013303, 2012.
20. M. Uhlmann, *Interface-resolved direct numerical simulation of vertical particulate channel flow in the turbulent regime*, Physics of Fluids, **20**, no. 5, 053305, 2008.
21. N. Sharma and N. A. Patankar, *Direct numerical simulation of the Brownian motion of particles by using fluctuating hydrodynamic equations*, J. Comput. Phys., **201**, 466–486, 2004.
22. Y. Chen, N. Sharma, and N. Patankar, *Fluctuating Immersed Material (FIMAT) dynamics for the direct simulation of the Brownian motion of particles*, in: IUTAM Symposium on Computational Approaches to Multiphase Flow, pp. 119–129. Springer, 2006.
23. R. Yamamoto, K. Kim, and Y. Nakayama, *Strict simulations of non-equilibrium dynamics of colloids*, Colloids and Surfaces A, **311**, 42, 2007.
24. F. Balboa Usabiaga, I. Pagonabarraga, and R. Delgado-Buscalioni, *Inertial coupling for point particle fluctuating hydrodynamics*, J. Comp. Phys., **235**, 701, 2013.
25. F. Balboa Usabiaga, R. Delgado-Buscalioni, B. E. Griffith, and A. Donev, "Inertial coupling method for particles in an incompressible fluctuating fluid", arXiv:1212.6427 [cond-mat.soft] (2012).
26. F. Balboa-Usabiaga, J. B. Bell, R. Delgado-Buscalioni, A. Donev, T. G. Fai, B. E. Griffith, and C. S. Peskin, *Staggered Schemes for Incompressible Fluctuating Hydrodynamics*, SIAM J. Multiscale Modeling and Simulation, **10**, no. 4, 1369–1408, 2012.

27. J. Wang and J. Dual, *Theoretical and numerical calculations for the time-averaged acoustic force and torque acting on a rigid cylinder of arbitrary size in a low viscosity fluid.*, The Journal of the Acoustical Society of America, **129**, no. 6, 3490–501, June 2011.
28. C. S. Peskin, *The immersed boundary method*, Acta Numerica, **11**, 479–517, 2002.
29. R. Delgado-Buscalioni and F. Balboa Usabiaga, "Particle hydrodynamics using hybrid models: from molecular to colloidal fluids", in: Particle-Based Methods II: Fundamentals and Applications, E. Oñate and R. Owen, (Eds.). International Center for Numerical Methods in Engineering, 2011.
30. H. Grabert, *Projection operator techniques in nonequilibrium statistical mechanics*, Springer-Verlag, 1982.
31. P. J. Morrison, *Hamiltonian description of the ideal fluid*, Rev. Mod. Phys., **70**, no. 2, 467, 1998.
32. R. Zwanzig and M. Bixon, *Compressibility effects in the hydrodynamic theory of Brownian motion*, J. Fluid Mech., **69**, 21–25, 1975.
33. A. J. Chorin, *Numerical Simulation of the Navier-Stokes Equations*, Mathematics of Computation, **22**, no. 104, 745–762, 1968.
34. J. B. Bell, P. Colella, and H. M. Glaz, *A Second Order Projection Method for the Incompressible Navier-Stokes Equations*, J. Comp. Phys., **85**, no. 2, 257–283, 1989.
35. C. W. J. Beenakker, *Ewald sum of the Rotne-Prager tensor*, Journal of Chemical Physics, **85**, 1581, 1986.
36. R. Clift, J. R. Grace, and M. E. Weber, *Bubbles, Drops and Particles*, Academic Press, 1978.
37. D. Ormières and M. Provansal, *Transition to Turbulence in the Wake of a Sphere*, Physical Review Letters, **83**, no. 1, 5–8, 1999.
38. M. Hill and N. R. Harris, *Ultrasonic Particle Manipulation*, in: Microfluidic Technologies for Miniaturized Analysis Systems, S. Hardt and F. Schönfeld, (Eds.), Sringer. 2007.
39. L. P. Gorkov, *On the forces acting on a small particle in an acoustic field in an ideal fluid*, Soviet Physics, Doklady, **6**, 773, 1962.

Theory and Practice of Adaptive Resolution Simulations

Raffaello Potestio and Kurt Kremer

Max Planck Institute for Polymer Research, Mainz, Germany
E-mail: {potestio, kremer}@mpip-mainz.mpg.de

In the last few decades computer simulations have become a fundamental tool in the field of soft matter science, allowing researchers to investigate the properties of a large variety of systems. Nonetheless, even the most powerful computational resources presently available are, in general, insufficient to simulate complex biomolecules over a few nanoseconds. An important limitation, hampering the achievement of larger length and time scales, is represented by the need to simulate with fine-grained detail a consistent fraction of the system, such as the solvent far from the solute's surface, which is eventually removed from the subsequent analysis. In order to overcome this problem, *adaptive resolution simulation schemes* have been developed, where a subregion of the system is described with a higher resolution -typically at the atomistic level- with respect to a surrounding thermal bath containing solvent molecules in a coarser representation; open boundaries between these regions and a position-dependent resolution switch guarantee that the correct thermodynamics is preserved in the high-resolution region of interest. This lecture provides an introduction to the Adaptive Resolution Simulation (AdResS) and the Hamiltonian AdResS (H-AdResS) schemes, focusing on their theoretical background. Applications of these methods will also be discussed.

1 Introduction

Since the pioneering work by Berni Alder[1] in the 50ies of 20th century, "*in silico*" experiments, such as Molecular Dynamics (MD) or Monte Carlo (MC) simulations, allowed researchers to obtain major advancements in the understanding of soft matter systems. Particularly during the last few decades the increasing accuracy of the force-fields, the improvement of the algorithms, and the steady boost of computer power, made it possible to perform insightful simulations of a broad variety of systems of increasing size and complexities, ranging from simple liquids -composed by idealized, point-like molecules interacting *via* simple potentials- to complex biomolecular machineries, such as protein assemblies. Nonetheless, the amount of available computational resources can be insufficient to simulate, for a physically meaningful time, even the simplest of the nontrivial macromolecules. It is often the case, in fact, that "interesting" phenomena in these systems occur on very long time-scales: a simple example of this is provided by the diffusion of a polymer in a melt[16,25], but the same behaviour is observed in conformational changes of proteins[28,23,34]. At the same time, in many cases the massive amount of data that are produced in a simulation is composed in large part by non-useful information. A prototypical example is given by the solvent: the water molecules that solvate a protein or a membrane are typically discarded from the analysis that follows the simulation, with the possible exception of a few solvation shells around the molecule itself. In this case a large fraction of the computational power is employed to the integration of the equations of motion of degrees of freedom which are extremely relevant *during* the simulations, but are completely neglected *afterwards*.

In order to overcome this limitation, *coarse-grained models*[24,55,19,30] have been developed, where the structure and interactions of the original system are replaced by simpler

ones, which are easier to describe, model, simulate and understand. The assumption underlying the coarse-graining of a system is that above a given length scale the atomistic, chemically-specific detail is not relevant to reproduce the behaviour of some large-scale properties. Two examples of systems for which this approach proved to be extremely successful are polymers[16,25], and elastic network models of proteins[52,2,29,37].

The smaller amount of degrees of freedom that are retained in coarse-grained models and the simpler force-fields employed allow to characterize relevant properties of a system at a cheaper computational cost compared to the high-resolution atomistic models; on the other hand, there are cases in which the chemical detail *in a small region of the system* plays a crucial role, such that no simplification of the description is possible: an example is given by the active site of a large enzyme, where fine-grained chemical processes take place. A high-resolution modelling of each part of the system is not necessary, but at the same time a coarse-graining approach would delete important information.

This last observation naturally leads us to identify a particular class of soft matter systems among those that are studied with the help of computer simulations. Specifically, we can consider those systems where the focus is on a small, well-defined subregion of the simulation box. To this class belong, for example, certain solvated (macro)molecules, active sites of enzymes, the interaction of specific polymer ends at a surface, or simply a small spherical region in a homogeneous fluid whose radius is of the length scale of the property we're interested in. For such systems the remaining, "non-interesting" region is composed by the volume containing all those degrees of freedom which will be eventually neglected and/or discarded once the simulation is done, such as the solvent or large parts of a macromolecule which do not take active role in the process of interest (e.g. all atoms sufficiently far from the active site of an enzyme). Usually, the detailed knowledge about structural, energetic and thermodynamical properties of these large sections of the system is not required; nonetheless these "non-interesting" degrees of freedom have to be explicitly present and integrated, inasmuch they "scaffold" the target object of the simulation and represent a reservoir of energy and molecules.

A method is thus desirable, that allows to perform a simulation where the largest part of the computational resources is concentrated on that region of the system that will be subsequently analyzed. *Adaptive resolution simulations methods*[38–41,12,32,35,9,42,36] were developed to solve the contradiction between the necessity of simulating all parts of the system and the fact that, eventually, the detailed information referred to a large subgroup of them will be neglected. The underlying idea is to replace these "non-interesting" degrees of freedom of the system with a simpler, coarse-grained representation, such that a sensibly smaller number of computations (e.g. force calculations) is required, while the "interesting" region is treated at a higher resolution.

This approach bears at least two important conceptual problems that have to be solved:

1. what is the smallest number of properties of the original system that have to be retained in the coarser model, and what are they
2. how to interface the low-resolution, "non-interesting" region and the high-resolution region to preserve the correct physics at least in the latter

These two problems are obviously interconnected, since the way the high- and low-resolution regions interact at the interface naturally depends on the specific properties of the models used in each of them.

In this lecture note we will discuss the strategy adopted in the Adaptive Resolution Simulation (AdResS)[38–41,12,32,35,9,42] and Hamiltonian AdResS[36] (H-AdResS) methods, that were developed to perform simulations of molecular fluids where molecules are free to diffuse across the whole simulation box, still preserving the correct thermodynamical properties in the high-resolution region.

This note is organized as follows: in Sec. 2 the basics of coarse-graining are given; in Sec. 3 adaptive resolution simulations are described; in Sec. 4 the AdResS and the H-AdResS methods are discussed in detail; finally, conclusions and perspectives are given in Sec. 5.

2 Coarse-Graining

As it was mentioned in the Introduction, there are many interesting physical problems for which a detailed description of the system at the all-atom (AA) level is not necessary to obtain the relevant information. In these cases a simpler model might be used, where a given high-resolution, computationally expensive model is replaced with a simpler one.

These Coarse-Grained (CG) models possess a number of features that make them particularly appealing. For example, a smaller amount of computational resources is required to perform a simulation: this is due to both the reduced number of degrees of freedom and the simpler form of the interactions. Another important characteristic is that since many interaction centres are replaced with a single one, the fluctuations of the force experienced by a molecule are generally much smaller; this results in smoother free energy profiles and, as a consequence, in faster diffusive processes, allowing to reach larger time-scales with less computations. Finally, coarse-grained models are designed to entail large length-scale properties of the system, such as the global, collective conformational changes of a protein[28,23,34] or the diffusive process of a polymer in a melt[16,25], that can be strongly insensitive to the fine-grained, chemistry-specific details; as a consequence, also the parametrization of the coarse-grained interactions is advantageously simpler.

To coarse-grain a high-resolution, atomistic system composed by M atoms into a low-resolution model made by N "super atoms" or CG sites, the first step is to provide a *map* that relates the coordinates of a group of n atoms $\mathbf{r}_i$ from the original system to those of the CG centre of interaction, $\mathbf{R}_\alpha$. This procedure can be formalized in terms of a mapping function $\mathcal{M}(\mathbf{r})$, that is commonly -but not necessarily- chosen to be a linear relation between atomistic degrees of freedom and their coarse-grained centre; in many situations, for example, the CG site is provided by the centre of mass (CoM) of the group of atoms, but different definitions of the coarse-grained centre are possible, that depend on the specific system: a water molecule, for example, can be aptly described in terms of the position of the oxygen atom, since it covers the largest fraction of the molecule's mass[56].

The second step, that is, to provide the coarse-grained sites with a meaningful potential energy V^{CG}, is the major issue in the business of coarse-graining[24,55,19,30]. The form of V^{CG} is dictated by specific problem under exam, i.e., it is determined by the properties of the AA system and by those that the CG model is asked to reproduce. A very general, physically meaningful requirement is that a statistical observable $\mathcal{Q}$, which depends on the CG degrees of freedom (e.g. the radial distribution function of the molecules' CoMs), has the same value when computed from the AA and the CG system. This requirement is automatically verified if the coarse-grained potential V^{CG} is given by the *potential of*

mean force (PMF) of the AA system, that is defined by:

$$e^{-\beta V^{CG}[\mathbf{R}]} = \int \mathcal{D}[\mathbf{r}]\delta[\mathbf{R} - \mathcal{M}(\mathbf{r})]e^{-\beta V^{AA}}. \quad (1)$$

In Eq. 1, the integral is performed over all configurations of the atomistic degrees of freedom, but the delta function constrains the CG coordinates $\mathcal{M}(\mathbf{r})$ to have the values $\mathbf{R}$. This definition of the coarse-grained potential can be shown[54] to provide the same partition function for the AA and CG systems, as well as the same ensemble averages.

Clearly, the PMF is not a honest potential energy, since it is temperature-dependent and contains the entropic contribution of the degrees of freedom that have been integrated out. Therefore, the dynamics of simulations performed making use of $V^{CG}[\mathbf{R}]$ cannot be seamlessly compared to the reference, atomistic one; on the other hand, if the PMF is available, the CG configurations sampled with the Boltzmann weight $p[\mathbf{R}] \propto exp\left[-\beta V^{CG}[\mathbf{R}]\right]$ are equivalent to those obtained from an atomistic simulation. To explicitly compute $V^{CG}[\mathbf{R}]$ would require a fully atomistic simulation, but since the PMF is a multi-dimensional function of all the CG coordinates $\mathbf{R}$ its practical use would be computationally expensive; also, it would be impossible to use this (free) energy function to simulate a system with a different number of CG coordinates. It is then necessary to resort on approximated methods, such as the force-matching or Iterative Boltzmann Inversion (IBI).

The first approach was pioneered by Ercolessi and Adams in 1994[10] and Tschop and coworkers[53] in 1998. Later on Izvekov and Voth[20,21] made use of the force-matching concept in the development of the Multi-Scale Coarse-Graining (MS-CG) method. The central idea is to project the true many-body PMF on the basis of functions that are used to define the CG force-field, *via* the minimization of a quadratic function of the difference between the two. Recent work by Scott Shell[48] showed insightful relationships between the optimization procedure defined by the MS-CG method and information theory, in particular the relative entropy[5] coarse-graining method.

Another very popular coarse-graining strategy is Iterative Boltzmann Inversion[43,53,55], in which the CG potential energy is initially taken to be the two-body PMF and iteratively refined so that the radial distribution function[54] of the CG system coincides with the one of the underlying AA system.

These two coarse-graining methods (both implemented in the VOTCA (Versatile Object-oriented Toolkit for Coarse-graining Applications)[47] package) both present features that make one preferable over the other in specific situations, as well as limitations and drawbacks. The MS-CG, for example, responds to the need of having a CG force-field of a given functional form as close as possible to the real many-body potential. The flexibility given by the choice of the CG functions permits a systematic improvement of the matching by including potential energy terms of arbitrary complexity; on the other hand, this comes at the expenses of a dramatic increase of the computational cost required to calculate forces. Moreover, the global character of the minimization procedure prevents from accurately reproduce a single specific property of the system, e.g. the RDF[46].

Iterative Boltzmann Inversion belongs to a class of coarse-graining methods that are, in some respect, complementary to MS-CG: in this scheme the two-body potential of mean force is iteratively refined in order to reproduce, as closely as possible, the atomistic reference RDF. If no other property of the system, such as higher-order correlations, total

potential energy or pressure, is explicitly included in the optimization procedure, no match with the reference values is to be expected. In particular, the pressure of the CG system usually turns out to be remarkably off with respect to the reference: a typical example is provided by the IBI-CG models of water, whose pressure is three-four orders of magnitude higher than the corresponding atomistic system[56]. It is possible to perform the iterative procedure introducing a "pressure correction"[43,56] term in the potential, in order to have the CG pressure matching to the atomistic reference. Unfortunately, this cannot be done without disrupting at least weakly the long-range behaviour of the RDF; in turn, the compressibility of the CG system is affected by this change in the structure. This is indeed no surprise, since the desired properties of the CG model coincide (in general) to the AA model ones just at the specified state point, but follow different equations of state: a model with very simple structure and forces, in fact, is not capable of reproducing more than a few properties of the underlying high-resolution system, which relies on a larger number of degrees of freedom and interaction parameters. It is here of great importance to stress that a model at a given resolution and its coarse-grained "version" *are not the same thing*: a CG model is a system on its own, specific properties of which behave in the same way as the relative AA model in a limited and well defined range of parameters (temperature, density...).

This short overview was intended to provide the reader with the most common concepts, strategies and issues in the field of coarse-graining. It should be now clear that no unique way exists to relate models with different resolutions and interaction types; moreover, each coarse-graining strategy provides specific advantages as well as it bears limitations and drawbacks with it: the choice of the appropriate method to coarse-grain a system strongly depends on the system itself and on the properties that one is interested in preserving.

3 Adaptive Resolution Simulations: Basic Concepts

In the introduction we considered that class of systems for which the focus of the researcher's interest concentrates on a (possibly small) subregion: this is the case, for example, of the hydrogen bond network at the surface of a solvated molecule in water. The bulk of water molecules has to be simulated in order to sustain the thermodynamical properties of the subsystem of interest -the interfacial water- and to provide the correct exchange of molecules. Nonetheless, the fine-grained detail of molecules far from the interface is not relevant; it would therefore be desirable to replace the atomistic, expensive interactions of hydrogen and oxygen atoms with a coarser model. We can then introduce a geometrical separation between an "inside" and an "outside", i.e. an all-atom (AA) and a coarse-grained (CG) region, and assign different types of representations and interactions to the molecules according to their position in the simulation domain.

This idea has a long and successful history: to investigate crack propagation in hard matter, for example, several authors[45,44,6,22,27] made use of a hybrid description of the system, where a "high resolution" description is employed only the area in proximity of the crack, and the material far from the latter is treated with a simpler model.

Another important example of hybrid resolution simulation is provided by Quantum Mechanics / Molecular Mechanics (QM/MM) methods[57,15,51,4,3]. In this case the structure of the system is described at the same (atomistic) level everywhere; the interactions,

though, are obtained from a classical force-field in the bulk of the system, but in a small region *ab initio* methods -such as Density Functional Theory, DFT- are employed to calculate the forces. Many different "flavours" of this approach have been developed; in all of them, though, one of the crucial aspects is how to interface the two domains where interactions are different. In general, one has to answer the two following questions:

1. how do two atoms/molecules in different domains interact?
2. how do the properties of an atom/molecule *change* in crossing the interface?

The last question is of particular importance for all systems whose components can diffuse on large length scales (at least of the order of the molecules' effective size) in the simulation time. It appears natural to introduce a *transition region* (often called hybrid region, or healing region) that allows for a smooth interpolation from a given representation of the molecule's structure/interaction to another. The choice of the specific way this interpolation is implemented depends, as we mentioned earlier, on the properties that have to be preserved in the CG region.

Irrespective of the chosen method to interface the two regions of the system, though, it is natural to expect that the equilibrium between them is not preserved *a priori*; and still, if the system reaches an equilibrium state, nothing guarantees that it is the desired one. A further crucial point is then to find the simplest way to impose the desired thermodynamics.

The central, strong requirement that has to be satisfied is that molecules should be free to diffuse from any region of the simulation box to any other. Additionally, in a hybrid resolution model thermal equilibrium should be preserved, i.e., the temperature of the system has to be constant during the simulation. Another possible constraint is to impose a uniform density across the box, irrespective of the specific resolution; nonetheless, we'll see that there are cases where this is not strictly necessary nor desirable.

These are the fundamental constraints that can be imposed to the system as a whole. Other, more specific ones can be introduced on the properties of the CG region as well as the transition region, which will "drive" us towards a specific formulation of a double-resolution simulation method.

4 AdResS and H-AdResS

4.1 AdResS: Theory

The Adaptive Resolution Scheme (AdResS) represents the first method to efficiently and effectively simulate a system where models at different resolution are *simultaneously* employed in different subregions of the simulation domain without barriers to the diffusion. A sketch of an AdResS setup is depicted in Fig. 1.

The basic constraint that was enforced in this scheme is that *Newton's 3rd law has to be exactly satisfied everywhere in the simulation domain*. This requirement rules out any form of potential energy interpolation: it can in fact be formally demonstrated[7] that there is no way to smoothly "blend" the interaction between two molecules from a given potential energy to another without generating forces that cannot be recast in a form that satisfies Newton's Third Law. In order to preserve the latter, then, a *force-interpolation scheme* is required, such that the force that a given molecule receives due to the interaction with a second one is antisymmetric under exchange of the molecules' labels:

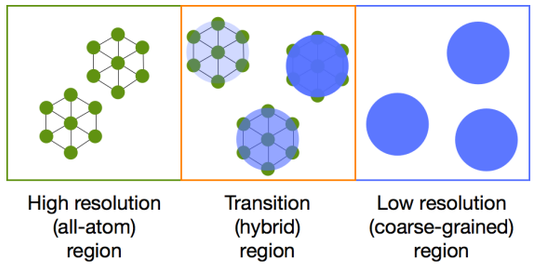

Figure 1. Typical scheme of an adaptive resolution simulation: a high-resolution region, where molecules are described at the atomistic level, is coupled to a low-resolution region where a simpler, coarse-grained model is employed. There two sub-parts of the system are interfaced *via* a hybrid region, in which the molecule's representation smoothly changes from one to the other, depending of their positions. It is on this last region and its properties (i.e. the way molecules change resolution) that the complexity of adaptive resolution schemes concentrates.

$$\mathbf{F}_{\alpha|\beta} = -\mathbf{F}_{\beta|\alpha} \tag{2}$$

A second, less strict requirement is that CG molecules possess CG degrees of freedom only; this determines the specific way the force mixing is performed: a molecule in the CG region loses completely its atomistic detail (thus retaining, for example, the center of mass coordinates only), and interacts with a molecule in the AA or even the transition region only *via* its CG degrees of freedom. Formally, this constraint imposes that the atomistic forces vanishes when at least one of the two interacting molecules is in the CG domain.

These two constraints are sufficient to define the force-field interpolation; the force that affects atom i in molecule α is given by:

$$\mathbf{F}_{\alpha i} = \mathbf{F}^{int}_{\alpha i} + \sum_{\beta,\beta\neq\alpha} \left\{ \lambda(X_\alpha)\lambda(X_\beta)\mathbf{F}^{AA}_{\alpha i|\beta} + (1-\lambda(X_\alpha)\lambda(X_\beta))\,\mathbf{F}^{CG}_{\alpha i|\beta} \right\} \tag{3}$$

In Eq. 3 $\lambda(x)$ is any smooth function that goes from 1 in the AA region to 0 in the CG region. X_α (resp. X_β) is the CoM coordinate of molecule α (resp. β). $\mathbf{F}^{int}_{\alpha i}$ is the force due to the interactions *internal* to the molecule (e.g. bonds with other atoms). $\mathbf{F}^{AA}_{\alpha i|\beta}$ and $\mathbf{F}^{CG}_{\alpha i|\beta}$ are the atomistic and the coarse-grained forces acting on atom i of molecule α due to the interaction with molecule β, respectively. These forces are given by:

$$\begin{aligned} \mathbf{F}^{AA}_{\alpha i|\beta} &\equiv \sum_{j=1}^{n_\beta} -\frac{\partial}{\partial \mathbf{r}_{\alpha i}} V(|\mathbf{r}_{\alpha i} - \mathbf{r}_{\beta j}|) \\ \mathbf{F}^{CG}_{\alpha i|\beta} &\equiv -\frac{m_{\alpha i}}{M_\alpha}\frac{\partial}{\partial \mathbf{R}_\alpha} V^{CG}(|\mathbf{R}_\alpha - \mathbf{R}_\beta|). \end{aligned} \tag{4}$$

The CG force is redistributed to atom i weighted by the ratio of the atom's mass to the mass of molecule[13] α. In the transition region this operation is required by the fact that

molecules interact at both the AA and the CG level. AA degrees of freedom thus *have* to be explicitly integrated. In the CG region, on the other hand, it is not necessary in principle to conserve the atomistic detail of the molecules, so that the CG force could be applied directly to the CoM coordinate; a molecule's internal structure can thus be removed when it enters the CG region, and reintroduced (e.g. taking it from a reservoir/repertoire of equilibrated atomistic molecules) as soon as it approaches the hybrid region. In all AdResS versions implemented so far, though, the atomistic DoF's are retained for simplicity of implementation[38]; the CoM of the molecule is nonetheless decoupled from the internal atomistic structure, and it evolves only subject to the CG force.

Because of the requirement of preserving Newton's 3rd law everywhere in the system, a force-based interpolation approach had to be chosen. It is evident, then, that the AdResS scheme cannot be formulated in terms of a Hamiltonian; this in turn makes it impossible to perform microcanonical, i.e. energy-conserving simulations[7]. The force-field used in the AdResS framework is not conservative in the transition region - that is, when molecules interact with a non-conservative linear combination of two conservative force-fields; when crossing this region, then, a molecule receives an unphysical surplus of energy that has to be removed in order to prevent the system from heating up and become unstable. This excess energy can be removed with a *local* thermostat, such as Langevin thermostat: in this way, the temperature of the system is kept constant everywhere. The equilibrium state of the system is then *dynamical*: the thermostat takes care of absorbing the extra heat produced in the transition region by non-conservative forces, and the system samples equilibrium configurations according to Boltzmann's distribution[38–41, 12, 32, 35, 9, 42].

The presence of the thermostat imposes a uniform temperature across the simulation domain, an establishes an equilibrium state. However, the different pressure between an AA system and its CG model at a given state point determines the onset of a non-uniform density profile. It was already mentioned, for example, that a one-site CG model of water obtained with IBI can have a pressure ~ 6000 times the atomistic reference value[56]. Therefore, the densities in the two subregions will change in order to equate the pressures. A possible solution to this density imbalance is to parametrize the CG potential to the target pressure[43], but this would result in an unphysical compressibility (see Sec. 2).

Another option to preserve a uniform density across the simulation domain without modifying the CG potential is to introduce a force which acts on single molecules and only in the transition region, whose effect is to push molecules in the domain where the system, at the reference temperature and density, has a lower pressure. This *thermodynamic force* can be obtained with an iterative procedure *via* the following expression[31, 13]:

$$\mathbf{f}_{th}^{i+1} = \mathbf{f}_{th}^{i} - \frac{1}{\rho^{\star}\kappa_T}\nabla\rho^{i}(r), \tag{5}$$

where $\rho^{\star}$ is the reference molecular density, κ_T is the system's isothermal compressibility and $\rho^{i}(r)$ is the molecular density profile as a function of the position in the direction perpendicular to the CG-AA interface. The thermodynamic force is initialized to zero, $\mathbf{f}_{th}^{0} = 0$, while the initial pressure profile is the one calculated from an AdResS simulation with $\mathbf{f}_{th} = 0$. As it can be easily seen, the iterative procedure converges once the density profile is flat ($\nabla\rho(r) = 0$). This approach guarantees a flat density profile without having to modify the CG potential: because of its very definition, the thermodynamic force only acts to those molecule that cross the hybrid region, but it leaves the others unaffected. It

can also be shown[13,38] that the integral of the thermodynamic force across the interface, i.e. the work due to this force performed by a molecule while crossing the hybrid region, is proportional to the pressure profile, the proportionality factor being the reference density $\rho^\star$.

In summary, the thermodynamic force allows us to couple a system at atomistic resolution to a coarse-grained counterpart whose pressure, for given value of density and temperature, is sensibly different. The global properties of the force, whose direct effect is restricted to the hybrid region, only depend on the pressure difference between the two coupled subsystems; the detailed profile of the force, on the other hand, can be obtained *via* a system-specific iterative procedure. This method not only allows to preserve the desired structure of the system in the CG region; in principle, in fact, an arbitrary CG force-field, with pressure *and structure* completely off from the atomistic target ones, can be used. Consequently, the AA region behaves as an open system[13] that exchanges energy and molecules with a reservoir: the molecule number fluctuations, the pressure and all other thermodynamically relevant quantities are the same as if the AA region were simply "cut" from a large all-atom simulations. It is relevant to stress here that because of the thermodynamic force this condition can be established *irrespective of the specific model used in the CG region*.

4.2 Classical-to-Quantum Coupling

The concept of coupling two different representations of the same systems can be extended beyond the AA-to-CG case: it is in fact possible to consider a situation where a *classical* and a *quantum* representation of a system are coupled. In order to do this, a quantum model of the system is required, that might be actually used in a MD simulation code. The appropriate language to this end is provided by Richard Feynman's formulation of quantum mechanics in terms of *Path Integrals*[11]. The partition function Z of a quantum system at thermal equilibrium can be written as a trace of the *Boltzmann operator* $e^{-\beta\hat{H}}$ over all possible configurations of the system:

$$Z = \int dx \, \langle x|e^{-\beta\hat{H}}|x\rangle, \tag{6}$$

with $\hat{H} \equiv \hat{p}^2/2m + \hat{V}$. The kinetic energy term $\hat{T} \equiv \hat{p}^2/2m$ and the potential energy operator $\hat{V}$ do not commute; this makes it impossible to explicitly calculate the matrix element in the integral for all nontrivial cases of interest. Nonetheless, an approximation to Eq. 6 is possible[54], through which the patrician function can be written as:

$$Z = \lim_{P\to\infty}\left[\frac{mP}{2\pi\hbar^2\beta}\right]^{P/2}\int dx_1\cdots dx_P \, exp\left[-\beta V_P(\bar{x})\right] \tag{7}$$

$$V_P(x_1, x_2, \cdots x_P) = \sum_{l=1}^{P'}\frac{mP}{2(\beta\hbar)^2}(x_l - x_{l+1})^2 + \frac{V(x_l)}{P}.$$

The prime on the P in the sum indicates that cyclic conditions are enforced, such that: $x_{l+P} = x_l$. The partition function of a quantum system can be expressed in terms of

classical degrees of freedom: a quantum particle of our system is mapped onto a closed necklace, or *polymer ring*, of beads coupled with first-neighbours via harmonic springs of elastic constant $mP/(\beta\hbar)^2$; each bead also interacts with other polymer rings: specifically, beads having the same label (Trotter index l in Eq. 7) interact via the rescaled intermolecular potential V/P. It is worth emphasizing that V is the *classical* interaction potential. This classical representation of the quantum system is suitable to be used in the framework of the AdResS method: in fact, it can be employed as a high-resolution description of the system, while an effective, purely classical interaction between the polymer rings' centres of mass would serve as a coarse-grained potential.

4.3 AdResS: Applications

The possibility of treating a system with a reduced number of degrees of freedom except where it is strictly necessary was explored, making use of the AdResS method, in several applications[38–41,8,12,32,35,14a]. From the numerical/computational point of view it clearly represents an advantage, since a much smaller number of force calculations are required in the coarse-grained region: this is particularly true for parallel MD codes such as GROMACS[18], where a dynamical decomposition of the simulation box allows to subdivide the latter with a finer grid in the AA and hybrid region, while a smaller number of processors is assigned to the CG region. For example, for a water system with an AA region covering $1/6$ of the total simulation box, simulated with GROMACS on a 16-cores processor, the speed-up is about a factor three. This factor is nonetheless small compared to what can be achieved with other simulation packages, such as ESPRESSO++[17]: in fact, water simulation in GROMACS is extremely optimized, and any hacking of the standard code can introduce a bottleneck.

A major strength of the AdResS method is the fact that it introduces a decoupling between a given region of the system and the rest while keeping the thermodynamic properties of both regions under control: as a consequence, it is possible to conceive numerical experiments in which the spatial extension of correlations in the system is investigated. More specifically, one can study the structural properties of the high-resolution region as a function of its size, in order to determine their dependency on the interaction with molecules in the bulk region. This kind of experiments differentiates from the study of finite-size effects: in the latter, in fact, the system has the same resolution and interaction type everywhere, and the change of a property with the box size depends on the asymptotic approach to the thermodynamic limit. In the AdResS setup, on the other hand, finite-size effect can be neglected for sufficiently large boxes, thus allowing to characterize the response of the system's properties in a small subregion when atomistic interactions with the bulk are switched off, but the thermodynamics is the same as in a fully-atomistic simulation[13,14]. An example of this applications is provided by the work in of Lambeth *et al.*[26]: here a molecule with both hydrophilic and hydrophobic interactions was solvated in water and put at the centre of the high-resolution region, while the water molecules far from the surface were treated at the coarse-grained level. The ordering degree of the hydrogen bond network on the molecule's surface was measured as a function of the size of the all-atom

[a] A detailed account of a specific application of the AdResS scheme, namely the simulation of a triglycine molecule in aqueous urea, can be found in the book chapter of this NIC series by D. Mukherji and K. Kremer.

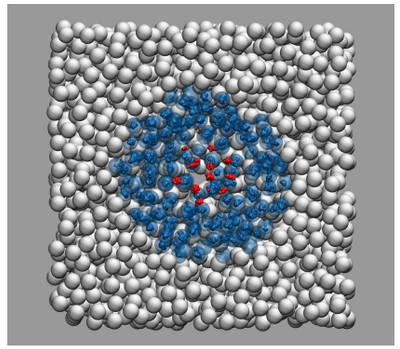

Figure 2. Set-up of the AdResS para-hydrogen simulation performed in by Potestio and Delle Site[35] (figure adapted from therein). A small sphere in the centre of the box, having radius as small as 0.6 nm, is treated at the path integral level (red rings), while the rest is described by point-like molecules (the white spheres); the hybrid region (blue) interfaces these two representations.

region: the results showed a dependency of the ordering for water molecules close to the surface of the repulsive solute, while no relevant effect was observed for the attractive case.

The same strategy has been applied to investigate the extent of spatial correlations in a quantum fluid, namely low-temperature para-hydrogen[33,35]. The latter is the spin-zero singlet state of molecular hydrogen. Because of the spherical symmetry of the global wave function, para-hydrogen in the solid and gas phase can be modelled as a classical, point-like particle interacting *via* a simple radial potential, such as Lennard-Jones or the more accurate Silvera-Goldman potential[50,49]. The latter classical potential, in particular, has been shown to correctly reproduce the experimental results both in the solid and the gas phase[49].

In the fluid phase, however, nuclear delocalization effects become important, and a quantum mechanical treatment of the problem is necessary. This can be achieved through the path integral formalism, that allows for the explicit inclusion of nuclear quantum effects in a "classical" description; unfortunately, this also implies a significant increase in the number of degrees of freedom that have to be simulated, since each molecules becomes a collection of P beads connected by springs. The possibility to simulate a quantum system in a classical framework, such as classical MD, makes it possible to couple quantum and classical descriptions with the AdResS scheme. In particular, a low-temperature para-hydrogen system was simulated[35] making use of the explicit path integral representation only in a small spherical subregion of the simulation domain, while the molecules in the outer region were treated at the purely classical level, i.e. point-like particles interacting through a coarse-grained potential; a snapshot of the simulation setup is shown in Fig. 2. This study showed that a few molecules in a small (~ 0.6 nm radius) region of the system are sufficient to reproduce the quantum pair correlation function obtained from a fully path integral simulation, but treating the molecules in the outer region at the CG level;

this result opens the way to simulate large systems of low-temperature para-hydrogen, and possibly other quantum fluids, taking advantage of a double resolution without disrupting the thermodynamical and structural properties of the small, purely quantum region, thus saving computational time in the CG region.

4.4 Hamiltonian Adaptive Resolution Simulation Scheme

As it was discussed in the previous section, the force-based AdResS method was developed on the basis of two central requirements: Newton's 3rd law had to be exactly satisfied everywhere, and CG molecules could possess CG degrees of freedom only; as a consequence, no Hamiltonian formulation of this scheme is possible[7]. Recently the Hamiltonian Adaptive Resolution Simulation (H-AdResS) method[36] was introduced, in which the aforementioned constraints are relaxed. The particular choice of energy "mixing" gives place to forces that do not comply with the first constraint; nevertheless, the physical interpretation of these terms is immediate and naturally points towards the solution -though approximate- of Newton's Third Law breakdown. The core idea of the energy-based approach is to weight the *total energy* of each molecule with a position-dependent function:

$$
\begin{aligned}
H &= \mathcal{K} + V^{int} + \sum_{\alpha} \left\{ \lambda_\alpha V_\alpha^{AA} + (1-\lambda_\alpha) V_\alpha^{CG} \right\} \qquad (8)\\
\mathbf{F}_{\alpha i} &= \mathbf{F}_{\alpha i}^{int} + \sum_{\beta,\beta\neq\alpha} \left\{ \frac{\lambda_\alpha + \lambda_\beta}{2} \mathbf{F}_{\alpha i|\beta}^{AA} + \left(1 - \frac{\lambda_\alpha + \lambda_\beta}{2}\right) \mathbf{F}_{\alpha i|\beta}^{CG} \right\} \\
&\quad - \left[V_\alpha^{AA} - V_\alpha^{CG} \right] \nabla_{\alpha i} \lambda_\alpha
\end{aligned}
$$

where $\mathcal{K}$ is the (all-atom) kinetic energy of the molecules The forces $\mathbf{F}_{\alpha i|\beta}^{AA}$ and $\mathbf{F}_{\alpha i|\beta}^{CG}$ and the redistribution of the CG force on the atomistic degrees of freedom follow the same rules given in the case of AdResS (see Eq. 4). The third term of the forces in Eq. 8 is the part that leads to the breakdown of Newton's Third Law: in fact, it cannot be written as a sum of terms antisymmetric under molecule label exchange. Such term is nonzero *only in the hybrid region* and depends on a single λ function, rather than the product of two. Therefore, it can be cancelled, on average, by introducing a compensation term in the Hamiltonian, as it was done in the AdResS scheme with the thermodynamic force:

$$
H_\Delta = H - \sum_{\alpha=1}^{N} \Delta H(\lambda(\mathbf{R}_\alpha)). \qquad (9)
$$

Appropriately choosing the $\Delta H(\lambda)$ function we can reestablish equilibrium between the AA and CG regions while preserving the Hamiltonian character of H. The H-AdResS represents a major step forward in terms of understanding and practical advantages. In fact, the existence of a Hamiltonian allows to formulate a statistical physics theory of double-resolution systems, to perform microcanonical simulations, and to make use of Monte Carlo simulations methods.

5 Conclusions

Adaptive resolution methods were developed in order to reduce the amount of resources dedicated to the simulation of large, non-interesting regions of a system by replacing the high resolution molecules contained therein with a simpler, coarse-grained representation. In the present work we discussed two methods to achieve this goal: the Adaptive Resolution Simulation (AdResS) scheme, based on the interpolation of two different force-fields, and its Hamiltonian formulation, H-AdResS, where the all-atom and coarse-grained potential energies are interpolated. These methods have been successfully applied to interface different molecular fluids, treated at the atomistic level, with their coarse-grained models; the different properties of the AA and the CG potentials naturally induce thermodynamical imbalances in the corresponding sub-regions, but simple and effective ways to overcome this problem have been described. A particularly important advantage of these strategies is that they provide a way to couple, to the AA region, a reservoir of molecules *interacting with an arbitrary force-field*, thus allowing one to use coarse-grained models without effectively performing a coarse-graining. One then has the possibility to replace vast regions of the simulated system with a crude, inexpensive representation and concentrate the computational resources on smaller parts while keeping the relative thermodynamics under control makes it possible to sensibly reduce the amount of calculations required to perform a simulation. Such methods open the way to a broad spectrum of applications, e.g. large-scale simulations of complex biomolecules in solution and efficient open-boundary simulations with varying number of particles.

Acknowledgements

The authors are indebted with Luigi delle Site, Matej Praprotnik, Davide Donadio, Sebastian Fritsch, Rafael Delgado Buscalioni, Pep Español and Ralf Everaers for fruitful collaboration, and with Debashish Mukherji for critical and helpful reading of this manuscript.

References

1. B. J. Alder and T. E. Wainwright. Phase transition for a hard sphere system. *J. Chem. Phys.*, 5(27), 1957.
2. I. Bahar, A. R. Atilgan, and B. Erman. Direct evaluation of thermal fluctuations in proteins using a single parameter harmonic potential. *Folding and Design*, 2:173–181, 1997.
3. R. E. Bulo, B. Ensing, J. Sikkema, and L. Visscher. Toward a practical method for adaptive qm/mm simulations. *J. Chem. Theor. Comp.*, 5(9):2212–2221, 2009.
4. P. Carloni, U. Rothlisberger, and M. Parrinello. The role and perspective of a initio molecular dynamics in the study of biological systems. *Accounts Chem. Res.*, 35(6):455–464, Jan 2002.
5. A. Chaimovich and M. S. Shell. Coarse-graining errors and optimization using a relative entropy framework. *J. Chem. Phys.*, 2011.
6. G. Csanyi, T. Albaret, M. C. Payne, and A. De Vita. "Learn on the fly": A hybrid classical and Quantum-Mechanical molecular dynamics simulation. *Phys. Rev. Lett.*, 93(17):175503, 2004.

7. L. Delle Site. Some fundamental problems for an energy-conserving adaptive-resolution molecular dynamics scheme. *Phys. Rev. E*, 76(4), 2007.
8. L. Delle Site, S. Leon, and K. Kremer. BPA-PC on a ni(111) surface: The interplay between adsorption energy and conformational entropy for different Chain-End modifications. *J. Am. Chem. Soc.*, 126(9):2944–2955, March 2004.
9. B. Ensing, S. O. Nielsen, P. B. Moore, M. L. Klein, and M. Parrinello. Energy conservation in adaptive hybrid Atomistic/Coarse-Grain molecular dynamics. *J. Chem. Theor. Comp.*, 3(3):1100–1105, 2007.
10. F. Ercolessi and J. B. Adams. Interatomic potentials from first-principles calculations: The force-matching method. *Europhys. Lett.*, 26, 1994.
11. R. P. Feynman. Atomic theory of the two-fluid model of liquid helium. *Phys. Rev.*, 94:262–277, Apr 1954.
12. S. Fritsch, C. Junghans, and K. Kremer. Structure formation of toluene around c60: Implementation of the adaptive resolution scheme (adress) into gromacs. *J. Chem. Theory Comput.*, 8(2):398–403, FEB 2012.
13. S. Fritsch, S. Poblete, C. Junghans, G. Ciccotti, L. Delle Site, and K. Kremer. Adaptive resolution molecular dynamics simulation through coupling to an internal particle reservoir. *Phys. Rev. Lett.*, 108(17), APR 27 2012.
14. P. Ganguly, D. Mukherji, C. Junghans, and N. F. A. van der Vegt. Preferential solvation of triglycine in aqueous urea: An open boundary simulation approach. *JCTC*, 8, 2012.
15. J. Gao, K. B. Lipkowitz, and D. B. Boyd. *Methods and applications of combined quantum mechanical and molecular mechanical potentials*. Wiley, 1995.
16. G. S. Grest and K. Kremer. Molecular dynamics simulation for polymers in the presence of a heat bath. *Phys. Rev. A*, 33:3628–3631, May 1986.
17. J. D. Halverson, T. Brandes, O. Lenz, A. Arnold, S. Bevc, V. Starchenko, K. Kremer, T. Stuehn, and D. Reith. Espresso++: A modern multiscale simulation package for soft matter systems. *Computer Physics Communications*, (0):–, 2012.
18. B. Hess, C. Kutzner, D. van der Spoel, and E. Lindahl. Gromacs 4: Algorithms for highly efficient, load-balanced, and scalable molecular simulation. *J. Chem. Theor. Comput.*, 4(3):435–447, 2008.
19. C. Hijón, E. Vanden-Eijnden, R. Delgado-Buscalioni, and P. Español. Mori-Zwanzig formalism as a practical computational tool. *Faraday discussions*, 144(1):301–22; discussion 323–45, 467–81, January 2010.
20. S. Izvekov and G. A. Voth. Effective force field for liquid hydrogen fluoride from ab initio molecular dynamics simulation using the force-matching method. *The Journal of Physical Chemistry B*, 109(14):6573–6586, 2005. PMID: 16851738.
21. S. Izvekov and G. A. Voth. Multiscale coarse graining of liquid-state systems. *The Journal of Chemical Physics*, 123(13):134105, 2005.
22. D. E. Jiang and E. A. Carter. First principles assessment of ideal fracture energies of materials with mobile impurities: implications for hydrogen embrittlement of metals. *Acta Materialia*, 52(16):4801–4807, 2004.
23. M. Karplus and J. A. McCammon. Protein structural fluctuations during a period of 100 ps. *Nature*, 277(5697):578–578, Feb 1979.
24. K. Kremer. Computer simulations in soft matter science. In *Soft and fragile matter: non equilibrium dynamics, metastability and flow*, volume 53 of *SUSSP proceedings*, pages 145–184. IOP Publishing Ltd., 2000.

25. K. Kremer, G. S. Grest, and I. Carmesin. Crossover from rouse to reptation dynamics: A molecular-dynamics simulation. *Phys. Rev. Lett.*, 61:566–569, Aug 1988.
26. B. P. Jr. Lambeth, C. Junghans, K. Kremer, C. Clementi, and L. Delle Site. Communication: On the locality of hydrogen bond networks at hydrophobic interfaces. *The Journal of Chemical Physics*, 133(22):221101, 2010.
27. G. Lu, E. B. Tadmor, and E. Kaxiras. From electrons to finite elements: A concurrent multiscale approach for metals. *Phys. Rev. B*, 73(2):024108, 2006.
28. J. A. McCammon and M. Karplus. Internal motions of antibody molecules. *Nature*, 268(5622):765–766, Aug 1977.
29. C. Micheletti, P. Carloni, and A. Maritan. Accurate and efficient description of protein vibrational dynamics: comparing molecular dynamics and gaussian models. *Proteins*, 55(3):635–645, May 2004.
30. W. G. Noid. *Systematic methods for structurally consistent coarse-grained models*, volume 924 of *Methods in Molecular Biology*. Humana Press, 2013.
31. S. Poblete, M. Praprotnik, K. Kremer, and L. Delle Site. Coupling different levels of resolution in molecular simulations. *J. Chem. Phys.*, 132(11):114101, 2010.
32. A. B. Poma and L. Delle Site. Classical to Path-Integral adaptive resolution in molecular simulation: Towards a smooth Quantum-Classical coupling. *Phys. Rev. Lett.*, 104(25):250201, June 2010.
33. A. B. Poma and L. Delle Site. Adaptive resolution simulation of liquid para-hydrogen: testing the robustness of the quantum-classical adaptive coupling. *Phys. Chem. Chem. Phys.*, 13:10510–10519, 2011.
34. F. Pontiggia, A. Zen, and C. Micheletti. Small and large scale conformational changes of adenylate kinase: a molecular dynamics study of the subdomain motion and mechanics. *Biophys J*, 95(12):5901–5912, Dec 2008.
35. R. Potestio and L. Delle Site. Quantum locality and equilibrium properties in low-temperature parahydrogen: A multiscale simulation study. *J. Chem. Phys.*, 136(5), FEB 7 2012.
36. R. Potestio, S. Fritsch, P. Espanol, R. Delgado-Buscalioni, K. Kremer, R. Everaers, and D. Donadio. Hamiltonian adaptive resolution simulation for molecular liquids. *arXiv:1212.474 [cond-mat.stat-mech]*, 2012.
37. R. Potestio, F. Pontiggia, and C. Micheletti. Coarse-grained description of proteins' internal dynamics: an optimal strategy for decomposing proteins in rigid subunits. *Biophys J*, 96, 2009.
38. M. Praprotnik, L. Delle Site, and K. Kremer. Adaptive resolution molecular-dynamics simulation: Changing the degrees of freedom on the fly. *J. Chem. Phys.*, 123(22):224106–14, 2005.
39. M. Praprotnik, L. Delle Site, and K. Kremer. Adaptive resolution scheme for efficient hybrid atomistic-mesoscale molecular dynamics simulations of dense liquids. *Phys. Rev. E*, 73:066701, 2006.
40. M. Praprotnik, L. Delle Site, and K. Kremer. A macromolecule in a solvent: Adaptive resolution molecular dynamics simulation. *J. Chem. Phys.*, 126:134902, 2007.
41. M. Praprotnik, L. Delle Site, and K. Kremer. Multiscale simulation of soft matter: From scale bridging to adaptive resolution. *Ann. Rev. Phys. Chem.*, 59(1):545–571, 2008.

42. M. Praprotnik, S. Poblete, L. Delle Site, and K. Kremer. Comment on “adaptive multiscale molecular dynamics of macromolecular fluids”. *Phys. Rev. Lett.*, 107:099801, Aug 2011.
43. D. Reith, M. Pütz, and F. Müller-Plathe. Deriving effective mesoscale potentials from atomistic simulations. *J. Comput. Chem.*, 24(13):1624–1636, 2003.
44. J. Rottler, S. Barsky, and M. O. Robbins. Cracks and crazes: On calculating the macroscopic fracture energy of glassy polymers from molecular simulations. *Phys. Rev. Lett.*, 89(14):148304, 2002.
45. R. E. Rudd and J. Q. Broughton. Concurrent coupling of length scales in solid state systems. *Phys. Status Solidi B-Basic Res.*, 217(1):251–291, JAN 2000.
46. V. Ruehle and C. Junghans. Hybrid approaches to coarse-graining using the votca package: Liquid hexane. *Macromolecular Theory and Simulations*, 20(7):472–477, 2011.
47. V. Rühle, C. Junghans, A. Lukyanov, K. Kremer, and D. Andrienko. Versatile Object-Oriented Toolkit for Coarse-Graining Applications. *J. Chem. Theor. Comput.*, 5:3211–3223, 2009.
48. M. S. Shell. The relative entropy is fundamental to thermodynamic ensemble optimization. *J. Chem. Phys.*, 2008.
49. I. F. Silvera. The solid molecular hydrogens in the condensed phase: Fundamentals and static properties. *Rev. Mod. Phys.*, pages 393–452, 1980.
50. I. F. Silvera and V. V. Goldman. The isotropic intermolecular potential for h2 and d2 in the solid and gas phases. *J. Chem. Phys.*, pages 4209–4213, 1978.
51. M. Svensson, S. Humbel, R. D. J. Froese, T. Matsubara, S. Sieber, and K. Morokuma. Oniom: A multilayered integrated mo+mm method for geometry optimizations and single point energy predictions. a test for diels-alder reactions and pt(p(t-bu)(3))(2)+h-2 oxidative addition. *J. Phys. Chem. Us*, 100(50):19357–19363, Jan 1996.
52. M. M. Tirion and D. ben Avraham. Normal mode analysis of g-actin. *JMB*, 230:186–195, 1993.
53. W. Tschoep, K. Kremer, J. Batoulis, T. Buerger, and O. Hahn. Simulation of polymer melts. i. coarse-graining procedure for polycarbonates. *Acta Polym.*, 49:6174, 1998.
54. M. E. Tuckermann. *Statistical Mechanics: Theory and Molecular Simulation*. Oxford University Press, 2010.
55. N. F. A. van der Vegt, C. Peter, and K. Kremer. *Structure-Based Coarse- and Fine-Graining in Soft Matter Simulations*. CRC Press - Taylor and Francis Group, 2009.
56. H. Wang, C. Junghans, and K. Kremer. Comparative atomistic and coarse-grained study of water: What do we lose by coarse-graining? *Eur. Phys. J. E*, 28(2):221–229, 2009.
57. A. Warshel and M. Levitt. Theoretical studies of enzymic reactions - dielectric, electrostatic and steric stabilization of carbonium-ion in reaction of lysozyme. *J. Mol. Biol.*, 103(2):227–249, Jan 1976.

Hamiltonian Adaptive Hybrid Atomistic/Coarse-Grain Molecular Dynamics

Bernd Ensing[1], **Alessandro Laio**[2], **and Steven O. Nielsen**[3]

[1] Van't Hoff Institute for Molecular Sciences, University of Amsterdam, Science Park 904, 1098 XH, Amsterdam, The Netherlands
E-mail: email: b.ensing@uva.nl

[2] Scuola Internazionale Superiore di Studi Avanzati (SISSA), via Bonomea 265, 34136 Trieste, Italy

[3] Department of Chemistry, The University of Texas at Dallas, 800 West Campbell Road, Richardson, Texas 75080, United States

In this lecture, we discuss two different approaches to treat an adaptive hybrid atomistic/coarse-grain simulation. Such a multiscale algorithm treats the most interesting part of the system in accurate fine-grained (atomistic) detail, whereas the environment is modelled at a less detailed and less computationally demanding resolution. Our interest is in open boundaries: molecules are allowed to diffuse between the different resolution regions and adapt their resolution on the fly. Here we compare our existing approach with a new approach based on a Lagrangian formulation which includes both resolution-switching forces and a constraint on the number of particles in each resolution region.

1 Introduction

Extending the time and length scales of molecular dynamics simulations of molecular processes has been a challenge since the earliest computer calculations. Multiscale modelling has become a powerful paradigm in simulations to meet this challenge by combining accurate, but computationally demanding, models with less detailed ones. Multiscale modelling can be done in a sequential manner or in a simultaneous fashion. In the sequential or hierarchical multiscale approach, information from an accurate and high-detail model is used in a second stage by a reduced model that can deal with longer and larger simulations, or vice versa. Instead, in the simultaneous multiscale approach, for example in adaptive multiscale molecular dynamics, the system is partitioned into different regions that are modelled at different resolutions in the same simulation. In this chapter, we focus on this second multiscale approach. In particular, we investigate whether it is possible to construct a Hamiltonian multiscale molecular dynamics with open boundaries. Open boundaries here mean that molecules that diffuse between the different resolution regions can adapt their resolution on the fly. Such adaptivity is important when modelling extended soft matter systems for long time scales, in which case matter is continuously exchanged between the different resolution regions. In the last decade, a number of adaptive multiscale methods have been developed[1–4], however, none of these algorithms is without difficulties.

Previously we developed an adaptive multiscale molecular dynamics algorithm that allows us to model part of the system in atomistic (AA) detail, while treating the rest of the system with a coarse-grain (CG) model[3,5,6]. An intermediate "healing region" (HR) couples the atomistic region (AR) to the coarse-grain region (CGR) and allows particles

to transform in a smooth manner from one representation to the other when they diffuse across the region boundaries. Although this "healing region" approach allows in principle for simulations of large soft matter systems for extensive times scales, the details of the coupling in the HR may affect the structural and dynamical behaviour of the system, which should be investigated carefully.

In the AA/CG method, particles adapt continuously from one potential energy surface to the other, which generates heat due to the equilibration of particles to their new, more (or less) detailed environment. The algorithm requires thermostats to remove this heat, and is therefore by definition a non-equilibrium method. By bookkeeping the energy that particles gain or loose when they switch representation and by adding these bookkeeping terms to the potential and kinetic energy terms, we recover an auxiliary total energy that behaves as a conserved quantity. Although this conserved quantity is an important handle in our method to control the integration of the equations of motions, in particular to choose the time step and the size of the HR, this energy is not a physical observable. It is therefore not useful for the comparison of total energies or enthalpies of different configurations and furthermore the calculation of, for example, the heat capacity of the system is not trivial. Also, the non-equilibrium nature of this approach makes it more difficult to apply standard statistical mechanics concepts.

The equilibration and heat production that takes place in the HR is not just an effect of the continuous fluctuation of the number of degrees of freedom that is inherent to the hybrid AA/CG method. Indeed, introducing the atomistic positions and velocities into a CG particle requires a much higher level of equilibration than the reverse process, in which information is merely removed. However, also in a 1:1 mapping, in which the number of degrees of freedom is conserved between regions, the system will nevertheless heat up, unless thermostats are used that work as a heat sink. An example of a 1:1 mapping is found in the adaptive QM/MM method that couples a quantum chemical description (QM) to a molecular mechanics (MM) model using a classical forcefield[7,8].

Heyden *et al.* have developed an alternative hybrid AA/CG method starting from a linear combination of Lagrangians[4]. Here all possible Lagrangians are included that can be constructed by considering each particle in the HR to be either fully in one representation or fully in the other. The equations of motion that are derived from this approach do not only smoothly switch the potential energy terms on and off as particles transform their representation, but also control the kinetic energy terms by scaling the masses of the particles. Although this scheme is more involved, as it requires for example a special integrator that can deal with variable masses, it has the advantage that it is Hamiltonian and thus conserves the (physical) total energy of the system. But there is also a disadvantage. The forces derived from the scalable potential energy terms contain terms that are likely to create a gradient over the HR and effectively drive particles from one region to the other.

The spurious driving force in the HR may lead to artifacts in the dynamics and the structure of the molecular system, as was shown by Bulo *et al.* who applied this scheme to a hybrid simulation of liquid water[7]. In that work a spherical region ("AR") with a radius of 4 Å was centred on the oxygen of a central water molecule that was described by the flexible SPC forcefield. A 1 Å skin around this region was taken as the HR and the water molecules in the environment (CGR) outside this region was described with the flexible TIP3P forcefield. The radial distribution around the central water molecule showed dramatic errors due to the gradient in the HR. Interestingly, the expected radial distribu-

tion function, a mixture of the purely SPC and TIP3P ones, was recovered by adding the bookkeeping terms to the potential energy.

The artifacts seen in the pair-correlation are due to the different chemical potentials of the coarse-grained and the fine-grained representations of the system, which induces a potential gradient over the HR that causes a flux of particles as well as spurious density fluctuations. In an instantaneous configuration, a particle may feel a spurious HR gradient for three different reasons: (1) the extra degrees of freedom of the fine-grain representation can contribute to an "internal" chemical potential that is missing in the CG representation, (2) there may be a mismatch in the chemical potential of the two representations because they were not optimized to represent the same thermodynamic state point, or (3) the particle is in a low-potential energy state in one representation, but has a high potential energy in the other representation. Careful tuning of the fine-grain and coarse-grain models to match their chemical potentials may minimize the occurrence of a potential gradient in the HR in the first two cases. The third case however may be unavoidable in a scheme in which atomistic degrees of freedom enter on one side of the HR with, on average, a high potential energy, and leave on the other side with a much lower energy. Poblete *et al.* observed, in simulations with their hybrid AdResS method, density fluctuations in the HR, which they attributed to variations in the chemical potential as a function of the switching in the HR[9].

In this chapter, we investigate an alternative scheme to circumvent the difficulties that appear due to differences in the chemical potential of two coupled representations, starting from a Lagrangian approach. Using Lagrange multipliers we can add holonomic constraints that fix the total number of particles in each region. By adding these extra terms to the Lagrangian we can in principle counteract a potential gradient that may exist in the HR while the undetermined Lagrange multipliers provide a direct measure of the chemical potential difference. We compare this approach to our previous non-Hamiltonian AA/CG algorithm.

The remainder of this chapter is organized as follows. We first describe the mathematical details of the methods, starting with the non-Hamiltonian AA/CG scheme followed by the Lagrangian AA/CG scheme. We then apply the method to a number of illustrative examples to explore the strengths and weaknesses of the two methods.

2 Theoretical Framework

We will compare two different approaches to construct a hybrid AA/CG molecular dynamics method: our previously developed non-conservative AA/CG scheme and a new Lagrangian scheme. Prerequisite to either one is a mapping between the coarse-grained and the fine-grained (atomistic) representations of the entire system and a partitioning of the system into AA and CG regions. We can choose for example a spherical atomistic region of a certain radius fixed in space, as illustrated in Fig. 1. But the AR can also be centred on a particular molecule and have a different shape. All particles are attributed a weight $s(\mathbf{r}) \in [0, 1]$ that sets their resolution. In the CGR $s(\mathbf{r})$ equals zero, in the AR $s(\mathbf{r})$ is one, and in the HR this weight function switches smoothly from zero to one. The weights are used to scale the pair-interactions between particles, as we will describe later.

In the following, we first describe the non-Hamiltonian AA/CG scheme, in which we point out that this algorithm does not conserve the total energy, but that, through the use of bookkeeping terms, we can recover a conserved quantity that we refer to as "auxiliary

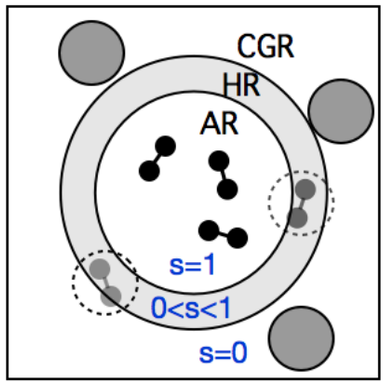

Figure 1. Schematic hybrid AA/CG setup showing the atomistic region (AR), the coarse-grain region (CGR) and the intermediate healing region (HR). All particles are attributed a scalar s that sets their AA/CG resolution.

total energy". We also show that in this case the forces on the particles only contain the scaled pair-wise interactions. A more detailed description is found in Refs. 3, 5, 6, 10. In the second part, our Lagrangian scheme is presented. This second scheme conserves total energy – at least in the case of a 1:1 mapping – and does not contain bookkeeping terms. The forces on the particles acquire additional terms due to the gradient of the scaling $s(\mathbf{r})$ in the HR, which we counteract using a constraint.

2.1 Non-Conservative AA/CG Scheme with Bookkeeping

The non-conservative AA/CG couples an atomistic description of the system with a coarse-grained one, by taking the interactions as a mixture of the atomistic and CG pair-potentials, Φ^{A} and Φ^{CG} respectively, as follows:

$$V = \sum_{\alpha\beta} \left((1-\lambda_{\alpha\beta})\Phi^{\mathrm{CG}}_{\alpha\beta} + \lambda_{\alpha\beta} \sum_{\substack{i\in\alpha \\ j\in\beta}} \Phi^{\mathrm{A}}_{ij} \right) + \sum_{\alpha} \sum_{i,j\in\alpha} \Phi^{\mathrm{A}}_{ij} + \Delta U^{\mathrm{A/CG}} + \Delta U^{\mathrm{intraCG}} \,. \tag{1}$$

Here, i and j refer to the atoms that are grouped into CG particles α and β. The scaling factors, $\lambda \in [0,1]$, depend on the CG particle positions and switch the interactions that span different CG groups. Previously, we have taken λ to be equal to the minimum weight, s, of the interacting particles[a] (Eq. 2). An alternative choice is using Eq. 3, in which λ is

[a] Actually, we used the maximum of s, but with $s = 0$ in the AR and $s = 1$ in the CGR.

the product of the weights. The latter is used in the AdResS method of Praprotnik *et al.*[2]:

$$\lambda_{\alpha\beta} = \min[s(\mathbf{r}_\alpha), s(\mathbf{r}_\alpha)]\,, \tag{2}$$

$$\lambda_{\alpha\beta} = s(\mathbf{r}_\alpha) \cdot s(\mathbf{r}_\beta)\,. \tag{3}$$

The third term in Eq. 1 describes the atomistic structure inside the CG groups, which are not scaled in the HR, but rather are frozen instantly when particles enter the CGR. The last two terms are the bookkeeping terms that account for the instantaneous potential energy differences that are manifested between the AA and CG descriptions of the particles that transform in the HR. The first, $\Delta U^{\mathrm{A/CG}}$, bookkeeps the gradual change in the potentials of all CG groups α that are in the HR, by summing over all other groups β as follows,

$$\Delta U^{\mathrm{A/CG}}(t) = \sum_{\alpha\in\mathrm{HR}} \int dt \sum_{\beta\neq\alpha} \frac{\partial \lambda_{\alpha\beta}}{\partial \mathbf{r}} \left(\Phi^{\mathrm{CG}}_{\alpha\beta} - \sum_{\substack{i\in\alpha \\ j\in\beta}} \Phi^{\mathrm{A}}_{ij} \right)\,. \tag{4}$$

Here, we explicitly write the time-dependence as $\Delta U^{\mathrm{A/CG}}(t)$ to point out that the bookkeeping energy is a history-dependent term that is not only a function of the current configuration. The second bookkeeping term, $\Delta U^{\mathrm{intraCG}}$, accounts for the atomic potential energy inside the CG groups, which is computed for all particles in the CGR *a priori* and is subtracted when a particle enters the HR, or, when it enters the CGR, it is recomputed and added:

$$\Delta U^{\mathrm{intraCG}} = \sum_{\alpha} \Theta(s_\alpha) \sum_{i,j\in\alpha} \tilde{\Phi}^{\mathrm{A}}_{ij}. \tag{5}$$

Here, $\Theta(s_\alpha)$ is the Heaviside step function that is equal to one for particles in the CGR and zero otherwise. The tilde indicates that the atomistic potential, $\tilde{\Phi}^{\mathrm{A}}_{ij}$, is evaluated at the moment that particle α crosses the HR/CGR boundary.

In the AR and HR, it is the atoms that are propagated, while their CG counterpart positions are simply updated by taking the centres of mass of the atoms belonging to the CG particle:

$$\mathbf{r}_\alpha = \frac{\sum_{i\in\alpha} m_i \mathbf{r}_i}{\sum_{i\in\alpha} m_i}\,. \tag{6}$$

Instead, in the CG region the CG particles are evolved, while the atomic positions are frozen and stored relative to their centres of mass. The kinetic energy is computed as the sum of the atomic and CG kinetic energies plus a third bookkeeping term that, analogously to $\Delta U^{\mathrm{intraCG}}$, stores or releases the kinetic energy difference between the two representations when the atoms are frozen or released when they cross the HR/CGR boundary:

$$T = \sum_{i\in\mathrm{AR,HR}} m_i \tilde{\mathbf{v}}_i^2 + \sum_{\alpha\in\mathrm{CGR}} m_\alpha \tilde{\mathbf{v}}_\alpha^2 + \Delta T^{\mathrm{A/CG}}\,, \tag{7}$$

$$\Delta T^{\mathrm{A/CG}} = \sum_{\alpha} \Theta(s_\alpha) \frac{1}{2} \left(m_\alpha \tilde{\mathbf{v}}_\alpha^2 - \sum_{i\in\alpha} m_i \tilde{\mathbf{v}}_i^2 \right)\,. \tag{8}$$

To maintain a constant temperature and to remove heat that is produced when particles are introduced and equilibrated in the HR, all particles are coupled to a thermostat. The sum of the above potential and kinetic energy terms, including the bookkeeping terms and the

energy terms of the thermostats adds up to an auxiliary total energy that is a conserved quantity.

Previously, we showed that a hybrid AA/CG simulation of molecules that are described by two or more bonded CG particles (e.g. hexane) requires that in the CGR the frozen groups of atoms associated with each CG particle maintain reasonable orientations with respect to the rest of the molecule[5,10]. Without preconditioning their orientation, the atom groups cannot be smoothly introduced when a CG particles leaves the CGR, even if the HR is extremely wide. However in this article we will only consider a simple model system of toy molecules that are each represented by a single CG particle, so that here we can omit the preconditioning of the atomic orientation.

The forces on the particles are derived from the scaled potentials (see Eq. 1), including the bookkeeping term:

$$\begin{aligned}\mathbf{f}_i = \sum_\beta \Bigg(& (1-\lambda_{\alpha\beta}) \frac{\partial \Phi^{\mathrm{CG}}_{\alpha\beta}}{\partial \mathbf{r}_\alpha} \frac{\partial \mathbf{r}_\alpha}{\partial \mathbf{r}_i} - \frac{\partial \lambda_{\alpha\beta}}{\partial \mathbf{r}_\alpha} \frac{\partial \mathbf{r}_\alpha}{\partial \mathbf{r}_i} \Phi^{\mathrm{CG}}_{\alpha\beta} \\ & + \sum_{j\in\beta} \left(\lambda_{\alpha\beta} \frac{\partial \Phi^{\mathrm{A}}_{ij}}{\partial \mathbf{r}_i} + \frac{\partial \lambda_{\alpha\beta}}{\partial \mathbf{r}_\alpha} \frac{\partial \mathbf{r}_\alpha}{\partial \mathbf{r}_i} \Phi^{\mathrm{A}}_{ij} \right) \Bigg) \\ & + \sum_{j\in\alpha} \frac{\partial \Phi^{\mathrm{A}}_{ij}}{\partial \mathbf{r}_i} + \frac{\partial \Delta U^{\mathrm{AA/CG}}}{\partial \mathbf{r}_i} + \frac{\partial \Delta U^{\mathrm{intraCG}}}{\partial \mathbf{r}_i} \end{aligned} \tag{9}$$

$$= \sum_\beta \left((1-\lambda_{\alpha\beta}) \frac{\partial \Phi^{\mathrm{CG}}_{\alpha\beta}}{\partial \mathbf{r}_\alpha} \frac{\partial \mathbf{r}_\alpha}{\partial \mathbf{r}_i} + \sum_{j\in\beta} \lambda_{\alpha\beta} \frac{\partial \Phi^{\mathrm{A}}_{ij}}{\partial \mathbf{r}_i} \right) + \sum_{j\in\alpha} \frac{\partial \Phi^{\mathrm{A}}_{ij}}{\partial \mathbf{r}_i}. \tag{10}$$

On the first line, we explicitly write the four terms that arise when we apply the product rule to take the derivative of the scaled CG pair-potentials and the atomistic pair-potentials in Eq. 1. Note that the derivative of the CG potential, Φ^{CG} is with respect to the position of the CG particle α that contains atom i, so that the atoms belonging to the CG particle feel the CG interaction working on their centre of mass, which is then multiplied with $\partial \mathbf{r}_\alpha / \partial \mathbf{r}_i$. The latter term is just weighting the CG force by the relative atom masses, as follows from taking the derivative of Eq. 6. It should also be noted that the first and third terms are the usual thermodynamic forces scaled by λ, whereas the second and fourth terms arise from taking the derivative of λ and thus yield forces due to a change in the scaling factor. Although these second and fourth terms have opposite sign, they will in practice not cancel exactly and therefore may create a potential gradient in the HR. However, in our scheme, taking the derivative of the first bookkeeping term, $\Delta U^{\mathrm{AA/CG}}$, yields exactly the same terms with the opposite signs, so that there is no potential gradient in the HR[6,10]. The derivative of the second bookkeeping term, $\Delta U^{\mathrm{intraCG}}$, is zero. As a result, the forces on the particles only contain the scaled forces due to the pair interactions and the atomistic (non-scaled) interactions of atoms that belong to the same CG group.

2.2 Lagrangian AA/CG Scheme Using a Number Constraint

To construct a conservative multiscale molecular modelling scheme, we start from a Lagrangian

$$L = T - V + \Lambda(f(\mathbf{r}_\alpha^N) - \tilde{N}^{\mathrm{AA}}), \tag{11}$$

which is the usual difference of the kinetic energy, T, and the potential energy, V, but with an added constraint on the number of particles in the system that find themselves in the atomistic resolution region, $\tilde{N}^{\mathrm{AA}}$. Here, Λ is the undetermined Lagrange multiplier and $f(\mathbf{r}_\alpha^N)$ is a function of all the particle positions that quantifies how many of them are represented in atomistic resolution. We take for this function the sum of weights attributed to all CG groups of atoms,

$$f = \sum_\alpha s(\mathbf{r}_\alpha), \tag{12}$$

where each individual weight s equals one in the AR, zero in the CGR, and smoothly switches from one to zero in the HR, as was described above.

T is simply the sum of the kinetic energy of the atoms in the AR plus HR and the kinetic energy of the CG particles in the CGR,

$$T = \sum_{i \in \mathrm{AR,HR}} m_i \tilde{\mathbf{v}}_i^2 + \sum_{\alpha \in \mathrm{CGR}} m_\alpha \tilde{\mathbf{v}}_\alpha^2. \tag{13}$$

The potential energy similarly to the non-conserving scheme above is taken as the mixed pair-potentials between particles that belong to different CG groups and the atomistic interactions within the CG groups,

$$V = \sum_{\alpha\beta} \left((1 - \lambda_{\alpha\beta}) \Phi_{\alpha\beta}^{\mathrm{CG}} + \lambda_{\alpha\beta} \sum_{\substack{i \in \alpha \\ j \in \beta}} \Phi_{ij}^{\mathrm{A}} \right) + \sum_\alpha \sum_{i,j \in \alpha} \Phi_{ij}^{\mathrm{A}} + \frac{1}{2} k (\sum_\alpha s(\mathbf{r}_\alpha) - \tilde{N}^{\mathrm{AA}})^2, \tag{14}$$

but now without any bookkeeping terms, and instead with an extra term due to the particle number constraint. For the latter, we have inserted Eq. 12, and we have replaced the holonomic constraint, which requires an iterative procedure such as SHAKE by a harmonic restraint on the number of AA particles in the system. For a large enough value of the force constant, k, this restraint will also confine the number of particles in the AR plus HR to the target value $\tilde{N}^{\mathrm{AA}}$. This automatically sets the number of particles in the CGR as the total number of particles counted as CG groups that can be in either representation is constant:

$$N_\alpha = N_\alpha^{\mathrm{AA}} + N_\alpha^{\mathrm{CG}}. \tag{15}$$

The forces on the particles are again derived from the potential energy (Eq. 14). In this case, not having the bookkeeping terms, the forces contain both the scaled thermodynamic forces as well as the contributions from the changing scaling factor:

$$\mathbf{f}_i = \sum_\beta \Bigg((1-\lambda_{\alpha\beta}) \frac{\partial \Phi^{\mathrm{CG}}_{\alpha\beta}}{\partial \mathbf{r}_\alpha} \frac{\partial \mathbf{r}_\alpha}{\partial \mathbf{r}_i} - \frac{\partial \lambda_{\alpha\beta}}{\partial \mathbf{r}_\alpha} \frac{\partial \mathbf{r}_\alpha}{\partial \mathbf{r}_i} \Phi^{\mathrm{CG}}_{\alpha\beta} + \sum_{j\in\beta} \left(\lambda_{\alpha\beta} \frac{\partial \Phi^{\mathrm{A}}_{ij}}{\partial \mathbf{r}_i} + \frac{\partial \lambda_{\alpha\beta}}{\partial \mathbf{r}_\alpha} \frac{\partial \mathbf{r}_\alpha}{\partial \mathbf{r}_i} \Phi^{\mathrm{A}}_{ij} \right) \Bigg) + \sum_{j\in\alpha} \frac{\partial \Phi^{\mathrm{A}}_{ij}}{\partial \mathbf{r}_i} + k \sum_\alpha (s(\mathbf{r}_\alpha) - \tilde{N}^{\mathrm{AA}}) \frac{ds}{d\mathbf{r}_\alpha} \frac{\partial \mathbf{r}_\alpha}{\partial \mathbf{r}_i}. \tag{16}$$

3 Model Setup

To compare the properties of the non-conservative AA/CG method and the Lagrangian scheme, we apply both methods to three illustrative model systems of toy molecules that move in a two dimensional space. The molecules consist in the "atomistic representation" of two atoms with a mass of 10 amu that are connected by a harmonic bond potential, in a square box with a length of $L = 10$ Å and with periodic boundary conditions. Taking the origin at the centre of the box, the AR is a rectangular strip defined as $|x| < 3$, flanked on both sides by a HR at $3 < |x| < 4$ and a CGR at $4 < |x|$. The switching function of the particle weight is taken as

$$s = \begin{cases} 1 & \text{if } x < |3| \\ 3(4-|x|)^2 - 2(4-|x|)^3 & \text{if } 3 \le |x| \le 4. \\ 0 & \text{if } x > |4| \end{cases} \tag{17}$$

We first consider a single diatomic molecule in a 1:1 mapping that moves through the different regions. The diatomic molecule is initially placed at the centre of the box in the AR, in a slightly tilted orientation with respect to the y-axis, with positions $\mathbf{r}_1 = (1.050, 0.0025)$ and $\mathbf{r}_2 = (-1.050, -0.0025)$. Both atoms are assigned a velocity of $\mathbf{v}_1 = (0.0000, 0.0025)$ Å/fs, so that the molecule moves towards the HR without rotating. The molecule vibrates due to a harmonic spring potential, which has an equilibrium bond length of 2.0 Å and a force constant of $k^{\mathrm{AA}}_{\mathrm{bond}} = 200$ kJ/mol/Å^2. In the CG representation, the molecule also contains two atoms with a spring, but the force constant is reduced by a factor of five to $k^{\mathrm{CG}}_{\mathrm{bond}} = 40$ kJ/mol/Å^2.

Secondly, we model two such molecules in the simulation unit cell. We add a non-bonded Lennard-Jones interaction, which acts between particles that are not bonded to each other. The Lennard-Jones interaction is identical in all regions, with $\epsilon = 0.1$ kJ/mol and $\sigma = 1.5$ Å. We also performed additional simulations with a Langevin thermostat[11] coupled to each particle, which has a target temperature of 30 K and a friction coefficient of 1 fs^{-1}.

The third case considers five molecules with a 2:1 mapping. Specifically, molecules interact with each other as diatomics (two interaction sites) in the AR and point particles (one interaction site) in the CGR. All such nonbonded interactions are Lennard-Jones in nature with $\epsilon = 0.1$ kJ/mol and $\sigma = 2.5$ Å. The harmonic bond force constant is 100 kJ/mol/Å^2 and the equilibrium bond length is 0.25 Å (so that the two AR beads are almost on top of one another). The CG (single) interaction site is taken as the centre of mass of the two

atoms. For simplicity, we do not actually replace the atoms by a CG particle, but instead propagate in all regions the atoms coupled by the harmonic bond potential, so that the number of degrees of freedom remains constant (see also the remarks in Sec. 6). The AR beads have a mass of 10 amu. The Langevin thermostat has a target temperature of 50 K and a friction coefficient of 0.03 fs^{-1}. When used, the harmonic restraint on the number of AR particles in the system is chosen as either $k_{\mathrm{low}} = 1$ kJ/mol or $k_{\mathrm{high}} = 5$ kJ/mol. The constraint number is taken as 3.5, which is simply the total number of particles multiplied by the volume fraction of the AR (including half the HR volume fraction). The minimum weight formula is used to compute λ. The square unit cell and region definitions are unchanged from the 1:1 mapping systems.

4 One Diatomic Molecule in a 1:1 Mapping

We compare the Lagrangian AA/CG scheme with the non-conservative algorithm for a single harmonic oscillator whose bond force constant changes value between regions. Also, for both methods we compare the two different ways of computing the potential scaling factor, either as the product of the particle weights (Eq. 3), or as the minimum of the particle weights (Eq. 2). The results of these four simulations are illustrated in Fig. 2 and Fig. 3.

Fig. 2 shows the velocity in the x-direction of one of the particles, during the first 2 ps of simulation. As long as the molecule travels through the AR, all four simulations show the same behaviour of the vibrating diatomic. In the non-conservative simulations (red lines), the vibration slows down in the HR, maintains a lower frequency in the CGR and then increases again the frequency in the next HR to its original frequency in the AR

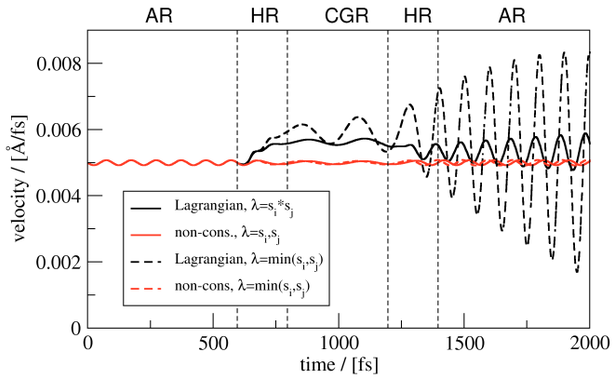

Figure 2. x-component of the velocity of particle 1 shown for a diatomic molecule (see inset) that moves in the x-direction, starting in the AR. Due to the tilt angle, particle 1 arrives first in the HR, which induces in the Lagrangian case a rotation when the molecule transforms into the CG representation.

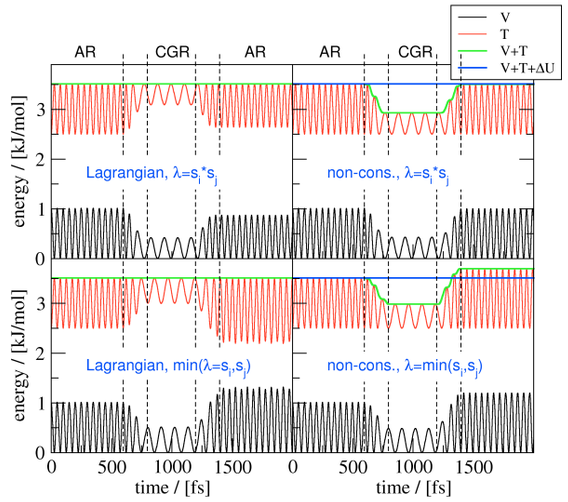

Figure 3. Energy components as a function of time for the diatomic molecule using the Lagrangian method (left panels) and the non-conservative method (right panels).

(of course, the amplitude is much larger in the y-component of the velocity). The two simulations using the Lagrangian scheme show a markedly different behaviour. In both cases, the molecule accelerates in the x-direction and it starts to rotate while it travels through the HR. The acceleration is rather similar for both scaling factor formulas, shown in Fig. 2 by an increase of the black line shortly after entering the HR. The rotation of the molecule is seen by the increased fluctuations in the x-velocity of the particle, which is more significant when using the minimum s-value.

Fig. 3 shows for the four simulations the potential energy (black line) and the kinetic energy (red line). The green line shows the sum of V and T, which is perfectly constant in the Lagrangian AA/CG simulations (left panels), but not in the non-conservative scheme (right). However, in the latter the auxiliary total energy, which includes the bookkeeping term (Eq. 4) is conserved, as shown by the blue line.

A remarkable difference between the Lagrangian and non-conservative schemes is seen by comparing the kinetic energy (red line) in the top panels. Whereas in the non-conservative scheme the average kinetic energy goes down with the potential energy in the CGR, instead in the Lagrangian scheme the average kinetic energy goes up. In the latter case, increased kinetic energy counterbalances the decreased potential energy, so that the total energy remains constant. The kinetic energy increase is due to the added translational and rotational motion that the molecule gains from the potential gradient in the HR. This gradient is absent in the non-conservative scheme.

The differences between the different formulas for computing the potential scaling factor are small. Taking the product of the particle weights results in faster switching so that in a sense the effect of the HR region is compressed to a shorter width. On the other hand, in the Lagrangian scheme, in which the gradients of λ take part in the forces (Eq. 10), using the minimum weight seems to strongly affect the dynamics in the HR, resulting in a fast-rotating molecule compared to using the product of weights.

Summarizing, we have seen that the Lagrangian AA/CG scheme conserves the total energy, whereas the non-conservative scheme only conserves an auxiliary total energy. However, in the Lagrangian scheme there is a potential gradient in the HR, which affects the dynamics of the molecule, by inducing rotational and translational acceleration.

5 Two Diatomic Molecules in a 1:1 Mapping

Adding one more molecule to the simulation unit cell, which also adds non-bonded forces to the system, displays an energy behaviour as summarized in Fig. 4. As expected, the Lagrangian treatment conserves energy and does not require a thermostat. Conversely, the non-conservative treatment heats up without the use of a thermostat. Even though the auxiliary total energy is conserved, the beads move faster and faster until the integration time step is no longer appropriate to adequately describe the dynamics. Use of a thermostat stabilizes the system and, once the energy provided by the thermostat is accounted for, the bookkeeping energy contribution is seen to be very small – it is the difference between the red and black curves in Fig. 4.

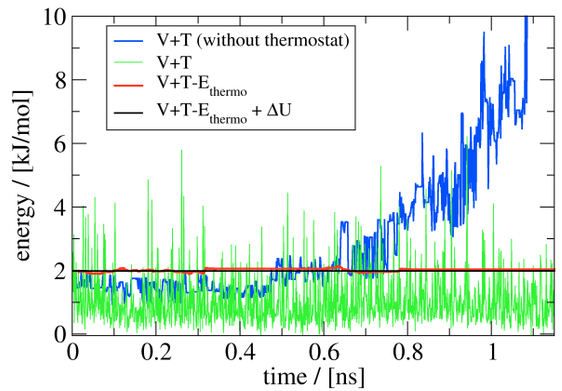

Figure 4. Energy behaviour of the two molecule 1:1 mapping system. In the non-conservative case, a thermostat must be used, otherwise the system energy (not including the bookkeeping terms) grows as shown in blue. Use of a thermostat stabilizes the system energy (shown in green) which is seen to have small fluctuations once the energy from the thermostat is accounted for (shown in red). Finally, including the bookkeeping energy contribution results in a conserved quantity (shown in black) which is identical to the energy of the Lagrangian case.

6 Mapping Several Atoms in a CG Particle

Sofar, we have mapped each atom to a single CG particle, in which case the Lagrangian scheme is energy conserving, while the non-conservative scheme heats up unless a thermostat is used. The above examples are illustrative for an adaptive hybrid quantum/classical (QM/MM) method. To move to an actual mixed AA/CG method, we have to go beyond the 1:1 mapping.

Let us consider for a moment the 2:1 mapping case of a single diatomic molecule that is replaced in the CGR by a single interaction site. Clearly, in our scheme in which the atomistic bond potential is instantaneously frozen and removed when it enters the CGR, the energy cannot be conserved (without bookkeeping). This is why instead in the Lagrangian scheme of Heyden *et al.* the atomistic intra-CG particle interactions are scaled in the HR analogous to the inter-CG particle interactions. However, to avoid that the atomistic molecules disintegrate when their atomistic intra-CG particle interactions are smoothly switched off, they also scale the atom masses, and thus the kinetic energy, smoothly to zero[4]. To keep things simple in our examples, we therefore do not actually freeze and replace the atoms by CG particles, but maintain the atoms throughout the entire system. However, these atoms, in the CGR, do not participate in nonbonded interactions. The nonbonded interactions are evaluated using the centre of mass of the atom group, in other words from the CG bead location. Then, the resulting force experienced by the CG bead is distributed over the atoms in a mass-weighted manner. In this way the number of particles in the system never changes. We nonetheless use the term "2:1 mapping" to denote the change in the inter-CG bead interactions.

Although this implementation of the Lagrangian scheme is thus significantly simplified, for the 2:1 mapping case the total energy is no longer conserved. In other words, the "Lagrangian scheme" is not actually Lagrangian when going beyond the 1:1 mapping example.

7 Five Molecules in a 2:1 Mapping

For the 2:1 mapping system a thermostat must be used in both the Lagrangian and the non-conservative treatments in order to stabilize the system. Thus one of the appealing features of the Lagrangian treatment in the 1:1 mapping case is lost – namely energy is no longer conserved.

Surprisingly, the thermostat removes orders of magnitude more energy in the Lagrangian case compared to the non-conservative case (see Fig. 5). Although this observation needs to be explored more thoroughly, we can speculate, by going back to Fig. 2 of the 1:1 mapping case, that the λ-derivative terms increase the particle velocities. Moreover, the λ-derivative terms contain unscaled atomistic potential energies; when a particle is near the CGR these energies may be very high.

8 Using a Harmonic Constraint on the Number of Particles

Another drawback of including the λ-derivative forces in the Lagrangian treatment is that they can drive molecules to enter or leave the CGR for unphysical reasons. The term "unphysical" is used here because the behaviour of the system should not depend on how it

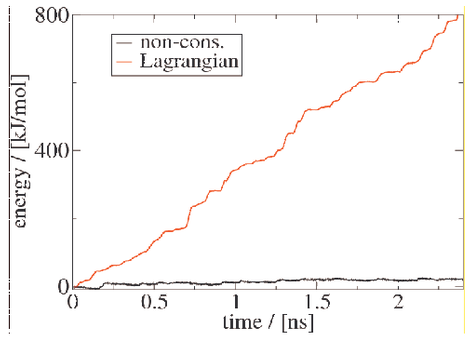

Figure 5. Energy removed by the thermostat in the 2-1 mapping system.

is represented. This behaviour is clearly seen in Fig. 6, where the Lagrangian description leads to an artificially high density of molecules in the CGR. This is not surprising because we chose all beads (regardless of representation) to experience the same Lennard-Jones pair interaction, yet there are twice as many beads present in the AA representation. Thus the AA and CG force fields are clearly (and deliberately) mismatched. Nonetheless, it would be appealing to have a methodology in which this mismatch does not deplete

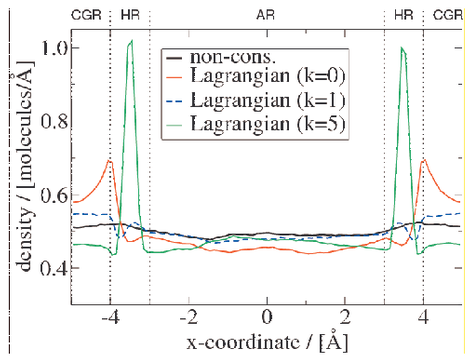

Figure 6. Density of molecules as a function of their x-coordinate for the 2-1 mapping system. The density is uniform throughout the unit cell in the non-conservative case. For the Lagrangian treatment without a restraint on the number of AA particles in the system, the AR is depleted of molecules and the CGR has more molecules in it as compared to the non-conservative case. Adding a stiff harmonic number constraint (k=5 kJ/mol) causes the number of molecules in the HR to double. Using a weaker constraint (k=1 kJ/mol) yields a density closest to the non-conservative case, although density artifacts are evident in the HR.

one region of molecules. The non-conservative algorithm does this, and of course for the Lagrangian case we have not yet considered the harmonic constraint on the number of particles in the AR that is specifically designed to overcome the undesirable λ-derivative density mismatch. The constraint number is taken as the total number of particles multiplied by the volume fraction of the AR to target a uniform system density. Unfortunately, when used with a large harmonic force constant of $k_{\mathrm{high}} = 5$ kJ/mol, the HR is found to have a density about twice that of the AR and CGR (see Fig. 6). This could be an artifact of having so few molecules in the system – on average there is less than one molecule in the HR. A larger system in which there are significant numbers of molecules in the HR should be explored. Using a small harmonic force constant of $k_{\mathrm{low}} = 1$ kJ/mol yields a density closest to the non-conservative case, although the HR still displays density artifacts.

9 Conclusion

We have compared two approaches to construct an adaptive hybrid atomistic/coarse-grain molecular dynamics method. The first approach was our previously developed multiscale algorithm based on mixed atomistic and coarse-grain pair-potentials and an intermediate healing region that allows particles to smoothly adapt their resolution when they diffuse between the atomistic and CG regions. This algorithm is non-conservative, but by bookkeeping the energy change each time that a molecule adapts its resolution, we recover an auxiliary total energy that is conserved. The bookkeeping terms also remove unphysical forces that can drive particles from one region to the other in the HR. The second hybrid AA/CG approach that we discussed was a new Lagrangian scheme that includes a restraint on the number of particles that are fine-grained and coarse-grained. This restraint was added to counteract the unphysical forces in the HR that are expected to be present, as here no bookkeeping terms are included. An advantage of the Lagrangian approach could be that the dynamics of the particles is Hamiltonian and that the total energy is conserved – at least in the case of a 1:1 mapping. We applied both schemes to three illustrative model systems to explore the features of the two different approaches.

The first application, a single diatomic molecule moving through the atomistic, healing and coarse-grained regions, showed that indeed in the Lagrangian scheme the total energy is perfectly conserved in the case of 1:1 mapping (one atom is mapped onto one CG particle), whereas in the non-conservative scheme only the auxiliary total energy (*i.e.* total energy plus bookkeeping terms) is conserved. However, in the Lagrangian case the unphysical forces induce a translational and rotational acceleration of the molecule in the HR. In the non-conservative scheme, these unphysical forces are not present.

Secondly, we consider two 1:1 diatomics in the system. The non-conservative simulation shows an increase of the temperature, unless thermostats are used to remove the heat. Instead, the Lagrangian scheme shows no heating up.

In the third application, the diatomic molecule is represented by a single particle in the CG resolution. In this 2:1 mapping, also the Lagrangian scheme does not conserve the total energy and a heat-up of the system is observed. Interestingly, the energy flux from the system to the thermostat is much larger in the Lagrangian scheme than in the non-conservative scheme. With five molecules in the system, the non-conservative simulation shows a rather flat density of molecules in the different regions of the system. Instead, in the Lagrangian scheme, the (deliberate) mismatch between the atomistic and CG force-

fields leads to strong unphysical forces in the HR that drive particles from the AR to the CGR and results in rather different particle densities between the regions. When we employ the restraint on the number of particles that find themselves in atomistic resolution, the large density variation between the regions can be significantly reduced, although a too stiff restraint leads to artifacts in the density in the intermediate healing region.

The comparison of the two adaptive AA/CG approaches is very insightful to understand the complexity involved when coupling a fine-grained and a coarse-grained model with open boundaries. The Lagrangian scheme with the particle restraint appears a promising route to address chemical potential differences between representations, although more work is needed to extend the method beyond the 1:1 mapping. The non-conservative AA/CG scheme couples the different resolutions in a robust manner, while avoiding unphysical forces and maintaining a conserved auxiliary total energy. Further elaboration of the strengths and weaknesses of these two approaches will allow us to address these difficult issues in a simplified and insightful manner.

Acknowledgements

BE acknowledges financial support through an NWO-CW VIDI grant. SON thanks the University of Amsterdam and the Amsterdam Center for Multiscale Modelling for support through a Computational Science visiting professorship.

References

1. C. Abrams, *Concurrent dual-resolution Monte Carlo simulation of liquid methane*, J. Chem. Phys., **123**, 234101, 2005.
2. M. Praprotnik, L. Delle Site, and K. Kremer, *Adaptive resolution molecular-dynamics simulation: Changing the degrees of freedom on the fly*, J. Chem. Phys., **123**, 224106, 2005.
3. B. Ensing, S. O. Nielsen, P. B. Moore, M. L. Klein, and M. Parrinello, *Energy conservation in adaptive hybrid atomistic/coarse-grain molecular dynamics*, J. Chem. Theory Comput., **3**, 1100–1105, 2007.
4. A. Heyden and D. G. Truhlar, *Conservative algorithm for an adaptive change of resolution in mixed atomistic/coarse-grained multiscale simulations*, J. Chem. Theory Comput., **4**, 217–221, 2008.
5. S. O. Nielsen, P. B. Moore, and B. Ensing, *Adaptive multiscale molecular dynamics of macromolecular fluids*, Phys. Rev. Lett., **105**, 237802, 2010.
6. S. O. Nielsen, R. E. Bulo, P. B. Moore, and B. Ensing, *Recent progress in multiscale molecular dynamics simulation of soft matter*, Phys. Chem. Chem. Phys., **12**, 12401–12412, 2010.
7. R. E. Bulo, B. Ensing, J. Sikkema, and L. Visscher, *Toward a Practical Method for Adaptive QM/MM Simulations*, J. Chem. Theory Comput., **5**, 2212–2221, 2009.
8. A. Heyden, H. Lin, and D. G. Truhlar, *Adaptive partitioning in combined quantum mechanical and molecular mechanical calculations of potential energy functions for multiscale simulations*, J. Phys. Chem. B, **111**, 2231–2241, 2007.
9. S. Poblete, M. Praprotnik, K. Kremer, and L. Delle Site, *Coupling different levels of resolution in molecular simulations*, J. Chem. Phys., **132**, 114101, 2010.

10. B. Ensing and S. O. Nielsen, *Multiscale molecular dynamics and the reverse mapping problem*, in: Trends in Computational Nanomechanics, T. Dumitrica, (Ed.), vol. 2 of *Challenges and Advances in Computational Chemistry and Physics*, pp. 25–59, Springer Netherlands. 2010.
11. G. Bussi and M. Parrinello, *Accurate sampling using Langevin dynamics*, Phys. Rev. E, **75**, 056707, 2007.

"Effective" Open Boundary Molecular Dynamics for Biologically Relevant Aqueous Mixtures

Debashish Mukherji and Kurt Kremer

Max-Planck Institut für Polymerforschung, Ackermannweg 10, 55128 Mainz, Germany
E-mail: {mukherji, kremer}@mpip-mainz.mpg.de

Coupling different level of resolutions within a unified molecular dynamics scheme seeks to attain large time and length scale while retaining the full chemical details only in the region of interest. One such multiscale technique is the adaptive resolution molecular dynamic scheme (AdResS). In AdResS, a high resolution all-atom region is coupled to a coarse-grained particle reservoir. Implementing the AdResS scheme for the (bio)macromolecular simulations is of particular importance where the full chemical details are only important within a few nanometers from the solvated protein. The remaining solvent molecules, that are present to maintain equilibrium with the bulk solution, can be represented by single site coarse-grained beads. The coupling leads to correct concentration fluctuations within the small all-atom region, making the all-atom region an "effective" open boundary system. We treat this small all-atom region within the framework of fluctuation theory of Kirkwood and Buff, derived for open systems. We will present examples where this open boundary approach is successfully used to calculate solvation free energies of aqueous mixtures.

1 Introduction

(Bio)macromolecular solvation in water is dictated by the presence of the small cosolvents within the hydration shell of the proteins[1–6]. While experiments often predict interesting physical properties of macromolecules in aqueous mixtures, that range from proteins[7,8] to polymers[9,10], the microscopic understanding to describes the structure, function and stability with respect to the specific interactions of macromolecules with cosolvents is lacking. Therefore, molecular simulations are of particular interest for the (bio)molecular simulations[11–20]. Furthermore, the numerical studies in the field are limited to the closed boundary schemes, which, however, suffer from severe system size effects[21–24]. More specifically, when the large scale conformational transitions are intimately linked to the large concentration fluctuations, the excess of cosolvents near a macromolecule lead to depletion elsewhere in a small sized closed boundary setup. This disturbs solvent equilibrium with the bulk solution. To a reasonable extent, this discrepancy can be overcome by choosing enormously large simulation domains[23–28]. However, attaining long time scales within large simulation domains are computationally too expensive, especially when studying the equilibrium conformational transitions of macromolecules that require full chemical details. The larger the solvated macromolecule the larger solvent box need to be chosen to maintain solvent equilibrium. Therefore, it is important to use an alternative simulation scheme that can capture local concentration fluctuations correctly within a computationally efficient framework. In this context, we have recently proposed an approach to simulate aqueous mixtures in an "effective" open boundary simulation scheme[24]. Our approach makes use of the previously developed Adaptive Resolution Scheme (AdResS)[29–33]. In AdResS, an high resolution region with full chemical details is coupled to a low resolution reservoir represented by single site coarse-grained particles. The particles can change their resolution,

on the fly, in full thermodynamic equilibrium. The AdResS method has been successfully implemented to study challenging molecular liquids and solvation properties[34–37]. Recently, we have shown that by coupling a small all-atom region, containing a small peptide (triglycine), to a much larger coarse-grained osmotic reservoir, the correct concentration fluctuations could be captured[24,28]. We treat the all-atom region within the framework of the fluctuation theory of Kirkwood and Buff[38], derived for the grand-canonical ensemble. In this book chapter, we present a brief overview of the "effective" open boundary approach and its application to calculate the solvation free energies of aqueous mixtures [a].

The remainder of the paper is organized as follows: In Sec. 2 we sketch the method where we give a brief summary of AdResS method together with KB theory of solutions. The results are presented in Sec. 3 and finally we give our conclusions in Sec. 4.

2 Methodology

2.1 The AdResS Scheme

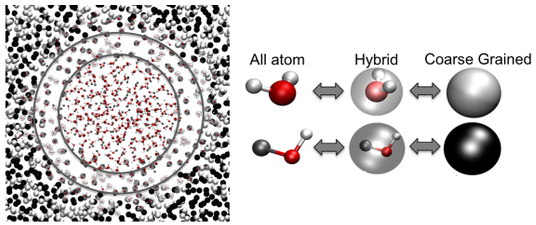

Figure 1. A typical AdResS simulation setup of a water methanol mixture at 50% mole fraction of methanol. The all-atom region of 2nm radius is coupled to a much larger coarse-grained reservoir. In between there is a hybrid region of width 1.3nm, allowing for the smooth transition between all-atom and coarse-grained representation of the molecules. The total linear dimension of the system is $\approx$ 10nm consisting of 20152 molecules. On the right panel, we show the mapping scheme. Coarse-grained methanol beads are rendered in black and silver is chosen for coarse-grained water. The CH_3 group of the methanol is treated as united atom represented by steel, the oxygen is rendered in red and the hydrogen in silver.

The Adaptive Resolution scheme[30,31], is a multi-scale approach that can couple a region of high resolution (e.g. all-atom) molecules and a region of low resolution (e.g. coarse-grained) reservoir. In between there is a "so called" hybrid region, where particles smoothly change their spacial resolutions from all-atom to coarse-grained and vice versa, allowing for free exchange of particles in full thermodynamic equilibrium[29]. This transition is governed by a weighting function $w(r) \in [0, 1]$. $w(r)$ is unity for the explicit system, zero for the coarse-grained, and smoothly varies between zero and unity in the hybrid region. In Fig. 1, we show a typical AdResS simulation setup of aqueous

[a]While this chapter predominantly deals with the solvation thermodynamics within AdResS setup, a more detailed description of AdResS method will be presented in the book chapter of this NIC series by Potestio and Kremer.

methanol mixture at 50% mole fraction of methanol. AdResS uses interpolated forces between molecules α and β,

$$\mathbf{F}_{\alpha\beta} = w(r_\alpha)w(r_\beta)\mathbf{F}^{\rm exp}_{\alpha\beta} + [1 - w(r_\alpha)w(r_\beta)]\,\mathbf{F}^{\rm cg}_{\alpha\beta}. \quad (1)$$

$\mathbf{F}_{\alpha\beta}$ is the total intermolecular force acting between two molecules and $\mathbf{F}^{\rm exp}_{\alpha\beta}$ is the sum of all high resolution pair-wise interactions between atoms of molecules α and β. $\mathbf{F}^{\rm cg}_{\alpha\beta} = -\bigtriangledown \mathrm{V}^{\rm cg}_{\alpha\beta}$ is the pair-wise coarse-grained force based on $\mathrm{V}^{\rm cg}_{\alpha\beta}$, the pairwise coarse-grained potential. r_α and r_β are the distances of the molecular centre-of-masses from the centre of the simulation domain.

The AdResS method using force interpolation has the limitation of not having an energy. However, the overall scheme can preserve the essential thermodynamics without the problem of energy conservation. An attempt for the possible coupling using potentials instead of forces would lead;

$$V_{\alpha\beta} = w(r_\alpha)w(r_\beta)V^{\rm exp}_{\alpha\beta} + [1 - w(r_\alpha)w(r_\beta)]\,V^{\rm cg}_{\alpha\beta}. \quad (2)$$

The calculation of pairwise force from the Eq. 2, would lead to a drift term that is related to the derivative of the interpolating function, $\bigtriangledown w(r)$. Thus the similar approach with the potential interpolation will lead to a series of problems whose solutions are not trivial[33,39,40].

2.2 Systematic Structural Coarse-Graining

An important ingredient of the AdResS setup is the description of the low resolution CG region. Here we represent the CG region by single site beads and the non-bonded interactions between these beads are derived from the iterative Boltzmann inversion (IBI) method[41], implemented in the VOTCA package[42]. The procedure starts from an initial guess for the potential using the radial distribution function $\mathrm{g}_{\rm target}(r)$ obtained from the all-atom simulation,

$$\mathrm{V}_0(r) = -k_{\rm B}T\ln\left[\mathrm{g}_{\rm target}(r)\right]. \quad (3)$$

Then the potential is updated over several iterations and the potential function after n^{th} iteration is given by,

$$\mathrm{V^{cg}}_n(r) = \mathrm{V^{cg}}_{n-1}(r) + k_{\rm B}T\ln\left[\frac{\mathrm{g}_{n-1}(r)}{\mathrm{g}_{\rm target}(r)}\right]. \quad (4)$$

After every iteration a 1ns long MD simulation is performed using the new potential and the new $\mathrm{g}_n(r)$ is calculated. This iterative procedure is followed till the obtained $\mathrm{g}(r)$ matches reasonably well with $\mathrm{g}_{\rm target}(r)$. This convergence criterion can be assessed by using the root-mean-squared deviations between the fitted and the target radial distribution functions $\triangle \mathrm{g}_n$[42],

$$\triangle \mathrm{g}^2_n = \int \left[\mathrm{g}_{\rm target}(r) - \mathrm{g}_n(r)\right]^2 dr. \quad (5)$$

We show the comparative $\mathrm{g}_n(r)$'s and $\triangle \mathrm{g}_n$ in the part (a) of Fig. 2. It can also be seen that even when $\triangle \mathrm{g}_n$ plateaus out for $n > 10$, there seems to be large noise in the structural equilibration. This noise can be attributed to the simultaneous potential updates of three

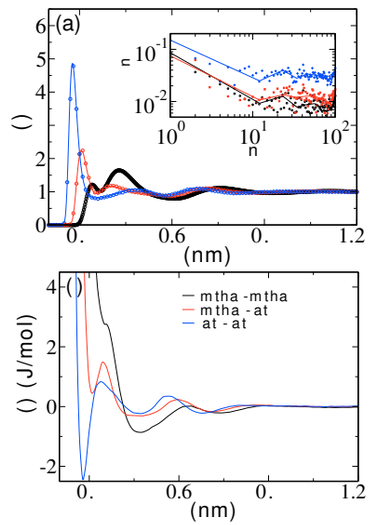

Figure 2. (a) The radial distribution functions $\mathrm{g}_{\mathrm{target}}(r)$ obtained from the all-atom target (symbols) and the fitted $\mathrm{g}(r)$ after iterative Boltzmann inversion (IBI). Inset shows the root-mean-squared deviation $\triangle \mathrm{g}_n$ between the fitted and the target $\mathrm{g}(r)$'s as a function of IBI iterations. (b)potential for methanol water mixture at a 50% methanol mole fraction. Data is shown for all three different pairwise interactions.

correlated pairs, where the update between a pair always re-adjusts the structure of other two pairs. However, we want to emphasize that the potentials obtained from this method reproduces the pairwise structure reasonably well and coupling of such single site CG system to an all-atom region does not alter the solvation properties within the chemically explicit region. In part (b) of Fig. 2, we show the best fitted pairwise non-bonded CG potentials between different components of a methanol water mixture at 50% methanol mole fraction. Note: because the structure based CG potential are non-transferable across concentrations, we derive CG potential for every concentration we study.

The potentials, as shown in Fig. 2, however, have a positive pressure, which is of the order of 6000 bars for pure water. This does not reflect the ambient thermodynamic conditions of the parent atomistic system. Therefore, a pressure correction can be employed using a linear function[41];

$$\Delta \mathrm{V}^{\mathrm{cg}}(r) = A_i \left(1 - \frac{r}{r_{\mathrm{cut}}}\right), \tag{6}$$

where the r_{cut} is the cut-off distance of the non-bonded interaction. A can be a constant or can be obtained from a virial expression for the pressure,

$$-\left[\frac{2\pi N\rho}{3r_{\mathrm{cut}}}\int_0^{r_{\mathrm{cut}}} r^3 \mathrm{g}_i(r)dr\right] A_i \approx \left(P_i - P_{\mathrm{target}}\right) V, \tag{7}$$

N is the number of particles, ρ the number density, V the volume of the system, P_i is the pressure in the i^{th} iteration and P_{target} is the pressure of the reference system[41]. This allows us to obtain a CG model, which has the structure and average pressure similar to that of the atomistic reference fluid. While the pressure correction works reasonably well, the correction leads to different compressibility in the CG system. Therefore, sometimes it is the matter of choice whether to have same pressure or same compressibility. However, we want to emphasize that the choice of the CG model does not affect the robustness of the AdResS method so long as the equilibrium between different regions is ensured. In our study, we do not use any pressure correction, rather the equilibrium is maintained using a thermodynamic force[29]. Use of thermodynamic force is of particular importance because it allows for the exchange of particles between different regions in full thermodynamic equilibrium. Additionally, because no pressure correction is employed, it also conserves compressibility in the all-atom and the CG region of the AdResS setup, which is important when studying the solvation properties of biological systems in aqueous mixtures. In the later sections, we will show, in detail, how the thermodynamic force allows us to maintain equilibrium within the simulation domain.

2.3 Fluctuation Theory: Kirkwood-Buff Integrals

Kirkwood-Buff (KB) theory, derived for the grand canonical ensemble, relates fluctuations in an open system to the integral of radial distribution functions $\mathrm{g}_{ij}(r)$ over the volume[38]. Thermodynamic quantities can be derived from the KB theory by making use of the "so-called" Kirkwood-Buff integrals (KBI)[22]. For the solution components i and j, these KBIs are defined as[38],

$$\begin{aligned} \mathrm{G}_{ij} &= V\left[\frac{\langle N_i N_j\rangle - \langle N_i\rangle\langle N_j\rangle}{\langle N_i\rangle\langle N_j\rangle} - \frac{\delta_{ij}}{\langle N_j\rangle}\right] \\ &= 4\pi\int_0^\infty \left[\mathrm{g}_{\mathrm{ij}}^{\mu\mathrm{VT}}(r) - 1\right] r^2 dr, \\ &\approx 4\pi\int_0^r \left[\mathrm{g}_{\mathrm{ij}}^{\mathrm{NVT}}(r') - 1\right] r'^2 dr', \end{aligned} \tag{8}$$

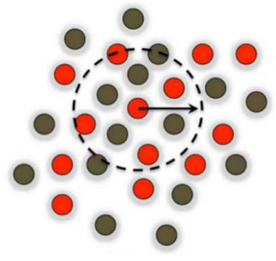

Figure 3. The Kirkwood-Buff integral can be interpreted as the change in the number of j molecules in a spherical region of radius r in the solution before and after placing a molecule i at the origin of that region.

where averages in the grand canonical ensemble are denoted by brackets $\langle\cdot\rangle$, V is the volume, N_i number of particles of species "i", δ_{ij} is the Kronecker delta, $\mathrm{g}_{ij}^{\mu\mathrm{VT}}(r)$ is the radial distribution function in the grand canonical (μVT) ensemble, $\mathrm{g}_{\mathrm{ij}}^{\mathrm{NVT}}(r)$ is the radial distribution function in the canonical (NVT) ensemble, and G_{ij}, the KBI, is a local quantity, which can be used as a measure of the affinity between solution components i and j. Physically, $\rho_j \mathrm{G}_{ij}$ can be interpreted as the change in the number of j molecules in a spherical region of radius r in the solution before and after placing a molecule i at the origin of that region (ρ_j is the number density of component j). A pictorial representation of the component affinity is shown in Fig. 3. In Eq. 8, we make the approximation $\mathrm{g}_{\mathrm{ij}}^{\mu\mathrm{VT}}(r) \approx \mathrm{g}_{\mathrm{ij}}^{\mathrm{NVT}}(r)$. For very big system this is nearly always safe as all ensembles are equivalent in the thermodynamic limit. In practice, however, the integration of $[\mathrm{g}_{\mathrm{ij}}(r) - 1]$ over the volume will hardly be feasible for systems with strong or long range fluctuations. In all cases the integration limit r in the last line of Eq. 8 must be chosen sufficiently large such that $G_{\mathrm{ij}}(r)$ converges to a plateau value or oscillates in a well controlled way around a mean value. The resulting average is well defined for very large NVT systems and for "effective" open boundary systems simulated with the AdResS scheme, as will be shown later. These plateau and/or average values also correspond to the particle fluctuations within the open boundary setup. A positive (or negative) value of G_{ij} refers to excess (or depletion) of component j around component i. In a binary system of cosolvent (c) and water (w), the link to the solvation free energy is given by[43],

$$\gamma_{\mathrm{cc}} = 1 + \left(\frac{\partial \ln \gamma_c}{\partial \ln \rho_c}\right)_{p,T} = \frac{1}{1 + \rho_c \left(\mathrm{G}_{cc} - \mathrm{G}_{cw}\right)}, \tag{9}$$

where γ_{c} is the molar cosolvent activity coefficient and $k_B T \ln \gamma_c$ is the cosolvent solvation free energy (at pressure p, temperature T, and cosolvent number density ρ_c) for a single cosolvent molecule in the aqueous cosolvent mixtures. A similar expression can be derived for the ternary systems that have a solute (s) at infinite dilution ($\rho_s \to 0$) in a aqueous cosolvent mixture. In this case, the variation of solvation free energy of the solute ($\Delta\mathcal{G}_s$) with the changing cosolvent concentration in water is given by[6,43],

$$\lim_{\rho_s \to 0} \left(\frac{\partial \Delta\mathcal{G}_s}{\partial x_c}\right)_{p,T} = \frac{RT\left(\rho_w + \rho_c\right)^2}{\eta} \left(\mathrm{G}_{sw} - \mathrm{G}_{sc}\right), \tag{10}$$

where x_c is the cosolvent mole fraction, R is the gas constant, $\eta = \rho_w + \rho_c + \rho_w \rho_c \left(\mathrm{G}_{ww} + \mathrm{G}_{cc} - 2\mathrm{G}_{cw}\right)$ is the preferential solvation parameter, and ρ is the number density of individual components of the aqueous solutions. G_{ij} values are separately calculated for every cosolvent concentration in a pure water-cosolvent mixture. Preferential solvation of the solute by cosolvent molecules ($\mathrm{G}_{sw} - \mathrm{G}_{sc} < 0$) results in a decrease of $\Delta\mathcal{G}_s$ upon increasing the cosolvent mole fraction x_c or molar concentration c_{c} (salting-in [b]).

[b]Note: Salting-in is a general terminology used in (bio)chemistry when $\mathrm{G}_{sw} < \mathrm{G}_{sc}$, which is nothing but the larger affinity of co-solvent near solute than water. It is not necessarily associated with the ionic solutions.

3 Results and Discussions

For the all-atom simulations, we use the GROMACS molecular dynamics package[44] and AdResS simulations are performed using a modified GROMACS code[37]. We will review results for aqueous methanol and a tri-glycine solvated in aqueous urea. The all-atom simulations are performed in a NpT ensemble, where the pressure is controlled with a Berendsen barostat at 1 atm pressure using a coupling time of 0.5 ps[45]. The temperature is set to 300K using a Berendsen thermostat with coupling time 0.1 ps. The integration time step is set to 2 fs. Electrostatics in the all-atom simulations are treated using particle mesh ewald and reaction field method is used for AdResS simulations. We use the Gromos43a1 force field[46] for methanol, the Kirkwood-Buff derived force field[47] for urea and the SPC/E water model[48]. The force field parameters for try-glycine are taken from Gromos43a1[46] (for more detail see Refs. 24, 28).

3.1 Closed Boundary All-Atom Simulations: System Size Effects

In order to derive thermodynamic quantities the KBI should show a reasonable convergence at large distances, which, however, severely suffers from the system size effects. Especially when they are calculated within a small (or moderate) sized closed boundary NVT (constant number of particles N, volume V and temperature T) or NpT (constant N, pressure p and T) systems. Therefore, we start by commenting on the results from the closed boundary NpT all-atom simulations. In Fig. 4, we show the KBI between the water molecules for an aqueous methanol mixture at 75% methanol mole fraction. It can be appreciated that the reasonable convergence in KBI, which is related to the thermodynamic quantities, is only obtained for the largest system size that has N = 20152, where N is the total number of molecules in the system. For smaller system sizes, severe depletion is observed at large distances as indicated by the non-convergence of the tail of $G(r)$. This indicates that the solvent equilibrium is disturbed unless a huge simulation box is chosen. Furthermore, we here only consider water-water KBI because the system

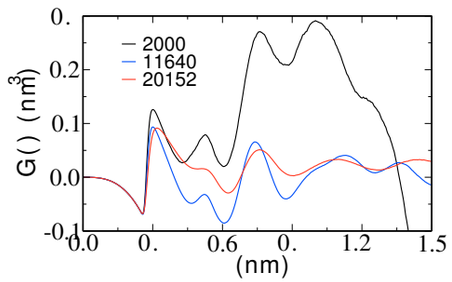

Figure 4. Running average of the Kirkwood-Buff integral between water molecules for a mixture at 75% mole fraction of methanol. Results are shown for three different system sizes (or number of molecules) and for 40ns data. Partially adopted from Ref. 24.

size effect is most severe at high methanol concentrations. Once we ensure a well defined convergence in water-water KBI, the other pairs, over the full concentration range, is guaranteed to show the convergence. It is still important to mention that even when a system size of N = 20152 is a good choice for the pure aqueous methanol mixture, a much larger simulation domain is needed when a large macromolecule is solvated in the mixture. Thus the closed boundary all-atom schemes become computationally much more demanding, because in most cases conformational transitions usually occur over very large time scales. More specifically, attaining large time scales for equilibrium conformational sampling of the phase space is almost impossible within the huge simulation domains with full chemical details. Therefore, a more suitable approach will be to device an approach that can capture correct particle fluctuation, thus can also be suitable for the study of the large scale equilibrium conformational transition of (bio)macromolecules. A close investigation would suggest that the chemical details are only important within a few nanometer from the solvated (bio)molecules and/or equivalent to the correlation length in the solution. Therefore, if an all-atom region is coupled to a much larger surrounding reservoir, then the all-atom region can be treated within a grand canonical framework[49]. Additionally, the surrounding reservoir that is "only" present to maintain solvent equilibrium with the bulk solution can be treated in a computationally inexpensive, single site, CG particle representation. Therefore, we now proceed to the discussion of this sort in the following section.

3.2 AdResS scheme: "Effective" Open Boundary Approach

3.2.1 Kirkwood-Buff Analysis of Aqueous Methanol Mixtures

We now focus on the simulation of liquid mixtures within an efficient multiscale AdResS scheme. For this purpose, we use the AdResS setup presented in Fig. 1. Note that the CG model used for the AdResS simulations is not pressure corrected. We start by running a 20ns long trajectory for the aqueous methanol mixture within the AdResS setup. However, due to the difference between the pressures in the all-atom region and the CG region, particles in the CG region feel an unphysical driving force towards the all-atom region. This results in a nonuniform density profile over the full simulation domain, as shown by the black curve in Fig. 5. A closer inspection of the curves in Fig. 5 suggest that even though the pressure is always higher (for both components) in the coarse-grained region, the methanol molecules are usually pushed out of the explicit region. This is because the pressure difference $\Delta P_{\mathrm{aa-cg}}$, between the all-atom and coarse-grained representations, is always higher for water molecules than the methanol molecules. Therefore, water molecules prefer the explicit region more than the methanol molecules, which finally affects the maximum particle packing density within the explicit region. This leads to a reduced density of methanol molecules inside the explicit region, as indicated in Fig. 5. This non-uniformity in the density profiles can be rectified by applying an iterative thermodynamic force[29,33],

$$\mathrm{f}_{th}^{n}(r) = \mathrm{f}_{th}^{n-1}(r) - \frac{1}{\rho^2 \kappa_T} \bigtriangledown \rho^{n-1}(r). \tag{11}$$

which predominantly depends on the slope of the density profiles within the hybrid region (for a detailed methodological description and applications see Refs. 24,29,37). Here κ_T is the isothermal compressibility of the solvent mixture. The thermodynamic force

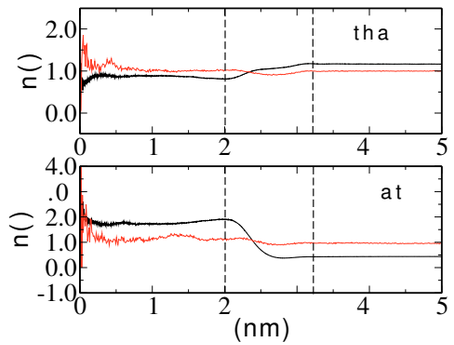

Figure 5. Normalized density profile for both components of the aqueous methanol mixture as a function of the distance from the centre of the simulation domain. Results are shown for both before (black curves) and after (red curves) the application of thermodynamic force, shown in Eq. 11. Large oscillations at the small r values are due to the poor statistics. Vertical lines represent the boundary of the hybrid region. Partially adopted from Ref. 24.

can be calculated over several iterations until a flat density profile is obtained. It can be appreciated that the overall uniform density profile is observed after the application of thermodynamic force, see the red curves in Fig. 5. This thermodynamic force is added together with the extrapolation forces in Eq. 1, then the full blown AdResS simulations are run for 40ns long trajectory. Using the AdResS simulation runs, we calculate KBIs within the all-atom region of the AdResS setup. In the top panel of Fig. 6, we show the comparative KBIs between water molecules calculated for a mixture of 75% methanol mole fractions. It can be appreciated that the KBI calculated within the all-atom region of the AdResS setup reproduces almost perfect convergence comparable to the full blown all-atom system of a much bigger system size. It still need to be mentioned that the all-atom region in the AdResS setup only accommodates approximately 700 molecules, yet we see perfect convergence of KBI, which otherwise would be impossible within a closed boundary all-atom setup of same system size consisting of 700 molecules. We have also shown the particle number fluctuation within the all-atom region of the AdResS setup, calculated using Eq. 8. Furthermore, the the running averages of KBI shows well controlled oscillations around the particle number fluctuation. This gives an indication that our approach captures correct concentration fluctuations and thus making the all-atom region, of the AdResS setup, an "effective" open boundary. To test the robustness of our approach, we have also calculated KBIs over full concentration range of methanol. Results are shown in the bottom panel of Fig. 6. G_{ij}'s are calculated using different methods are consistent and also shows reasonably good agreement with the existing experiments[43,50]. Note: Ideally the value of KBI should be calculated when the $G(r)$ converges to a plateau. However, within the mid sized simulation domains, $G(r)$ still shows oscillations upto a maximum distances that are possible from these system sizes. Therefore, we take the average of $G(r)$ between 0.9nm and 1.5nm over which $G(r)$ oscillates in a controlled manner around an average value.

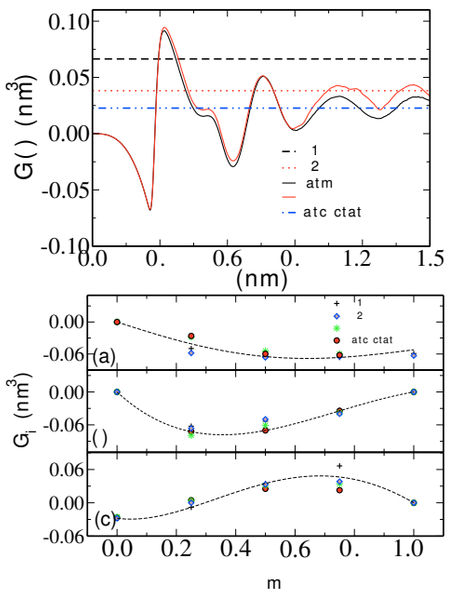

Figure 6. (top panel) Running averages of Kirkwood-Buff integral $G(r)$ between water molecules at a 75% methanol mole fraction. We present two experimental sets of data and three sets of simulation data. The all-atom and the AdResS data is derived by integrating the pair distribution functions $g(r)$. For AdResS data, we calculate $g(r)$ within the explicit region of 2nm radius and the particle fluctuation is calculated using Eq. 8 within the same explicit region. (bottom panel) Kirkwood-Buff integrals G_{ij} as a function of methanol mole fraction for (a) methanol-methanol, (b) methanol-water, and (c) water-water. Note: For the calculation of G_{ij}, we take the average between 0.9nm and 1.5nm of $G(r)$. Experimental value of KBI corresponding to legend exp 1 is taken from Ref. 43 and for exp 2 we take the value from Ref. 50. Partially adopted from Ref. 24.

3.2.2 Solvation of Tri-Glycine in Aqueous Urea

In this section, we will focus on the calculation of the solvation free energies of a peptide solvated in aqueous urea using the effective open boundary approach. Urea has been known as a common protein denaturant for more than hundred years. Presence of urea in water destroys the hydrophobic core of the protein and hence makes the protein more solvable in water. For example, two "controversial" mechanisms are proposed: One claims that urea denatures proteins by disrupting the water structure and thus makes the protein hydrophobic residues less compact. Another mechanism can be due to the interactions of urea with protein, either through stronger electrostatic interactions with backbone and/or polar residues[7,8,11,13–20]. More specifically, the solvation free energy of protein decreases with increasing urea concentration and reaches a preferential extremum at around 8M urea[7,13].

Here we start by calculating the solvation free energy of an isolated urea molecule in

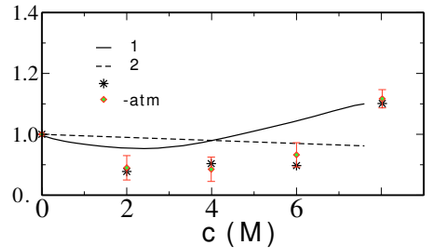

Figure 7. γ_{uu} as a function of urea molar concentration c_{u} (see Eq. 9). Error bars are standard deviations calculated out of six stochastically independent all-atom runs. The data set for exp 1 is taken from Ref. 47, 51 and for exp 2 data is taken from Ref. 52. Partially adopted from Ref. 28.

the aqueous urea mixtures at different urea molar concentrations c_u. We again ensure that the density profile is uniform (as shown in the previous section) and calculate the KBI within the all-atom region of the AdResS setup. Using Eq. 9 we calculate γ_{uu} and the results are shown in Fig. 7. All-atom and AdResS data show excellent agreement over the full concentration range. For comparison, we also include experimental data [47,51]. While the simulation data could not exactly reproduce experimental values, the trend follows very closely the first experimental data set of Ref. 51. This is a surprisingly close agreement, suggesting that the chosen force-field properly captures interaction differences between urea and water over a significant concentration range. Furthermore, we also observe a speedup of up to three times by using AdResS over all-atom simulations. At a first look this might appear to be small. However, in the case when the conformational transition of a large (bio)macromolecule drives a large number of urea molecules towards the protein, a much larger surrounding osmotic reservoir is needed to maintain correct solvent equilibrium. Therefore, use of our approach will more significantly increase the computational efficiency.

Having shown the results for aqueous urea solutions, we now focus on studying the solvation thermodynamics of tri-glycine in aqueous urea mixtures at different c_u. A typical AdResS setup for the solvated triglycine in aqueous urea is shown in Fig. 8. The derivative of the solvation free energy $\left(\partial\Delta\mathcal{G}_s/\partial x_{\mathrm{u}}\right)_{p,T}$ can be calculated using Eq. 10. In part (a) of Fig. 9, we show a comparative plot of $\left(\partial\Delta\mathcal{G}_s/\partial x_{\mathrm{u}}\right)_{p,T}$ using all-atom and AdResS simulations. It is clear from the plot that the AdResS (or open boundary) scheme can effectively reproduce the generic (bio)physical behaviour observed from a more computationally expensive all-atom simulation of the solvated tri-glycine. It is still important to mention that for all concentrations of urea we observe salting-in (i.e. $\left(\partial\Delta\mathcal{G}_{\mathrm{tg}}/\partial x_{\mathrm{u}}\right)_{p,T} < 0$), suggesting the preferential interaction of urea with the tri-glycine over water. Furthermore, the trend of Fig. 9(a) also suggest that $\Delta\mathcal{G}_{\mathrm{tg}}$ decreases with increasing urea concentration (see Fig. 9(b)), which is nothing but the preferred solvation of tri-glycine at higher urea concentrations. While the variation of $\Delta\mathcal{G}_{\mathrm{tg}}$ with c_{u} usually follows a linear dependence in experiments[53], simulations usually observe a quadratic dependence[12]. Here, the deviation from the linear dependence in the Ref. 12 can be attributed to the (a) choice of force fields

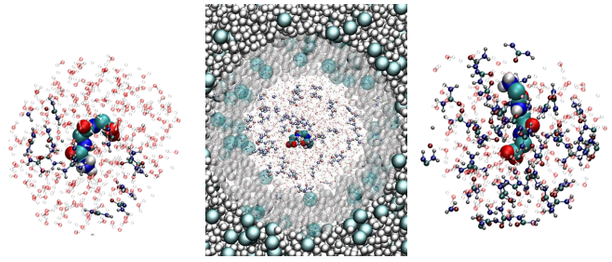

Figure 8. In the middle panel, we shown the AdResS setup of the tri-glycine solvated in aqueous urea. The all-atom region is chosen to be of 2nm in radius and the hybrid region has the width of 1.3nm. The centre-of-mass of the tri-glycine is constrained at the centre of the simulation domain and hence the peptide stays within the all-atom region throughout the simulation run. The coarse-grained urea molecules are rendered in green and the coarse-grained water molecules are rendered in silver. The magnified snapshot of the tri-glycine in 2.00M and 8.02M solutions are shown in the left and right panels, respectively. Partially adopted from Ref. 28.

and (b) the calculation of KBIs. As of (a), by comparing different force fields, it was shown that the deviation from the linear dependence was more for peptide simulated using AMBER than the GROMOS force field. (b) The peptide used in Ref. 12 consisted of ten amino acids, where the calculation of KBI from the pair distribution function is nontrivial and can lead to uncontrolled deviations of the solvation free energies that are extremely sensitive to the values of KBIs (see Eq. 10). In our study, for a triglycine, we observe a nice linear dependence for $c_{\mathrm{u}} \leq 6\mathrm{M}$ urea concentration. For $c_{\mathrm{u}} > 6\mathrm{M}$, $\Delta\mathcal{G}_{\mathrm{tg}}$ deviates away from the linear dependence to somehow approach a plateau value (see Fig. 9(b)). These observations are consistent with the known facts that the thermodynamic driving force, towards better solubility, at around 8.02M urea[7,13] and thus leading to protein denaturation in aqueous urea solutions. Another quantity that can be derived from the Fig. 9(b) is the m-value for peptide solvation, which is defined as

$$\text{m-value} = \frac{\partial \Delta\mathcal{G}_{\mathrm{tg}}}{\partial c_{\mathrm{u}}}. \tag{12}$$

If we take the m-value (per residue) from the slope of the linear fit in the Fig. 9(b), we find $-0.164\ \mathrm{KJ\ mol^{-2}L}$. This value is in a close agreement with the experimental value of $-0.163\ \mathrm{KJ\ mol^{-2}L}$[12,54]. It is yet important to mention that the calculation of m-values from the simulations assume the equal contribution of each residue of a tri-glycine, which is reasonable as long as we choose a peptide with only a few amino acids. However, for large peptides this approximation leads to extreme deviations from the experimentally observed value, as in the case of decaglycine where m-value was found to be three times larger that the expected experimentally value[12]. Therefore, our new open boundary simulation approach, applied to a simple test case of tri-glycine, could capture all the necessary ingredients of the solvation thermodynamics of the bio(macro)molecules.

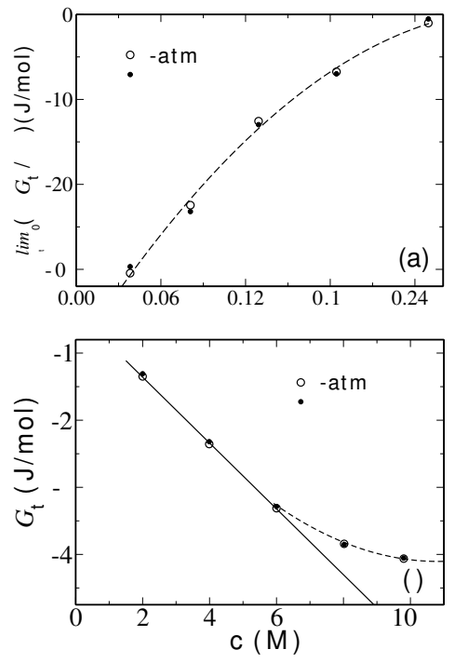

Figure 9. Part (a) shows derivative of tri-glycine solvation free energy ($\partial\Delta\mathcal{G}_{\rm tg}/\partial x_{\rm u}$) (see Eq. 10) as a function of urea mole fraction $x_{\rm u}$. Note: here we use urea mole fraction (instead of urea molar concentration $c_{\rm u}$) in the abscissa to be consistent with the Eq. 10. So, the numerical integration can directly lead to solvation free energy $\Delta\mathcal{G}_{\rm tg}$. In part (b) we show the solvation free energy $\Delta\mathcal{G}_{\rm tg}$ as a function of molar concentrations $c_{\rm u}$. Dashed lines are quadratic fits to the data in the both main plots with the colour of the lines being consistent with the colour of the symbol. Solid line in part (b) is linear fit between 2M and 6M. Partially adopted from Ref. 28.

4 Conclusions

We present a brief discussion of the "effective" open boundary molecular dynamics approach applied to biologically relevant aqueous mixtures. Our approach makes use of the adaptive resolution molecular dynamics scheme (AdResS). We present results for aqueous methanol and solvation of tri-glycine in aqueous urea. The solvation free energies are calculated using the fluctuation theory of solutions derived by Kirkwood and Buff for open systems. We obtain well converged solvation free energies within the small all-atom region of the AdResS setup that are impossible in a brute force all-atom MD of similar size. Though we have only tested relatively simple cases of aqueous methanol and tri-glycine in the aqueous urea solutions, this approach can possibly be further used to study the concentration driven conformational transition of more complex (bio)macromolecules.

Acknowledgements

The development of this work has greatly benefited from the fruitful collaborations with Nico van der Vegt and Luigi Delle Site, which we take this opportunity to gratefully acknowledge. Christine Peter, Christoph Globisch, Christoph Junghans, Sebastian Fritsch, and Simone Poblete are acknowledged for many stimulating discussions. We thank Biswaroop Mukherjee and Jia-Wei Shen for critical reading of the manuscript. Snapshots in this manuscript are rendered using VMD[55].

References

1. W. Kauzmann, Adv. Prot. Chem. **14**, 1 (1959).
2. J. Wyman, Adv. Prot. Chem. **19**, 223 (1964).
3. A. Ben-Naim, J. Phys. Chem. **71**, 4002 (1967).
4. K. Dill, Biochemistry **29**, 7133 (1990).
5. M. T. Record, W. T. Zhang, and C. F. Anderson, Adv. Prot. Chem. **51**, 281 (1998).
6. N. F. A. van der Vegt and W. F. van Gunsteren, J. Phys. Chem. B **108**, 1056 (2004).
7. C. B. Afinsen, Science **181**, 223 (1973).
8. E. J. Guinn, L. M. Pegram, M. W. Capp, M. N. Pollock, and M. T. Record Jr, Proc. Natl. Acad. Sci. **108**, 16932 (2011).
9. M. J. Hey, J. M. Clough, and D. J. Taylor, Nature **262**, 807 (1976).
10. G. Zhang and C. Wu, Phys. Rev. Lett. **86**, 822 (2001).
11. L. Ma, L. Pegram, M. T. Record, and Q. Cui, Biochemistry **49**, 1954 (2010).
12. D. Horinek, and R. R. Netz, J. Phys. Chem. A **115**, 6125 (2011).
13. B. J. Bennion, and V. Daggett, Proc. Natl. Acad. Sci. **100**, 5142 (2003).
14. R. D. Mountain and D. Thirumalai, J. Am. Chem. Soc. **125**, 1950 (2003).
15. M. C. Stumpe and H. Grubmüller. Plos Comput. Biol. **4**, e1000211 (2008).
16. Z. Gattin, S. Riniker, P. J. Hore, K. H. Mok, and W. F. van Gunsteren, Prot. Sci. **18**, 2090 (2009).
17. A. Berteotti, A.Barducci, and M. Parrinello, J. Am. Chem. Soc. **133**, 17200 (2011).
18. R. Zhou, J. Li, L. Hua, Z. Yang, and B. J. Berne, J. Phys. Chem. B **115**, 1323 (2011).
19. J. Walter, J. Sehrt, J. Vrabec, and H. Hesse, J. Phys. Chem. B **116**, 5251 (2012).
20. A. K. Tucker and M. J. Stevens, Macromolecules **45**, 6697 (2012).
21. M. E. Lee and N. F. A. van der Vegt, J. Chem. Phys **122**, 114509 (2005).
22. S. Weerasinghe and P. E. Smith, J. Phys. Chem. B **109**, 15080 (2005).
23. S. K. Schnell, X. Liu, J. Simon, A. Bardow, D. Bedeaux, T. J. H. Vlugt, and S. Kjelstrup, J. Phys. Chem. B **115**, 10911 (2011).
24. D. Mukherji, N. F. A. van der Vegt, K. Kremer, and L. Delle Site, J. Chem. Theory Comput. **8**, 375 (2012).
25. E. Ruckenstein, and I. L. Shulgin, Adv. Colloid Interface Sci. **123**, 97 (2006).
26. I. L. Shulgin and E. Ruckenstein, Biophys. J. **90**, 704 (2006).
27. S. Karunaweera, M. B. Gee, S. Weerasinghe, and P. E. Smith, J. Chem. Theory Comput. **8**, 3493 (2012).
28. D. Mukherji, N. F. A. van der Vegt, and K. Kremer, J. Chem. Theory Comput. **8**, 3536 (2012).

29. S. Fritsch, S. Poblete, C. Junghans, G. Ciccotti, L. Delle Site, and K. Kremer, Phys. Rev. Lett. **108**, 170602 (2012).
30. M. Praprotnik, L. Delle Site, and K. Kremer, J. Chem. Phys. **123**, 224106 (2005).
31. M. Praprotnik, L. Delle Site, and K. Kremer, Annu. Rev. Phys. Chem. **59**, 545 (2008).
32. S. Poblete, M. Praprotnik, K. Kremer, and L. Delle Site, J. Chem. Phys. **132**, 114101 (2010).
33. M. Praprotnik, S. Poblete, and K. Kremer, J. Stat. Phys. **145**, 946 (2011).
34. M. Praprotnik, S. Matysiak, L. Delle Site, K. Kremer, and C. Clementi, J. Phys. Cond. Mat. **19**, 292201 (2007).
35. B. P. Lambeth, Jr., C. Junghans, K. Kremer, C. Clementi, and L. Delle Site, J. Chem. Phys. **133**, 221101 (2010).
36. A. B. Poma and L. Delle Site, Phys. Rev. Lett. **104**, 250201 (2010).
37. S. Fritsch, C. Junghans, and K. Kremer, J. Chem. Theory Comput. **8**, 398 (2012).
38. J. G. Kirkwood and F. P. Buff, J. Chem. Phys. **19**, 774 (1951).
39. L. Delle Site Phys. Rev. E **76**, 047701 (2007).
40. M. Praprotnik, S. Poblete, L. Delle Site, and K. Kremer, Phys. Rev. Lett. **107**, 099801 (2011).
41. D. Reith, M. Pütz, and F. Müller-Plathe, J. Comput. Chem. **24**, 1624 (2003).
42. V. Rühle, C. Junghans, A. Lukyanov, K. Kremer, and D. Andrienko, J. Chem. Theory Comput. **3211**, 5 (2009).
43. A. Ben-Naim, *Molecular Theory of Solutions* (Oxford University Press, New York, 2006).
44. E. Lindahl, B. Hess, D. van der Spoel, J. Mol. Mod. **7**, 306 (2001).
45. H. J. C. Berendsen, J. P. M. Postma, W. F. van Gunsteren, A. DiNola, and J. R. Haak, J. Chem. Phys. **81**, 3684 (1984).
46. W. F. van Gunsteren, S. R. Billeter, A. A. Eising, P. H. Hünenberger, P. Krüger, A. E. Mark, W. R. P. Scott, and I. G. Tironi, Hochschulverlag AG an der ETH Zürich (1996).
47. S. Weerasinghe and P. E. Smith, J. Phys. Chem. B **107**, 3891 (2003).
48. H. J. C. Berendsen, J. R. Grigera, and T. P. Straatsma, J. Phys. Chem. **91**, 6269 (1987).
49. L. Landau and E. Lifshitz, *Statistical Physics, 3rd ed.* (Butterworth-Heinemann, UK 1980).
50. Y. Marcus, Phys. Chem. Chem. Phys. **1**, 2975 (1999).
51. R. H. Stokes, Aust. J. Chem. **20**, 2087 (1967).
52. O. Miyawaki, A. Saito, T. Matsuo, and K. Nakamura, Biosci. Biotechnol. Biochem. **61**, 466 (1997).
53. G. I. Makhatadze, J. Phys. Chem. B **103**, 4781 (1999).
54. M. Auton, and D. Wayne Bolen, Proc. Natl. Acad. Sci. **102**, 15065 (2005).
55. W. Humphrey, A. Dalke, and K. Schulten, J. Mol. Graph. **14**, 33 (1996).

Speeding-Up Particle Simulations of Multicomponent Polymer Systems by Coupling to Continuum Descriptions

Marcus Müller

Institute for Theoretical Physics,
Georg-August University, 37077 Göttingen, Germany
E-mail: mmueller@theorie.physik.uni-goettingen.de

The simulation of structure formation by particle-based simulations poses a computational challenge because of (i) the wide spread of time scales or (ii) the presence of free-energy barriers along the transformation path. A prototypical example of the former difficulty of multiple disparate time scales is the simultaneous presence of stiff bonded interactions, defining the molecular architecture of polymer systems and the weak non-bonded interactions, giving rise to macrophase separation or self-assembly in dense multicomponent systems. A characteristic illustration of the latter problem are nucleation barriers or metastable intermediate states in the course of morphology transformation. Continuum models, in turn, describe the system by a collective order-parameter field, e.g., the composition, rather than particle coordinates, and often do not suffer from these limitations because (i) the stiff molecular degrees of freedom have been integrated out and (ii) advanced numerical techniques, like the string method, exist that identify free-energy barriers and most probable transition paths. Using field-theoretic umbrella sampling, we determine an approximation of the continuum free-energy functional for a specific particle-based model. We illustrate how (i) the on-the-fly string method can identify the minimal free-energy path for the formation of an hourglass-shaped passage (stalk) between two apposing bilayer membranes and (ii) the continuum free-energy functional can be used in conjunction with a heterogeneous multiscale method (HMM) to speed-up the simulation of Lifshitz-Slyozov coarsening in a binary polymer blend by two orders of magnitude.

1 Soft, Coarse-Grained Particle-Based Models

1.1 Length, Time, and Energy Scales in Multicomponent Polymer Melts

Soft matter and in particular multicomponent polymer systems are characterized by (i) widely disparate time, length and energy scales, (ii) responsiveness to small driving forces, (iii) a multitude of metastable states, and (iv) structural and chemical complexity of the materials. These challenges require a multiscale approach that often relies on the development and validation of coarse-grained models and the development of new computational strategies.

The length, time, and energy scales on the atomic scale, e.g. associated with a covalent bond along the backbone of a polymer, are on the order of Angstrom (bond length), sub-picoseconds (molecular vibrations), and electron Volts (bond energy). The scales associated with a polymer molecule are its root mean-squared end-to-end distance, R_e that is on the order of tens of nanometers, the time scale to diffuse its own molecular extension, $\tau \sim$ seconds, and the repulsive interaction free energy between different polymers in a blend, $\chi N k_\mathrm{B}T \sim k_\mathrm{B}T$, where $k_\mathrm{B}T$ denotes the thermal energy scale, χ the Flory-Huggins parameter, and N the number of effective coarse-grained interactions centres along the molecular contour. Length and time scales associated with the collective dynamics of structure formation, i.e. phase separation in a binary homopolymer blend or self-assembly in

block copolymer materials, exceed micrometers and hours, respectively. It is quite obvious that no single computational approach can simultaneously address all these different scales and it remains a daunting challenge for a systematic coarse-graining procedure to start out with bond energies of eV and devise a coarse-grained model where free energy differences between effective coarse-grained segments on the order of $\chi k_{\mathrm{B}}T \sim 10^{-2} k_{\mathrm{B}}T \sim 10^{-4} eV$ dictate the qualitative behaviour. Additionally, these effective interactions between the coarse-grained segments are free energies, and therefore there is only a limited transferability of the coarse-grained model from one thermodynamic state to another[1].

The appropriate choice of the coarse-grained computational models reflects the physical phenomena that one intends to study, i.e. the crystallization of polymers, the glass transition in polymer materials, or phase separation and self-assembly require the coarse-grained description to capture different relevant characteristics of a dense polymer melt. In the following, we will restrict ourselves to structure formation in dense, binary AB polymer materials. These systems are characterized by minute forces that drive structure formation and that cannot yet be adequately predicted by *ab initio* quantum theory. Therefore the parameters of such models must often be determined directly from experiment. These coarse-grained models describe collective phenomena that can be quantitatively compared to experiments in order to validate the coarse-grained model and, additionally, they provide molecular insights into the structure and dynamics that are often not available experimentally.

The wide spread of length, time, and energy scales between the atomistic structure and the morphology imparts a large degree of universality onto the structure formation in multicomponent polymer melts, i.e. systems with different atomistic architectures and interactions exhibit similar behaviour on the mesoscopic scale. The appropriate level of description for the study of the mesoscale structure of multicomponent polymer system is the level of an entire macromolecule. On this level of coarse-graining, there are three relevant interactions: (i) bonded interactions, which define the macromolecular architecture, (ii) excluded volume interactions of segments that impart near-incompressibility onto the dense polymer melt, and (iii) repulsion between unlike segment species, which drive the structure formation (i.e. phase separation or self-assembly). These three interactions can be parameterized by three, experimentally accessible, coarse-grained parameters. The length scale of a linear flexible macromolecule, which adopts a Gaussian random-walk configuration, is set by R_{e}. The high free-energy costs associated with fluctuations of the total density are set by the inverse isothermal compressibility, κ. Note that in a coarse-grained model it is not necessary to enforce incompressibility down to the scale of a chemical repeat unit or atom but is suffices to limit density fluctuations on the relevant length scale, which is a small fraction of R_{e}. Within mean-field theory, the correlation length of density fluctuations is given by $\xi = R_{\mathrm{e}}/\sqrt{12\kappa N}$. The low free-energy scale of interactions between unlike polymer molecules (in a blend) or distinct block in copolymer materials is set by χN in units $k_{\mathrm{B}}T$. This repulsion gives rise to domain formation, and the width of the interfaces between domains is given by $w_0 = R_{\mathrm{e}}/\sqrt{6\chi N}$ in the limit of large incompatibility. The three coarse-grained parameters, R_{e}, κN, and χN, describe the strengths of the relevant interactions, and they are invariant under changing the number, N, of effective interaction centres that are used to describe the molecular contour.

There is one additional, fourth relevant quantity that dictates the behaviour of dense polymer melts – the invariant degree of polymerization, $\bar{N} = \left(\rho {R_{\mathrm{e}}}^2/N\right)^2$, where ρ is

the segment number density. Since in a dense melt, $R_\mathrm{e} = b\sqrt{N}$, the invariant degree of polymerization is proportional to the number of segments along the chain contour, $\bar{N} = (\rho b^3)^2 N$. The physical meaning of $\bar{N}$ consists in quantifying the number of neighbouring molecules a reference chain interacts with. Since the Gaussian chain conformations are fractal, a Gaussian polymer in three spatial dimensions does not fill space but there are on the order $\sqrt{\bar{N}}$ other molecules pervading the volume of the reference chain. This large number of neighbours is one of the important characteristics of dense polymer melts that sets them apart from mixtures of small molecules. In the limit $\bar{N} \to \infty$, a molecule interacts with infinitely many neighbours and fluctuations of the collective density (or interactions with all the surrounding molecules) are strongly suppressed such that the mean-field theory for polymers – denoted self-consistent field theory – becomes accurate. One important role of computer simulations is to assess the corrections to the mean-field approximation. Likewise, the depth of the correlation hole in the intermolecular pair correlation function, which is important for relating molecular interactions to the Flory-Huggins parameter, or corrections to the Gaussian chain conformations in a dense melt decrease in the limit of large $\bar{N}$. Therefore it is important for a coarse-grained model to be able to describe systems with experimentally relevant degree of polymerization.

It is important to realize that on this level of coarse-graining one segment corresponds to many chemical repeat units of a chemically realistic representation. While atoms cannot overlap, the centres of mass of a collection of atoms may sit on top of each other. In fact, systematic coarse-graining procedures aiming at reproducing the liquid-like correlations between the coarse-grained segments reveal that the interactions between the coarse-grained segments become the softer the more chemical repeat units a coarse-grained segment represents. As discussed above, the repulsive segmental interactions in the coarse-grained model needs not to be so strong as to enforce incompressibility on the length scale of an atom but we can weaken the repulsive segmental interactions to a level that they are sufficient to suppress density fluctuations on the relevant length scale of a small fraction of R_e. This softening of the excluded volume interactions allows for a larger time step in molecular-dynamics simulations or facilitates the use of non-local Monte-Carlo moves (e.g. molecular insertions/deletions via the configuration-bias algorithm).

The softness of the interaction is also crucial for representing an experimentally large invariant degree of polymerization, $\bar{N} = 10^4$. Modelling large values of $\bar{N} = (\rho b^3)^2 N$ with particle-based models that include harsh excluded volume interactions between the coarse-grained segments (e.g. lattice models[2–5] or Lennard-Jones potential[6,7]) one faces a formidable challenge. The size of a segment, σ, as defined by the range of the harsh repulsive interactions, and the statistical segment length of a flexible chain, $b \equiv R_\mathrm{e}/\sqrt{N}$, are comparable, $\sigma \approx b$. The segment density of a polymer fluid cannot be increased significantly beyond $\rho\sigma^3 \approx 1$, because the liquid of segments either crystallizes into a solid or it vitrifies into a glass. Thus, a value of $\bar{N} = 10^4$ requires a large number of segments per chain, $N = \bar{N}/(\rho b^3)^2 \approx \bar{N}/(\rho\sigma^3)^2 \sim 10^4$. A small system of linear dimension $L = R_\mathrm{e}$ is comprised of $n = \rho L^3 = N\sqrt{\bar{N}}(L/R_\mathrm{e})^3 \approx \bar{N}^{3/2} = 10^6$ effective segments. In a dense melt, these long entangled chains will reptate[8,9], and the time to diffuse a distance R_e scales like $\tau = \tau_0 N^3 \sim \bar{N}^3$ where τ_0 is a N-independent microscopic time scale. To follow the system over one characteristic time one needs about $\bar{N}^{9/2} = 10^{18}$ elementary segment moves. Contrary, if the harsh excluded volume interaction is replaced by a soft repulsion, one will eliminate the constraint $\rho_o b^3 \lesssim 1$, because solidification or vitrification

can be avoided. In this case, one can choose a much larger segment density, $\rho b^3 \sim \sqrt{\bar{N}}$. For instance, choosing $\rho b^3 = 18$, we can model a value of $\bar{N} = 10^4$ by using $N = 31$ segments along the molecular contour. This discretization of the molecular architecture is still sufficient to capture the characteristics of the random-walk-like conformations on the scale R_e. Within the soft coarse-grained model, a system of size $L = R_\mathrm{e}$ contains only 3 200 segments. Moreover, these non-entangled polymers obey Rouse dynamics with a relaxation time $\tau = \tau_\mathrm{o} N^2$. Thus the simulations require only $N^3\sqrt{\bar{N}} \approx 3 \cdot 10^8$ elementary moves, which is 11 orders of magnitude less than in coarse-grained models, where excluded volume is enforced on the scale of a segment. For this reason, soft coarse-grained models are very efficient in describing polymer systems with a realistically large value of $\bar{N}$ and allow us to study collective phenomena on the length scale of R_e and beyond. This ability can be traced back to the rather coarse representation of the molecular contour and the concomitant large number of monomeric repeat units that are lumped into an effective coarse-grained segment.

In order to identify the length and time scales of the soft coarse-grained model let us consider a melt of polystyrene with a molecular weight of $M_w = 100\,000$ or 962 chemical repeat units C_8H_8. The statistical segment length of a chemical repeat unit is about 0.7 nm yielding $R_\mathrm{e} = 21.7$ nm. A mass density of 1.06 g/cm^3 translates into an invariant degree of polymerization of $\bar{N} \approx 4200$. Using a typical self-diffusion coefficient of $D = 10$ nm^2/s[10], we obtain a characteristic time scale of $\tau = {R_\mathrm{e}}^2/D = 47$ s. In computer simulations of soft, coarse-grained models one can study systems with a few million coarse-grained segments. Assuming a chain discretization of $N = 32$, i.e. one coarse-grained segment correspond to 30 chemical repeat units, a typical system is comprised of some 30 000 molecules corresponding to a linear extension $L \sim 8R_\mathrm{e} \sim 0.17$ μm of a cubic system. A typical simulation with 10^6 elementary steps per segment corresponds to 100 τ or 1.5 hours. Thus soft, coarse-grained models are able to reach the experimentally relevant length and time scales of phase separation and self-assembly in polymer blends and block copolymer materials.

1.2 Soft, Coarse-Grained Particle-Based Models for Multicomponent Polymer Melts

We use a minimal, soft, coarse-grained model that captures the three relevant interactions. In the following, we distinguish between bonded interactions, which define the molecular shape and its fluctuations, and non-bonded interactions, that impart near-incompressibility onto the dense melt and drive the structure formation.

Since a coarse-grained segments is comprised of many chemical repeat units, the distance distribution between neighbouring coarse-grained segments along the macromolecule is Gaussian due to the central limit theorem and orientational correlations along the backbone of the chemical structure have decayed on the length scale of a coarse-grained segment. Therefore, we model the universal aspects of the molecular shape by the discretized Edwards Hamiltonian.

$$\frac{\mathcal{H}_\mathrm{b}[\mathbf{r}_i(s)]}{k_B T} = \sum_{s=1}^{N-1} \frac{3(N-1)}{2{R_\mathrm{e}}^2} \left[\mathbf{r}_i(s+1) - \mathbf{r}_i(s)\right]^2 , \tag{1}$$

where we consider n polymers with N segments in a volume V. $\{\mathbf{r}_{i,s}\}$ with $i = 1, \cdots, n$ and $s = 1, \cdots, N$ denotes the set of segment coordinates that completely specifies the configuration of our system. The density of the melt is $\rho = nN/V$ and R_e denotes the root mean-squared end-to-end distance of an ideal chain, i.e. in the absence of non-bonded interactions.

The soft, pairwise interactions can be re-written in the form of a free-energy functional[11]

$$\mathcal{H}_\mathrm{nb}(\{\mathbf{r}\}) = F_\mathrm{nb}[\hat{\phi}_A(\mathbf{r}|\{\mathbf{r}\}), \hat{\phi}_B(\mathbf{r}|\{\mathbf{r}\})] \tag{2}$$

where the local microscopic densities, $\hat{\phi}_A$ and $\hat{\phi}_B$, depend on the particle coordinates, $\{\mathbf{r}\}$.

$$\hat{\phi}_A(\mathbf{r}|\{\mathbf{r}\}) = \frac{1}{\rho_0} \sum_{i_A} \delta(\mathbf{r} - \mathbf{r}_{i_A}) \tag{3}$$

The sum runs over all A segments irrespectively to which molecule they belong.

A typical local free-energy functional for non-bonded interactions in an AB binary melt can be written as

$$\frac{F_\mathrm{nb}[\hat{\phi}_A, \hat{\phi}_B]}{k_\mathrm{B}T} = \sqrt{\bar{N}} \int \frac{\mathrm{d}\mathbf{r}}{{R_\mathrm{e}}^3} \left[\frac{\kappa N}{2} (\hat{\phi}_A + \hat{\phi}_B - 1)^2 - \frac{\chi N}{4} (\hat{\phi}_A - \hat{\phi}_B)^2 \right] \tag{4}$$

where χ is the bare Flory-Huggins parameter, and κ is the bare, dimensionless, inverse isothermal compressibility. Like the end-to-end distance, the actual energy of mixing or compressibility slightly deviates from the parameters of the Hamiltonian due to fluctuation/correlation effects. The advantage of this formulation is that it offers a general strategy to systematically incorporate thermodynamic information into the soft, coarse-grained model.

Eqs. 3 and 4 are not suitable for computer simulation; the δ-function needs to be regularized. Either one computes the local densities by smearing the δ-function out over a volume ΔL^3 or one employs a collocation lattice of grid spacing ΔL. Typically, ΔL is comparable to the statistical segment length, $b = R_\mathrm{e}/\sqrt{N}$ of the coarse-grained model and smaller than the width of the AB interfaces, w_0.

In the first method, one represents the δ-function in Eq. 3 as a limit of a weighting function, ω, and defines a weighted density[12]

$$\hat{\phi}_{A,\omega}(\mathbf{r}|\{\mathbf{r}\}) = \int \frac{\mathrm{d}^3\mathbf{r}'}{\Delta L^3}\, \omega(|\mathbf{r} - \mathbf{r}'|) \hat{\phi}_A(\mathbf{r}'|\{\mathbf{r}\}) = \frac{1}{\rho \Delta L^3} \sum_{i_A} \omega(|\mathbf{r} - \mathbf{r}_{i_A}|) \tag{5}$$

with normalization $\int \mathrm{d}^3\mathbf{r}\ \omega(|\mathbf{r}|) = \Delta L^3$. In the simplest case, ω is proportional to the characteristic function of a sphere. A quadratic term in the excess free energy yields a density-dependent pairwise potential[13,14].

$$\sqrt{\bar{N}} \int \frac{\mathrm{d}^3\mathbf{r}}{{R_\mathrm{e}}^3}\, \hat{\phi}_A(\mathbf{r}|\{\mathbf{r}\}) \hat{\phi}_B(\mathbf{r}|\{\mathbf{r}\}) = \frac{1}{N^2} \sum_{i_A, j_B} v(\mathbf{r}_{i_A}, \mathbf{r}_{j_B}) \tag{6}$$

which is translationally invariant and isotropic, i.e., $v(|\mathbf{r}' - \mathbf{r}''|) = \frac{1}{\sqrt{\bar{N}}} \frac{{R_\mathrm{e}}^3}{\Delta L^3} \int \frac{\mathrm{d}^3\mathbf{r}}{\Delta L^3}$ $\omega(|\mathbf{r} - \mathbf{r}'|)\omega(|\mathbf{r} - \mathbf{r}''|)$. The $\bar{N}$-dependence of the integrated strength, $\int \frac{\mathrm{d}^3\mathbf{r}}{{R_\mathrm{e}}^3}\, v(|\mathbf{r}|) = \frac{1}{\sqrt{\bar{N}}}$, guarantees that the limit of high density remains well defined.

In the grid-based scheme, one discretizes space in cubic cells of linear dimension, ΔL. Each cell is identified by its index, $\mathbf{c}$. We define the local microscopic densities on the grid by assigning particle positions to the grid cells according to[13,15]

$$\hat{\phi}_A(\mathbf{c}|\{\mathbf{r}\}) = \int \frac{\mathrm{d}^3\mathbf{r}}{\Delta L^3}\, \Pi(\mathbf{c},\mathbf{r})\hat{\phi}_A(\mathbf{r}) = \frac{1}{\rho\Delta L^3}\sum_{i_A}\Pi(\mathbf{c},\mathbf{r}_{i,s}) \tag{7}$$

The assignment function fulfills $\sum_{\mathbf{c}}\Pi(\mathbf{c},\mathbf{r}) = 1 \quad \forall\mathbf{r}$ and $\int \mathrm{d}^3\mathbf{r}\ \Pi(\mathbf{c},\mathbf{r}) = \Delta L^3 \quad \forall\mathbf{c}$ i.e. the contribution of a particle to all cells adds up to unity irrespectively of its position, and the volume assigned to each grid cell is ΔL^3. In the simplest case, $\Pi(\mathbf{c},\mathbf{r})$ is the characteristic function of a grid cell. The grid-based method also yields pairwise interactions according to Eq. 6 but, since they make reference to the underlying lattice, they are no longer translationally and rotationally invariant, $v(\mathbf{r}',\mathbf{r}'') = \frac{1}{\sqrt{\bar{\mathcal{N}}}}\frac{{R_\mathrm{e}}^3}{\Delta L^3}\sum_{\mathbf{c}}\Pi(\mathbf{c},\mathbf{r}')\Pi(\mathbf{c},\mathbf{r}'')$. Therefore, one needs to resort to special simulation techniques for computing the pressure and care hat to be exerted to control the effect of self-interactions[16]. However, in the grid-based approach, the energy of a segment with its surrounding can be very efficiently computed from the knowledge of the density on the collocation lattice. In the former weighting-function method, in turn, the energy involves the explicit computation of the pairwise interactions between a segment and its neighbours. This calculation is performed via a cell list, where the cell's linear dimension is the range of the pairwise interaction, $\mathcal{O}(\Delta L)$. All interactions in the 27 cells around the one that contains the segment have to be considered. For a typical choice of parameters, $N = 32$, $\bar{\mathcal{N}} = 10^4$, $\Delta L/R_\mathrm{e} = 1/6$ this amounts to $\mathcal{O}(10^2)$ interaction pairs. Thus the grid-based technique offers a significant computational advantage for dense polymer systems.

1.3 Strong Bonded and Weak Non-Bonded Forces and SCMF Simulations

Due to the computational speed-up we use the grid-based approach in the following. Since the pairwise interactions are not translationally invariant, we explore the configuration space of the soft, coarse-gained model by Monte-Carlo simulations. It is worth noting that for fine discretization of the molecular contour, $N \gg 1$, there is a pronounced difference between the strong bonded forces, f_b, that define the molecular architecture and the weak non-bonded forces, f_nb, that drive structure formation.

$$f_\mathrm{b} \sim \frac{k_\mathrm{B}T}{b} \sim \frac{k_\mathrm{B}T}{R_\mathrm{e}}\cdot\sqrt{N} \qquad \text{and} \qquad f_\mathrm{nb} \sim \frac{\chi k_\mathrm{B}T}{w_0} \sim \frac{k_\mathrm{B}T}{R_\mathrm{e}}\cdot\sqrt{6(\chi N)^3}\cdot\frac{1}{N} \tag{8}$$

i.e. $f_\mathrm{b}/f_\mathrm{nb} \sim N^{3/2}$. In molecular dynamics simulations, one would use multiple time-step integrators (rRESPA)[17] to cope with this disparity of forces. In Monte-Carlo simulations, one can use the Single-Chain-in-Mean-Field (SCMF) algorithm[15,18] to exploit the separation between the strong, rapidly fluctuating, bonded interactions, which dictate the size of a segmental movement in one Monte Carlo step, and the weak, non-bonded interactions, which only very slowly evolve in time. In SCMF simulations, we temporarily replace the pairwise interactions, Eq. 2, of a segment with its surroundings by the interaction of a segment with an external field, i.e. $\frac{\mathcal{H}_\mathrm{nb}^\mathrm{SCMF}}{k_\mathrm{B}T} = \frac{\rho\Delta L^3}{N}\sum_{\mathbf{c}}\left[w_A(\mathbf{c})\hat{\phi}_A(\mathbf{c}|\{\mathbf{r}\}) + w_B(\mathbf{c})\hat{\phi}_B(\mathbf{c}|\{\mathbf{r}\})\right]$, where the external field, w_A/N that acts on A segments is frequently calculated from the local fluctuating densities according

to $w_A(\mathbf{c}) = \frac{N}{\rho \Delta L^3} \frac{\partial F_{\rm nb}}{\partial \phi_A(\mathbf{c})}$. A SCMF simulation cycle is comprised of two parts: 1) evolve the polymer conformations in the external fields, w_A and w_B, for a small, fixed amount of Monte-Carlo steps. We employ Smart-Monte-Carlo moves, using the strong bonded forces to bias the proposal of a trail displacement[19]. During these Monte-Carlo simulations the molecules do not interact with each other and the simulation of independent chain molecules can be straightforwardly implemented on parallel computers. 2) recalculate the external fields from the instantaneous densities. In this second step, fluctuations and correlations are partially restored. Then the simulation cycle commences again. The quasi-instantaneous field approximation that consists in replacing the interactions via frequently updated, fluctuating, external fields will be accurate, if the change of the local composition between successive updates of the external fields is small. This property is controlled by the parameter, $\varepsilon = \frac{1}{N \rho \Delta L^3}$, which plays a similar role as the Ginzburg parameter in a mean-field calculation. In contrast to the Ginzburg parameter, however, ε depends on the discretization of space, ΔL, and molecular contour, N, and these parameters are chosen such that the quasi-instantaneous field approximation is accurate[13].

1.4 Barrier and Time-Scale Problem of Particle-Based Models

In spite of the benefits of soft, coarse-grained models, the investigation of the kinetics of phase separation or self-assembly in computer simulations of particle-based models is computationally demanding. Two effects contribute to this difficulty:

(i) barrier problem – In the course of structure formation, multiple free-energy barriers must be overcome. Since collective structure formation involves many molecules, free-energy barriers typically exceed $k_{\rm B}T$, and rare thermal fluctuations are required to overcome them. For the favourable case in which it is possible to identify a suitable and simple reaction coordinate, or when one can identify a low-dimensional subspace that characterizes the barriers, a variety of computational techniques have been devised to "flatten" the free-energy landscape and facilitate the exploration of phase space or to compute the saddle-points of the free-energy landscape that dictate the kinetics of structure formation[20,21].

(ii) time-scale problem – Even if the time evolution is completely down hill in free energy, the kinetics of the order parameter can be intrinsically slow because the thermodynamic driving force does not efficiently generate a concomitant current. A prototypical example is the diffusion of one molecule from one domain to another, as it occurs in Lifshitz-Slyozov coarsening in binary blends[22], the diffusion across lamellae in symmetric block copolymers, or the exchange of amphiphiles between micellar aggregates. In these cases, molecules have to "tunnel" through an unfavourable domain, and this thermally activated process dramatically slows down the current.

These two types of problems can be addressed by concurrent coupling of the particle-based model to a continuum description.

2 Continuum Models

2.1 Order Parameter and Free-Energy Landscape

In a continuum approach, the system configuration is entirely described through a collective order-parameter, i.e. a continuum field that does not make references to the properties of individual molecules. The choice of the order parameter is critical and crucially

depends on the problem at hand. In the following we consider examples where the difference between the local A and B densities provides an appropriate order parameter, $m(\mathbf{r}) = \phi_A(\mathbf{r}) - \phi_B(\mathbf{r})$. Then, one can define the free energy as a functional of the order parameter $m(\mathbf{r})$ via the trace over all particle conformations compatible with $m(\mathbf{r})$

$$e^{-\frac{F[m]}{k_\mathrm{B}T}} \equiv \int \frac{\prod_{i=1}^{n_{AB}} \prod_{t=1}^{N} \mathrm{d}\mathbf{r}_{i,t}}{n_{AB}! \lambda_T^{3 n_{AB} N}} \, e^{-\frac{\mathcal{H}(\{\mathbf{r}\})}{k_\mathrm{B}T}} \prod_{\mathbf{r}} \delta \left[m(\mathbf{r}) - \hat{\phi}_A(\mathbf{r}|\{\mathbf{r}\}) + \hat{\phi}_B(\mathbf{r}|\{\mathbf{r}\}) \right] \quad (9)$$

where we considered n_{AB} molecules consisting of N segments. λ_T is the thermal de-Broglie wavelength, and $\mathcal{H}(\{\mathbf{r}\})$ denotes the interactions of the underlying particle-based model. Eq. 9 guarantees that the partition functions of the particle-based model and of the continuum description are identical $\int \frac{\prod_{i=1}^{n_{AB}} \prod_{t=1}^{N} \mathrm{d}\mathbf{r}_{i,t}}{n_{AB}! \lambda_T^{3 n_{AB} N}} \, e^{-\frac{\mathcal{H}(\{\mathbf{r}\})}{k_\mathrm{B}T}} = \int \mathcal{D}m \, \exp\left[-\frac{F[m]}{k_\mathrm{B}T}\right]$.

Knowledge of the free-energy functional (or landscape) allows one to draw important conclusions: (i) Within the mean-field approximation, minima of $F[m]$ correspond to (meta)stable states. (ii) If there is a clear separation of time scales between the fast single-chain dynamics and the slow kinetics of the order-parameter, the molecular conformations will be in equilibrium with the *instantaneous* order-parameter, *i.e.*, they sample the equilibrium distribution that is compatible with the order-parameter field, Eq. 9. In this limit, the qualitative features of the order-parameter dynamics can be inferred from the free-energy landscape. Most importantly neglecting thermal fluctuations, one can distinguish two types of structure formation kinetics – spinodal self-assembly or phase separation and nucleation.

Having identified the free-energy landscape as a function(al), $F[m]$, of a slowly evolving order parameter, one can compute the thermodynamic force, $\nabla \frac{\delta F}{\delta m(\mathbf{r})}$, that drives structure formation. The Onsager coefficient, Λ, connects this thermodynamic force to the current of the order parameter:

$$\mathbf{j}(\mathbf{r}) = -\int \mathrm{d}\mathbf{r}' \, \Lambda(\mathbf{r}, \mathbf{r}') \nabla' \frac{\delta F}{\delta m(\mathbf{r}')} \quad (10)$$

Since the order parameter is related to the densities of the different species, it is conserved and obeys the continuity equation[23–25]

$$\frac{\partial m}{\partial t} = -\nabla \mathbf{j} \quad (11)$$

In an incompressible systems, the currents of A and B segments cancel and $\Lambda \sim \phi_A \phi_B = (1 - m^2)/4$. It is this factor that gives rise to intrinsically slow dynamics, cf. Sec. 1.4, i.e. in strongly segregated systems the kinetics can be protracted even if there is a strong thermodynamic driving force. [a]

[a] General expressions for relating the Onsager coefficient to the dynamics of the underlying macromolecules have been devised[26]. For the Rouse model with inverse friction $\frac{1}{\zeta} = \frac{ND}{k_\mathrm{B}T}$ one obtains

$$\begin{aligned} \Lambda(\mathbf{r}, \mathbf{r}') &\approx \left\langle \sum_i \frac{\partial}{\partial \mathbf{r}_i} [\hat{\phi}_A(\mathbf{r}|\{\mathbf{r}\}) - \hat{\phi}_B(\mathbf{r}|\{\mathbf{r}\})] \cdot \frac{1}{\zeta} \cdot \frac{\partial}{\partial \mathbf{r}_i} [\hat{\phi}_A(\mathbf{r}'|\{\mathbf{r}\}) - \hat{\phi}_B(\mathbf{r}'|\{\mathbf{r}\})] \right\rangle \\ &\approx \frac{ND}{\rho k_\mathrm{B}T} (1 - m^2) \frac{g(\mathbf{r}, \mathbf{r}')}{V} \end{aligned}$$

where the last expression refers to a symmetric homopolymer blend in the disordered state and the non-locality is characterized by the single-chain correlation function, $g(\mathbf{r})$.

Eqs. 10 and 11 can be augmented by random noise terms such that the dynamics is able to overcome barriers in the free-energy landscape[27,28]. Thermal fluctuations are often neglected and the mean-field approximation is invoked; in order to address fluctuation effects one has to cope with short-length scale fluctuations, which lead to UV-divergencies.

Different simple forms of the free-energy functional, $F[m]$, have been proposed on the basis of general symmetry principles. A common description of binary blends is provided by the Ginzburg-Landau square-gradient functional[29]. Microphase separation of block copolymer materials can be described by the Otha-Kawasaki functional[30] or the Swift-Hohenberg approach[31]. The small number of parameters that enter such a continuum description can be qualitatively related to physically accessible quantities like the segregation inside the domains or the intrinsic widths of interfaces. Because they ignore all molecular degrees of freedom, these continuum models are computationally efficient. Additionally, sophisticated methods have been devised to identify barriers and minimal free-energy paths[32], and the effects of small Onsager coefficients can be mitigated by using a large time step for integrating Eq. 11.

3 Systematic Parameterization of a Continuum model: Field-Theoretic Umbrella Sampling and Force Matching

The barrier and time-scale problem in particle-based models can be addressed by coupling them to a continuum model in the framework of the heterogeneous multiscale method (HMM)[33,34]. To this end, one has to estimate the free-energy functional, $F[m]$, of the particle-based model. Two computational strategies have been devised to this end: field-theoretic umbrella sampling[35] and field-theoretic force matching[16]. In both cases, one does not directly obtain the free-energy functional but rather the chemical potential, $\mu(\mathbf{r}|m) \equiv \frac{\delta F}{\delta m(\mathbf{r})}$, for a specific configuration of the order parameter.

In field-theoretic umbrella sampling[35], one adds to the interactions of the particle-based model an umbrella potential that restrains the local microscopic densities, $\hat{\phi}_A(\mathbf{r}|\{\mathbf{r}\}) - \hat{\phi}_B(\mathbf{r}|\{\mathbf{r}\})$, to the local value of the order-parameter, $m(\mathbf{r})$, at each point in space

$$\mathcal{H}_{\mathrm{fup}}(\{\mathbf{r}\}) = \int \mathrm{d}\mathbf{r}\, \frac{\lambda}{2} \left[m(\mathbf{r}) - \left(\hat{\phi}_A(\mathbf{r}|\{\mathbf{r}\}) - \hat{\phi}_B(\mathbf{r}|\{\mathbf{r}\}) \right) \right]^2 \tag{12}$$

The integral in Eq. 12 is evaluated using a collocation lattice (see. Sec. 1.2). In the limit, $\lambda \to \infty$, the Boltzmann factor of this field-theoretic umbrella potential converges to the δ-function constraint in Eq. 9 that projects out the microscopic particle configurations compatible with the order parameter[35,36], and free energy of the restrained system with the field-theoretic umbrella potential, $F_\lambda[m]$, converges towards the constraint free-energy. The chemical potential can be calculated according to

$$\mu_\lambda(\mathbf{r}|m) \equiv \frac{\delta F_\lambda}{\delta m(\mathbf{r})} = \left\langle \frac{\delta \mathcal{H}_{\mathrm{fup}}}{\delta m(\mathbf{r})} \right\rangle_\lambda = \lambda \left\langle m - \left(\hat{\phi}_A - \hat{\phi}_B \right) \right\rangle_\lambda \overset{\lambda\to\infty}{\to} \frac{\delta F}{\delta m(\mathbf{r})} = \mu(\mathbf{r}|m) \tag{13}$$

where the average $\langle \cdots \rangle_\lambda$ is performed in the restrained system. Independent from λ, this average has to be sampled for about one molecular relaxation time, τ to accurately calculate the local chemical potential[35].

In field-theoretic force matching, one alternatively can use the thermodynamic relation between the force, $\mathbf{K}_A(\mathbf{r})$, acting on A-segments in a volume element around position, $\mathbf{r}$, and the gradient of the excess chemical potential[16]:

$$\rho \, \langle \mathbf{K}_A(\mathbf{r}) \rangle|_{m(\mathbf{r})} = -\nabla \left[\mu_A(\mathbf{r}|m) - \rho k_\mathrm{B} T \ln \phi_A(\mathbf{r}) \right] \tag{14}$$

and $\mu = \mu_A - \mu_B$. The force is determined in configurations that are characterized by the order parameter, $m(\mathbf{r})$. The advantage of this technique is that it does not rely on the limit $\lambda \to \infty$ or the use of a collocation grid. For polymers, however, there are large cancellation effects of forces similar to the atomistic expressions for the virial pressure.

4 Applications

4.1 Barrier Problem: Minimum Free-energy Path (MFEP) of Stalk Formation

In order to overcome the barrier problem and find a suitable path along which structure formation proceeds, one can adopt an equation-free approach, where no Ansatz for the explicit form of the free-energy functional is required[37]. Knowing the chemical potential $\mu(\mathbf{r}|m)$, we use the string method[32] to find the minimal free energy path (MFEP) that connects the starting and ending order-parameter configurations[38–40]. The MFEP is a string of morphologies, $m_s(\mathbf{r})$, where s denotes the contour parameter along the string and the squared distance between two neighbouring morphologies, $m_s(\mathbf{r})$ and $m_{s'}(\mathbf{r})$, along the string is given by $\Delta^2_{s,s'} \propto \int \mathrm{d}\mathbf{r} \, [m_s(\mathbf{r}) - m_{s'}(\mathbf{r})]^2$. The MFEP is defined by the condition that the thermodynamic force in the direction perpendicular to the path vanishes

$$\nabla_\perp \mathcal{F}[m_s] = \mu(\mathbf{r}|m_s) - \frac{\mathrm{d}m_s(\mathbf{r})}{\mathrm{d}s} \frac{\int \mathrm{d}\mathbf{r}' \, \mu(\mathbf{r}'|m_s) \frac{\mathrm{d}m_s(\mathbf{r}')}{\mathrm{d}s}}{\int \mathrm{d}\mathbf{r}' \, \left(\frac{\mathrm{d}m_s(\mathbf{r}')}{\mathrm{d}s} \right)^2} \tag{15}$$

Thus the defining condition for the MFEP can be solely expressed by the chemical potential that we obtain in the particle-based model via field-theoretic umbrella sampling, Eq. 13. The MFEP is efficiently determined numerically by the improved string method[32,38], which consists of a two-step cycle: (i) $\mathcal{F}$ is minimized by evolving the morphologies according to $\Delta m_s(\mathbf{r}) = -\mu(\mathbf{r}|m_s)\Delta\varepsilon$ with $\mu(\mathbf{r}|m) = \frac{\delta \mathcal{F}[m]}{\delta m(\mathbf{r})}$; and (ii) $m_s(\mathbf{r})$ is re-parameterized via a third-order spline at each point, $\mathbf{r}$, to restore uniform distance of the morphologies along the string.

One application is illustrated in Fig. 1, where this techniques has been employed to study the formation of an hour-glass shaped, hydrophobic passage (stalk) between two apposing lamellar sheets in a copolymer-homopolymer mixture[40]. By virtue of the universality of the structure of amphiphilic systems[41], this model can be conceived as a representation of lipid membranes – the A and B blocks corresponding to hydrophobic tails and hydrophilic heads of lipid molecules and the B-homopolymers representing the solvent.

The MFEP, $m_{s_i}(\mathbf{r})$, is discretized into 24 particle-based systems and intermediate values of s are obtained by point-wise spline interpolation. The free energy along the MFEP is obtained by $\frac{\mathrm{d}\mathcal{F}[m_s]}{\mathrm{d}s} = \int \mathrm{d}\mathbf{r} \, \frac{\partial m_s(\mathbf{r})}{\partial s} \frac{\delta \mathcal{F}[m_s]}{\delta m(\mathbf{r})}$. and the transition state, m^*, is identified as the maximum on the MFEP, $\frac{\mathrm{d}\mathcal{F}[m_s]}{\mathrm{d}s} = 0$.

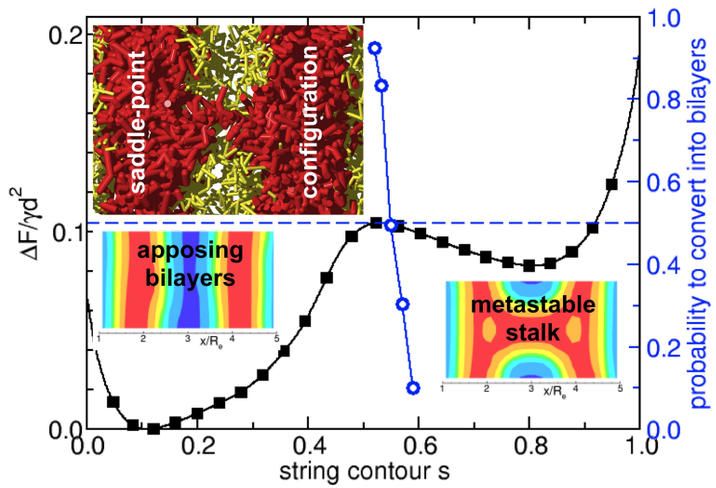

Figure 1. Minimum free-energy path (MFEP) obtained by the on-the-fly string method of stalk formation. Adapted from Ref. 40.

The left axis of Fig. 1 presents the free energy, $F[m_s]$, along the MFEP in units of γd^2, where $\gamma {R_\mathrm{e}}^2/\sqrt{\mathcal{N}}k_\mathrm{B}T \approx \sqrt{\chi_0 N/6}$ and $d \approx 1.82R_\mathrm{e}$ denote the AB (oil-water) interface tension and the lamella (bilayer) thickness, respectively. Typical experimental values of lipid membranes are $d \approx 3.6$nm and $\gamma d^2 = 155k_\mathrm{B}T$. The contour plots depict cross sections of the order parameter, $m_s(\mathbf{r})$, for the stable, apposing-bilayer morphology and the metastable stalk morphology. The snapshot depicts a particle configuration restrained by the field-theoretic umbrella potential, Eq. 12, using the order parameter, $m_{s^*}(\mathbf{r})$, at the saddle point, $s^* = 0.532$, of the MFEP. Hydrophilic beads are coloured yellow, hydrophobic beads are shown in red, solvent (homopolymer) particles are not shown. Only every 10^th copolymer is depicted corresponding to a typical density in a lipid system.

This static information is complemented by the probability that configurations along the MFEP have transformed in the course of simulations into two apposed bilayers at a specified time after the restraining field-theoretic umbrella potential has been removed (blue, right axis). Results have been obtained for 256 independent configurations at each value of s. The probability is a sharply varying function along the MFEP and the position, s, at which there is a $50-50$ chance of reaching either the morphology of two apposing bilayers or the stalk, agrees with the saddle-point of the MFEP.

The hydrophobic bridge that connects the two lamellae – denoted by stalk – has attracted much interest in the context of bilayer membrane fusion[42]. Our particle-based sim-

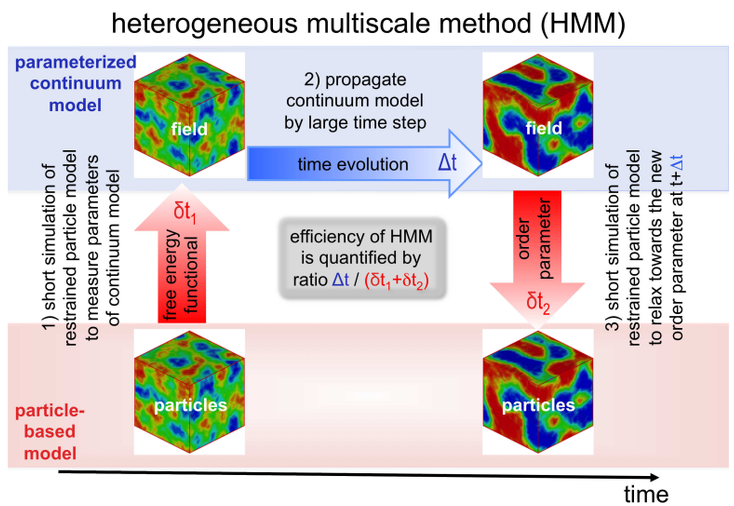

Figure 2. Illustration of one cycle of HMM for the initial stages (spinodal decomposition) of phase separation in a homopolymer blend. Adapted from Ref. 43.

ulations provide direct microscopic insights into the transition state that consists of only few hydrophobic tails that bridge between the bilayers and that constitutes a free-energy barrier of $16k_{\mathrm{B}}T$ in a lipid system.

4.2 Time-Scale Problem: Heterogeneous Multiscale Method Applied to Lifshitz-Slyozov Coarsening in a Binary Polymer Blend

By knowing the free-energy functional, $F[m]$, one can also mitigate the time-scale problem by concurrently coupling the particle model to the corresponding continuum model. This HMM[33–35] comprises three steps, which are illustrated in Fig. 2: 1) estimate the parameters of the continuum description, 2) propagate the continuum model for a large time step, Δt, and 3) seamlessly generate a new particle configuration compatible with the new order-parameter field. Then the cycle commences again.

In step 1), one needs to compute the chemical potential, μ, and the Onsager coefficient, Λ, for a specific configuration of the particle model. The former can be obtained by field-theoretic umbrella sampling or field-theoretic force matching. This equation-free strategy, however, would require the chemical potential be frequently computed because the local chemical potential significantly changes on the time scale where an AB interface has moved a distance comparable to its intrinsic width. Therefore, rather than using

the chemical potential directly, it is useful to exploit the knowledge of $\mu(\mathbf{r}|m)$ to parameterize an explicit Ansatz, $F_{\mathrm{trial}}[m]$, for the free-energy landscape that contains a small number of variational parameters, $\{\alpha\}$, like e.g. the Flory-Huggins parameter and the coefficient of the square-gradient term. Using the measured μ, one can adjust these parameters to minimize the deviation between F and F_{trial}, i.e. we choose $\{\alpha\}$ such that $\int \mathrm{d}\mathbf{r}\ \left(\mu(\mathbf{r}|m) - \frac{\delta F_{\mathrm{trial}}[m]}{\delta m(\mathbf{r})}\right)^2 \rightarrow \min$.

This Ansatz tacitly assumes that $F_{\mathrm{trial}}[m]$ with the same set of $\{\alpha\}$ is able to describe the entire system, e.g. it can simultaneously describe the composition inside large domains and the profiles across AB interfaces. If the Ansatz were perfect, the parameters, $\{\alpha\}$, would not depend on the order-parameter configuration, and one could employ the once-parameterized free-energy functional to predict the entire kinetics of structure formation of the particle-based model. In practice, the optimal parameters will slightly depend on the specific $m(\mathbf{r})$. For instance, we anticipate changes of F_{trial} when the segregation of the domains changes or the structure of the AB interfaces is altered. The residual minimum indicates the quality of the Ansatz, F_{trial}, signals the need for re-parameterization, and allows for a systematic improvement of F_{trial} by including additional terms. Moreover, the computational time required for computing the small number of parameters, $\{\alpha\}$, is significantly smaller than accurately computing the chemical potential at each point in space because one can substitute the time average of a local quantity by a spatial average over the entire system.

It is important to realize that changes of the thermodynamic state that require re-parameterization occur on a time scale that is much longer than the motion of interfaces. Hence, $F_{\mathrm{trial}}[m]$ can predict the structure formation for a much larger time interval than $\mu(\mathbf{r}|m)$, and the time step, Δt, of a single cycle can be significantly larger in HMM than in an equation-free scheme that directly uses the local chemical potential[44].

Since the continuum model is not explicitly concerned with the stiff bonded degrees of freedom, the time scale can be adjusted to the intrinsically slow process and step 2) of the HMM scheme takes a vanishingly small computation time compared to the propagation of the particle-based model.

To seamlessly generate a new particle configuration in step 3), which corresponds to the new order-parameter field, $m(\mathbf{r}, t + \Delta t)$, we use the same field-theoretic umbrella potential that has been employed to compute the chemical potential. Using the new order-parameter at time $t + \Delta t$ in the field-theoretic umbrella potential, Eq. 12, one creates a large thermodynamic force, $-\lambda k_{\mathrm{B}} T \nabla[m(\mathbf{r}, t+\Delta t) - (\hat{\phi}_A - \hat{\phi}_B)]$ towards the new order-parameter configuration. This strong force amplifies the weak thermodynamic driving forces of the non-bonded interactions in the original model by a factor that is proportional to the strength λ, speeding-up the relaxation towards $m(\mathbf{r}, t+\Delta t)$ compared to the original dynamics of structure formation. This rational suggests that λ should be chosen as large as possible in order to achieve the maximal speed-up. There are, however, two limitations: (i) The thermodynamic force of the field-theoretic umbrella potential should amplify the weak thermodynamic driving force of the original model, but they must not exceed the strong non-bonded forces that dictate the single-molecule dynamics. Otherwise, the underlying particle dynamics will be altered and the time step used to evolve the particle-based model has to be reduced. (ii) The estimate of the speed-up relies on linear response theory that fails already at moderately large values of λ. In this case, one might need an additional time

τ to relax the molecular conformations to the equilibrium statics within the field-theoretic umbrella potential.

This step 3) also provides a strategy for computing the Onsager coefficient from the last stage of relaxation towards the new equilibrium in the restrained system. In the case of large λ the field-theoretic umbrella potential dominates the thermodynamic force and, since the difference $m - (\hat{\phi}_A - \hat{\phi}_B)$ is small, linear response theory is appropriate and predicts an exponential relaxation towards the restrained equilibrium. Alternatively, one can estimate Λ by comparing the kinetics of structure formation of the original particle-based model with the prediction of continuum approach.

One can additionally speed-up the relaxation towards the new order-parameter field by computing the average current, $\bar{\mathbf{j}}$, during the time interval, Δt, from the continuum model and estimate the concomitant time-averaged velocity fields, $\bar{\mathbf{v}}_A(\mathbf{r})$ and $\bar{\mathbf{v}}_B(\mathbf{r})$. Then, one couples these flow fields to the particle model via an additional drag force, $\mathbf{F}_i = \gamma \bar{\mathbf{v}}_A(\mathbf{r}_i)$ acting on an A particle at position, $\mathbf{r}_i$. γ is a friction coefficient. Applying this force at the initial stage of relaxation towards the new order parameter, one accelerates the generation of a new particle configuration. Also in this case, an additional molecular relaxation time without flow is required to bring the molecular conformations into equilibrium with the field-theoretic umbrella potential.

Steps 1) and 3) of HMM require a time of the order of the molecular relaxation time, τ. The computational cost of propagating the continuum model is negligible and thus the computational speed-up is of the order $\Delta t/\tau$. Using an accurate free-energy functional, F_{trial}, that is suitable for describing the slow structure formation over a long time interval, Δt, without the need for re-parameterization, large speed-ups are feasible. The so-generated particle configurations can subsequently be used to investigate the single-chain conformations and dynamics, which is not accessible in the continuum model.

One application of HMM is illustrated in Fig. 3 where the evaporation of chains from a drop in a binary AB homopolymer blend is investigated. The system of geometry $12R_{\mathrm{e}} \times 6R_{\mathrm{e}} \times 6R_{\mathrm{e}}$ is comprised of two A domains – a spherical drop with excess Δ_A of A segments and a planar slab-like domain that spans the system via the periodic boundary conditions. The morphologies are illustrated in the inset images. Due to the curvature of the drop's interface, the chemical potential is inside the drop is higher than in the planar domain and A molecules evaporate from the drop and condense onto the planar domain (Lifshitz-Slyozov coarsening[22]). This process is protracted because the Onsager coefficient inside the strongly segregated B-rich matrix is very small. Fig. 3 depicts the linear shrinking of the drop's volume with time. The red solid line corresponds to the simulation of the particle-based model and the black dashed line depicts the prediction of the continuum model. The continuum model is a Ginzburg-Landau square-gradient model where we have adjusted the effective incompatibility and the coefficient of the square-gradient term. The Onsager coefficient was determined by comparing the time evolution of the particle-based model and the continuum model at early times. The so-parameterized continuum model accurately describes the entire drop evaporation. The steep doted lines show the relaxation of the particle-based model towards the new order parameter at a later time Δt using the field-theoretic umbrella potential and an initial coupling to $\mathbf{j}$. The green and black lines with symbols present the free time evolution of the particle-based model restarted after one HMM step. The unrestrained particle simulation restarted with the new configuration captures the behaviour of the original trajectory after time Δt indicating that the HMM

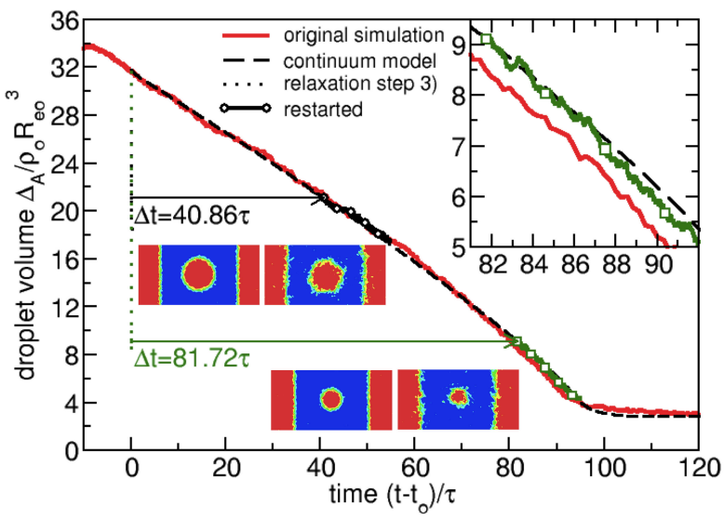

Figure 3. HMM of macrophase separation in a soft, coarse-grained model of an AB homopolymer blend, $\chi N = 5$. The inset presents an enlargement of the main panel. Snapshots illustrate configurations of the particle-based model (right) at $t_0 + 41\tau$ and $t_0 + 82\tau$ along the original time evolution and the corresponding configurations after the relaxation step 3) of one HMM-cycle. (left). Adapted from Ref. 44.

scheme also captured the decay of the composition across the B-matrix, which dictates the evaporation rate. In this example speed-ups of $\Delta t/\tau = 41$ and 82 are achieved with respect to SCMF simulations of the particle-based model[44].

5 Concluding Remarks

Soft, coarse-grained models are well suited to efficiently investigate the universal equilibrium behaviour of multicomponent polymer blends and copolymer materials in the liquid state. They can successfully address the relevant time and length scales of structure formation and allows us to systematically explore the structural and chemical diversity of multicomponent materials and provide structural and dynamic insights on the molecular level that are often not readily available in experiments. These models are a good starting point for investigating the collective dynamics of phase separation and self-assembly in nanostructured materials. Given the multitude of metastable states, there is a great potential in controlling and directing the dynamics of structure formation and identifying mechanisms of collective structure transformations. Due to the widely spread time and length scales, understanding and reliably predicting the practically important relation be-

tween the single-molecule dynamics and the kinetics of morphological changes remains a formidable challenge and computational techniques that seamlessly couple different levels of description will be instrumental in exploring how the collective dynamics can be tailored by the underlying motion of the molecules or application of external fields.

Acknowledgements

I am indebted to K. Ch. Daoulas, A.-C. Shi, J. J. de Pablo, Y. Smirnova, S. Glatz, G. Marelli, and M. Fuhrmans for fruitful and enjoyable collaborations. Financial support by the Volkswagen foundation and the SFB 803-B3 are gratefully acknowledged. I thank the Jülich Supercomputer Centre and the HLRN Hannover/Berlin for generous allocation of computational resources.

References

1. A. A. Louis, *Beware of Density Dependent Pair Potentials*, J. Phys.: Condens. Matter, **14**, 9187–9206, 2002.
2. P. J. Flory, *Thermodynamics of High Polymer Solutions*, J. Chem. Phys., **9**, 660, 1941.
3. M. L. Huggins, *Solutions of Long Chain Compounds*, J. Chem. Phys., **9**, 440, 1941.
4. I. Carmesin and K. Kremer, *The bond fluctuation method: a new effective algorithm for the dynamics of polymers in all spatial dimensions*, Macromolecules, **21**, 2819–2823, 1988.
5. M. Müller, *Miscibility Behavior and Single Chain Properties in Polymer Blends: a Bond Fluctuation Model Study*, Macromol. Theory Simul., **8**, 343–374, 1999.
6. G. S. Grest and K. Kremer, *Molecular dynamics simulations for polymers in the presence of a heat bath*, Phys. Rev. A, **33**, 3628, 1986.
7. M. Murat, G. S. Grest, and K. Kremer, *Statics and Dynamics of Symmetric Diblock Copolymers: a Molecular Dynamics Study*, Macromolecules, **32**, 595–609, 1999.
8. P. G. de Gennes, *Reptation of a polymer chain in presence of fixed obstacles*, J. Chem. Phys., **55**, 572, 1971.
9. M. Doi and S. F. Edwards, *The Theory of Polymer Dynamics*, Oxford University Press, New York, 1994.
10. M. Antonietti, J. Coutandin, and H. Sillescu, *Chain length and temperature dependence of self-diffusion coefficients in polystyrene*, Makromol. Chem., Rapid Comm., **5**, 525–528, 1984.
11. K. C. Daoulas and M. Müller, *Comparison of Simulations of Lipid Membranes with Membranes of Block Copolymers*, Adv. Polym. Sci., **224**, 197–233, 2010.
12. M. Laradji, H. Guo, and M. J. Zuckermann, *Off-lattice Monte Carlo simulation of polymer brushes in good solvent*, Phys. Rev. E, **49**, 3199, 1994.
13. K. Ch. Daoulas and M. Müller, *Single Chain in Mean Field simulations: Quasi-instantaneous field approximation and quantitative comparison with Monte Carlo simulations*, J. Chem. Phys., **125**, 184904, 2006.
14. F. A. Detcheverry, D. Q. Pike, P. F. Nealey, M. Müller, and J. J. de Pablo, *Monte Carlo simulation of coarse grain polymeric systems*, Phys. Rev. Lett., **102**, 197801, 2009.

15. M. Müller and G. D. Smith, *Phase separation in binary mixtures containing polymers: a quantitative comparison of Single-Chain-in-Mean-Field simulations and computer simulations of the corresponding multichain systems*, J. Polym. Sci. B: Polymer Physics, **43**, 934–958, 2005.
16. M. Müller, *Studying amphiphilic self-assembly with soft coarse-grained models*, J. Stat. Phys., **145**, 967, 2011.
17. M. Tuckerman, B. J. Berne, and G. J. Martyna, *Reversible multiple time scale molecular dynamics*, J. Chem. Phys., **97**, 1990, 1992.
18. K. Ch. Daoulas, M. Müller, J. J. de Pablo, P. F. Nealey, and G. D. Smith, *Morphology of Multi-Component Polymer Systems: Single-Chain-in-Mean-Field Simulation Studies*, Soft Matter, **2**, 573–583, 2006.
19. P. J. Rossky, J. D. Doll, and H. L. Friedman, *Brownian Dynamics as Smart Monte-Carlo Simulation*, J. Chem. Phys., **69**, 4628–4633, 1978.
20. F. G. Wang and D. P. Landau, *Efficient multiple-range random walk algorithm to calculate the density of states*, Phys. Rev. Lett., **86**, 2050–2053, 2001.
21. A. Laio and M. Parrinello, *Escaping free-energy minima*, Proc. Natl. Acad. Sci. USA, **99**, 12562–12566, 2002.
22. I. M. Lifshitz and V. V. Slyozov, *The kinetics of precipitation from supersaturated solid solutions*, J. Phys. Chem. Solids, **19**, 35, 1962.
23. J. W. Cahn, *Phase separation by spinodal decomposition in isotropic systems*, J. Chem. Phys., **42**, 93–99, 1965.
24. P. C. Hohenberg and B. I. Halperin, *Theory of dynamic critical phenomena*, Rev. Mod. Phys., **49**, 435–479, 1977.
25. U. M. B. Marconi and P. Tarazona, *Dynamic Density Functional Theory of Fluids*, J. Chem. Phys., **110**, 8032–8044, 1999.
26. K. Kawasaki and K. Sekimoto, *Dynamical theory of polymer melt morphology*, Physica A, **143**, no. 3, 349–413, 1987.
27. H. E. Cook, *Brownian motion in spinodal decomposition*, Acta Metallurgica, **18**, 297–306, 1970.
28. R. Petschek and H. Metiu, *Computer simulation of the time-dependent Ginzburg-Landau model for spinodal decomposition*, J. Chem. Phys., **79**, 3443–3456, 1983.
29. J. W. Cahn and J. E. Hilliard, *Free energy of a nonuniform system I: Interfacial free energy*, J. Chem. Phys., **28**, 258–267, 1958.
30. T. Ohta and K. Kawasaki, *Equilibrium Morphology of Block Copolymer Melts*, Macromolecules, **19**, 2621–2632, 1986.
31. J. Swift and P. C. Hohenberg, *Hydrodynamic fluctuations at the convective instability*, Phys. Rev. A, **15**, 319–328, 1977.
32. W. E, W. Ren, and E. Vanden-Eijnden, *Simplified and improved string method for computing the minimum energy paths in barrier-crossing events*, J. Chem. Phys., **126**, 164103, 2007.
33. W. E, B. Engquist, X. T. Li, W. Q. Ren, and E. Vanden-Eijnden, *Heterogeneous Multiscale Methods: A Review*, Comm. Computational Phys., **2**, 367–450, 2007.
34. W. E., W. Q. Ren, and E. Vanden-Eijnden, *A general strategy for designing seamless multiscale methods*, J. Comp. Phys., **228**, 5437–5453, 2009.
35. M. Müller, *Concurrent coupling between a particle simulation and a continuum description*, Eur. Phys. J. Special Topics, **177**, 149, 2009.

36. L. Maragliano and E. Vanden-Eijnden, *A temperature accelerated method for sampling free energy and determining reaction pathways in rare events simulations*, Chem. Phys. Lett., **426**, 168–175, 2006.
37. I. G. Kevrekidis, C. W. Gear, and G. Hummer, *Equation-Free: The computer-aided analysis of complex multiscale systems*, AICHE J., **50**, 1346–1355, 2004.
38. L. Maragliano and E. Vanden-Eijnden, *On-the-Fly string method for minimum free energy paths calculation*, Chem. Phys. Lett., **446**, 182–190, 2007.
39. M. Venturoli, E. Vanden-Eijnden, and G. Ciccotti, *Kinetics of phase transitions in two dimensional Ising models studied with the string method*, J. Math. Chem., **45**, 188–222, 2009.
40. M. Müller, Y. G. Smirnova, G. Marelli, M. Fuhrmans, and A. C. Shi, *Transition path from two apposed membranes to a stalk obtained by a combination of particle simulations and string method*, Phys. Rev. Lett., **108**, 228103, 2012.
41. M. Müller, K. Katsov, and M. Schick, *Coarse-Grained Models and Collective Phenomena in Membranes: Computer Simulation of Membrane Fusion*, J. Polym. Sci. B: Polymer Physics, **41**, 1441–1450, 2003.
42. Y. Kozlovsky and M. M. Kozlov, *Stalk model of membrane fusion: solution of energy crisis*, Biophys. J., **82**, 882–895, 2002.
43. M. Müller and J. J. de Pablo, *Computational approaches for the dynamics of structure formation in self-assembling polymeric materials*, Annu. Rev. Mater. Sci., **43**, submitted, 2013.
44. M. Müller and K. Ch. Daoulas, *Speeding up intrinsically slow collective processes in particle simulations by concurrent coupling to a continuum description*, Phys. Rev. Lett., **107**, 227801, 2011.

Modelling Atomic Scale Structure and Dynamics at Interfaces on Diffusive Timescales

Jörg Rottler

Department of Physics and Astronomy, The University of British Columbia,
6224 Agricultural Road, Vancouver, BC V6T 1Z1, Canada
E-mail: jrottler@phas.ubc.ca

1 Introduction

Many processes in materials physics occur near interfaces on diffusive timescales and involve mass transport driven by thermodynamic driving forces as well as long ranged elastic interactions. Important examples include liquid-solid transitions and dendritic growth, solid-solid phase transformations via grain boundary motion and coarsening, and adsorption and epitaxial growth at surfaces. All of these fall in a broader class of pattern formation phenomena that are out of reach for direct molecular modelling: in a crystal with lattice spacing a, the relevant timescale is set by the diffusivity a^2/D, which is many orders of magnitude slower than the phononic timescale a/c_s of molecular dynamics (MD). Efficient continuum level order parameter (phase field) methods are operating in the relevant regime, but are devoid of any atomistic level features. Key properties that govern the long time scale dynamics such as anisotropic surface energies or grain boundary mobilities can be obtained from atomistic calculations but must be put in by hand. Moreover, individual defects cannot be resolved but often play a key role, e.g. near grain boundary triple junctions or step edges.

The purpose of this article is to familiarize the reader with a new modelling paradigm that alleviates the difficulties described above by operating on atomic length and diffusive time scales. This Phase Field Crystal (PFC) method was introduced 10 years ago[1,2] and has since developed rapidly, as it has proved to be capable of capturing for instance grain boundary energies, grain boundary solidification, alloy thermodynamics, dislocation dynamics, elastic defect interactions, grain coarsening and plasticity on a scaling level. Quantitative results for specific metallic systems have also been obtained in selected cases. We will provide an introduction, a brief overview of some recent developments, selected applications that showcase the potential of the method as well as a discussion of outstanding challenges. Readers interested in further technical details may consult a comprehensive recent review article[3].

2 The Phase Field Crystal Concept

2.1 The Basic Idea

The basic premise of the PFC method is to consider energy functionals that are minimized by periodic density fields. One of the simplest possible forms for such a functional, origi-

nally due to Brazovskii[4], is

$$\beta\mathcal{F}[n(\vec{r})] = \int d^3r \left[\frac{n}{2}\left(r + \lambda(k_0^2 + \nabla^2)^2\right) n + u\frac{n^4}{4}\right], \tag{1}$$

where n is a reduced density and r and λ are parameters that can be related to the degree of undercooling (in the context of liquid-solid transitions) and elastic moduli. Due to the presence of the gradient terms, this functional is minimized by periodic states that match the wavevector k_0. In 2D, these include striped phases and triangular lattices while in 3D one can obtain bcc, fcc and hcp lattices. In polymer physics, these have been used for many years to model the rich phase behaviour of block copolymer melts[5], which can appear in lamellar, spherical, cylindrical phases, etc. The PFC model was created in a seminal paper by Elder and coworkers[1] with the (re)interpretation of n as (lightly) coarse grained atomic density field representing atoms on a periodic lattice with lattice spacing $a = 2\pi/k_0$. One is now in posession of a theory in which deviations from this "ground state" are penalized by elastic interactions. Specifically, defects in the form of dislocations and grain boundaries emerge naturally and automatically as "excitations". A simple conserved relaxational dynamics may be postulated that drives the system towards the ground state,

$$\frac{\partial n}{\partial t} = M\nabla^2\frac{\delta\mathcal{F}}{\delta n} \tag{2}$$

where M is a mobility parameter that sets the absolute timescale of the problem. The field dynamics is driven by the relaxation of the long ranged elastic interactions between defects; a polycrystal will coarsen until trapped in a metastable configuration or until it reaches a defect-free lattice. This from of relaxational dynamics is appropriate as the processes can be assumed to be overdamped.

Why is the above procedure faster than MD? The answer to this question can be understood by realizing that there are no stable vacancies in the PFC lattice. While topologically protected defects can only be removed by mutual annihilation, local density fluctuations relax rapidly as the model is phonon-free. The PFC dynamics does not explicitly represent the atomistic atom-vacancy exchange mechanism of diffusion, but instead averages over it so that the long-time dynamics is obtained. As a result, the method can indeed be viewed as simulating diffusive timescales, which is its principal advantage. A PFC simulation is, however, not simply a clever way of accelerating MD. An immediate consequence of Eq. 2 is that only the total density is conserved, but not individual peaks ("atoms") of the density field. The density modulation is also not sharply peaked at the equilibrium lattice positions, but varies much more smoothly than in a real solid. The PFC represents a material with the correct crystal symmetry and geometry, but is composed of "soft" atoms without a hard core. One can expect, however, that the peaks of the density field that minimizes the PFC equation does represent a physically relevant atomic configuration at the end of a nonequilibrium process.

2.2 Elementary Tests

Immediately after introducing the PFC model, Elder and Grant showed that a 2D PFC system possesses elastic moduli predicted from a single mode approximation of the ground state density field[2]. In order to show that the model also reproduces key properties of grain

boundaries and elastic strain effects, they calculated the grain boundary energy as a function of mismatch angle in a triangular lattice and showed that it matches the continuum elasticity result of Read and Shockley. The critical height for nucleation of a misfit dislocation in a growing film also agrees with the corresponding continuum prescription. These results give confidence in the basic promise of the PFC model as a theory for describing elastic effects in dynamical pattern formation problems.

2.3 Relationship to Classical Density Functional Theory

While the PFC free energy functional described so far is motivated on phenomenological grounds, it can also be viewed as a simplified version of the more formal classical density functional theory (CDFT). CDFT is a microscopic theory that expresses the free energy of a many-body system as a functional of the one-body particle density and has extensive applications in complex fluids. Several papers discuss in detail how the simpler PFC functional may be obtained formally from a general CDFT setup[6,7]. The salient point is that the functional can be recast in a form equivalent to the DFT of freezing introduced by Ramakrishnan and Yussouff (RY)[8]. In CDFT, one separates the free energy difference ΔF with respect to a uniform reference state into entropic contributions from an ideal gas and all other excess contributions. With $n(\vec{r}) = \rho(\vec{r})/\rho_o - 1$ describing the local deviation from a uniform reference density ρ_0 one writes,

$$\Delta F[n(\vec{r})] = \Delta F_{id}[n(\vec{r})] + \Delta F_{ex}[n(\vec{r})], \tag{3}$$

where

$$\frac{\Delta F_{id}}{\rho_o k_B T} = \int d\vec{r}[\rho(\vec{r})(\ln(\rho(\vec{r})) - 1)] \approx \int d\vec{r}\left[\frac{n(\vec{r})^2}{2} - \frac{n(\vec{r})^3}{6} + \frac{n(\vec{r})^4}{12}\right] \tag{4}$$

The local entropy term can be expanded up to forth order, thereby restricting the dimensionless density to small deviations from zero. The nonlocal excess part responsible for interactions can be expanded in a functional Taylor series. The RY approximation consists in truncating this series after the second term,

$$\frac{\Delta F_{ex}}{\rho k_B T} = -\frac{1}{2}\int d\vec{r}\, n(\vec{r}) \int d\vec{r'}\left[C_2(|\vec{r} - \vec{r'}|)n(\vec{r'})\right]. \tag{5}$$

In CDFT, the central object linking this theory to the microscopic structure is the *direct correlation function* $C_2(|\vec{r} - \vec{r'}|)$, which is assumed to be isotropic and formally related to the total correlation $h(r) = g(r) - 1$ of the fluid via the *Ornstein-Zernike equation*

$$\hat{C}_2(k) = \frac{\hat{h}(k)}{1 + \rho_0 \hat{h}(k)}. \tag{6}$$

Here the hat denotes the Fourier transform. These equations must be closed with approximations, which can lead for instance to the well-known Percus-Yevick formula for hard spheres. The PFC model Eq. 1 can also be viewed as an approximation in the form of a low-k expansion of the direct correlation function,

$$\hat{C}_2(k) = -r + 1 - (k_0 - k^2)^2, \tag{7}$$

or correspondingly in real space

$$C_2(|\vec{r} - \vec{r'}|) = (C_0 - C_1\nabla^2 + C_2\nabla^4)\delta(|\vec{r} - \vec{r'}|). \quad (8)$$

Despite this elegant derivation from the fundamental equations of CDFT, it is important to realize that the PFC model is not a microscopic theory. It does not use the true direct correlation function of the solid it attempts to model. Doing so is also not desired, as the resulting density field would vary so rapidly that an extremely fine discretization would be needed to integrate the equation of motion[9]. However, PFC captures the long wavelength properties of a solid very well. The question of how accurately it also describes short scale features is a topic of intense current research.

2.4 Refinement of the Functional

2.4.1 Multiple Modes

In a single mode approximation of the density field, the PFC functional as described above predicts a triangular lattice in 2D and a bcc structure in 3D. The full phase diagram determined from unconstrained energy relaxation does include regimes where close packed lattices (fcc/hcp) are stable, but the regions are rather narrow and accessing them requires fine tuning of parameters[10,11]. This limitation arises from the fact that the PFC direct correlation function in reciprocal space has only one peak and hence promotes growth of one single frequency only. It was shown many years ago[12] that approximating only the first peak in the static structure factor always leads to bcc lattices. In order to stabilize other structures, higher frequencies must be included. The comparison with CDFT shows that these frequencies should correspond to the magnitudes of the shortest reciprocal lattice vectors of the lattice of interest. Two extensions discussed in the literature realize this idea. Wu and Karma introduced a two-mode model for fcc lattices by considering the kernel function[13]

$$\hat{C}_2(k) = -r + 1 - \lambda(k_0 - k^2)^2(r_1 - (k_1 - k^2)^2), \quad (9)$$

The presence of the second frequency k_1 produces a phase diagram with a much wider fcc region. Greenwood et al.[14,15] also introduced multi-mode PFC kernels, in which each reciprocal lattice vector contributes a Gaussian peak of the form

$$C_2(k)_i = -r + \exp(-\sigma^2 k_i^2/2)\exp(-(k - k_i)^2/2\alpha_i^2). \quad (10)$$

The complete kernel is then obtained as an envelope to the Gaussian peaks. A representation in reciprocal space is also numerically advantageous as FFT methods can be used to evaluate the convolution integrals. The parameters in this model provide a significant amount of flexibility for simulating materials phenomena. The Debye-Waller like prefactor $\exp(-\sigma^2 k_i^2/2)$ introduces a temperature parameter σ that modulates the relative peak heights. In this way, phase transformations from one lattice symmetry to another can be realized through temperature quenches. The Gaussian widths α_i control the energy for defects and the surface tension. For instance, the liquid solid interface width $W_i \propto \alpha_i^{-1}$ and the elastic constants $\propto \alpha_i^{-2}$. Even the degree of elastic anisotropy can be tuned by varying the ratio α_1/α_2. Greenwood et al. showed that this form of the PFC model realizes square lattices in 2D as well as fcc and hcp lattices in 3D with maximally three peaks at the lowest reciprocal lattice vectors[15]. This strategy even describes stable 2D quasicrystals with 5 and 7-fold symmetry[16].

2.4.2 Anisotropic Interactions

All PFC models discussed so far exhibit rotational invariance, i.e. the free energy functional is independent of the lattice orientation. While this is an advantage when modelling polycyrstals composed of multiple grains, there are other materials where the constituents are anisotropic, e.g. ellipsoidal colloids. Directional anisotropy can be introduced by replacing $k^2 \rightarrow \sum_{ij} a_{ij} k_i k_j$ and $k^2 \rightarrow \sum_{ijkl} b_{ijkl} k_i k_j k_l k_m$ with a_{ij} and b_{ijkl} appropriate 2nd and 4th rank elastic tensors[17].

2.4.3 Orientable Particles

Free energies that aim to capture the rich physics of liquid crystals require the introduction of additional order parameters that depend on the orientation $\mathbf{u}_i$ of particle i. The functional then contains terms that include not only the translational density, but also the polarization P_i describing the average orientational order and the nematic tensor Q_{ij} that couples to quadrupolar order in nematics[18,19]. A plethora of phases including nematic and smectic phases emerges from the resulting gradient expansion of the free energy that are only beginning to be explored[20].

2.4.4 Binary Alloys

An important rationale for using PFC modelling over MD is its ability to include thermodynamic driving forces that lead to compositional segregation and patterning through diffusive processes. From an engineering standpoint, alloys are far more important in structural applications than pure materials. A generalized functional for binary (AB) alloys was introduced by Elder et al.[6] and refined in later works[21,22]. The entropic component of the free energy now contains the sum of the ideal free energy of the individual density fields ρ_A and ρ_B,

$$\frac{\Delta F_{id}}{k_B T} = \rho_A \ln(\rho_A/\rho_A^o) - \delta\rho_A + \rho_B \ln(\rho_B/\rho_B^o) - \delta\rho_B \tag{11}$$

while the excess term describes interactions between the two density fields

$$\frac{\Delta F_{ex}}{k_B T} = \sum_{ij} \Delta F_{ij} = -\frac{1}{2} \sum_{ij} \delta\rho_i(r) \int dr' C_2^{ij}(|\vec{r} - \vec{r'}|) \delta\rho_j(r') \tag{12}$$

Here the sum is taken over the pairwise interactions AA, AB and BB, resp. It is convenient to recast these equations in terms of the total density $n = (\rho_A + \rho_B)/(\rho_A^o + \rho_B^o) - 1$ and the solute concentration field $c = \rho_B/(\rho_A + \rho_B)$. One can now make the approximation that the solute concentration varies more slowly than the atomic density field. After some modifications one can obtain the form[22]

$$\begin{aligned} \Delta F = \int dr \Bigg\{ & \frac{n^2}{2} - \frac{n^3}{6} + \frac{n^4}{12} + (n+1)\Delta F_{mix}(c) \\ & - \frac{1}{2} n \int dr' C_{\text{eff}}^n(|r - r'|) n' + \alpha |\vec{\nabla} c|^2 \Bigg\} \end{aligned} \tag{13}$$

where $\Delta F_{mix}(c)$ denotes the entropy of mixing,

$$\Delta F_{mix}(c) = \left\{ c \ln\left(\frac{c}{c_o}\right) + (1-c)\ln\left(\frac{1-c}{1-c_o}\right)\right\} \tag{14}$$

and the form of the effective correlation function $C^n_{\text{eff}}(|\vec{r}-\vec{r'}|)$ can be chosen to interpolate conveniently between the pure density fields. One may view Eq. 13 as a modified Cahn-Hilliard model plus a PFC contribution that provides symmetry and geometry of the crystalline phase. As in the one-component PFC model, vacancies are delocalized so that concentration gradients equilibrate rapidly due to chemical and elastic driving forces.

2.4.5 Propagative Dynamics for Driven Systems

In the dynamics of Eq. 2, density and elastic interactions relax on the same timescale. While this approximation is reasonable for equilibrium calculations and coarsening, it surely fails when the material is plastically deformed. It is possible to reintroduce a separation of timescales and enable elastic modes to propagate much faster than density modes by considering propagative (i.e. wavelike) dynamics,i.e.

$$\frac{\partial^2 n}{\partial t^2} + \beta \frac{\partial n}{\partial t} = \alpha^2 \nabla^2 \frac{\delta \mathcal{F}}{\delta n} \tag{15}$$

where the parameters α and β are related to the sound speed and damping rate[23]. At this point, a fundamental advantage over MD becomes obvious: the sound speed is not a consequence of interaction potential, temperature and density, but instead a tunable parameter. With this modification, it is possible to shrink the large gap between phononic and diffusional timescales by simulating a material with an effective sound speed much slower than the physical sound speed. This approximation is justified as long as elastic modes still propagate fast enough so that the interaction is quasiinstantaneous. Similar ideas are used in Car-Parrinello dynamics[24] for electronic degrees of freedom and local Coulomb algorithms for MD[25].

3 Selected Applications

The following examples are chosen to give an impression of the class of problems that can be successfully addressed with the PFC framework. It is not a comprehensive review of all PFC studies performed to date.

3.1 Nucleation and Growth

Many first order phase transitions begin with the nucleation and growth of a daughter phase in the parent phase. The PFC model as a simplified density functional theory can provide insight into atomistic aspects of these processes in the diffusion controlled regime. One of the properties that can be calculated relatively easily is the nucleation barrier as function of size of the nucleus[26]. Since this is an equilibrium property, it can be obtained directly from the extremal solution of the free energy functional (Euler-Lagrange equation) and does not require integrating the equations of motion[11,27]. The nuclei are faceted as the free

energy landscape has many local minima from different crystallographic orientations. This method can also be used to compute the phase diagram and the structure of the precursors to nucleation. Alternatively, one can use the dynamical Eq. 2 and add conserved white noise to kick the system over metastable energy barriers. Among the predictions for the nucleation pathways that emerge are amorphous precursors to stable bcc nuclei[28]. Studies of heterogeneous nucleation, e.g. in the presence of a substrate, are also possible[29].

In the ensuing growth of the clusters, the PFC model naturally incorporates anisotropic growth in different crystallographic directions due to its atomistic nature[27]. It also predicts interesting dynamical transitions between slow and fast growth modes that when combined can lead to alternating faceted dendritic growth and fractal like patterns. Rich behaviour can also be observed when nucleation and clustering takes place in alloys[30]. Here the binary PFC model reveals the importance of dislocations in lowering the nucleation barrier for precipitates, an effect that is intimately coupled with the diffusive relaxation of the concentration fields in the presence of the strain field of the quenched defects.

3.2 Surface Physics

A second set of problems ideally suited for PFC modelling is the morphology and dynamics of (sub)monolayers coupled to a substrate with differing lattice parameter and/or symmetry. Such systems can be described by adding a substrate-monolayer interaction term of the form $V(x)n(x)$ to the free energy, where $V(x)$ describes the substrate potential. The resulting scenario resembles in many ways the well-known Frenkel-Kontorowa model, but includes plasticity and defects in a self-consistent way. Several studies explored the phase diagram of such commensurate/incommensurate transition as well as depinning transitions and sliding friction[31–33]. The emergence of highly disordered glassy phases was also observed[34]. For a monolayer adsorbed on quasicrystalline surfaces with 5-and 7-fold symmetry, a PFC simulation predicted the sequence of film morphologies as the interaction strength was varied from a freely floating film to a strongly adsorbed isomorphic structure[16]. These studies also showcase the computational efficiency with which a broad range of parameters can be quickly explored with the PFC model. An alternative investigation via particle-based Monte Carlo or MD would require significantly more effort than the (fast) minimization of the PFC functional.

In semiconductor heteroepitaxy, it is very important to understand the effect of strain on the morphology of the growing film. Here the PFC model can provide a general overview of the types of instabilities that may lead to the formation of islands, which is relevant for the fabrication of quantum dots[35,36]. Although these calculations are not yet material specific, they provide valuable trends and give insight into the limitations of continuum elasticity theory.

Two recent studies showcase the complexity of phases that can emerge from the interplay between alloy thermodynamics and elastic interactions. Muralidharan and Haataja considered a monolayer film of CoAg on a Ru(0001) surface and found nanoscale domain formation upon carefully matching the PFC parameters to experimental values[37]. A subsequent study explored strained alloys on quasicrystalline surfaces[38]. Elder et al. implemented a similar approach for the metal/metal systems Cu on Ru(0001) and P(111) and obtained various superstructures of stripe, honeycomb and triangular symmetry[39]. In both studies the agreement with experiment is striking, which shows that quantitative PFC modelling is possible at least for metals without directional bonding.

3.3 Grain Boundary Phenomena

Controlling the distribution of grain sizes is one of the core engineering challenges in physical metallurgy as the grain microstructure determines the mechanical properties of the material. When quenched from the melt, a PFC material will crystallize into multiple grains that merge and coarsen over time. The grain boundary (GB) mobilities and surface energies that control the coarsening dynamics depend on the atomic level structure of the interface and emerge in the PFC model automatically without further input. The GB dynamics in metals is always overdamped and therefore an ideal match for the PFC model. The refinements outlined in the previous section permit the simulation of fairly complex thermal histories. As a 2D example, Greenwood et al. studied a thermal quench from a liquid phase into a region of the phase diagram where triangular lattice symmetry is stable, which leads to the formation of polycrystal with triangular grains. After a second quench into a region where square symmetry has the lower free energy[14], grains with square symmetry nucleated at the triple junctions of the grains and coarsened into the triangular lattice. Other studies have explored some of the properties of static GBs, in particular the melting of GBs a function of mismatch angle[40,41]. Systematic studies of GB mobilities would also be very useful as they could provide important validation that all relevant atomic scale processes are captured in the PFC model.

3.4 Plasticity

One of the most exciting prospects of PFC modelling is an application to crystal plasticity. It is clear that the fundamental atomistic process underlying plastic deformation of crystals, dislocation glide, is captured correctly. An extensive study by Berry et al. on sheared 2D PFCs showed that dislocations possess a Peierls barrier and switch from stick-slip motion to continuous glide as the rate of deformation is increased[42]. The collective critical behaviour of multiple dislocations was explored in the work of Chan et al. [43] The authors employed the propagative dynamics Eq. 15 and studied the distribution of avalanche sizes in steadily sheared 2D triangular crystal. Dislocations emerge in bursts and mutually annihilate each other due to rapid glide. The size distribution of the energy drops follows a power law in agreement with a mean-field model in close analogy to the intermittent dynamics of earthquakes.

In the above example, the PFC simulation behaves essentially like a MD simulation as diffusive processes are not important for plasticity. A powerful rationale for future work would be to study plasticity problems that also involve aspects of dislocation climb. All MD simulations to date miss such processes since vacancy diffusion is too slow. As a result, the yield stress is often higher than in experiments. Although dislocation climb does occur readily in the PFC model, it is unfortunately at present not known how to systematically control the climb rate.

3.5 Binary Alloys

Immediately after introducing the binary alloy PFC model, Elder and coworkers applied it to one of the paradigmatic multiscale problems: eutectic solidification[6]. Due to phase separation, the concentration field often forms lamellar bands with a periodicity that is several orders of magnitude larger than the atomic length scale. The beauty of the PFC method

is that both scales can be included in a single simulation. Atomic scale density variations are resolved at the liquid solid interface, but the method is efficient enough that multiple lamellae can be simulated in a periodic simulation box. The PFC description can be further coarse-grained using a technique called amplitude expansions. With this approach, intrinsically atomistic processes emerge such as the segregation of solute concentration towards dislocations that nucleate at the lamellar boundaries[44].

Being based on a regular solution model, the phase diagram of the PFC alloy captures all main qualitative features of eutectic phase diagrams[22]. The flexibility of the multi-mode PFC free energies opens up the possibility of modelling rather complex scenarios. Greenwood et al. studied 2D lamellar growth in a two-component alloy where the two components individually prefer triangular and square symmetry. As the misorientation between the lamellae is altered, the coarsening rate and lamellar spacing changes as a result of different surface tensions and elastic interactions at the interfaces between the lamellae. It is important to realize that the PFC model captures these effects automatically and self-consistently without further fitting parameters[22].

Another example of a problem that combines alloy thermodynamics with diffusive dynamics is solute drag. This dynamical effect is important for GB migration and refers to the lowering of GB mobilities due to the addition of solutes and is exploited in practical engineering applications to control the grain size. As the solute segregates towards the GB, the moving GB is surrounded by a cloud of solute concentration that may impede its motion. The PFC model is able to capture all main aspects of this phenomenon and permits a study of the deformation of the solute cloud with increasing driving pressure[45]. It resolves locally inhomogeneous structure of the boundaries, but still shows good agreement with classical continuum theories.

4 Current Status, Opportunities and Challenges

Given the simplicity of the PFC free energy functional Eq. 1, the breadth of materials phenomena that can be described with it is quite remarkable. It fulfils in many ways the physicist's aspiration of a unifying and universal theory that explains natural phenoma on the basis of symmetry, geometry, and dimensionality alone. The beauty of this result cannot be questioned. The PFC approach is extremely powerful in providing a computationally efficient overview of possible emergent structures controlled by elasticity in concert with thermodynamics. Especially in the context of surface physics, experiments have been explained[39] and predictions have been made that can be experimentally challenged[16,38].

Despite these successes, it is important to realize also some of the limitations of PFC modelling. One of the more serious ones is well revealed in the CDFT inspired formulation: the excess free energy expansion is truncated at 2nd order and neglects multibody correlations. This approximation may appear arbitrary already at the liquid-solid interface and even more so in the highly ordered solid state. So far no serious attempts have been made to include such higher order terms, mainly because they would surely have a detrimental effect on computational efficiency. Even on the level of the RY approximation, there is an inherent tension in finding direct correlation functions that optimize both crystal stability and defect stability. This effect was showcased explicitly in recent work by Berry et al., who found that dislocations in fcc crystals only emerged with the correct properties when relatively broad (in reciprocal space) direct correlation functions

were used that permit the simultaneous coexistence of many frequencies[46]. By contrast, multi-mode PFC models that stabilize bulk phases more easily have difficulties describing split-partial dislocations correctly. These results point to inherent limitations in the PFC method to accurately model highly local properties in solids.

A second challenge consists in transcending beyond scaling level results and turn the PFC model into a quantitatively predictive tools for modelling of real materials. At present it is possible to fit PFC parameters to lattice symmetry, bulk elastic constants, and surface energies. Some studies have made explicit efforts to match material specific parameters[37]. We have also learned how to control the stacking fault energy, but it may prove difficult to capture more local properties without addition of many more parameters. In this regard, a clearer link to an atomistic pair potential would be helpful. Despite these challenges, the PFC model is a promising complementary method to MD when atomic displacements couple explicitly to diffusional processes. The amplitude expansion formalism[44] furthermore serves as a starting point for improved phase field models.

Acknowledgements

I thank my colleagues J. Berry, M. Greenwood, N. Provatas and C. Sinclair for a wonderful collaboration on PFC fundamentals and applications. This work has benefited from many stimulating discussions with K. A. Dahmen, N. Goldenfeld, M. Haataja, K. R. Elder, M. Militzer, and D. J. Srolovitz. Financial support from the Natural Science and Research Council of Canada (NSERC) is gratefully acknowledged.

References

1. K. R. Elder, M. Katakowski, M. Haataja, and M. Grant, *Modeling Elasticity in Crystal Growth*, Phys. Rev. Lett., **88**, no. 24, 245701, June 2002.
2. K. R. Elder and M. Grant, *Modeling elastic and plastic deformations in nonequilibrium processing using phase field crystals*, Phys. Rev. E, **70**, no. 5, 051605, Nov. 2004.
3. H. Emmerich, H. Löwen, R. Wittkowski, T. Gruhn, G. I. Tóth, G. Tegze, and L. Gránásy, *Phase-field-crystal models for condensed matter dynamics on atomic length and diffusive time scales: an overview*, Advances in Physics, **61**, no. 6, 665–743, 2012.
4. S. A. Brazovskii, Zh. Eksp. Teor. Fiz, **68**, 175, 1975.
5. G. H. Fredrickson and K. Binder, *Kinetics of metastable states in block copolymer melts*, The J. Chem. Phys., **91**, no. 11, 7265–7275, Dec. 1989.
6. K. R. Elder, N. Provatas, J. Berry, P. Stefanovic, and M. Grant, *Phase-field crystal modeling and classical density functional theory of freezing*, Phys. Rev. B, **75**, no. 6, 064107, Feb. 2007.
7. S. van Teeffelen, R. Backofen, A. Voigt, and H. Löwen, *Derivation of the phase-field-crystal model for colloidal solidification*, Phys. Rev. E, **79**, no. 5, 051404, May 2009.
8. T. V. Ramakrishnan and M. Yussouff, *First-principles order-parameter theory of freezing*, Phys. Rev. B, **19**, no. 5, 2775–2794, Mar. 1979.

9. A. Jaatinen, C. V. Achim, K. R. Elder, and T. Ala-Nissila, *Thermodynamics of bcc metals in phase-field-crystal models*, Phys. Rev. E, **80**, no. 3, 031602, Sept. 2009.
10. A. Jaatinen and T. Ala-Nissila, *Extended phase diagram of the three-dimensional phase field crystal model*, J. Phys.: Condens. Matter, **22**, no. 20, 205402, May 2010.
11. G. I. Tóth, G. Tegze, T. Pusztai, G. Tóth, and L. Gránásy, *Polymorphism, crystal nucleation and growth in the phase-field crystal model in 2D and 3D*, J. Phys.: Condens. Matter, **22**, no. 36, 364101, Sept. 2010.
12. S. Alexander and J. McTague, *Should All Crystals Be bcc? Landau Theory of Solidification and Crystal Nucleation*, Phys. Rev. Lett., **41**, no. 10, 702–705, Sept. 1978.
13. K.-A. Wu, A. Adland, and A. Karma, *Phase-field-crystal model for fcc ordering*, Phys. Rev. E, **81**, no. 6, 061601, June 2010.
14. M. Greenwood, N. Provatas, and J. Rottler, *Free Energy Functionals for Efficient Phase Field Crystal Modeling of Structural Phase Transformations*, Phys. Rev. Lett., **105**, no. 4, 045702, July 2010.
15. M. Greenwood, J. Rottler, and N. Provatas, *Phase-field-crystal methodology for modeling of structural transformations*, Phys. Rev. E, **83**, no. 3, 031601, Mar. 2011.
16. J. Rottler, M. Greenwood, and B. Ziebarth, *Morphology of monolayer films on quasicrystalline surfaces from the phase field crystal model*, J. Phys.: Condens. Matter, **24**, no. 13, 135002, Apr. 2012.
17. R. Prieler, J. Hubert, D. Li, B. Verleye, R. Haberkern, and H. Emmerich, *An anisotropic phase-field crystal model for heterogeneous nucleation of ellipsoidal colloids*, J. Phys.: Condens. Matter, **21**, no. 46, 464110, Nov. 2009.
18. H. Löwen, *A phase-field-crystal model for liquid crystals*, J. Phys.: Condens. Matter, **22**, no. 36, 364105, Sept. 2010.
19. R. Wittkowski, H. Löwen, and H. R. Brand, *Derivation of a three-dimensional phase-field-crystal model for liquid crystals from density functional theory*, Phys. Rev. E, **82**, no. 3, 031708, Sept. 2010.
20. C. V. Achim, R. Wittkowski, and H. Löwen, *Stability of liquid crystalline phases in the phase-field-crystal model*, Phys. Rev. E, **83**, no. 6, 061712, June 2011.
21. N. Provatas and S. Majaniemi, *Phase-field-crystal calculation of crystal-melt surface tension in binary alloys*, Phys. Rev. E, **82**, no. 4, 041601, Oct. 2010.
22. M. Greenwood, N. Ofori-Opoku, J. Rottler, and N. Provatas, *Modeling structural transformations in binary alloys with phase field crystals*, Phys. Rev. B, **84**, no. 6, 064104, Aug. 2011.
23. P. Stefanovic, M. Haataja, and N. Provatas, *Phase-Field Crystals with Elastic Interactions*, Phys. Rev. Lett., **96**, no. 22, 225504, June 2006.
24. R. Car and M. Parrinello, *Unified Approach for Molecular Dynamics and Density-Functional Theory*, Phys. Rev. Lett., **55**, no. 22, 2471–2474, Nov. 1985.
25. J. Rottler and A. C. Maggs, *Local Molecular Dynamics with Coulombic Interactions*, Phys. Rev. Lett., **93**, no. 17, 170201, Oct. 2004.
26. R. Backofen and A. Voigt, *A phase-field-crystal approach to critical nuclei*, J. Physics: Condens. Matter, **22**, no. 36, 364104, Sept. 2010.
27. G. Tegze, L. Gránásy, G. I. Tóth, F. Podmaniczky, A. Jaatinen, T. Ala-Nissila, and T. Pusztai, *Diffusion-Controlled Anisotropic Growth of Stable and Metastable Crystal Polymorphs in the Phase-Field Crystal Model*, Phys. Rev. Lett., **103**, no. 3, 035702, July 2009.

28. G. I. Tóth, T. Pusztai, G. Tegze, G. Tóth, and L. Gránásy, *Amorphous Nucleation Precursor in Highly Nonequilibrium Fluids*, Phys. Rev. Lett., **107**, no. 17, 175702, Oct. 2011.
29. G. I. Tóth, G. Tegze, T. Pusztai, and L. Gránásy, *Heterogeneous Crystal Nucleation: The Effect of Lattice Mismatch*, Phys. Rev. Lett., **108**, no. 2, 025502, Jan. 2012.
30. V. Fallah, J. Stolle, N. Ofori-Opoku, S. Esmaeili, and N. Provatas, *Phase-field crystal modeling of early stage clustering and precipitation in metal alloys*, Phys. Rev. B, **86**, no. 13, 134112, Oct. 2012.
31. C. V. Achim, M. Karttunen, K. R. Elder, E. Granato, T. Ala-Nissila, and S. C. Ying, *Phase diagram and commensurate-incommensurate transitions in the phase field crystal model with an external pinning potential*, Phys. Rev. E, **74**, no. 2, 021104, Aug. 2006.
32. C. V. Achim, J. A. P. Ramos, M. Karttunen, K. R. Elder, E. Granato, T. Ala-Nissila, and S. C. Ying, *Nonlinear driven response of a phase-field crystal in a periodic pinning potential*, Phys. Rev. E, **79**, no. 1, 011606, Jan. 2009.
33. J. A. P. Ramos, E. Granato, S. C. Ying, C. V. Achim, K. R. Elder, and T. Ala-Nissila, *Dynamical transitions and sliding friction of the phase-field-crystal model with pinning*, Phys. Rev. E, **81**, no. 1, 011121, Jan. 2010.
34. E. Granato, J. A. P. Ramos, C. V. Achim, J. Lehikoinen, S. C. Ying, T. Ala-Nissila, and K. R. Elder, *Glassy phases and driven response of the phase-field-crystal model with random pinning*, Phys. Rev. E, **84**, no. 3, 031102, Sept. 2011.
35. Z.-F. Huang and K. R. Elder, *Mesoscopic and Microscopic Modeling of Island Formation in Strained Film Epitaxy*, Phys. Rev. Let., **101**, no. 15, 158701, Oct. 2008.
36. Z.-F. Huang and K. R. Elder, *Morphological instability, evolution, and scaling in strained epitaxial films: An amplitude-equation analysis of the phase-field-crystal model*, Phys. Rev. B, **81**, no. 16, 165421, Apr. 2010.
37. S. Muralidharan and M. Haataja, *Phase-Field Crystal Modeling of Compositional Domain Formation in Ultrathin Films*, Phys. Rev. Lett., **105**, no. 12, 126101, Sept. 2010.
38. S. Muralidharan, R. Khodadad, E. Sullivan, and M. Haataja, *Multilayer thin film growth on crystalline and quasicrystalline surfaces: A phase-field crystal study*, Phys. Rev. B, **85**, no. 24, 245428, June 2012.
39. K. R. Elder, G. Rossi, P. Kanerva, F. Sanches, S-C. Ying, E. Granato, C. V. Achim, and T. Ala-Nissila, *Patterning of Heteroepitaxial Overlayers from Nano to Micron Scales*, Phys. Rev. Lett., **108**, no. 22, 226102, May 2012.
40. J. Berry, K. R. Elder, and M. Grant, *Melting at dislocations and grain boundaries: A phase field crystal study*, Phys. Rev. B, **77**, no. 22, 224114, June 2008.
41. J. Mellenthin, A. Karma, and M. Plapp, *Phase-field crystal study of grain-boundary premelting*, Phys. Rev. B, **78**, no. 18, 184110, Nov. 2008.
42. J. Berry, M. Grant, and K. R. Elder, *Diffusive atomistic dynamics of edge dislocations in two dimensions*, Phys. Rev. E, **73**, no. 3, 031609, Mar. 2006.
43. Pak Yuen Chan, Georgios Tsekenis, Jonathan Dantzig, Karin A. Dahmen, and Nigel Goldenfeld, *Plasticity and Dislocation Dynamics in a Phase Field Crystal Model*, Phys. Rev. Lett., **105**, no. 1, 015502, June 2010.
44. K. R. Elder, Z.-F. Huang, and N. Provatas, *Amplitude expansion of the binary phase-field-crystal model*, Phys. Rev. E, **81**, no. 1, 011602, Jan. 2010.

45. M. Greenwood, C. Sinclair, and M. Militzer, *Phase field crystal model of solute drag*, Acta Materialia, **60**, no. 16, 5752–5761, Sept. 2012.
46. J. Berry, N. Provatas, J. Rottler, and C. W. Sinclair, *Defect stability in phase-field crystal models: Stacking faults and partial dislocations*, arXiv:1210.1527, Oct. 2012.

Methods for Multiscale Quantum/Atomistic Coupling

William A. Curtin

Laboratory for Multiscale Mechanics Modeling, Institute of Mechanical Engineering,
École Polytechnique Fédérale de Lausanne, CH-1015 Lausanne, Switzerland
E-mail: william.curtin@epfl.ch

Multiscale coupling of quantum mechanical (QM) domains to domains having a coarser-scale material description is necessary for non-periodic problems that may also involve long-range deformation fields such as caused by dislocations or crack tips. The goal of a multiscale method is to compute the interactions of the quantum domain with the surrounding domain with the same accuracy as would be obtained if the surrounding domain were fully quantum mechanical. The QM domain inevitably requires some type of cluster calculation, and the major errors then stem from electronic effects at the cluster surface extending into the cluster interior and generating spurious forces and incorrect physical configurations. Here, we discuss two recent methods to achieve robust coupling using full Kohn-Sham DFT methods. The first method uses a thick buffer region of quantum ions and electrons in which the ionic displacements are determined by elasticity or atomistic methods. The second method uses the concept of constrained DFT to force the electronic configuration near the outer boundary of the cluster to be identical to an approximate bulk electronic charge density, with the ion positions again controlled by elasticity or atomistic methods. The success of the two methods is demonstrated through application to several simple test problems.

1 Introduction

Despite ever increasing computational power, modelling and simulation of complex materials at the atomic level remains an enormous challenge. Quantum mechanical (QM) calculations are essential for treating chemical reactions, charge transfer, electron excitation, and magnetism, but are often so expensive that no more than a few hundreds atoms can be handled. For problems involving long-range deformations, such as due to dislocations or crack tips, a few hundred atoms is woefully insufficient to obtain accurate results. Thus, multiscale methods that couple a quantum domain to a surrounding domain treated by less-expensive methods, such as interatomic potentials or elasticity theory, have been actively pursued over the last decade[1–9]. For metallic systems, the highly delocalized electrons and a long-ranged density matrix[10] pose a particular challenge for any multiscale method. One feature of the coupling that is particularly difficult is the capturing of the non-additive kinetic energy of the system when only one portion is described quantum mechanically. One solution for the latter problem is to use Orbital-Free DFT[11–17] – a true DFT method – but which is confined, to date, to only a few materials for which the approximate kinetic energy functionals and local pseudopotentials are sufficiently accurate. The ultimate goal is to obtain a method that provides the accuracy of standard Kohn-Sham DFT. In this paper, we present two recent multiscale approaches that use Kohn-Sham DFT and several coupling approaches to capture the non-additive kinetic energy and thereby generate proper forces and quantum energies within a quantum domain of interest[18,19]. We emphasize here some commonalities between the two methods, and present some limited results to demonstrate that they provide robust and accurate coupling strategies using full Kohn-Sham DFT.

2 Multiscale Methods: Energies and Forces

We start from the premise that the goal of the multiscale method is first to accurately capture the deformation (ion positions and electron density) in some specified QM domain, and second to provide an accurate estimate of the total energy of the entire system or the energy change due to some local phenomenon. An alternative viewpoint is often taken wherein a single total energy functional of the coupled system is defined, from which the configurational forces on each ion are derived directly. While preferable in principle, in a multiscale method involving two fundamentally different descriptions of the material, there are inevitably errors in the energy in the regions near the interface between the QM and non-QM domain, and these errors lead to errors in forces, which then lead to incorrect ionic positions and incorrect electron densities. Thus, while the energy and force are self-consistently determined, the ground-state solution for the problem is not accurate. By developing a method where forces and deformation are captured accurately, we take the viewpoint that the estimated energy for the accurate configuration is preferable to a very accurate energy for an incorrect configuration.

We consider a single-crystal-elemental metal containing a region where QM accuracy is required. The multiscale methods discussed here start by identifying three domains of ions/atoms, as shown schematically in Fig. 1. An inner domain labelled as Region I, contains all defects, chemical interactions and inelastic behaviour and will be described fully by QM methods. An outer domain labelled as Region III surrounds the defective region and captures the deformation fields caused by the defects in Region I and transfers the externally-applied loads/deformations into Region I. An intermediate domain, Region II, lies between Regions I and III, and is the domain through which Regions I and III are coupled. Like Region III, Region II must have small deformations, no defects, and no chemical reactions. We then define two energy functionals, one for the combination of Regions I and II and one for the combination of Regions I, II and III. The energy of Region

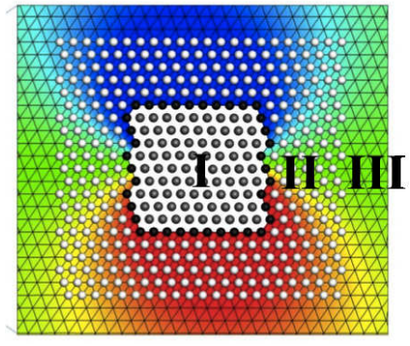

Figure 1. Schematic division of a large domain into Regions I, II, and III. Region III shows only mesh nodal points at the locations of ions. The black circled ions merely indicate the outer boundary of Region I.

I+II is computed as a function of the ion positions $\{R_i\}$ $i \in$ I, II via a QM method,

$$E^{\text{I+II}} = E^{\text{QM}}(\{R_i\}, i \in \text{I, II}) \,. \tag{1}$$

The energy of Regions I+II+III is computed as a function of the ion positions $\{R_i\}$ $i \in$ I, II, III and is computed using a classical method (interatomic potentials[20]; elasticity via finite elements; elasticity via Green's functions[21]; hyperelasticity using finite elements and the Cauchy-Born rule[22]),

$$E^{\text{I+II+III}} = E^{\text{cl}}(\{R_i\}, i \in \text{I, II, III}) \,. \tag{2}$$

Note that these two energies both include Regions I and II.

The forces on ions in Regions II and III are computed using the classical energy functional, which is reasonable because the deformations in these two domains are small so that elasticity (or hyperelasticity) is valid. That is, the forces on an ion in Region II or III is given by

$$f_i = -\frac{\partial E^{\text{I+II+III}}}{\partial R_i} = -\partial E^{\text{cl}}(\{R_j\}, j \in \text{I, II, III})/\partial R_i \; i \in \text{II, III} \,, \tag{3}$$

where the ions in Region I are fixed at the positions dictated by the QM calculation on Regions I+II. The forces on ions in Region I are computed using the QM energy functional, so that

$$f_i = -\frac{\partial E^{\text{QM}}}{\partial R_i} = -\partial E^{\text{QM}}(\{R_j\}, j \in \text{I, II})/\partial R_i \; i \in \text{I} \,, \tag{4}$$

where the ions in Region II are fixed at the positions dictated by the classical calculation on Regions I+II+III. The QM forces on ions in Region II are ignored – they are not accurate because these ions are close to an outer vacuum domain and the QM forces are not those that these ions would experience in the full system. The classical forces in Region I are ignored – they are not accurate because this region experiences deformation and chemistry that are outside the validity of the classical method. Given the forces on each ion as computed above, the ionic configuration of the entire system is incrementally evolved using a convenient numerical scheme (conjugate gradient; steepest descents; etc). After each incremental step of ion displacements, new forces are computed using the new ionic configurations derived from the current energy functional.

From a mechanics viewpoint, the coupling is achieved by imposed ionic/atomic displacement boundary conditions in each problem. In each increment, the QM problem is executed while holding Region II ions at the current positions dictated by the classical problem while the classical problem is executed while holding the Region I ions at the current positions dictated by the QM problem. By using ionic positions as boundary conditions, the proper forces are generated on the various domains using the same energy functional: Region I ions are driven by QM forces derived from the positions of the Region II ions while Region II and III ions are driven by classical forces derived from the positions of the Region I ions. Such an iterative incremental scheme generally eliminates the occurrence of so-called "ghost forces" that emerge when attempting to use a single energy functional for the entire system.

Once the entire system has been driven to equilibrium, i.e. zero forces on all ions in the entire system, the energy of the entire system can be estimated, if necessary. Note, however, that calculation of the entire energy is not necessary to achieve the equilibrium

configuration. Unfortunately, the QM energy cannot be decomposed into an ion-by-ion energy. Therefore, the energy E^{QM}(I+II) must be used in its entirety, which can thus include spurious energies due to any electronic relaxations at the outer surfaces of the cluster-type QM calculation. However, the classical energy is easily decomposed into an atom-by-atom energy E_i^{cl} for any ion/atom i. Therefore, the best estimate that can be made of the total system energy is

$$E^{\text{tot}} = E^{\text{QM}}(\{R_i\}, i \in \text{I, II}) + \sum_{i \in \text{III}} E_i^{\text{cl}}(\{R_j\}, j \in \text{I, II, III})\,. \tag{5}$$

In classical methods using interatomic potentials (e.g. Ref. 20), the interactions between atoms have a finite range. In classical methods using finite elements and linear elasticity or the Cauchy-Born rule, effective interactions between "atoms" are limited to near-neighbours only that define the local deformation gradient. If the width of Region II is such that atoms in Region III do not directly interact with atoms in Region I, then the second term in Eq. 5 does not actually depend on the positions of ions in Region I, and can be written as

$$E^{\text{tot}} = E^{\text{QM}}(\{R_i\}, i \in \text{I, II}) + \sum_{i \in \text{III}} E_i^{\text{cl}}(\{R_j\}, j \in \text{II, III})\,. \tag{6}$$

Eq. 6 shows that the errors in the estimated total energy are primarily associated with the errors in the QM energy in Region II and any errors in the equilibrium positions of the ions in all three Regions I, II, and III, caused by any force errors mainly due to ions in Region II.

The accuracy of a coupling method based on the above formulation hinges on the following issues. First, the classical method must accurately capture equilibrium lattice constant and the small-deformation (elastic) response of the material as computed by the DFT method. Second, the QM method must minimize spurious forces in Region I generated by electronic relaxations around the outer surface of the Region I+II QM cluster calculation. Third, the positions of the ions in Region II, controlled by forces determined by the classical method, must be sufficiently accurate relative to their true positions in the hypothetical infinite QM system. In the next sections, we introduce two methods that address these key issues in different ways, and present the computational evidence that the methods can achieve the goal of high accuracy of deformations in the QM Region I.

3 Coupled Atomistic/Discrete Dislocation Method with Quantum Mechanics (CADD-QM)

As the name implies, CADD was originally developed to enable simultaneous dislocation plasticity in both atomistic and continuum domains[23,24]. The simulation of discrete dislocation plasticity relies on linear elasticity theory in the continuum, and hence CADD-QM uses linear elasticity in the "classical" domain of Regions II+III, and uses a QM cluster calculation for Regions I+II[18]. Errors in the CADD-QM coupling are minimized as follows.

Linear elasticity in Regions II+III uses the exact anisotropic elastic stiffness tensor components C_{ijkl} as computed by DFT using exactly the same DFT physical and numerical parameters (e.g XC functional, pseudopotentials, energy cut-offs, smearing parameter, etc.). The reference structure for the continuum calculation is the perfect crystal lattice

having the lattice constant a_o computed by DFT (for simplicity here we consider cubic materials only). Within the approximation of linear elasticity, the classical material therefore exactly matches the QM material.

Errors due to electronic relaxation at the outer boundaries (vacuum surfaces) of Region II lead, at zero temperature, to electron density oscillations propagating far into the "bulk" material; these are the Friedel oscillations arising from the sharp Fermi surface. The spurious effects of the surface are minimized in CADD-QM by two means. First, a relatively large "smearing parameter" or, similarly, effective electron temperature, is used. This is a numerical approach to smooth out the sharp Fermi surface sufficiently to diminish the range of the Friedel oscillations. Second, a relatively thick Region II is used. Together, these can ensure that any spurious forces in Region I caused by the Friedel oscillations are below the force convergence value used in the computations. The main potential problems with the above approach are that (i) a thick Region II is computationally costly and (ii) the material properties and ionic forces can depend on the smearing parameter itself and so the DFT calculation may not be yielding accurate properties for the real material. Regarding (i), we find that problems with through-thickness periodicity (cracks and dislocations) can be treated with $\sim$500 total ions, which is computationally costly but not prohibitive. Regarding (ii), for Al, we have used a smearing parameter of 1.0 eV, which is larger than the typical values of 0.1-0.2 eV used in most DFT codes. However, we have computed the material properties of Al as a function of the smearing parameter up to 2.0 eV, and find that a value of 1.0 eV yields very good values for a range of mechanical properties

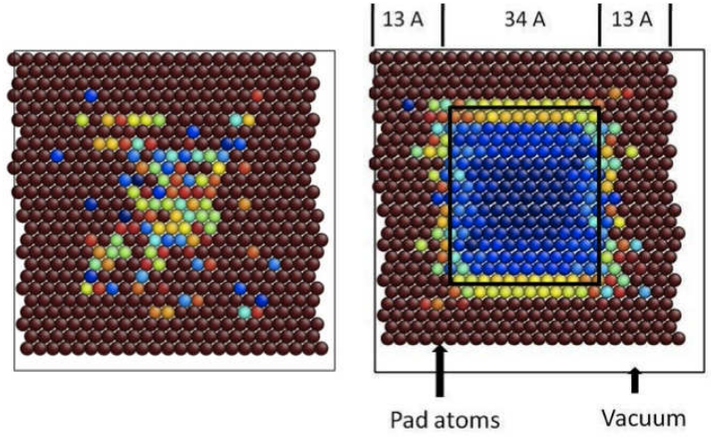

(a) (b)

Figure 2. Regions I and II for a perfect undeformed Al crystal for (a) small (0.2 eV) and (b) large (1.0 eV) smearing parameters; colours indicate computed ionic forces on each ion, with blue corresponding to 8 meV/Å or less.

relevant in Al (lattice constant, elastic constants, surface energies, stacking fault energies). While the value of the smearing parameter and thickness of Region II must be determined through careful testing of reference problems, these are assessable and controllable approximations. Fig. 2 shows the ionic forces on the ions in Regions I and II of a perfect crystal of undeformed Al, for both small and large smearing values. For a Region II of thickness 13 Å and a smearing parameter of 1 eV (Fig. 2b), the forces in Region I (in the box indicated) are less than 8 meV/Å, which is a typical conservative convergence limit for DFT calculations. Thus, the spurious electronic effects in Fig. 2a have been eliminated.

Finally, the positions of Region II ions are determined by continuum elasticity. Continuum mechanics is a local approximation, so the solution to the elasticity problem in Regions II+III uses only those ion positions on the outer boundary of Region I as boundary conditions. Details of the complex deformations deeper in Region I are irrelevant. Regions II and III respond according to elasticity as dictated solely by the displacements at the outer boundary of Region I. If electronic effects due to defects or deformation in Region I are sufficiently large that the response in Region II is not well-approximated by linear elasticity, then Region I must be made larger. This issue is difficult to assess, since the QM Region I+II calculation is constrained by the Region II ion displacements dictated by the finite elements. In other words, the coupling method forces the outer Region I ions to be near the elastic solution, and thus simply examining converged displacements does not reveal underlying errors in the method. However, it is possible to obtain estimates of errors in the outer ions of Region I by taking a converged solution for a given problem and analyzing the QM forces on the inner Region II ions (those adjacent to Region I). If these forces are significant, and compared to the expected forces from the Friedel oscillations, then Region I is too small. Alternatively, a second computation using a smaller Region I' and larger Region II' can be performed, and the displacements of those ions that are at the boundary, i.e. in Region II' but previously in Region I, can be examined.

Fig. 3 shows an application of the method to the computation of the core structure of a screw dislocation in Al. The dislocation dissociates into two closely-spaced partial dislocations, as indicated by the Nye tensor plot[25] showing the edge components of the two partials. These results agree well with those obtained using the Lattice-Green's Function

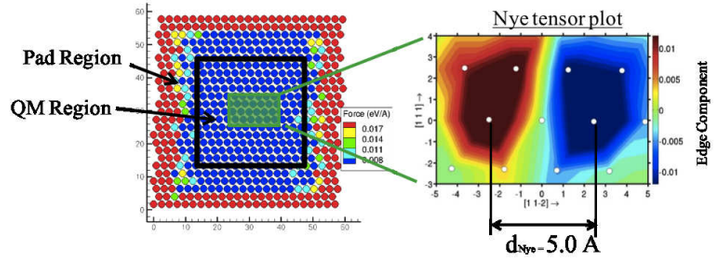

Figure 3. Core structure of a screw dislocation in Al, showing converged forces within Region I ("QM region") and the forces in Region II ("Pad Region") that are influenced by the outer vacuum boundary in the overall DFT computation on Regions I+II.

Method of Rao and Woodward[26], and other results on edge dislocations agree well with results obtained by the QM/MM method of Lu and colleagues[15,16]. The method has also been applied to study both cleavage fracture and dislocation emission at crack tips in Al[18,27] and, more recently, the effects of atomic oxygen and hydrogen on inhibiting dislocation emission from cracks in Al[28]. These first applications demonstrate the power of the multiscale method to capture accurate chemistry in small focused regions of metals using accurate DFT methods in configurations with long range fields and non-periodic geometries.

4 QM/MM Based on Constrained DFT

The main problem in CADD-QM is that the relaxation of the electrons near the outer surface of the QM cluster calculation generates Friedel oscillations and spurious ionic forces in Region I. While avoided by using a large Region II and large smearing parameter, it is fruitful to solve the problem more elegantly. Our new QM/MM (Quantum-Mechanics/Molecular-Mechanics) using a constrained DFT problem achieves this well[19], allowing for the use of a smaller Region II (and thus a cheaper QM computation) and typical DFT smearing parameters of 0.1–0.2 eV.

The idea underlying the constrained DFT method is that, as the name suggests, the DFT cluster calculation is constrained to have, in principle, the exact correct electronic charge density at the outer boundary of Region II. If the charge density in this region is accurate, then there are no Friedel oscillations induced in the system, and no spurious forces generated in Region I. Of course, the exact electronic charge density is not known *a priori*, thus a sufficiently accurate surrogate target charge density must be used. Furthermore, the constraint can only be implemented by imposing an additional constraint potential into the standard Kohn-Sham equations emerging from the DFT theory, and the constraint cannot be satisfied exactly. Thus, the two main issues in the constrained DFT method are (i) determination of the target charge density and (ii) implementation of an appropriate constraint potential.

In work to date, we generate a target charge density by using a sum of "atomic" charge densities associated with each ion i. That is, given an atomic charge density $\rho_{\text{at}}(\vec{r}-\vec{R})$ centred on ion $\vec{R}$, the target charge density at an arbitrary point $\vec{r}$ is computed as

$$\rho_{\text{target}}(\vec{r}) = \sum_i \rho_{\text{at}}(\vec{r}-\vec{R}_i)\,. \tag{7}$$

The atomic charge density $\rho_{\text{at}}(\vec{r}-\vec{R})$ is first parameterized using a linear combination of atomic orbital functions containing variational parameters as

$$\rho_{\text{at}}(\vec{r}) = \sum_{lm} c_{lm}|R(l)Y_{lm}(\theta,\varphi)|^2\,, \tag{8}$$

where (r,θ,φ) are spherical coordinates, and l and m are angular and magnetic quantum numbers. c_{lm} are coefficients ensuring that $\sum_{lm} c_{lm}$ equals the number of valence electrons of the atom. The Y_{lm} are the spherical harmonic functions, and the radial functions $R(l)$ are Gaussian functions given by

$$R_l(r) = r^l A(l,\alpha_{lm})e^{-\alpha_{lm}r^2}\,, \tag{9}$$

where the $A(l, \alpha_{lm})$ are normalization factors. The parameters c_{lm} and α_{lm} in the variational function of Eq. 8 are then obtained by fitting $\rho_{\text{target}}(\vec{r})$ to the exact perfect crystal charge density $\rho_{\text{perfect crystal}}(\vec{r})$ over the unit cell volume using a least-squares procedure. Such a target density is then exact, within fitting errors, for the perfect crystal. For the deformed crystal, the ion positions change but the electron densities attached to each ion do not change. However, properties of the approximate material that uses the electron density specified by $\rho_{\text{target}}(\vec{r})$ in a non-self-consistent Kohn-Sham analysis yields a very accurate lattice constant, cohesive energy, and also bulk modulus (associated with deformation) as compared to the full self-consistent K-S result. Thus, the target charge density gives a good representation of the true charge density and linear elastic material properties.

Given the ion positions, whether computed from DFT, EAM, or FEM methods, the target charge density can be computed in any region of space. The purpose of the constraint method is to constrain the otherwise-spurious charge relaxations that would occur on near the outer surface of Region II. The target charge density is therefore imposed as a constraint on the electronic charge density computed in the DFT only in a domain denoted as Ω_c at the outer boundary of Region II, where the charge densities from ions in Region II and ions in Region III would normally overlap in the infinite material. Specifically, given charge densities computed by QM in Regions I+II, $\rho^{\text{QM}}(\vec{r})$, and computed by superimposing atomic charge densities at the ion positions in Region III, $\rho^{\text{cl}}(\vec{r})$, the domain of Ω_c is defined as those points $\{\vec{r}\}$ satisfying

$$\vec{r} \ni \min\left[\rho^{\text{QM}}(\vec{r}), \rho^{\text{cl}}(\vec{r})\right] < \rho_{\text{cf}}\,, \tag{10}$$

where $\rho_{\text{cf}} = 10^{-4}$ Å^{-3} is a numerical cut-off parameter.

Within the domain Ω_c the constraint is imposed by defining a potential energy "penalty function" that is proportional to the Coulomb potential energy due to the difference between the desired target charge density and the computed charge density and is given by

$$v_c^{\lambda}(\vec{r}) = \lambda \int_{\Omega_c} \frac{\rho^{\text{QM}}(\vec{r'}) - \rho_{\text{target}}(\vec{r'})}{\left|\vec{r} - \vec{r'}\right|} d\vec{r'}\,, \tag{11}$$

where λ is a penalty parameter. The constraint potential in Eq. 11 is then localized to operate only in the domain of Ω_c by multiplying it by a weighting function given by

$$\begin{aligned} w(\vec{r}) &= \quad 1 \qquad && \rho' = \min\left[\rho^{\text{QM}}(\vec{r}), \rho^{\text{cl}}(\vec{r})\right] < 2\rho_{\text{cf}}\,, \\ w(\vec{r}) &= \tfrac{\rho'}{\rho_{\text{cf}}} - 1 && \rho_{\text{cf}} < \rho' = \min\left[\rho^{\text{QM}}(\vec{r}), \rho^{\text{cl}}(\vec{r})\right] < 2\rho_{\text{cf}}\,, \\ w(\vec{r}) &= \quad 0 && \rho' = \min\left[\rho^{\text{QM}}(\vec{r}), \rho^{\text{cl}}(\vec{r})\right] < \rho_{\text{cf}}\,. \end{aligned} \tag{12}$$

The constraint potential is added as an additional external potential in the otherwise standard Kohn-Sham equations, and the modified equation is solved to self-consistency for the QM charge density $\rho^{\text{QM}}(\vec{r})$. Forces are computed in the normal manner as the entire system (Regions I+II+III) is evolved toward the configuration corresponding to mechanical equilibrium. At the equilibrium configuration, the energy of the QM domain is computed from the DFT-computed energy by subtracting off the energy of the constraint potential, which was added solely to enforce the constraint on the charge density as

$$E^{\text{I+II}} = E^{\text{QM}}(\{R_i\}, i \in \text{I, II}) = E^{\text{constrained DFT}} - \int \rho^{\text{QM}}(\vec{r}) w(\vec{r}) v_c^{\lambda}(\vec{r}) d\vec{r}\,. \tag{13}$$

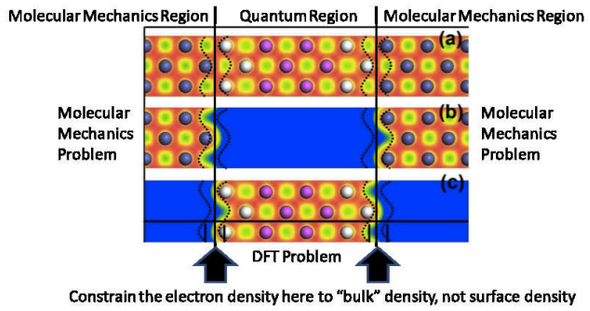

Figure 4. Schematic of the Constrained DFT Quantum-Mechanics/Molecular-Mechanics coupling method. Pink ions are in Region I, white ions in Region II, and blue ions in Region III. A constraint on the electron density is imposed in a region around the boundary between Regions II and III. Colours are contours of electron density from blue (0 /Å^3) to red (0.24 /Å^3).

There are a few numerical aspects to the implementation of the constrained DFT method outlined above. These are discussed in the original publication and are not addressed further here[19]. One important parameter in the model is the penalty parameter λ. Increasing λ enforces adherence to the constraint but also makes convergence more difficult, and thus a compromise must be struck between increased accuracy of the solution and computational time to achieve convergence. For any given material, a suitable value for λ can be determined using small unit cell calculations and this value can be used for any subsequent studies on the same material. We have determined that values of λ = 20, 5, and 2 are suitable for Al, Pd, and Fe, respectively. For magnetic materials such as Fe, a constraint is developed for each of the two independent spin densities but otherwise the theory is the same as given above.

Accuracy of the method has been assessed by examination of several simple problems, and comparisons to standard periodic-cell DFT studies for problems where the periodic DFT is very accurate. For a perfect lattice of undeformed Al with Regions I+II consisting of a cube having the lateral dimension shown in Fig. 4, the method generates forces of 25 meV/Å on the outer ions in the cell, which is slightly higher than in the CADD-QM method, but for a much smaller system and small smearing parameter (0.2 eV). Inserting a single vacancy in the centre of the Al lattice, we compute the vacancy formation energy to be 0.79 eV as compared to the value 0.75 eV computed using a similar-sized but fully-periodic QM domain. We consider this level of accuracy to be very good. Increasing the size of Region I by one additional layer of Al atoms, we again obtain the vacancy formation energy of 0.79 eV. Reducing λ to 10 yields a vacancy formation energy of 0.81 eV while increasing it to 30 yields 0.79 eV. Thus, the results using the original size and λ are robust and suitably converged.

We have applied the Constrained-DFT QM/MM method to predict the core structure of an edge dislocation in Fe. The atomic core structure is shown in Fig. 5 along with contours of a simple local strain deformation measure and Regions I, II, and III as noted in the cap-

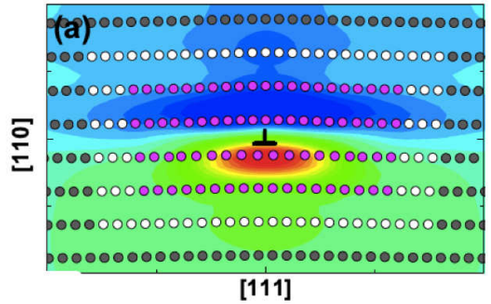

Figure 5. Converged edge dislocation core structure in Fe as predicted by the constrained DFT QM/MM method. Regions I and II are shown as the pink and white ions, while Region III ions are shown in grey and are treated using a tuned EAM potential. Colour contours show a simple strain measure (blue -0.04 to red 0.08) that is useful for gauging the extent of the large deformations around the core (centred at the symbol shown).

tion. The core of the dislocation is not dissociated, but the Burgers vector is spread along the slip plane over a width of approximately 10 Å (from 0.2b to 0.8b). There are no other calculations of this core in the published literature. This is, in part, because full periodic DFT calculations of such cores requires the use of dislocation multipoles (e.g. Ref. 29), and the computational limitations on the number of atoms feasible in DFT requires these dislocations to be quite closely spaced, which can impose artificial and unknown forces that distort the core. While the Lattice Green's Function method or the CADD-QM method have both been used, as shown in Fig. 3 for instance, both require the use of a much larger Region II and are thus far more costly.

5 Conclusion

We have introduced two novel multiscale methods in which quantum mechanics, via density functional theory, is used in a small central region while less-expensive atomistic or continuum methods are employed in the surrounding domain. The intent of this paper has been to present the two different frameworks through one common framework, and discuss how each method deals with the challenges of outer boundary artifacts that arise in many other multiscale methods involving quantum mechanics. The CADD-QM method has been implemented to date using continuum elasticity in the outer Region III, while the constrained-DFT QM/MM method has been implemented to date using semi-empirical interatomic potentials for the atomic degrees of freedom in Region III. Either method could be adopted to use the other approach in Region III. The choice of method in Region III is dictated by other considerations, such as the availability of suitable interatomic potentials and/or the expectation that linear elasticity is sufficiently accurate in Region III. These are largely secondary details. The QM domain needed for any given problem cannot be chosen *a priori*, but the methods here can be made adaptive and can, in principle, adjust on the fly as defects evolve or move.

We note here that neither method can be subjected to strict mathematical assessments of convergence in a formal sense. This is not unexpected for methods where two entirely different energy functionals, having overlapping domains, are used in the formulation. Thus, application of the methods requires some preliminary evaluation of simple problems and numerical assessments of convergence of results for energies or forces. However, the efficiency of the multiscale methods can enable such additional studies, and many aspects can be established once for a given material and then used reliably across different classes of problems.

These methods have no serious inherent restrictions on application across the periodic table, within the limits of application of Kohn-Sham DFT methods, and can deal with arbitrary geometries including non-periodic systems. As such, they are valuable tools for performing accurate first-principles calculations for problems that might otherwise not be computationally feasible.

Acknowledgements

The author acknowledges support for the work on constrained QM DFT from the Army Research Office through a MURI grant W911NF-11-1-0353, and thanks collaborators D. Warner, A. Nair, G. Lu, and X. Zhang for their major contributions to the work reviewed here.

References

1. F. F. Abraham, N. Bernstein, J. Q. Broughton, and D. Hess; *Dynamic fracture of silicon: Concurrent simulation of quantum electrons, classical atoms, and the continuum solid*; MRS Bulletin **25**(5); 27-32; 2000.
2. N. Bernstein, J. R. Kermode, and G. Csanyi; *Hybrid atomistic simulation methods for materials systems*; Rep. Prog. Phys. **72**(2); 2009.
3. J. Q. Broughton, F. F. Abraham, N. Bernstein, and E. Kaxiras; *Concurrent coupling of length scales: Methodology and application*; Phys. Rev. B **60**(4); 2391-2403; 1999.
4. N. Choly, G. Lu, W. E, and E. Kaxiras; *Multiscale simulations in simple metals: A density-functional-based methodology*; Phys. Rev. B **71**(9); 2005.
5. G. Csanyi, T. Albaret, M. C. Payne, and A. De Vita; *"Learn on the fly": A hybrid classical and quantum-mechanical molecular dynamics simulation*; Phys. Rev. Lett. **93**(17); 2004.
6. J. W. Kermode, G. Csanyi, and M. C. Payne; *DFT Embedding and Coarse Graining Techniques*; Multiscale Simulation Methods in Molecular Sciences, NIC Series Volume **42**; 215-228; 2009.
7. G. Lu, E. B. Tadmor, and E. Kaxiras; *From electrons to finite elements: A concurrent multiscale approach for metals*; Phys. Rev. B **73**(2); 2006.
8. S. Ogata, E. Lidorikis, F. Shimojo, A. Nakano, P. Vashishta, and R. K. Kalia; *Hybrid finite-element/molecular-dynamics/electronic-density-functional approach to materials simulations on parallel computers*; Comp. Phys. Comm. **138**(2); 143-154; 2001.
9. P. Suryanarayana, V. Gavini, T. Blesgen, K. Bhattacharya, and M. Ortiz; J. Mech. Phys. Sol. **58**; 256; 2010.

10. S. Ismail-Beigi and T. A. Arias; Phys. Rev. Lett. **82**; 2127; 1999.
11. T. A. Wesolowski and A. Warshel; J. Phys. Chem. **97**; 8050; 1993.
12. N. Govind, Y. A. Wang, A. J. R. da Silva and E. A. Carter; Chem. Phys. Lett. **295**; 129; 1998.
13. P. Huang and E. A. Carter; J. Chem. Phys. **125**; 084102; 2006.
14. M. Hodak, W. Lu, and J. Bernholc; J. Chem. Phys. **128**; 014101; 2008.
15. X. Zhang, Q. Peng and G. Lu; Phys. Rev. B **82**; 134120; 2010.
16. X. Zhang and G. Lu; Phys. Rev. B **76**; 245111; 2007.
17. X. Zhang, C. Y. Wang, and G. Lu; Phys. Rev. B **78**; 235119; 2008.
18. A. K. Nair, D. H. Warner, R. G. Hennig, and W. A. Curtin; Scripta Mater. **63**; 1212-1215; 2010.
19. X. Zhang, G. Lu, and W. A. Curtin; submitted to Phys. Rev. B.
20. M. S. Daw and M. I. Baskes; Phys. Rev. B **29**; 6443; 1984.
21. C. Woodward and S. Rao; Phys. Rev. Lett. **88**; 216402; 2002.
22. V. B. Shenoy, R. Miller, E.B. Tadmor, D. Rodney, R. Phillips, and M. Ortiz; *Adaptive finite element approach to atomic-scale mechanics - the quasicontinuum method*; J. Mech. Phys. Sol. **47**(3); 611-642; 1999.
23. L. E. Shilkrot, R. E. Miller, and W. A. Curtin; *Coupled atomistic and discrete dislocation plasticity*; Physical Review Letters **89**(2); 2002.
24. L. E. Shilkrot, R. E. Miller, and W. A. Curtin; *Multiscale plasticity modeling: Coupled atomistics and discrete dislocation mechanics*; J. Mech. Phys. Sol. **52**(4); 755-787; 2004.
25. C. S. Hartley and Y. Mishin; *Characterization and visualization of the lattice misfit associated with dislocation cores*; Acta Materialia **53**(5); 1313-1321; 2005.
26. C. Woodward, D. R. Trinkle, L. G. Hector, and D. Olmsted; *Prediction of dislocation cores in aluminum from density functional theory*; Phys. Rev. Lett. **100(4)**; 4; 2008.
27. A. K. Nair, D. H. Warner, and R. G. Hennig, J. Mech. Phys. Sol. **59**; 2476; 2011.
28. R. Zamorra. A. K. Nair, R. G. Hennig, and D. H. Warner, Phys. Rev. B **86**; 060101 (R); 2012.
29. L. Ventelon and F. Willaime, J. Comput. Aided Mater. Des. **14**; 85; 2007.

Modelling the Dielectric Response of Atomistic and Continuous Media with the Split-Charge Method

Martin H. Müser

Jülich Supercomputing Centre, Institute for Advanced Simulation,
Forschungszentrum Jülich, 52425 Jülich, Germany
E-mail: m.mueser@fz-juelich.de

Many processes involving ions, polar molecules, or polar moieties take place in an external medium with heterogeneous dielectric properties. Examples range from protein folding in a polarizable solvent to contact electrification induced by the rubbing of two dislike solids. When simulating such processes, it is not appropriate to decompose the electrostatic forces between the central atomistic degrees of freedom into (effective) two-body contributions. Instead, one needs to consider the dielectric response of the external medium, which one may want to represent as a continuum. In this contribution, we show that the split-charge equilibration (SQE) method can be used to describe continua with well-defined dielectric properties, although it was originally designed to assign atomic charges on the fly. As such, SQE bears much potential for hybrid particle-continuum simulations. The comparison of dielectric response functions as obtained by SQE and point-dipole methods reveals many advantages for SQE. The main points are: SQE requires fewer floating-point operations, non-local dielectric properties are more easily embedded, and the leading-order corrections to the continuum limit are isotropic on the simple cubic lattice in contrast to point dipole models.

1 Introduction

The electrostatic polarization of an embedding medium can strongly affect the interaction between ions, polar molecules, or other polar degrees of freedom. To illustrate this point, consider an anion with elementary charge close to a surface of a highly polarizable medium, such as water or, in the extreme case, a metal. If we neglect the surface dipole of the polarizable medium and the induced dielectric response, no (long-range) interaction takes place. However, assuming an ideal mirror charge, the anion feels a Coulomb attraction $V = -e^2/4\pi\varepsilon_0 d$, where d is the distance between the anion and its mirror image. The numerical value of the correction to a non-polarizable treatment for $d = 10$ Å amounts to as much as $V \approx 1.44$ eV, which is roughly 55 times the thermal energy k_BT at room temperature. This number distinctly exceeds the typical energy difference of ten times k_BT between the ground state energy of a folded protein and the first meta-stable conformation.

If the ion is part of a fluid or a solid, that is, if it is part of the central zone of interest, the "effective self-interaction" that the ion experiences from the external medium is not quite as strong as if the ion is in isolation. This is because condensed matter tends to arrange such that it avoids local electrostatic monopoles. The ion then experiences not only its own induced mirror charge but also that of a nearby charge-balancing counterion. As an example, an ideal point dipole of 1.85 D (the value for an isolated water molecule) must be as close as 5.5 Å to its mirror dipole to acquire an effective self-interaction energy of roughly k_BT. Yet, the annihilation of the induced forces may not be sufficiently systematic to make polarization corrections negligible, because polar molecules or moieties can adopt a preferential orientation near interfaces formed by two materials with different dielectric

properties. For this and related reasons, the electric polarization needs to be accounted for in accurate simulations of ionic and polar media[1–4]. Since most systems are heterogeneous and boundary conditions are more complicated than those of semi-infinite metal walls, it is futile to derive effective interactions between the explicitly treated atomistic degrees of freedom. Instead, it is desirable to compute the polarization of the embedding medium, ideally by exploiting continuum descriptions and appropriate meshing far away from the zone of interest.

Often, polarization in condensed matter systems is accounted for by placing inducible (point) dipoles onto atoms or (super) atoms[5–7]. However, in addition to electrostatic polarization of atoms, there can be charge transfer between them. Although there is no *unique* scheme breaking down the polarization into intra- and inter-atomic contributions[8] (mainly because atomic charges cannot be defined unambiguously[9]), recent advances show that it is yet both meaningful and practical to do so[10]. We shall not repeat the arguments here and instead simply assume as a heuristic working hypothesis that charge transfer between atoms and the polarization of atoms can be assigned meaningfully.

Determining the set of atomic charges $\{Q\}$ and/or atomic dipoles $\{\boldsymbol{\mu}\}$ – plus potentially higher-order multipoles – is usually done using minimization principles[11]. The idea is to find an approximation for the potential energy of the system $V = V(\{Q, \boldsymbol{\mu} ...\})$ by Taylor expanding V with respect to the set of the (small) parameters $\{Q, \boldsymbol{\mu}, ...\}$ and to find well-motivated expressions for the expansion coefficients. In this work, we will base this expansion on the split-charge equilibration (SQE) model[12], in which atomic charges result from the charge transfer through chemical bonds. In addition to fractional charges, atoms can receive integer charges, which, however, are not subjected to bond energy penalties but only to on-site interactions. The SQE method has been recently justified from density-functional theory based arguments[10]. The gist of this justification is that the non-locality of the kinetic energy in DFT (which leads to the shell structure of atoms and to band gaps in solids) can be expressed correctly in leading order by the split-charge terms (which are needed to yield a dielectric response differing from that of metals).

The SQE method was proposed as a unified model of the original chemical-potential-equalization method also known as charge equilibration[13,14] (QE) and the atom-atom charge transfer approach (AACT)[15]. It turns out that SQE avoids the (mutually exclusive) disadvantages of QE and AACT method without introducing new ones. For example, QE automatically produces a metallic response, i.e., a diverging dielectric permittivity, ε_r, while AACT can only mimic systems for which $\varepsilon_\mathrm{r} - 1 \lesssim 1$ holds[16]. In contrast, SQE can reproduce any arbitrary value of $\varepsilon_\mathrm{r} > 1$. In this contribution, we focus on the dielectric properties of SQE and compare them to those produced by approaches in which the dielectric response results from point dipoles.

The remaining part of this chapter is organized as follows: In Sec. 2, the charge transfer and point dipole models are introduced within one common framework. In Sec. 3, the continuum limit is derived for a pure point-dipole model and a pure SQE model on the simple cubic lattice. Further properties of charge-equilibration methods, that is, those pertaining to molecular systems, are summarized in Sec. 4. Conclusions are drawn in Sec. 5.

2 Charge Transfer Approaches and the Split Charge Model

As mentioned in the introduction to this chapter, the goal is to find an expansion for the energy as a function of the partial charges and the dipoles – plus potentially higher-order electrostatic multipoles – as a function of the atomic coordinates:

$$V(\{\mathbf{R}, Q, \boldsymbol{\mu}\}) = V(\{\mathbf{R}, Q_0, \boldsymbol{\mu}_0\}) + \sum_i \left\{ \frac{\partial V}{\partial Q_i} \Delta Q_i + \frac{\partial V}{\partial \mu_{i\alpha}} \Delta \mu_{i\alpha} \right\}$$
$$+ \sum_{i,j} \left\{ \frac{1}{2} \frac{\partial^2 V}{\partial Q_i \partial Q_j} \Delta Q_i \Delta Q_j + \frac{\partial^2 V}{\partial Q_i \partial \mu_{j\alpha}} \Delta Q_i \Delta \mu_{j\alpha} + \frac{1}{2} \frac{\partial^2 V}{\partial \mu_{i\alpha} \partial \mu_{j\beta}} \Delta \mu_{i\alpha} \Delta \mu_{j\beta} \right\} \quad (1)$$

We truncate after second order and after the dipole terms. Here, $\{Q_0\}$ and $\{\boldsymbol{\mu}_0\}$ denote, respectively, a set of reference values for atomic charges and dipoles. In the following, we will assume that these can be set to zero unless mentioned otherwise. Moreover, Roman indices refer to atom numbers while Greek indices enumerate Cartesian coordinates, e.g., $\mu_{i\alpha} \equiv \mu_{i\alpha 0} + \Delta\mu_{i\alpha}$ is the α component of the dipole on (super)atom i. For Cartesian indices, we use the summation convention. Some terms in the Taylor expansion Eq. 1 can be readily interpreted.

For isolated atoms, $\partial V/\partial Q_i$ corresponds to the electronegativity χ_i (plus potentially a coupling to an external electrostatic potential), while $\partial^2 V/\partial Q_i^2$ can be associated with the chemical hardness κ_i. They can be parameterized via finite-difference approximations of the ionization energy I_i and electron affinity A_i. The latter two quantities can be be obtained by removing or adding an elementary charge e from atom i,

$$I_i = \frac{\kappa_i}{2} e^2 + \chi_i e \quad (2)$$

$$A_i = -\frac{\kappa_i}{2} e^2 + \chi_i e \quad (3)$$

and thus $\kappa_i = (I_i - A_i)/e^2$ and $\chi_i = (I_i + A_i)/2e$. (These quantities are commonly stated in units of eV, which means that the underlying unit system uses the elementary charge as the unit of charge.) In principle, κ_i and χ_i should depend on the environment, but within a reasonable approximation, they can be taken from values measured for isolated atoms. In practical applications, i.e., when allowing κ_i and χ_i to be free fit parameters, they turn out within $\mathcal{O}(10\%)$ of their experimentally determined values[12,17]. Furthermore, it is tempting to associate the mixed derivative $\partial^2 V/\partial Q_i \partial Q_j$ ($i \neq j$) with the Coulomb potential, at least if $\mathbf{R}_i$ and $\mathbf{R}_j$ are sufficiently distant. For nearby atoms, one may want to screen the Coulomb interaction at short distance to account for orbital overlap.

All terms related to the atomic dipoles can be interpreted in a straightforward fashion. The negative of $\partial V/\partial \mu_{i\alpha}$ is the α component of the electrostatic field at $\mathbf{R}_i$ due to external charges. The single-atom terms $\partial^2 V/\partial \mu_{i\alpha} \partial \mu_{i\beta}$, can be associated with the inverse polarizability $1/\gamma_i$ of atom i. Unlike for the charges, practical applications find a large dependence of the polarizability on the chemical environment (in particular for anions)[18], including a direction dependence for directed bonds. The two-atom terms $\partial^2 V/\partial Q_i \partial \mu_{j\alpha}$ and $\partial^2 V/\partial \mu_{i\alpha} \partial \mu_{j\beta}$ correspond to the charge-dipole and dipole-dipole Coulomb interaction, respectively, at least for large distances R_{ij} between atoms i and j.

Unfortunately, it is incorrect to assume that the second-order derivatives $\partial V^2/\partial Q_i \partial Q_j$ quickly approach the Coulomb interaction as R_{ij} increases beyond typical atomic spacings, which one might conclude from the argument that chemistry is local. This can be

seen as follows: we know that isolated fragments (such as atoms or molecules) take integer charges, in many cases zero charge. If we separate two atoms, such as sodium and chlorine to large separation, we would find that the fragments carry a fractional charge

$$Q_{\mathrm{Na,Cl}} = \pm \frac{\chi_{\mathrm{Cl}} - \chi_{\mathrm{Na}}}{\kappa_{\mathrm{Na}} + \kappa_{\mathrm{Cl}} - 1/(4\pi\varepsilon_0 R_{\mathrm{NaCl}})}, \tag{4}$$

assuming that $\partial V^2/\partial Q_i \partial Q_j$ quickly approaches the Coulomb potential. Using element-specific numerical values[19], one obtains partial charges of $\pm 0.4\ e$ for a completely dissociated dimer. However, both atoms should be neutral, because $I_{\mathrm{Na}} > A_{\mathrm{Cl}}$, which requires one to prevent non-local (fractional) charge transfer.

What needs to be done is to penalize the transfer of (fractional) charge over long distances, i.e., when the overlap of orbitals of isolated atoms or ions ceases to be of importance. This can be done as follows. We write the charge of an atom as[12,16]

$$Q_i = n_i e + \sum_j q_{ij}, \tag{5}$$

where n_i is called the oxidation state of the atom and q_{ij} is the charge donated from atom j to atom i, which is called the split charge. By definition, $q_{ij} = -q_{ji}$. (One may object that such an assignment is meaningless as electrons are indistinguishable. However, assignments can be made unique, e.g., by defining an appropriate Penrose inverse for the reconstruction of split charges from charges[10].) Next, we do not only penalize built-up of charge on atoms but also the transfer of charge. Thus, the terms in Eq. 1 exclusively related to atomic charges become

$$\begin{aligned} V(\{\mathbf{R}, Q, \cdots\}) = &\sum_i \left\{ \frac{\kappa_i}{2} Q_i^2 + (\chi_i + \Phi_i^{\mathrm{ext}}) Q_i \right\} \\ &+ \sum_{i,j>i} \left\{ \frac{\kappa_{ij}}{2} q_{ij}^2 + \frac{S_{ij}(R_{ij})}{4\pi\varepsilon_0 R_{ij}} Q_i Q_j \right\} + \mathcal{O}(\boldsymbol{\mu}). \end{aligned} \tag{6}$$

Here, we have introduced the split-charge or bond hardness κ_{ij}, which is generally distance and also environment dependent, i.e., it diverges as R_{ij} becomes large, prohibiting the transfer of charge over long distances. Moreover, $S_{ij}(R_{ij})$ denotes a screening at small distances with $S_{ij}(R_{ij}) \to 1$ for $R_{ij} \to \infty$.

Eq. 6 represents the SQE model. The original QE arises in the limit of vanishing bond hardness term κ_{ij}, while the AACT model neglects the atomic-hardness terms κ_i. Partial charges of atoms are deduced by minimizing the energy with respect to the split charges q_{ij}. The total charge of the system automatically adjusts to $Q_{\mathrm{tot}} = \sum_i n_i e$ owing to the $q_{ij} = -q_{ji}$ symmetry. The minimization of V with respect to the split charges can be done with the usual strategies for finding minima of second-order polynomials, such as steepest descent (good and easy for systems with large band gap, i.e., large values of κ_{s}, reasonable convergence in two or three iterations), extended Lagrangians (not efficient for systems with zero or small band gap), or conjugate gradient (probably best when dealing with small or zero band gap systems). Matrix inversion of the Hessian matrix is strongly disadvised due to unfavourable scaling with particle number. Once the partial charges are determined, forces arising due to electrostatic interactions can be computed from $\partial V(\{\mathbf{R}, Q, \cdots\})/\partial R_{i\alpha}$.

The numerical overhead of SQE versus QE is minimal, if present at all. As a matter of fact, since QE models all materials as metallic (as we shall see in Sec. 3.2), SQE requires much fewer iterations to convergence than QE, at least for systems with a band gap. However, there is a memory overhead within the SQE formulation. For example, assuming 12 neighbours per atom on average, one obtains six split charges per atom, which need to be stored in memory. Despite of this memory overhead in SQE, the number of floating-point operations per SQE minimization step is not much larger than for QE. The reason is that the bulk of the calculations is related to the evaluation of the Coulomb potential V_{C} and the derivatives $\partial V_{\mathrm{C}}/\partial Q_i$. Once the latter are known and stored in arrays, the derivatives $\partial V_{\mathrm{C}}/\partial q_{ij}$ can be obtained with little CPU time via

$$\frac{\partial V_{\mathrm{C}}}{\partial q_{ij}} = \frac{\partial V_{\mathrm{C}}}{\partial Q_i} - \frac{\partial V_{\mathrm{C}}}{\partial Q_j}, \tag{7}$$

since $dQ_k/dq_{ij} = \delta_{ik} - \delta_{jk}$.

3 The Continuum Limit of Charge Equilibration Models

In this section, the (static) dielectric response function of the SQE model (augmented with inducible point dipoles) is explored in the continuum limit. Such a treatment contains the original QE and the AACT model as limiting cases. The presentation here explores a similar model discussed previously[20], i.e., a simple cubic crystal in which a "slowly" varying electrostatic field $\mathbf{E}^{\mathrm{ext}}(\mathbf{R})$ produced by "external" charges is added. [a] The derivation of the dielectric permittivity pursued is simplified with respect to the original one and moreover, we no longer restrict ourselves to the capacitor geometry.

The charge $Q(\mathbf{R})$ at lattice site $\mathbf{R}/a = l\mathbf{e}_x + m\mathbf{e}_y + n\mathbf{e}_z$ (a being lattice constant) can be calculated through the following second-order, finite-difference approximation

$$Q(\mathbf{R}) = -\sum_{\Delta\mathbf{R}} \Delta\mathbf{R} \cdot \nabla q(\mathbf{R}, \Delta\mathbf{R}), \tag{8}$$

where $\Delta\mathbf{R}$ is a lattice vector. For $\Delta\mathbf{R}$ being a nearest-neighbour vector, the split-charge field $q(\mathbf{R}, \Delta\mathbf{R})$ shall be interpreted as follows: $q([x + a/2, y, z], a\mathbf{e}_1)$ is the split-charge donated from the atom located at (x, y, z) to that at $(x + a, y, z)$. (This way, the expression $\Delta\mathbf{R}\, q(\mathbf{R}, \Delta\mathbf{R})$ can be seen as a dipole centred at $\mathbf{R} + \Delta\mathbf{R}/2$.) Because similar relations hold for split charges shared between next-nearest atoms, etc., the summation in Eq. 8 can be generalized to any lattice vector $\Delta\mathbf{R}$. To clarify Eq. 8, we note that the split-charge field on the r.h.s. is a function defined on a continuous variable $\mathbf{R}$. The field is chosen such that it is as smooth as possible but nevertheless represents exactly the true split charge exchanged between nearest (or farther) neighbours at the centre of the (imaginary) bond of the two atoms exchanging a split charge. The l.h.s. of Eq. 8 is a discrete charge at lattice site $\mathbf{R}$. By dividing $Q(\mathbf{R})$ through a^3, it can be turned into a continuous charge density.

[a] It is probably more meaningful to refer to a continuous-background charge distribution that is not treated explicitly rather than to an external charge distribution. Moreover, the term "slowly varying" shall imply that the charge distribution is continuous, e.g., it only lives on one single wavelength within the first Brillouin zone of the crystal.

In reciprocal space, Eq. 8 becomes

$$\tilde{Q}(\mathbf{k}) = -i \sum_{\Delta\mathbf{R}} \mathbf{k} \cdot \Delta\mathbf{R}\; \tilde{q}(\mathbf{k}, \Delta\mathbf{R}). \tag{9}$$

A difficulty that arises when exchanging split charges with next-nearest neighbours is that we need additional split charge fields, i.e., those living on lattice sites for which $l + m + n$ is odd and those for which $l + m + n$ is even. This means that our simple cubic lattice needs to be subdivided into two interpenetrating face-centred cubic lattices, which makes the analytical discussion intransparent. The need for different lattices will disappear for external fields that have a wavelength much exceeding a lattice constant. It is only in this latter case that the conversion from a discrete theory to a continuum theory as initiated in Eq. 9 is meaningful. Short wavelengths would have to be treated differently. At this point, it shall suffice to state that it is possible, in principle, to tune the next-nearest neighbour bond hardness independently from that of nearest neighbours. This would mean that the polarizability at a wavelength $2a$ can be set independently from that at wavelength a. Similar comments apply when including third-nearest neighbours, etc. Therefore, it should be possible to design a dielectric permittivity such that it reproduces a desired wavelength dependence. For reasons of clarity, we keep Eq. 9 without introducing independent split charges fields living on different sublattices. (Of course, an alternative approach to increasing the unit cell would be to couple different $\mathbf{k}$ vectors defined for the original unit cell.)

Including point dipoles to the lattice sites, the split-charge energy for a perfect (monoatomic, $\chi \equiv 0$) lattice reads

$$\begin{aligned} V = & \sum_{\mathbf{R}} \left\{ \frac{\kappa}{2}\, Q^2(\mathbf{R}) + \sum_{\Delta\mathbf{R}} \frac{\kappa_{\mathrm{s}}(\Delta\mathbf{R})}{2}\, q^2(\mathbf{R}, \Delta\mathbf{R}) - \mathbf{E}^{\mathrm{ext}}(\mathbf{R}) \cdot \Delta\mathbf{R}\; q(\mathbf{R}, \Delta\mathbf{R}) \right\} \\ & + \sum_{\mathbf{R}} \left\{ \frac{1}{2\gamma} \mu_\alpha^2(\mathbf{R}) - E_\alpha^{\mathrm{ext}}(\mathbf{R}) \mu_\alpha(\mathbf{R}) \right\} + \sum_{\mathbf{R},\mathbf{R}'} \left\{ \frac{J(\Delta\mathbf{R})}{2} Q(\mathbf{R}) Q(\mathbf{R}') \right. \\ & \left. + \; J_\alpha(\Delta\mathbf{R}) Q(\mathbf{R}) \mu_\alpha(\mathbf{R}') + \frac{J_{\alpha\beta}(\Delta\mathbf{R})}{2} \mu_\alpha(\mathbf{R}) \mu_\beta(\mathbf{R}') \right\}. \end{aligned} \tag{10}$$

Here, $J(\Delta\mathbf{R})$ is the (screened) Coulomb interaction between the charges $Q(\mathbf{R})$ and $Q(\mathbf{R}')$, the singly-indexed $J_\alpha(\Delta\mathbf{R})$ represents the (screened) charge-dipole interaction, and the doubly-indexed $J_{\alpha\beta}(\Delta\mathbf{R})$ is the dipole-dipole interaction. Moreover, $\Delta\mathbf{R} \equiv \mathbf{R} - \mathbf{R}'$ and any Coulomb coupling (from monopole-monopole to dipole-dipole interaction) is set to zero for $\Delta\mathbf{R} = 0$.

Eq. 10 is easily transformed into reciprocal space, as only bilinear coupling occurs. To do so, one needs to replace sums over $\mathbf{R}$ with sums over $\mathbf{k}$ and follow the known rules for Fourier transforms, for instance, the atomic hardness term becomes $\sum_{\mathbf{k}} \kappa \tilde{Q}(\mathbf{k}) \tilde{Q}^*(\mathbf{k})/2$. See also Sec. 3.3, where more details on the dipole-dipole interactions in real and reciprocal space are stated.

The solutions $\tilde{q}(\mathbf{k}, \Delta\mathbf{r})$ minimizing V must satisfy $\partial V / \partial \tilde{q}(\mathbf{k}, \Delta\mathbf{R}) = 0$, which reads

$$\left\{ \kappa + \tilde{J}(\mathbf{k}) \right\} k_\alpha \Delta R_\alpha \tilde{Q}(\mathbf{k}) + \kappa_{\mathrm{s}}(\Delta\mathbf{R}) \tilde{q}(\mathbf{k}, \Delta\mathbf{R}) = \tilde{E}_\alpha^{\mathrm{eff}}(\mathbf{k}) \Delta R_\alpha \tag{11}$$

with

$$\tilde{E}_\alpha^{\mathrm{eff}}(\mathbf{k}) = \tilde{E}_\alpha^{\mathrm{ext}}(\mathbf{k}) - k_\alpha \tilde{J}_\beta(\Delta\mathbf{k}) \tilde{\mu}_\beta(\mathbf{k}). \tag{12}$$

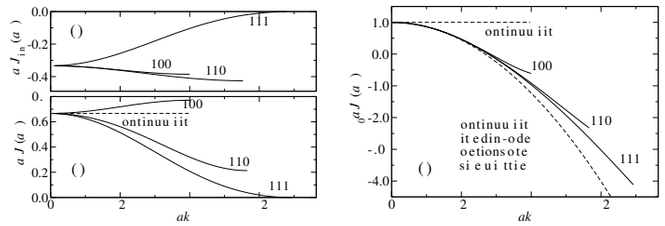

Figure 1. (a) Minimum eigenvalues of the dipole coupling matrix $\tilde{J}_{\alpha\beta}(\mathbf{k})$ for selected paths in the first Brillouin zone of the simple cubic lattice. (b) The coupling of dipoles oriented parallel to the given $\mathbf{k}$ vector as a function of the wavenumber along selected paths. (c) Fourier transform of the Coulomb interaction $\tilde{J}_{\mathrm{C}}(a\mathbf{k})$ for the simple cubic lattice.

In reciprocal space, the minimization condition $\partial V/\partial \boldsymbol{\mu}_i(\mathbf{R}) = 0$ becomes

$$\left\{ \frac{\delta_{\alpha\beta}}{\gamma} + \tilde{J}_{\alpha\beta}(\mathbf{k}) \right\} \tilde{\mu}_\beta(\mathbf{k}) = \tilde{E}^{\mathrm{ext}}_\alpha(\mathbf{k}) - \tilde{J}_\alpha(\mathbf{k}) \tilde{Q}(\mathbf{k}). \tag{13}$$

From the set of coupled Eqs. 11 and 13, one can deduce the dielectric response to an external field. We will discuss these solutions in a separate paper. In this contribution, for reasons of simplicity, we focus on the limit in which the coupling between monopoles and dipoles can be neglected. This allows one to work out the differences between the dielectric response functions that are due to either pure dipole or pure bond polarization.

3.1 Pure Dipole Polarizability

We start our analysis of the dielectric response by neglecting charge transfer. For reasons of simplicity, we consider a sinusoidal electrostatic field that is aligned parallel to the z-axis of our simple cubic solid, i.e., $\mathbf{E}^{\mathrm{ext}}(\mathbf{r}) = E_3 \mathbf{e}_3 \exp(ik_3 z)$. To this end, we need expressions for the $\tilde{J}_{\alpha\beta}(k_3\mathbf{e}_3)$ elements, see Sec. 3.3. The off-diagonal elements must be zero (for $\mathbf{k}$ parallel to z) for reasons of symmetry. Numerically, we find for unscreened dipole-dipole interactions that the diagonal elements can be represented quite accurately via

$$\tilde{J}_{11}(k_3\mathbf{e}_3) = \tilde{J}_{22}(k_3\mathbf{e}_3) \approx \frac{\delta_{k_30} - 1}{3\varepsilon_0 a^3} \left\{ 1 + 0.156(5) \sin^2(ak_3/2) \right\} \tag{14}$$

$$\tilde{J}_{33}(k_3\mathbf{e}_3) = -2\tilde{J}_{11}(k_3\mathbf{e}_3), \tag{15}$$

which includes the discontinuous drop from a finite value at $k_3 = 0^+$ to zero at $k = 0$. It is furthermore well known[21] that the dispersion of the $\tilde{J}_{\alpha\beta}(\mathbf{k})$ depends on $\mathbf{k}$. This dependence is sketched along some lines in the first Brillouin zone in Fig. 1(b). One can see that the corrections to the continuum limit depend not only on the magnitude of $\mathbf{k}$ but also on its orientation.

We start our discussion with the analysis of the split charges exchanged in a direction normal to the external field, i.e., in x-direction. According to Eq. 9

$$\left\{ \frac{1}{\gamma} + \tilde{J}_{11}(k_3\mathbf{e}_3) \right\} \tilde{\mu}_1(k_3\mathbf{e}_3) = 0, \tag{16}$$

using Eq. 14 for $\tilde{J}_{11}(k_3\mathbf{e}_3)$, one can see that the prefactor on the l.h.s. of the equation can become zero at a finite density ρ, which is defined as $\rho = 1/a^3$. This means that the system can acquire a finite polarization without energy penalty, which in turn implies a polarization catastrophe. For small but non-zero k_3, this happens at the same density $\rho = 3\varepsilon_0/\gamma$ at which the Clausius-Mossotti (CM) relation for dipoles (see Eq. 23 for $k_3 \to 0$) indicates a diverging dielectric constant, namely for $\gamma\rho = 3\varepsilon_0$.

The discrete simple cubic solid becomes unstable at an even smaller density, e.g., for dipoles associated with the wavevector $\mathbf{k} = \pi(0,0,1)/a$ and at even smaller densities for $\mathbf{k} = \pi(1,1,0)$, as one can see from Fig. 1a. Specifically, dipoles with the wavevector $(\pi/a)(1,1,0)$ already become unstable at a density of $\rho = \varepsilon_0/0.4259(3)\gamma$ rather than at $3\varepsilon_0/\gamma$ as in CM.

We next analyze the split-charge response parallel to the z axis. Deriving the regular CM relation from the present treatment is not easily possible. The reason is that the sum over dipoles is only conditionally convergent – hence the discontinuity of the $\tilde{J}_{\alpha\beta}(\mathbf{k})$ at the Γ point. Due to the conditional convergence, the shape of the material matters when determining its dielectric response. For the regular capacitance geometry, the static dielectric constant consistent with CM relation requires summing up planes of interacting dipoles, where each plane is normal to the the z axis[22]. Here, we proceed using a different approach, previously pursued to derive the (macroscopic) dielectric response function[23].

What we seek is a relation between the polarization $\mathbf{P} \equiv \langle\mu_\alpha\rangle\mathbf{e}_\alpha/a^3$ and the coarse-grained total electrostatic field $\mathbf{E}^{\rm tot}$ through the equation

$$\frac{1}{a^3}\tilde{\mu}_\alpha(\mathbf{k}) = \varepsilon_0 \left\{\tilde{\varepsilon}_{\alpha\beta}(\mathbf{k}) - \delta_{\alpha\beta}\right\} \tilde{E}^{\rm tot}_\beta(\mathbf{k}), \tag{17}$$

where $\tilde{\varepsilon}_{\alpha\beta}(\mathbf{k})$ is the dielectric tensor. So far, we only have a relation between the dipoles and the electrostatic field due to external charges, i.e., for the z-component

$$\left\{\frac{1}{\gamma} + \tilde{J}_{33}(k_3\mathbf{e}_3)\right\} \tilde{\mu}_3(k_3\mathbf{e}_3) = \tilde{E}^{\rm ext}_3(k_3\mathbf{e}_3). \tag{18}$$

The total field is the superposition of a slowly varying field due to external charges and a rapidly varying field produced by the dipoles. The latter consists of two contributions. One is the field coming from "outside" the dipoles, i.e., the one we used to sum up the dipole-dipole interactions. The other contribution stems from the "internal" field within the point dipole[23]. It can be represented as a δ-function if the dipole is located at the origin, see Sec. 3.3:

$$E^{\rm int}_\alpha(\mathbf{r}) = -\mu_\alpha \frac{\delta(\mathbf{r})}{3\varepsilon_0}. \tag{19}$$

At a given lattice point, we define the coarse-grained field according to

$$E^{\rm tot}_\alpha(\mathbf{R}) = E^{\rm ext}_\alpha(\mathbf{R}) + \frac{1}{a^3}\int_{V_{\rm E}(\mathbf{R})} d^3r \left\{E^{\rm dip}_\alpha(\mathbf{r}) - \frac{\mu_\alpha(\mathbf{R})}{3\varepsilon_0}\right\}, \tag{20}$$

where $V_{\rm E}(\mathbf{R})$ is a cubic elementary cell of size a^3 with its centre of mass located at $\mathbf{R}$. With this choice, the dipole field from the dipole contained in $V_{\rm E}(\mathbf{R})$ does not contribute to the coarse-grained field. To leading order, we approximate the value of $E^{\rm dip}_\alpha(\mathbf{r})$ within

$V_{\mathrm{E}}(\mathbf{R})$ through $E_\alpha^{\mathrm{dip}}(\mathbf{R})$ produced by dipoles from outside of $V_{\mathrm{E}}(\mathbf{R})$. This makes the $\tilde{J}_{33}(k_3\mathbf{e}_3)$ term on the r.h.s. of Eq. 18 disappear and thus

$$\left\{\frac{1}{\gamma}-\frac{1}{3\varepsilon_0 a^3}\right\}\tilde{\mu}_3(k_3\mathbf{e}_3)\approx\tilde{E}_3^{\mathrm{tot}}(k_3\mathbf{e}_3). \tag{21}$$

At this level of approximation, i.e., for $\langle E_\alpha^{\mathrm{dip}}(\mathbf{r})\rangle_{V_{\mathrm{E}}(\mathbf{R})}\approx E_\alpha^{\mathrm{dip}}(\mathbf{R})$, the response function is dispersion-free and moreover continuous at the Γ point. However, each mode becomes unstable at the same value of k_3. This contradicts our previous result (exact for point dipoles) for the polarization catastrophe in x direction, which – for simple cubic – is symmetry related to that in z. The problem can be fixed by re expressing Eq. 21 as

$$\varepsilon_0 a^3\left\{\frac{1}{\gamma}-\frac{\delta_{k_30}}{3\varepsilon_0 a^3}-\frac{J_{33}(k_3\mathbf{e}_3)}{2}\right\}\frac{\tilde{\mu}_3(k_3\mathbf{e}_3)}{a^3}=\varepsilon_0\tilde{E}_3^{\mathrm{tot}}(k_3\mathbf{e}_3), \tag{22}$$

where we have introduced some factors to simplify the comparison to Eq. 17. Such a comparison yields

$$\begin{aligned}\tilde{\varepsilon}_{33}(k_3\mathbf{e}_3)-1&=\frac{\gamma/\varepsilon_0 a^3}{1-\gamma\delta_{k_30}/3\varepsilon_0 a^3-\gamma\tilde{J}_{33}(k_3\mathbf{e}_3)/2}\\&=\frac{\gamma/\varepsilon_0 a^3}{1-\gamma/3\varepsilon_0 a^3\left\{1+0.156(5)\sin^2(ak_3/2)\right\}}\end{aligned} \tag{23}$$

The last two relations state that the dielectric tensor element $\tilde{J}_{33}(k_3\mathbf{e}_3)$ is continuous at the Γ point. Furthermore, Eq. 23 is equivalent to the CM relation at $k_3=0$ and $k_3\to 0$.

The treatment parallel to other (symmetry) directions is similar to the one presented so far. However, it becomes more complicated when $\mathbf{k}$ does not lie on a symmetry line, because the eigenvectors of the coupling matrix are no longer purely parallel or orthogonal to $\mathbf{k}$. This means that the polarization induced in the crystal is no longer parallel to the (static) electrostatic field induced by the external charge distribution. Thus, the dielectric response functions quickly deviates from being isotropic with increasing wavenumber.

3.2 Pure Charge Transfer Polarizability

As argued before, one of the promising properties of the SQE model is that one can define non-local charge transfer resulting in non-local response functions. However, there are quite a few differences between point-dipole polarizability and split-charge polarizability at a level where we only allow for charge transfer between adjacent atoms on the simple cubic lattice.

To keep the formalism transparent, we will first restrict split charges to nearest neighbours. [b] In analogy to our previous treatment[20], we write nearest-neighbour split charges as a vector $q_\alpha(\mathbf{R})$, where $q_1(\mathbf{R}+a\mathbf{e}_1/2)$ is the split charge donated from the atom located at $\mathbf{R}$ to the one at $\mathbf{R}+a\mathbf{e}_1$. This allows one to rewrite Eq. 9 as

$$\tilde{Q}(\mathbf{k})=-iak_\alpha\tilde{q}_\alpha(\mathbf{k}). \tag{24}$$

[b] When describing non-local charge transfer on the continuum scale through Eq. 9, one can proceed as done in the current text. One only needs to divide Eq. 11 by $\kappa_{\mathrm{s}}(\Delta\mathbf{R})$, multiply the equation with the wavenumber and sum it over all $\Delta\mathbf{R}$. This way, one obtains an equation for $\tilde{Q}(\mathbf{k})$ with effective values for the split-charge hardness and the Coulomb interaction.

Assuming the same sinusoidal electrostatic field parallel to the z axis as in the previous section and no point dipoles on atoms, Eq. 11 can be written as

$$\left[\left\{\kappa + \tilde{J}(k_3\mathbf{e}_3)\right\}(ak_3)^2 + \kappa_\mathrm{s}\right]\tilde{q}_3(k_3\mathbf{e}_3) = a\tilde{E}_3^\mathrm{ext}(k\mathbf{e}_3). \tag{25}$$

To derive the expression for the dielectric permittivity, we proceed similarly as in the previous section, rather than as in the original literature[20]. First we identify $aq_3(\mathbf{R})$ as the dipole per volume $V_\mathrm{E} = a^3$ and thus $P_3(\mathbf{R}) = q_3(\mathbf{R})/a^2$ is the local polarization. Next, we convert from an external electrostatic field to a total, coarse-grained field on the r.h.s. of the equation by eliminating the Coulomb interaction on its l.h.s. The difference to the previous section is that we do not need to take care of internal dipole fields, because the Coulomb interactions are solely related to point charges. Thus,

$$a\varepsilon_0\left\{\kappa(ak_3)^2 + \kappa_\mathrm{s}\right\}\frac{\tilde{q}(k_3\mathbf{e}_3)}{a^2} = \varepsilon_0\tilde{E}_3^\mathrm{tot}(k\mathbf{e}_3). \tag{26}$$

Comparison with Eq. 17 yields

$$\tilde{\varepsilon}_{33}(k_3\mathbf{e}_3) - 1 = \frac{1}{\varepsilon_0 a\{\kappa_\mathrm{s} + \kappa(ak_3)^2\}}, \tag{27}$$

which is equivalent to Eq. (27) in Ref. 16 but contains, in addition, a dispersion correction due to atomic hardness. Here, we note that we used simple finite-difference approximations to deduce the charges from the split-charge field. This is why $\tilde{\varepsilon}_{33}(\mathbf{k})$ does not turn out periodic in the Brillouin zone. The problem can be easily fixed without changing the leading-order behaviour of the dielectric susceptibility by replacing Eq. 27 with

$$\tilde{\varepsilon}_{33}(k_3\mathbf{e}_3) - 1 = \frac{1}{\varepsilon_0 a\{\kappa_\mathrm{s} + 4\kappa\sin^2(ak_3/2)\}}, \tag{28}$$

which is equivalent to replacing Eq. 24 with the accurate relation $\tilde{Q} = \sum_{\Delta\mathbf{R}}\{\exp(-i\mathbf{k}\cdot\Delta\mathbf{R}) - 1\}\,\tilde{q}(\mathbf{k}, \Delta\mathbf{R})$.

Formally, Eq. 28 expresses a similar functional dependence of $\tilde{\varepsilon}_{33}(k_3\mathbf{e}_3)$ on k_3 as that derived for pure dipole polarization, see Eq. 23. However, there are differences between them in practice. First, the leading continuum corrections for small but finite k are isotropic for the SQE model but not for the point-dipole model. Second, the prefactor to the corrections is small for dipoles, i.e., of order 0.1. Conversely, the ratio κ/κ_s tends to be of order unity or much greater. This is because $\kappa_\mathrm{s}e^2$ can be associated with the band gap of solids[16] (in fact, κ_s is an upper bound for the band gap), so that κ_s (for true chemical bonds) can be anything between zero and values a few times the atomic hardness. Next, the dielectric response in the SQE formalism does not automatically diverge at high density for fixed dipole or bond polarizability. The reason is that the total Hessian can be made positive definite through the choice of large atomic hardness. This is different from the AACT model, which necessitates small bond polarizability to keep the Hessian positive definite.

Fig. 2 demonstrates that the dielectric permittivity, $\varepsilon_\mathrm{r} = \tilde{\varepsilon}_{33}(0)$, is indeed independent of the atomic hardness. Moreover, one recognize that the dielectric response does not diverge even if κ_s is very small. For the smallest value of the bond hardness ($\kappa_\mathrm{s} = 1/4\varepsilon_0 a$), the point-dipole model with equivalent local polarization ($\gamma = a^2/\kappa_\mathrm{s}$) would have been already beyond the polarization catastrophe, i.e., it would have produced a negative dielectric constant of $\varepsilon_\mathrm{r} = 4/(1 - 4/3) = -12$.

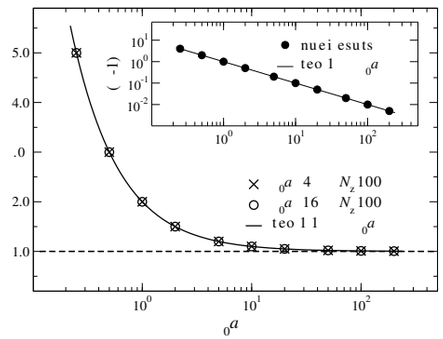

Figure 2. Dielectric permittivity for different choices of κ and κ_{s}. The numerical results were obtained in a regular capacitor geometry, in which $N_z = 100$ layers containing 10×10 atoms were placed into a simulation cell. Periodic boundary conditions were applied in all three spatial dimensions, however, in the direction of the electrostatic field, a gap was introduced. The dielectric permittivity was obtained by measuring the coarse-grained total electrostatic field within and outside the material. Adapted from Ref. 16.

The reason why κ_{s} can be made small even at large density is that the atomic hardness impedes large local dipole gradients. Thus, the atomic hardness must introduce some smearing of the response function. To elucidate this claim, we analyze the split-charge response in a capacitor geometry. Thus, we consider an external electrostatic potential that has a constant slope in a periodically repeated cell $\Phi(z) = E_3 z$ but goes back to zero when the periodic image is repeated. The required non-zero Fourier coefficients for the resulting electrostatic field read[16]

$$\tilde{E_3}(k_3\mathbf{e}_3) = -2E_3 \text{ for } k_3 = 2\pi n/L, n \in \mathbb{N}. \tag{29}$$

The associated split charge response is

$$\tilde{q}(k_3) \approx \frac{-2E_0}{\left\{\kappa + \tilde{J}(k_3\mathbf{e}_3)\right\}(ak_3)^2 + \kappa_{\mathrm{s}}}, \tag{30}$$

where a reasonable approximation to $\tilde{J}(\mathbf{k})$ was found to be[20]

$$\tilde{J}(\mathbf{k}) = \frac{1 - \nu(ak)^2}{\varepsilon_0 a(ak)^2}. \tag{31}$$

A value of $\nu = 0.22578$ expresses the (isotropic) leading-order discretization corrections for the simple cubic lattice, see Fig. 1. Inserting Eq. 31 into Eq. 30 can be written as follows

$$\tilde{q}_{\mathrm{s}}(k_3) = \frac{-2E_0}{\kappa'(ak)^2 + \kappa'_{\mathrm{s}}} \tag{32}$$

with $\kappa' = \kappa - \nu/\varepsilon_0 a$ and $\kappa'_{\mathrm{s}} = \kappa_{\mathrm{s}} + 1/\varepsilon_0 a$. When solving the response of the dielectric medium, i.e., with the help of the residue theorem, it becomes clear that the roots of the

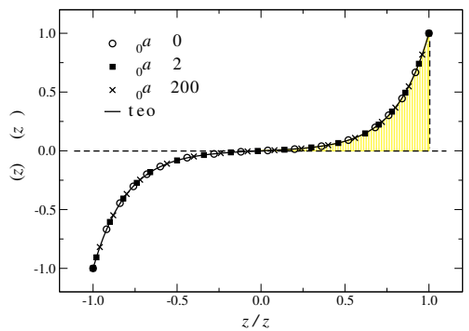

Figure 3. Charge density of a simple cubic SQE model in a constant external electrostatic field as a function of the coordinate z normal to the surface. The bond stiffness varies from metallic to extremely dielectric. The atomic hardness was adjusted such that the penetration depth as defined in Eq. 33 remained constant. The shaded area can be interpreted as total polarization charge. From Ref. 16.

denominator of Eq. 32 have the meaning of an inverse (exponential) decay length δ^{-1}. This can be solved to yield

$$\delta = a\sqrt{\frac{\varepsilon_0 a\kappa - \nu}{1 + \varepsilon_0 a\kappa_\mathrm{s}}}. \tag{33}$$

Thus, the split charge field decays with $q(z) \propto \exp(-|z - z_0|/\delta)$ from the surface located at z_0. The surface polarization charge must obey the same exponential law, because it is proportional to the derivative of $q(z)$. Fig. 3 demonstrates that the expected behaviour is borne out in numerical simulations. Their set-up is described in the caption of Fig. 2.

It is instructive to analyze the properties in the limits where either the bond hardness κ_s disappears (as in conventional QE methods) or the atomic hardness κ (as in AACT). First, for $\kappa_\mathrm{s} = 0$ the dielectric constant diverges for small wavevectors according to Eq. 27. This is the behaviour of an ideal metal. This result implies that electric field lines are perpendicular to the surface of material modelled within the QE approach. (This is observed in simulations, which shall not be shown here.) Second, for $\kappa = 0$, the dielectric constant is finite. However, a problem that arises is that the Hessian must be positive definite. The smallest value that $\tilde{J}(\mathbf{k})$ takes for unscreened Coulomb interactions on the simple cubic lattice is $-(3\pi^2)M/4\pi\varepsilon_0 a$, where $M = 1.748$ is the Madelung constant of the rock salt lattice. Thus, κ_s must exceed the largest negative eigenvalue of the $\tilde{J}_{\alpha\beta}(\mathbf{k})$ matrix. This is found at $\mathbf{k} = (\pi/a)(1, 1, 1)$ and the resulting limitation for the the dielectric permittivity is $\varepsilon_\mathrm{r}^{\mathrm{AACT}} - 1 < 1/1.748$, at least for unscreened Coulomb potentials. This is less than the corresponding value of any condensed matter material. Very small values observed in reality are, for example $\varepsilon_\mathrm{r} \gtrsim 2$ for Teflon or polyethylene. These values are similar to $\varepsilon_\mathrm{r}^{\infty}(\mathrm{NaCl}) = 2.56$.

3.3 Dipole-Dipole Interactions in Real and Reciprocal Space

The field of a dipole $\boldsymbol{\mu}$ centred at the origin can be represented according to

$$\begin{aligned}\mathbf{E}(\mathbf{r}) &= \frac{1}{4\pi\epsilon_0}\nabla\left(\boldsymbol{\mu}\cdot\nabla\frac{1}{r}\right)\\ &= \frac{1}{4\pi\epsilon_0}\left(\frac{3(\boldsymbol{\mu}\cdot\mathbf{r})\mathbf{r}-\boldsymbol{\mu}r^2}{r^5}\right)-\frac{\boldsymbol{\mu}}{3\epsilon}\delta(\mathbf{r})\end{aligned} \tag{34}$$

Thus, the potential energy V gained when a second dipole is placed at $\mathbf{r}\neq 0$ reads in tensor notation

$$V = J_{\alpha\beta}(\mathbf{r})\mu_{1\alpha}\mu_{2\beta} \tag{35}$$

with

$$J_{\alpha\beta}(\mathbf{r}) = \frac{-1}{4\pi\epsilon_0}\frac{3r_\alpha r_\beta - r^2\delta_{\alpha\beta}}{r^5}. \tag{36}$$

If dipoles are placed onto a Bravais lattice, such as the simple cubic lattice, it is readily shown – using the properties of the Fourier transform – that the net potential energy

$$V = \frac{1}{2}\sum_{i,j\neq i} J_{\alpha\beta}(\mathbf{R}_i-\mathbf{R}_j)\mu_\alpha(\mathbf{R}_i)\mu_\beta(\mathbf{R}_j) \tag{37}$$

can be expressed in reciprocal space as

$$V = \frac{1}{2}\sum_{\mathbf{k}} \tilde{J}_{\alpha\beta}(\mathbf{k})\tilde{\mu}_\alpha(\mathbf{k})\tilde{\mu}^*_\beta(\mathbf{k}), \tag{38}$$

where $\mathbf{k}$ is a reciprocal lattice vector. Moreover

$$\tilde{J}_{\alpha\beta}(\mathbf{k}) = \sum_{\mathbf{R}\neq 0}\frac{-1}{4\pi\epsilon_0}\frac{3R_\alpha R_\beta - R^2\delta_{\alpha\beta}}{R^5}\exp(-i\mathbf{k}\cdot\mathbf{R}), \tag{39}$$

where the summation runs over all lattice vectors $\mathbf{R}$.

Similar comments apply to the point-point and point-dipole interactions.

4 Further Properties of Charge Equilibration Models

Most charge-transfer studies do not focus on periodic systems but are predominantly concerned with molecules. In that context, deficiencies of various models were noted before the analysis presented in the previous section had been conducted. Here, we summarize some of the results on molecular systems.

One of the first problems noted with regular QE is that it does not obey the neutral dissociation limit[24], as can be seen from Eq. 4. The original proposition to fix this problem was to screen chemical potential differences as a function of distance[24]. Unfortunately, this fix is hardly justified in reality and its implementation actually leads to artifacts, e.g., batteries could not work if the chemical potentials between atoms were screened as a function of distance. Screening is only meaningful for electrostatic field lines when there is a medium whose influence is not considered explicitly. But even if field lines were screened,

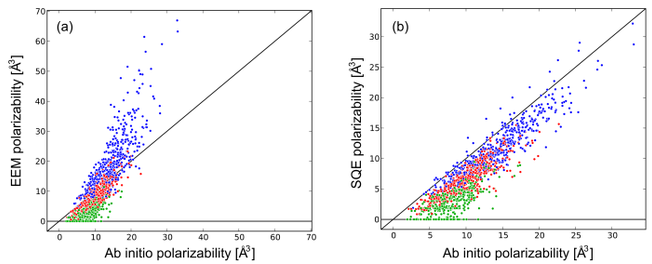

Figure 4. Polarizability of (a) QE and (b) SQE as a function of the polarizability deduced from quantum mechanical calculations on a variety of molecules. Green, red, and blue data points reflect the smallest, the medium, and the largest eigenvalue of the polarizability tensor for different molecules (including varying conformations). From Ref. 17.

this does not mean that energy differences would be completely damped out. The line integral from one point to another would still remain finite owing to near-field contributions. Moreover, how can screening be justified for a dimer placed in vacuum?

Approaches in which the concept of bond hardness is introduced can be easily parameterized to yield dissociation limits in which the atoms are neutral[12,25] – or have non-zero integer charge[16,26]. All that needs to be done is to make the bond hardness diverge when two atoms or two molecular fragments are moved to large separation. In fact, a quantitative analysis revealed that making the bond stiffness between two atoms simply a function of the distances between the two atoms (without including an environment dependence) already lead to reasonably accurate atomic charges of the reactants (initially and near the transition state) and of the products of the bond breaking[25].

It had also been observed that the polarizability of polymers $\gamma(N)$ (e.g. simple alkanes) as treated with QE growths with the third power of the degree of polymerization N in the limit of large N. The correct scaling is linear[27,17]. Some representative results are shown in Fig. 4 and compared to quantum chemical calculations. One can see that the QE model systematically overestimates polarizabilities while SQE shows the correct trend. The SQE data only tends to lie slightly below the quantum chemical results, which is easily explained because the employed SQE model did not allow for atom polarizability. Lastly, QE models ignoring the bond hardness term produce alcohols whose dipole moment increases as the fatty tail of the molecule is made longer, while the dipole quickly levels off at a realistic value within an SQE type treatment[28].

The AACT models do not suffer from the shortcomings of pure QE models. However, they have different deficiencies. For example, they barely show any dispersion of the alkene polarizability $\gamma(N)$ at small N in contrast to the real behaviour and that exhibited by SQE models[27]. This behaviour can be rationalized from the small (zero) penetration depth δ derived for solids in the last section. Moreover, the AACT model produces negative (chemical) hardnesses of molecules when excess charge is added to a molecule[16].

In conclusion, neither pure bond nor conventional QE model produce the correct con-

stitutive equations, while their combination in form of SQE can be parameterized to reproduce meaningful numbers. In fact, even absolute numbers turn out reasonable[12], e.g., atomic charges deduced from SQE were within $\mathcal{O}(10\%)$ accuracy as compared to DFT-based results while QE and AACT deviated by $\mathcal{O}(30\%)$. A comprehensive comparison between SQE and QE also found that SQE clearly outperformed the original QE in all 23 benchmark tests on a set of more than 500 organic molecules[17].

The true advantage of SQE, when applied at a molecular level, might yet be a different one: It allows one to introduce formal oxidation states and to treat meaningfully excess integer charge in molecular systems[16,26]. This makes it possible to reproduce the generic features of contact electrification as well as the discharge of batteries, which will be shown in future work.

5 Concluding Remarks

The main part of this contribution is the analysis of the dielectric permittivity as produced by the regular split-charge equilibration model and a model in which point dipoles are placed on discrete lattice sites. While both methods have similar low-density, long-wavelength response functions, there are quite a few differences between them. First, the SQE model is based on summing up (eventually screened) Coulomb interactions between point charges while the point dipole models are based on dipole-dipole interactions. Since the resulting sums are conditionally convergent in both cases, neither one can be cut off at a finite distance without uncontrollable errors. The advantage of the SQE model is that fewer floating-point operations are required to evaluate pair interactions, since the coupling of point charges is described by a scalar rather than by a tensor of rank two as for dipoles. Moreover, fast summation methods for Coulomb interactions are readily available. Second, the SQE model produces response functions on the (easy-to-code) simple cubic lattice that are isotropic not only in the continuum limit but also with respect to their leading-order continuum corrections, which are of order k^2. Point dipole models on the simple cubic lattice have direction-dependent k^2 interactions.

A potentially useful advantage of SQE over point-dipole models is that the SQE model can reflect non-local dielectric response functions. This can be done, in principle, by introducing non-local charge-transfer variables. This ability makes the SQE model a promising candidate as a coarse-grained model for water, which is known to have a strong wavelength dependent dielectric constant[29]. Another advantage of the SQE model is that it is isomorphic to elastic models. The split charges can be treated in analogy to (elastic) displacements in the solid. Thus, coarse-graining of the region and adaptive mashing of SQE can be done in analogy to elastic models.

Acknowledgements

The author thanks W. Dapp and J. Jalkanen for useful discussions.

References

1. A. Warshel and M. Levitt. *J. Mol. Biol.*, 103:227–249, 1976.
2. B. Honig and A. Nicholls. *Science*, 268:1144–1149, 1995.
3. P. Jungwirth and D. J. Tobias. *Chem. Rev.*, 106:1259–1281, 2006.
4. A. Warshel, P. K. Sharma, M. Kato, and W. W. Parson. *Biochim. Biophys. Acta*, 1764:1647–1676, 2006.
5. J. Applequist, J. R. Carl, and K.-K. Fung. *J. Am. Chem. Soc.*, 94:2952, 1972.
6. B. Thole. *Chem. Phys.*, 59:341, 1981.
7. A. Papazyan and A. Warshel. *J. Phys. Chem. B*, 101:11254–11264, 1997.
8. K. G. Denbikh. *Trans. Faraday Soc.*, 36:936–948, 1940.
9. J. Meister and W. H. E. Schwarz. *J. Phys. Chem.*, 98:8245–8252, 1994.
10. T. Verstraelen, P. W. Ayers, V. Van Speybroeck, and M. Waroquier. (submitted to J. Chem. Phys.).
11. S. W. Rick and S. J. Stuart. *Rev. Comp. Chem.*, 18:89, 2002.
12. R. A. Nistor, J. G. Polihronov, M. H. Müser, and N. J. Mosey. *J. Chem. Phys.*, 125:094108, 2006.
13. R. P. Iczkowski and J. L. Margrave. *J. Am. Chem. Soc.*, 83:3547–3551, 1961.
14. W. J. Mortier, K. van Genechten, and J. Gasteiger. *J. Am. Chem. Soc.*, 107:829, 1985.
15. R. Chelli, P. Procacci, R. Righini, and S. Califano. *J. Chem. Phys.*, 111:8569–8575, 1999.
16. M. H. Müser. *European Physical Journal B*, 85:135, 2012.
17. T. Verstraelen, V. Van Speybroeck, and M. Waroquier. *J. Chem. Phys.*, 131:044127, 2009.
18. P. W. Fowler and P. A. Madden. *J. Phys. Rev. B*, 29:1035–1042, 1984.
19. J. Robles and L.J. Bartolotti. *J. Am. Chem. Soc.*, 106:3723–3727, 1984.
20. R. A. Nistor and M. H. Müser. *Phys. Rev. B*, 79:104303, 2009.
21. M. H. Cohen and F. Keffer. *Phys. Rev.*, 99:1128–1134, 1955.
22. B. R. A. Nijboer and F. W. De Wette. *Physica*, 6:422–431, 1958.
23. J. H. Hannay. *Eur. Phys. J.*, 4:141–143, 1983.
24. J. Morales and T. J. Martinez. *J. Phys. Chem. A*, 105:2842, 2001.
25. D. Mathieu. *J. Chem. Phys.*, 127:224103, 2007.
26. W. B. Dapp and M. H. Müser. (in preparation).
27. G. L. Warren, J. E. Davis, and S. Patel. *J. Chem. Phys.*, 128:144110, 2008.
28. P. T. Mikulski, M. T. Knippenberg, and J. A. Harrison. *J. Chem. Phys.*, 131:241105, 2009.
29. P. A. Bopp, A. A. Kornyshev, and G. Sutmann. *Phys. Rev. Lett.*, 76:1280–1283, 1996.

Multiscale Fluid Dynamics Simulation Applied to Micellar Solution

Takahiro Murashima, Masatoshi Toda, and Toshihiro Kawakatsu

Department of Physics, Tohoku University,
Aramaki-Aoba, Aoba-Ward, Sendai, 980-8578, Japan
E-mail: murasima@cmpt.phys.tohoku.ac.jp

The relationship among macroscopic flow behaviour and microscopic properties of wormlike micellar solution confined to a channel is analyzed with multiscale simulation that is composed of the fluid dynamics simulation and the coarse-grained micellar dynamics simulation describing the microscopic states of micelles. The flow profile of the wormlike micellar solution has reflected elasticity coming from the orientation of fully grown wormlike micelles.

1 Introduction

Macroscopic dynamics of soft matter (e.g. polymer melts, colloidal suspensions, liquid crystals, micellar solutions and so on) highly depends on each microscopic states in which a mesoscopic scale structure is formed. The relaxation time of the mesoscopic structure is very long and comparable to the time scale of the macroscopic dynamics even if the size of the mesoscopic structure is much smaller than the length scale of the macroscopic dynamics. When we consider the macroscopic dynamics of soft matter, we have simultaneously to take into account its microscopic dynamics.

Recently, we have developed a multiscale simulation method[1–4] that is composed of macroscopic fluid dynamics simulation and microscopic coarse-grained polymer dynamics simulation to investigate a polymer melt flow. And then, we have applied the multiscale simulation to wormlike micellar solution[5].

In the previous work[5], we have investigated the flow behaviour of wormlike micellar solution confined to a channel and found that the wormlike micellar solution shows the elastic flow behaviour. We have predicted that this elasticity is coming from the gel state of wormlike micelles without any evidence. In this work, we investigate microscopic details of wormlike micelles, such as orientation order, percolation, and topological information. We clarify the relationship among the macroscopic dynamics and the microscopic properties in the wormlike micellar solution.

2 Multiscale Simulation for Wormlike Micellar Solution

Surfactants consist of a hydrophilic head and a hydrophobic tail. In a water, surfactants form spherical micelles where the hydrophobic tails aggregate in the micelles and the hydrophilic heads are in the surrounding water. When counter ions exist in the water, the spherical micelles aggregate and form wormlike micelles. Because there is a quite large gap between the sizes of the surfactants and the wormlike micelles, we need a course-graining method for describing this system. One of the authors[6] has developed a new course-graining technique that is taking account of the elastic energy of the membrane

made of the surfactants. This course-graining model for micelles reproduces the breakup and/or coalescence of the wormlike micelles without directly treating the surfactants. Using this model as a microscopic simulator in our multiscale simulation, we can simulate the macroscopic flow behaviour of the micellar solution.

2.1 Macroscopic Part

Macroscopic flow behaviour of micellar solution is described by the Cauchy momentum equation:

$$\frac{\mathrm{D}\boldsymbol{v}(\boldsymbol{r})}{\mathrm{D}t} = \frac{1}{\rho}\boldsymbol{\nabla}\cdot\overleftrightarrow{\boldsymbol{\sigma}}(\boldsymbol{r}) - \frac{1}{\rho}\boldsymbol{\nabla}p(\boldsymbol{r}), \tag{1}$$

where $\boldsymbol{v}(\boldsymbol{r})$, $\overleftrightarrow{\boldsymbol{\sigma}}(\boldsymbol{r})$ and $p(\boldsymbol{r})$ are the velocity, the stress tensor, and the hydrostatic pressure at the position $\boldsymbol{r}$, respectively, and ρ is the density assumed to be constant. The stress tensor is obtained from the microscopic structure of micelles. A flow in an infinitely long channel with two parallel infinite flat walls has a translational symmetry under parallel displacement along the flat walls, and then, Eq. 1 reduces to the one-dimensional equation:

$$\partial_t v_x(y) = \partial_y \sigma_{yx}(y)/\rho + a_x, \tag{2}$$

where $a_x = -\partial_x p/\rho$ is the acceleration due to the pressure gradient between up- and down-streams. x-axis is the flow direction and y-axis is perpendicular to the walls. In the one-dimensional flow, the velocity gradient is only a shear component $\dot{\gamma} = \partial_y v_x$. Here we define zero-shear viscosity as $\mu = \lim_{\dot{\gamma}\to 0}\sigma_{yx}/\dot{\gamma}$. Comparing the orders of magnitude in both sides of Eq. 2 in the limit of zero shear rate, we obtain the Stokes number St defined by $\mathrm{St} = \rho \mathrm{L}^2/\mu\mathrm{T}$, where L and T is the characteristic length and time, respectively, of the macroscopic flow.

2.2 Microscopic Part

The stress tensor $\overleftrightarrow{\boldsymbol{\sigma}}$ depends on local microscopic states that are influenced by the flow history (the experienced strain-rate) of a fluid particle. To describe the local microscopic states in a fluid particle, we perform microscopic simulation, "the particle-field hybrid model"[6]. This model consists of three parts; discrete particle dynamics, continuous fluid dynamics and reaction mechanism (elementary processes). In the wormlike micellar solution, hydrodynamic interaction among micelles is screened out because the concentration of micelles is high. Therefore, we now do not consider the continuous fluid dynamics at the microscopic level, just assume a linear shear flow field $\dot{\gamma}$ obtained at the macroscopic level.

A particle, which represents a spherical micelle, obeys the following overdamped Langevin dynamics:

$$\frac{\mathrm{d}}{\mathrm{d}t}\widetilde{\boldsymbol{r}}_i(t) = \dot{\gamma}\widetilde{y}_i\boldsymbol{e}_x - \frac{1}{\zeta}\frac{\partial H(\{\widetilde{\boldsymbol{r}}_j(t)\})}{\partial\widetilde{\boldsymbol{r}}_i(t)} + \boldsymbol{\xi}_i(t), \tag{3}$$

where $\widetilde{\boldsymbol{r}}_i(t)$ ($[\mathrm{L_m}]$) is the position of the i-th particle ($i = 1, \cdots, N_\mathrm{s}$) in the microscopic coordinate system (Unit length of $\widetilde{\boldsymbol{r}}_i$ is $\mathrm{L_m}$.), ζ is the friction coefficient, $H(\{\widetilde{\boldsymbol{r}}_i(t)\})$ is the Hamiltonian in the microscopic system, $\boldsymbol{\xi}_i(t)$ is white noise: $\langle\boldsymbol{\xi}_i(t)\rangle = \boldsymbol{0}$, $\langle\boldsymbol{\xi}_i(t)\boldsymbol{\xi}_j(t')\rangle =$

$2\zeta^{-1}k_{\mathrm{B}}T\delta_{ij}\delta(t-t')\overleftrightarrow{\mathbf{1}}$, where k_{B} is the Boltzmann constant and T is the absolute temperature.

When spherical micelles aggregate, the spherical shape of micelles turns into an ellipsoidal shape, a wormlike one, and a branched one, and so on. In the Hamiltonian $H(\{\widetilde{\boldsymbol{r}}_i(t)\})$ in Eq. 3, the following Helfrich's bending energy coming from the shapes of micelles is taken into account:

$$H_{\mathrm{Helfrich}} = \sum_i \int \mathrm{d}\boldsymbol{a}_i [2\kappa(c_{\mathrm{m}}(\boldsymbol{a}_i) - c_0)^2 + \bar{\kappa} c_{\mathrm{G}}(\boldsymbol{a}_i)], \tag{4}$$

where $c_{\mathrm{m}}(\boldsymbol{a}_i)$ and $c_{\mathrm{G}}(\boldsymbol{a}_i)$ are the mean curvature and the Gaussian one, respectively. (κ and $\bar{\kappa}$ are elastic constants.) Restricting the shapes of curvature to sphere, half sphere, cylinder, tripod and tetrapod according to the connectivity of micelles (surface area $\boldsymbol{a}_i$ is assigned on the i-th particle $\widetilde{\boldsymbol{r}}_i$), we can approximately evaluate the bending energy at $\widetilde{\boldsymbol{r}}_i$ (the integral in Eq. 4)[6].

The reaction mechanism describes the association and dissociation process of micelles. The dominant processes are the following four: (a) scission, (b) fusion, (c) end interchange, (d) bond interchange. The Gaussian curvature energy (the second term in Eq. 4) $H_{\mathrm{G}} = 2\pi\chi\bar{\kappa}$ (χ is the Euler characteristic) is calculated from these elementary processes. The reaction rate is assumed to be proportional to the transition probability $\mathrm{e}^{-\beta\Delta E}/(1+\mathrm{e}^{-\beta\Delta E})$ where ΔE is the energy difference before and after reaction. The association and/or dissociation processes are determined with the Monte Carlo method.

The stress tensor of micelles $\overleftrightarrow{\boldsymbol{\sigma}}_{\mathrm{m}}$ in the microscopic system is composed of the virial stresses coming from two and three body forces:

$$\overleftrightarrow{\boldsymbol{\sigma}}_{\mathrm{m}} = -\frac{1}{V}\sum_{i=1}^{N_{\mathrm{s}}}\sum_{\substack{j=1\\ j\neq i}}^{N_{\mathrm{s}}} \widetilde{\boldsymbol{r}}_i \boldsymbol{F}_{ij}^{(2)} - \frac{1}{V}\sum_{i=1}^{N_{\mathrm{s}}}\sum_{\substack{j=1\\ j\neq i}}^{N_{\mathrm{s}}}\sum_{\substack{k=1\\ k\neq i}}^{N_{\mathrm{s}}} \widetilde{\boldsymbol{r}}_i \boldsymbol{F}_{ijk}^{(3)}. \tag{5}$$

The units of time, length and energy in the microscopic system are $\mathrm{T_m} = \rho a^3/\zeta$, $\mathrm{L_m} = a$, and $\mathrm{E_m} = \zeta^2/\rho a$, respectively, where a is the size of spherical micelle. The boundary conditions are periodic in x- and z-direction while Lees-Edwards boundary condition is assumed in y-direction.

2.3 Macro-Micro Conversion and Model Parameters

The macroscopic simulation and the microscopic simulation connect with each other through the shear rate $\dot{\gamma}$ and the shear stress σ_{yx}. Since the units of time and length are different between the macroscopic and microscopic simulations, we need conversion rules for the shear rate and the shear stress. When one macroscopic time step Δt corresponds to n microscopic time steps Δt_{m}, $\Delta t[\mathrm{T}] = Cn\Delta t_{\mathrm{m}}[\mathrm{T_m}]$, where $C = \Delta t/(n\Delta t_{\mathrm{m}})[\mathrm{T}/\mathrm{T_m}]$ is a conversion constant. Then,

$$\dot{\gamma}_{\mathrm{m}} = C\dot{\gamma}, \tag{6}$$

where $\dot{\gamma}_{\mathrm{m}}$ is the shear rate with the inverse of the microscopic time unit. Taking account of the viscosity of the solvent in the microscopic system, the relationship between the

macroscopic shear stress σ_{yx} and the microscopic shear stress σ_{yx}^{m} is

$$\frac{1}{\mu}\partial_y \sigma_{yx} = (1-\beta)\frac{1}{C\eta_0}\partial_y \sigma_{yx}^{\mathrm{m}} + \beta\partial_y^2 v_x, \tag{7}$$

where $\eta_0 = \lim_{\dot{\gamma}_{\mathrm{m}}\to 0}\eta(\dot{\gamma}_{\mathrm{m}})$, $\eta(\dot{\gamma}_{\mathrm{m}}) = \lim_{t\to\infty}\sigma_{yx}^{\mathrm{m}}(t)/\dot{\gamma}_{\mathrm{m}}$, β is a ratio of a purely viscous component in the shear stress in the microscopic system[3]. Eq. 7 is not sufficient for describing the macroscopic stress because the number of degrees of freedom in the microscopic system is too small compared to that in the macroscopic fluid element. To increase the number of degrees of freedom in a fluid element, we prepare N_{b} microscopic simulation boxes with different random seeds for describing one fluid element. Averaging over N_{b} simulation boxes, the thermal noise decreases according to $1/\sqrt{N_{\mathrm{b}}}$. We replace σ_{yx}^{m} with $\langle\sigma_{yx}^{\mathrm{m}}\rangle = \frac{1}{N_{\mathrm{b}}}\sum^{N_{\mathrm{b}}}\sigma_{yx}^{\mathrm{m}}$ in Eq. 7. Because of this ensemble average method, we can regard the microscopic simulator as a macroscopic constitutive equation in the multiscale simulation. Because each microscopic simulation box is independent of the other simulation boxes in a time interval Δt, we utilize a parallel computer based on a distributed memory architecture. For communication among processors on the parallel computer, we implement Message Passing Interface.

Parameters in the multiscale simulation are summarized in Tab. 1.

Variable	Value	Unit
(macroscopic part)		
L	1.0	(Width of channel)
T	1.0	$[\rho \mathrm{L}^2/\mu\mathrm{St}]$
St	1.0	$[\rho \mathrm{L}^2/\mu\mathrm{T}] = [\ ]$
Δt	0.0001	$[\mathrm{T}]$
Δy	0.05	$[\mathrm{L}]$
a_x	0.1	$[\mathrm{L}/\mathrm{T}^2]$
(macro-micro conversion part)		
β	0.2	$[\ ]$
C	0.1	$[\mathrm{T}/\mathrm{T}_{\mathrm{m}}]$
N_{b}	100	$[\ ]$

Variable	Value	Unit
(microscopic part)		
T_{m}	1.0	$[\rho a^3/\zeta]$
L_{m}	1.0	$[a]$
E_{m}	1.0	$[\zeta^2/\rho a]$
Δt_{m}	0.001	$[\mathrm{T}_{\mathrm{m}}]$
a	1.0	$[\mathrm{L}_{\mathrm{m}}]$
$\sqrt[3]{V}$	$32a$	$[\mathrm{L}_{\mathrm{m}}]$
N_{s}	3000	$[\ ]$
κ	0.5	$[\mathrm{E}_{\mathrm{m}}]$
$\overline{\kappa}$	-0.1	$[\mathrm{E}_{\mathrm{m}}]$
c_0	0.3	$[1/\mathrm{L}_{\mathrm{m}}]$
η_0	0.45	$[\mathrm{E}_{\mathrm{m}}\mathrm{T}_{\mathrm{m}}/{\mathrm{L}_{\mathrm{m}}}^3]$

Table 1. Set of parameters in the multiscale simulation.

3 Simulation Results

We investigate Startup flow of micellar solution confined to a channel. Initial condition is that fluid state is stationary and the spherical micelles are randomly distributed in each microscopic simulation box. Namely, the initial state of this solution is sol. As soon as the micellar solution starts to flow, the spherical micelles aggregates to form the wormlike micelles. The initial sol state turns into the gel state within $10[\mathrm{T}_{\mathrm{m}}]$ under the parameter sets in Tab. 1. Space-time plots of macroscopic and microscopic information of micellar

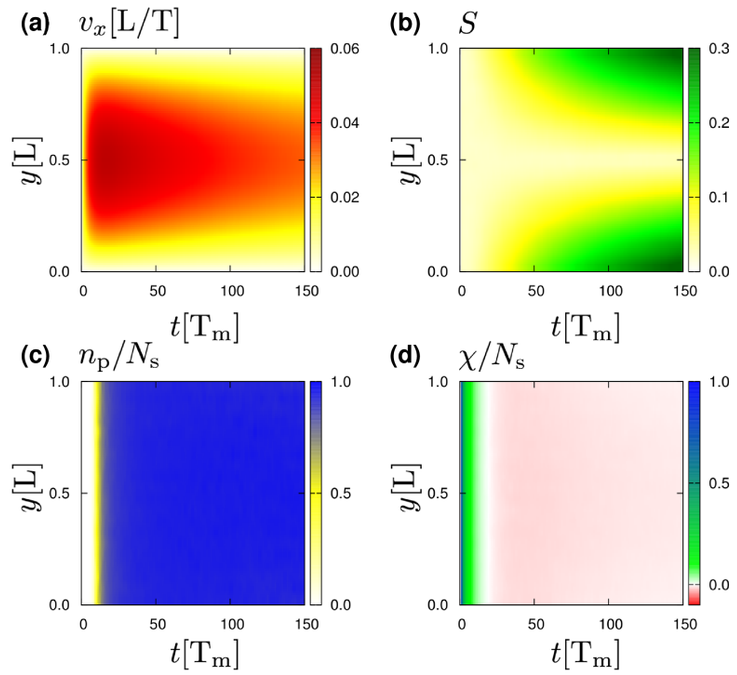

Figure 1. (Colour online) Space-time plots of the micellar solution obtained with the multiscale simulation. The figures show (a) velocity profile ($v_x[\mathrm{L/T}]$), (b) nematic order parameter (S), (c) number of percolated particles ($n_\mathrm{p}/N_\mathrm{p}$), and (d) Euler characteristic (χ/N_p) within a time interval from 0 $[\mathrm{T_m}]$ to 150 $[\mathrm{T_m}]$.

solution are summarized in Fig. 1; (a) Velocity field $v_x[\mathrm{L/T}]$, (b) Nematic order parameter $S = \langle \frac{3}{2}(\boldsymbol{u}\cdot\boldsymbol{n})^2 - \frac{1}{2}\rangle$ ($\boldsymbol{u}$ is a normalized bond vector connecting between neighbouring particles and $\boldsymbol{n}$ is a local director), (c) The number of percolated particles n_p normalized by N_s, and (d)Euler characteristic $\chi = 2(n_\mathrm{c} - n_\mathrm{h})$ normalized by N_s (n_c is the number of clusters and n_h is the number of holes in a cluster). Figs. 1 (c) and (d) characterize the fluid state. After $t = 10[\mathrm{T_m}](= t_\mathrm{p})$, a cluster in a fluid element percolates between the opposite boundaries in a microscopic simulation box and the rest of the clusters immediately belong to the percolated clusters, as shown in Fig. 1 (c). Fig. 1 (d) shows a steady state after t_p, corresponding to Fig. 1 (c). Because Euler characteristic is negative after t_p, the clusters have many holes as reported by one of authors[6]. After t_p, the magnitude of v_x decreases with increasing nematic order parameter S from the neighbourhoods of the walls. This nematic order parameter reflects local strain which results in a stress that restores to an isotropic state.

4 Concluding Remarks

We have investigated the start-up flow of micellar solution confined to a channel with the multiscale simulation. The multiscale simulation has revealed that the elastic flow behaviour of micellar solution is caused by the gel states and the orientation of the worm-like micelles. The multiscale simulation enables us to investigate the relationship among macroscopic states and microscopic states.

We have assumed the translational symmetry in an infinitely long channel. However, this assumption breaks at the microscopic level because microscopic states are different in each fluid element and do not have the translational symmetry. To consider the microscopic states precisely, we need to treat the Cauchy momentum equation 1 with a Lagrangian method[1]. We will consider a more general situation using a Lagrangian method in the near future.

Acknowledgements

We would like to thank Professor Ryoichi Yamamoto and Professor Takashi Taniguchi for providing their computer facilities. Some of the calculations in our works were done using the computer facilities of the Institute of Solid State Physics (ISSP) Super Computer Center (University of Tokyo). This work was supported by JSPS KAKENHI Grant Number 23340120 and 24350114.

References

1. T. Murashima and T. Taniguchi, *Multiscale Lagrangian fluid dynamics simulation for polymeric fluid*, J. Polym. Sci. B **48**, 886–893, 2010.
2. T. Murashima and T. Taniguchi, *Multiscale simulation of history-dependent flow in entangled polymer melts*, EPL **96**, 18002, 2011.
3. T. Murashima and T. Taniguchi, *Flow-History-Dependent Behavior of Entangled Polymer Melt Flow Analyzed by Multiscale Simulation*, J. Phys. Soc. Jpn. **81**, SA013, 2012.
4. T. Murashima, S. Yasuda, T. Taniguchi,and R. Yamamoto, *Multiscale Modeling for Polymeric Flow: Particle-Fluid Bridging Scale Methods*, J. Phys. Soc. Jpn. **82**, 012001, 2013.
5. T. Murashima, M. Toda, and T. Kawakatsu, *Multiscale Simulation for Soft Matters: Application to Wormlike Micellar Solution*, (submitted to AIP Conference Proceedings).
6. M. Toda, *Dynamics of Wormlike Micellar Systems*, (Ph. D. Thesis, Tohoku University, 2012); M. Toda and T. Kawakatsu, *Structure and Rheology of Wormlike Micellar Systems*, (submitted to AIP Conference Proceedings).

A Hybrid Particle-Continuum Method in Soft Condensed Matter Simulations

Shuanhu Qi, Hans Behringer, and Friederike Schmid

Institut für Physik, Johannes Gutenberg-Universität Mainz,
Staudingerweg 9, D-55099 Mainz, Germany
E-mail: {*qish, behringh, friederike.schmid*}*@uni-mainz.de*

A multiscale hybrid model combining a particle-description method and a continuum-field-description method is developed for simulations in soft condensed matter systems. The hybrid model treats part of the system as particles, and the other part as continuum fields, and particles in different resolution regions can switch and migrate on the fly. The switch and migration of particles from different resolution regions are controlled by an inhomogeneous "chemical potential". The hybrid model is tested for a polymer solution with implicit solvent with the comparison to that of the pure particle representation method, and good agreements are reached.

1 Introduction

Hybrid simulation schemes are rapidly developing in the community of multiscale modelling[1–3]. A hybrid description means that the system under consideration is partitioned into a few regions, each of which is represented by a model depending on its resolution level, and the information from different regions can be exchanged on the fly[4]. These diverse resolution methods are chosen according to the problems that one is interested in, and if the proper ones are set up investigating the properties of the system, not only the intrinsic physics can be kept, but the time consumption of the simulation can be decreased. As an example, we consider a polymer solution confined in a large box. This solution shows very sharp interfaces near the boundaries and wide bulk region around the centre of the box. The configurations of polymers in the interface may be interesting, so a detailed particle representation method is required in the description, while in the large bulk region, only the knowledge of density profile is enough, so the coarser continuous field representation in such region is sufficient. The hybrid particle-continuum method is quite suitable for such a system, and similar systems are ubiquitous in soft condensed matter science. Further, many successful and powerful strategies are widely used in dealing with the problems in the continuous model[5], and the implementation of such strategies in the hybrid model will make it more applicable in practice. Hence, this hybrid particle-continuum method would be attractive.

2 Methodology

In this section, the methodology for our hybrid particle-continuum simulations is sketched. The construction of this hybrid model proceeds mainly through two steps, in which two crucial questions, i.e., how one extracts the coarser degrees of freedom from finer ones and how one couples these two types of degrees of freedom, are answered. These two questions are always encountered in multiscale modelling, and the ways to solve them

not only characterise the hybrid method but also determine the extent to which the model reflects reality.

In order to show the construction more clearly and make the notation simple, we come back to the polymer solution mentioned in the introduction. By several steps which will be discussed in more detail elsewhere, we can rewrite the partition function *exactly* as

$$Z = \sum_{\{\tau_\alpha\}} \int \mathcal{D}\omega_f \mathcal{D}\rho_f \int \prod_{\{\alpha,j\}} d\mathbf{R}_{\alpha,j} \exp\Big\{ - H_{\text{eff}} + \sum_{\{\alpha\}} [\Delta\mu(\mathbf{R}_{\alpha,0})\tau_\alpha - \ln(e^{\Delta\mu}+1)] \Big\}, \tag{1}$$

where the $\tau_\alpha = 0, 1$ are auxiliary variables, the ω_f and ρ_f are auxiliary fluctuating fields, and the integral $\prod d\mathbf{R}_{\alpha,j}$ runs over chains with $\tau_\alpha = 1$ only (which we shall denote 'p'-chains in the following). The effective Hamiltonian H_{eff} contains the contribution from pure p-chains H_p, the contribution from the remaining chains (denoted 'f'-chains), and a coupling term $H_{\text{coup}} = v \int d\mathbf{r} \hat{\rho}_p \rho_f$, where $\hat{\rho}_p$ is the density contributed from only p-chains. The Hamiltonian for 'f'-chains is given by $H_f = \frac{v}{2} \int d\mathbf{r} \rho_f^2 - \int d\mathbf{r} i\omega_f \rho_f - n_f \ln Q_f$, where Q_f is the single chain partition function in an external fluctuating field ω_f, and n_f the number of f-chains. Obviously, we have described some of the chains (the 'f'-chains) by an equivalent fluctuating field representation. The particle description, the continuum field description as well as the hybrid one are equivalent in describing the macroscopic quantities by construction. However, they have different types of degrees of freedom, since the particle-based description refers to the particle coordinates, while for the continuum-based description refers to the fluctuating field.

The partition function Eq. 1 is the exact and complete form for the present hybrid model, and it is also the starting point for the incorporation of various approximations in order to make the hybrid model more practical, simple, and efficient in case of the central physics being kept. One important approximation usually implemented is the saddle point approximation[8] to reduce the number of fluctuating fields. It can be seen from the partition function, there are two fluctuating variables in the continuum representation part. The saddle point approximation is used to approximately perform the integration over one field, for example, the auxiliary potential, and in doing so the complex sampling of the potential is also avoided. This approximation can be safely implemented in case of high f-chain densities. Further approximations can also be performed for numerical convenience, i.e., a variable transformation from the density to auxiliary potential to avoid a time-consuming inverse solution in finding the auxiliary potential at a given density. Finally, the particle coordinates and auxiliary potential are the basic degrees of freedom for the present hybrid model.

3 Simulation Method

The Monte Carlo (MC) method[9] is used to sample the polymer configurations and continuum fields, and calculate statistical averages. In the MC simulation process, we performed a few thousand MC steps to equilibrate the system and another few thousand MC steps for the calculation of ensemble averages. During each MC step, one bead is averagely updated once. One MC step is split into 3 substeps to update the relevant variables, and in each substep Metroplis rule is used to evaluate the acceptance probability. Substep 1): update the configurations of p-chains[10] keeping all fields fixed. For the p-chains, one could perform

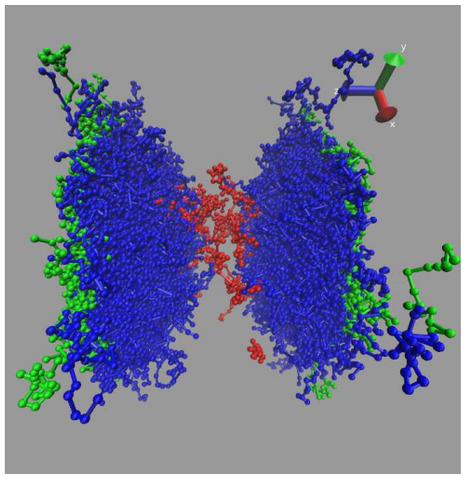

Figure 1. Snapshot of p-chains obtained by the hybrid model in different regions of the system, near the boundaries of $z = \pm Lz/2$ (green), in the bulk (red), and others (blue). There are obviously very few p-chains in the bulk region. The parameters are set $\mu_e = 3.0$, $\mu_m = -4.5$, and in such case the number of p-chains is about 4000 out of the total 10000.

a normal move or a bias-configuration move. Substep 2): update the auxiliary potential a few steps, keeping the p-chain configurations fixed. In this step there are a few different ways to generate the new potential. One is the dynamic density functional scheme, where the fluctuation in the field is neglected; the other one could be referred to as the simple un-biased fluctuation algorithm, meaning that the potential is updated by adding small random numbers; for the third, one updates the potential by some field-biased method called the field-biased fluctuation algorithm. The new potentials obtained using the dynamic density functional scheme are always accepted. Substep 3): perform the identity switch a few times keeping the configuration and field fixed. Choose a chain at random, if it is a p-chain, we will transform it into an f-chain, meaning that this p-chain disappears and the number of f-chains increases by one. If an f-chain is picked up, it will be transformed to a p-chain, i.e., one new p-chain is generated according to the Gaussian distribution function, and the number of p-chains increase by one. A few hundred switching steps are performed in each MC step.

4 Results and Conclusion

To test our approach, we study a system of $n_t = 10000$ polymer chains with $N = 20$ beads in each chain, both in the bulk and in a confined slab geometry . The volume of the system is set as $V = L_x \cdot L_y \cdot L_z = 8 \cdot 8 \cdot 16 R_g^3$, where $R_g \equiv \sqrt{Nb^2/6}$ is the mean

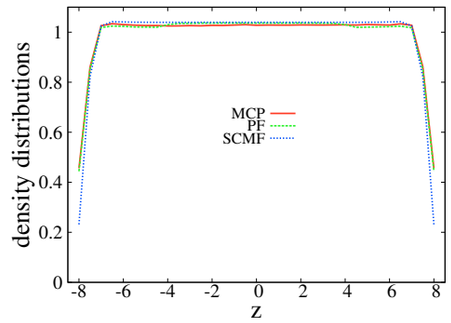

Figure 2. Normalized total density distributions with respect to z calculated by pure particle model (MCP), the hybrid model (PF), and the self-consistent mean field theory (SCMF). Large deviation happens near the boundaries, since SCMF theory is not suitable modelling the real boundaries.

radius of gyration (for ideal polymers), and b is the bond length. The system is discretized into $n_x \cdot n_y \cdot n_z = 16 \cdot 16 \cdot 32$ cells. The boundary conditions along the x direction and the y direction are always set to be periodic, so the density distributions along these two directions are always homogeneous. In the z direction, it is chosen periodic for bulk simulations, or impenetrable for confined slab simulations. In the pure particle model, impenetrable means that bonds may not cross the boundaries. In the continuum field model the impenetrable boundaries are introduced by imposing an infinite external potential at the boundaries. In principle, one can set the chemical potential $\Delta\mu(r)$ to any forms and any values. In the present work, it is chosen

$$\Delta\mu(\mathbf{r}) = \frac{\mu_e + \mu_m}{2} + \frac{\mu_e - \mu_m}{2\tanh\eta}\tanh\left[\eta\cos\frac{2\pi}{L_z}\Big(z + \frac{L_z}{2}\Big)\right] \tag{2}$$

where μ_e, μ_m and η are free parameters, and the former two control the magnitude and average value of $\Delta\mu(\mathbf{r})$, while the third controls the width of the transition region. In the following we set $\mu_e = 3.0$, $\mu_m = -4.5$, and $\eta = 11$.

Fig. 1 is a snapshot of the p-chain configurations obtained by the hybrid model with impenetrable boundary conditions in the z direction. As expected, in the high chemical potential region $\mu_e = 3.0$, most of the chains are p-chains, while in the low chemical potential region $\mu_m = -4.0$, there is only a very small number of p-chains (in red), i.e., in the bulk region, they are all most f-chains. We emphasize again that the particle description near the boundaries is preferred, since it allows one to model the interactions between boundaries and chains at a microscopic level. In the middle of the system, the chains behave like ideal chains, therefore the field description should be sufficient.

Fig. 2 shows the comparison of the total density (normalized by the average bead density) distributions obtained from the pure particle model, the hybrid model, and the SCF method. In the hybrid method, the potential is updated by a dynamic density functional scheme, so the field fluctuation is not taken into account. However, it can be seen that near

the boundaries, the curves calculated from the pure particle model and that from the hybrid one are almost superposed. For the SCF calculation, a small deviation happens near the boundaries, meaning that the SCF method can not capture the real boundary effect correctly. In the bulk region the densities obtained by these three methods almost agree with each other.

In summary, the hybrid model dynamically couples the particle description method and continuum field description method together allowing them to show their individual advantages in both analytical derivation and numerical calculations. The hybrid model has the potential to be more efficient than the pure particle model. The degrees of freedom sampled in the particle model correspond to the total number of beads, while in the field one they are given by the total number of grid points, so larger number of polymers will increase the time consumption for the particle method, but not for the field one. Very large systems with small regions calling for a particle description, while the remaining large part requiring only a continuum description, will be treated more efficiently by a hybrid description. Hence, this model is especially suitable to investigate very large systems in which there exist large regions that can be described by lower resolution models. Future studies include the optimization of the hybrid model to make it more efficient, exploiting the applications in other systems, as well as trying to construct a "self-determined" chemical potential.

Acknowledgements

We are indebted to S. Meinhardt, S. Dolezel, and J. Zhou for helpful discussion and suggestions. This work was funded in part by the German Science foundation.

References

1. M. J. Field, P. A. Bash, and M. Karplus, *A combined quantum mechanical and molecular mechanical potential for molecular dynamics simulations*, J. Comp. Chem. **11**, 700–733, 1990.
2. J. Baschnagel, K. Binder, P. Doruker, A. A. Gusev, O. Hahn, K. Kremer, W. L. Mattice, F. Müller-Plathe, M. Murat, W. Paul, S. Santos, U. W. Suter, and V. Tries, *Bridging the gap between atomistic and coarse-Grained models of polymers: status and perspectives*, Adv. Polym. Sci. **152**, 41–156, 2000.
3. S. A. Baeurle, *Multiscale modeling of polymer materials using field-theoretic methodologies: a survey about recent developments*, J. Math. Chem. **46**, 363–426, 2009.
4. A. B. Poma, and L. Delle Site, *Classical to path-integral adaptive resolution in molecular simulation: towards a smooth quantum-classical coupling*, Phys. Rev. Lett. **104**, 250201, 2010.
5. G. H. Fredrickson, *The Equilibrium Theory of Inhomogeneous Polymers* (Oxford University Press, Oxford, 2006).
6. D. A. Kofke and E. D. Glandt, *Monte Carlo simulation of multicomponent equilibria in a semigrand canonical ensemble*, Mol. Phys. **64**, 1105–1131, 1988.
7. F. Schmid, *Self-consistent-field theories for complex fluids* , J. Phys.: Condens. Matter **10**, 8105–8138, 1998.
8. A.-C. Shi, J. Noolandi, and R. C. Desai, *Theory of anisotropic fluctuations in ordered block copolymer phases*, Macromolecules **29**, 6487–6504, 1996.

9. D. Frenkel, and B. Smit, *Understanding Molecular Simulation: From Algorithms to Applications* (Academic Press, New York, 2002).
10. G. Besold, H. Guo and M. J. Zuckermann, *Off-lattice Monte Carlo simulation of the discrete Edwards model*, J. Poly. Sci. Part B: Polym. Phys. **38**, 1053–1068, 2000.

AA: A Super Coarse-Grained Model for Disordered Proteins

Ali Ghavami, Erik Van der Giessen, and Patrick Onck

Zernike Institute for Advanced Materials, University of Groningen,
9747AG, Groningen, the Netherlands
E-mail: {A.Ghavami, P.R.Onck, E.van.der.Giessen}@rug.nl

Recent studies have revealed the key role of natively-unfolded proteins in many important biological processes. In order to study the conformational changes of these proteins, a one-bead-per-amino-acid (AA) coarse grained model is developed and a method is proposed to extract the potential functions for the local interactions between beads. Experimentally obtained Ramachandran data for the coil regions of proteins are converted into distributions of pseudo-bond and pseudo-dihedral angles between neighbouring alpha-carbons in the polypeptide chain. These are then used to derive bending and torsion potentials, which are residue and sequence specific.

1 Introduction

Despite the classical view that a protein can attain its biological function only upon folding into a unique structure, there is increasing evidence that unfolded proteins play a key role in many important biological functions[1]. The basic functions of this class of proteins exploit the absence of a stable secondary structure in their polypeptide chain. An example is the so-called Nuclear Pore Complex (NPC): a huge molecular assembly with an estimated mass of 40–70 MDa, which provides bidirectional pathways for passive transport of small molecules and active transport of larger proteins. The NPC is a nearly cylindrical channel with a diameter of around 50 nm, which is composed of approximately 30 different proteins called Nucleoporins (Nups). Although the transport process of large molecules is not well understood, it has been shown that a subset of about 30% of the Nups containing many phenylalanine-glycine (FG) repeats in their amino acid sequence is key. These FG-nups are lined-up at the central channel of the NPC and are natively unfolded. Much research is going on to unravel the role of the FG-nups, but theoretical work is strongly constrained by the fact that Nups are large amino acids and are highly dynamic because they are not folded.

The dynamics of large disordered proteins amplifies the limitations of atomic-level molecular dynamics in terms of (biologically interesting) time and length scales. These limitations have drawn researchers towards the development of coarse-grained (CG) models to reduce the degrees of freedom and, thus, to increase the spatial and temporal domains of interest. Available CG models can be categorized into different classes according to the level of coarse-graining, the treatment of the solvent environment, and the method used for the force field parametrization[2]. Here we summarize an implicit-solvent method tailored for problems involving large numbers of unfolded proteins. In this approach, amino acids (AA) are represented by single beads with force fields that retain residue specificity – henceforth, the name AA model.

We first present the basics of the AA model[3], including local interaction potentials that are derived from experimental Ramachandran plots. Next, we present the long-range force fields that describe the electrostatic and hydrophobic interactions between as well as inside proteins[4]. The closing section discusses AA model predictions of the Stokes radius of Nups, in comparison with experimental results.

2 Coarse-Grained Model and Local Interactions

The central idea of the method is to represent each amino acid with a single bead. The coarse graining thus obtained is illustrated in Fig. 1. Since the atomic bond lengths and

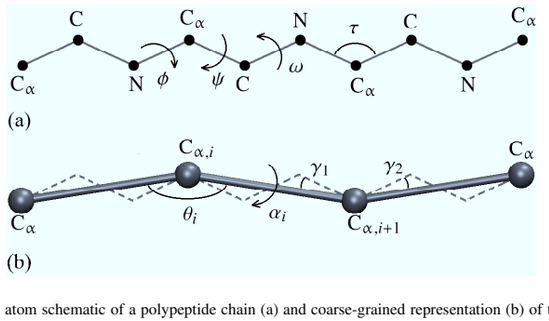

Figure 1. All atom schematic of a polypeptide chain (a) and coarse-grained representation (b) of the backbone with pseudo-bending and torsion angles. In (b) the dashed lines represent the polypeptide chain and the solid lines are the pseudo-bonds between C_α carbons which represent the coarse-grained geometry.

bond angles vary only slightly from their average values, the pseudo-bond lengths between subsequent C_α's can be taken to have a fixed value of $b = 0.38$ nm as defined by geometry. In the simulations this is achieved by a stiff harmonic potential $\Phi_{\rm bond} = K_{\rm b}(r-b)^2$ with $K_{\rm b} = 8038\ {\rm kJ}\cdot{\rm mol}^{-1}$.

The pseudo-bending angle θ and pseudo-dihedral angle α along the CG chain are defined between three and four consecutive C_α's and can also be computed from the backbone dihedral angles (ϕ, ψ) (see Fig. 1a). CG bending and torsion potentials can, in principle, be derived from atomistic simulations, but the absence of any structure in disordered proteins makes this impractical. Instead we have proposed[3] to extract them directly from Ramachandran plots – density distributions of the backbone ϕ and ψ values – of proteins by means of Boltzmann inversion. By confining attention to the coil regions, long range hydrophobic or electrostatic interactions are negligible.

The CG bending and torsion potentials depend on three and four subsequent residues respectively. For the total number of 20 amino acids this would require a humongous number of different potentials. Fortunately, the Ramachandran plots for many amino acids are very similar, and they can be classified into three types: Glycine (G), Proline (P) and the rest of the amino acids (X). This greatly reduces the number of interaction potentials,

but for bending it is important whether or not the next residue is P. This leads to a total of six bending potentials and nine torsion potentials, which are shown in Figs. 2 and 3, respectively.

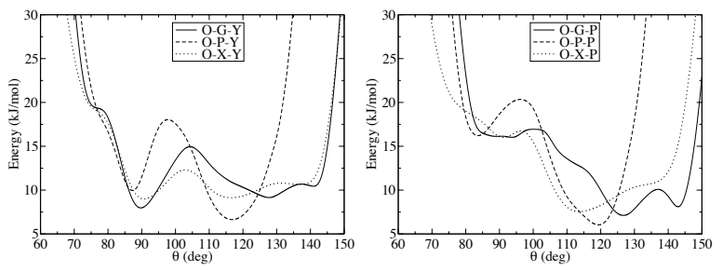

Figure 2. Bending potentials for fragments with G, P or X as central residues that (a) do not and (b) do have a Proline (P) following them. O represents any type of amino acid, while Y is any type except P.

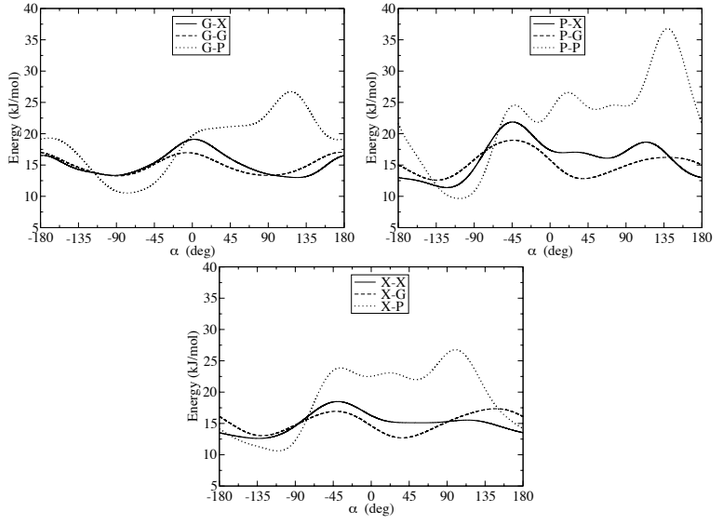

Figure 3. Torsion potentials for all combinations of three-letter amino acids.

The potentials presented above are applied to all beads in the polypeptide chain. In addition to the long-range interactions to be discussed in the next section, beads of different chains interact through a purely repulsive potential with a repulsive radius of $R_{\rm rep} = 0.38$ nm to represent excluded volume effects.

3 Long-Range Interactions

The most important non-bonded interactions among disordered proteins – namely hydrophobic and electrostatic interactions – are incorporated in two force fields, which are designed to combine specificity and simplicity.

Hydrophobicity is implemented by making use of experimentally obtained hydrophobicity scales for all amino acids. After normalization, each amino acid bead i is attributed a relative hydrophobic strength $\pi_i \in [0, 1]$, see Tab. 1. The interaction strength ε_{ij} for each pair (i, j) of amino acids is defined as

$$\varepsilon_{ij} = \varepsilon_{\rm hp} \sqrt{(\pi_i \pi_j)^\alpha}\,, \tag{1}$$

where α and the strength of the most hydrophobic amino acids $\varepsilon_{\rm hp}$ are fit parameters. The intensity of repulsive hydrophilic interactions is set by a parameter $\bar{\varepsilon}_0$. Hydrophobic/hydrophilic interactions are incorporated in the form of a modified Lennard-Jones potential:

$$\Phi_{\rm hp}(r) = \begin{cases} \bar{\varepsilon}_0 \left(\dfrac{\sigma}{r}\right)^8 - \varepsilon_{ij} \left[\dfrac{4}{3}\left(\dfrac{\sigma}{r}\right)^6 - \dfrac{1}{3}\right] & \text{for } r \le \sigma \\ (\bar{\varepsilon}_0 - \varepsilon_{ij}) \left(\dfrac{\sigma}{r}\right)^8 & \text{for } r > \sigma \end{cases} \tag{2}$$

where σ is the distance at which $\bar{\varepsilon}_0 = \varepsilon_{ij}$.

AA	A	R	N	D	C	Q	E	G	H	I
π_i	0.7	0	0.33	0.0005	0.68	0.64	0.0005	0.41	0.53	0.98
charge	0	1	0	-1	0	0	-1	0	0	0
AA	L	K	M	F	P	S	T	W	Y	V
π_i	1	0.0005	0.78	1	0.65	0.45	0.51	0.96	0.82	0.94
charge	0	1	0	0	0	0	0	0	0	0

Table 1. Relative hydrophobicity and charge of all amino acids, as used in Eqs. 2–3.

The electrostatic interactions between charged amino acids is taken to be governed by a modified Coulomb law,

$$\Phi_{\rm el}(r) = \frac{q_i q_j}{4\pi\epsilon_0 \epsilon_r(r) r} e^{-\kappa r}\,, \tag{3}$$

where the exponential part is included to incorporate the screening effect of the free ions in the solution, using a Debye screening coefficient of $\kappa = 1\ \text{nm}^{-1}$. Expression 3 also accounts for the polarity of the aqueous solvent (recall that we use an implicit solvent model) through a distance-dependent dielectric constant of the solvent $\epsilon_r(r)$, given by

$$\epsilon_r(r) = 1 + S_s \left[1 - \left(\frac{r}{z}\right)^2 \frac{e^{(r/z)}}{(e^{(r/z)} - 1)^2}\right]\,, \tag{4}$$

such that the dielectric constant changes from 1 at very short distances ($r << z = 0.25$nm) to that of the solvent, $S_s = 80$.

4 Application to Nucleoporins

The local interactions incorporated in the model have been validated by comparison of the predicted Stokes radii of individual denatured proteins[3]. The non-bonded potentials contain two free parameters: the exponent α in the definition 1 of ε_{ij} and the hydrophilicity $\bar{\varepsilon}_0$. With a view on the projected application of the CG model to the NPC, Ghavami et al.[4] have fitted the parameter values by benchmarking against the Stokes radii of the most important Nups in the NPC.

The Stokes radius of all nups in the NPC is computed from Langevin dynamics simulations carried out at 300 K using Gromacs[5]. The time-step size is fixed at 0.02 ps and the Langevin friction coefficient is set to $50\ \mathrm{ps}^{-1}$ which is similar to the collision frequency of water molecules. Each Nup is simulated for 200 ns and the average Stokes radius R_S is computed from all generated conformations. A low-charge and a high-charge segment of two Nups have been used for tuning the fit parameters. Comparison of the predicted versus the experimental values of the Stokes radii reveals that the maximum error is no more than 24%.

References

1. A. L. Fink, *Natively unfolded proteins*, Curr. Op. Struct. Biol. **15**, 35–41, 2005.
2. V. Tozzini, *Multiscale Modeling of Proteins*, Acc. Chem. Res **43**, 220–230, 2010.
3. A. Ghavami, E. Van der Giessen, and P. R. Onck, *Coarse-grained potentials for local interactions in unfolded proteins*, J. Chem. Theory Comput. , doi:10.1021/ct300684j, 2013 (in print).
4. A. Ghavami, E. Van der Giessen, and P. R. Onck, *In preparation*.
5. B. Hess, C. Kutzner, D. Van der Spoel, and E. Lindahl, *Gromacs 4: Algorithms for highly efficient, load-balanced, and scalable molecular simulation*, J. Chem. Theory Comput. **4**, 435447, 2008.
6. J. Yamada, J. Phillips, S. Patel, et al., *A bimodal distribution of two distinct categories of intrinsically- disordered structures with separate functions in FG nucleoporins*, Molecular & Cellular Proteomics **9**, 2205–2224, 2010.

Modelling the Oral Bacterial Ecosystem and Other Biofilms

David A. Head

School of Computing, University of Leeds, Leeds LS2 9JT, United Kingdom
E-mail: d.head@leeds.ac.uk

Biofilms are sessile microbial communities that arise frequently in nature, and form an integral part of our own microbiome. Modelling biofilms is challenging as it couples biology (microbe growth and division) to chemistry (reaction, diffusion and advection of nutrients and metabolites) to physics (biofilm elasticity in the presence of flow). Natural biofilms exhibit chemical gradients and architectural structures on cellular length scales, thus a representative model must treat the biofilm as particulate, while retaining a continuum description for small dissolved molecules. Here I will present work developing a software platform coupling all of the key features mentioned above, and highlight two early applications. (1) Modulating dental plaque to be in its healthy state by subjecting the system to low doses of fluoride; (2) The rapid growth of surface roughness and how it is smoothed by shear flow.

1 Introduction

Biofilms are surface-associated microbial communities encased in a polymeric mesh (EPS) at least partly of their own production, and represent the dominate mode of existence of bacteria in nature[1]. Although often commensal to human existence, they are sometimes pathogenic or otherwise problematic, but can be difficult to treat due to their enhanced resistance to antibiotics. Alternative treatment strategies are urgently being sought, but the development cycle is hampered by a lack of understanding of the complex web of intercellular communications and other interactions within biofilms, and the often lengthy and expensive experiments needed to trial novel ideas.

Mathematical modelling can address both of these problems by providing full and non-invasive data extraction of systems of reduced complexity, and by acting as a rapid pre-screening tool for experimental trials. Biofilm models tend to fall into two groups: *Continuum* models, well suited to single-species films, where both the biomass and the dissolved agents (*i.e.* small molecules such as nutrients, metabolites *etc.*) are represented as scalar fields[2]. Multi-species films, however, are known to exhibit chemical gradients on the length scales of cells, giving rise to *micro-environments* that cannot be naturally represented at the continuum level. For such systems, which represent the norm for natural biofilms, an *agent-based* description of the biomass is more suitable, while maintaining a continuum representation of the dissolved molecules. The combined model is in this sense hybrid.

Here we describe the initial development and early results for a biofilm modelling tool capable of representing multi-species films within a mechanically consistent, immersed biofilm. The achievable spatial range spans from $\approx \mu m$ to $\approx 100\mu m$ or mm in each direction, thus individual molecules cannot be explicitly represented and their influence must be incorporated as input parameters or calibration curves. Due to separation of timescales for each of the primary processes, the temporal domain spans milliseconds to years. Coupling

to fluid flow is incorporated, a first for multi-species models, but currently at a restricted level as explained below. The methodology is described first, before presenting results for two applications and outlining some future directions.

2 Model Definition

A popular and well-known example of the hybrid approach to biofilm modelling is known as the *Individual-based Model* or IbM. This model is too complex to describe in detail here, instead we just give an overview of the main points and direct the interested reader elsewhere for details[3,7]. In this class of model, there are M scalar fields $c^\alpha(\mathbf{x})$, $\alpha = 1 \dots M$, which obey the steady-state reaction-diffusion equations

$$0 \equiv \partial_t c^\alpha(\mathbf{x}) = \nabla \cdot [D^\alpha(\mathbf{x}) \nabla c^\alpha(\mathbf{x})] + \sum_{i=1}^{N(t)} r_i^\alpha \delta(\mathbf{x} - \mathbf{x}^i) \,, \quad \alpha = 1 \dots M, \qquad (1)$$

where the diffusion coefficient $D^\alpha(\mathbf{x})$ may be inhomogeneous. The second term on the right-hand side of Eq. 1 represents the coupling to the biomass. At any given time t, there are $N(t)$ biomass particles $i = 1 \dots N(t)$ with centres at spatial coordinates $\{\mathbf{x}^i\}$. Each particle represents a single cell or a small aggregate of genetically-identical cells. For all chemical reactions metabolised by particle i, there is a total reaction rate r_i^α for each scalar field α. For instance, nutrient uptake is represented by a rate $r_i^\alpha < 0$ for the α corresponding to the nutrient field. Although first-order reaction kinetics are sometimes used, a more common choice is Michaelis-Menten kinetics of the form $r \propto c/(K_{1/2} + c)$, so that the reaction term in Eq. 1 generates a non-linear coupling between the c^α.

The steady-state scalar fields $c^\alpha(\mathbf{x})$ (and hence reaction rates r_i^α) are found by simultaneously solving Eq. 1 for all α. The change in particle masses can then be determined by employing some chosen rule, typically by scaling the rate of nutrient uptake by a growth (yield) factor. It is then possible to update the particle diameters d_i given a predefined density parameter. Particles divide (*i.e.* are replaced by two daughter particles with the same total mass) according to a selected threshold criterion, such as a maximum diameter.

In the original IbM template, excluded volume interactions are mediated by 'pushing' rules that do not admit adhesive interactions within the biomass. This rules out coupling to any flow in the surrounding fluid, which is known to be an important factor in determining the morphology of many natural biofilms[5]. A particle-based model with adhesive interactions and coupling has been developed[6], but not yet applied to growing multi-species films. A future goal of this project is to incorporate hydrodynamic coupling to a growing film by combining these methods. In the current version, however, fluid flow is incorporated only as a predefined velocity field $\mathbf{v} \equiv (v_x, v_y, v_y) = (\dot{\gamma} z, 0, 0)$ corresponding to an affine shear with rate $\dot{\gamma}$ (here z is the height from the base of the film). The reaction-diffusion Eq. 1 is extended to include an advection term (note we now also assume homogeneous diffusion),

$$0 \equiv \partial_t c^\alpha(\mathbf{x}) = D^\alpha \nabla^2 c^\alpha(\mathbf{x}) + \sum_{i=1}^{N(t)} r_i^\alpha \delta(\mathbf{x} - \mathbf{x}^i) - \mathbf{v} \cdot \nabla c^\alpha(\mathbf{x}) \qquad (2)$$

The mechanical stability of the biomass is incorporated by three steps: (i) each particle has a shell of EPS associated with it, with a mass m_i^{EPS} and diameter d_i^{EPS} determined

analogously to the cellular mass and diameter; (ii) particles with overlapping EPS shells are connected by a simple Hookean spring with spring constant determined from the m_i^{EPS}; and (iii) particle positions $\{\mathbf{x}_i\}$ are simultaneously solved to ensure force balance is obeyed for each particle. This includes the EPS-mediated spring forces, and (for $\mathbf{v} \neq \mathbf{0}$) a *drag force* $\mathbf{f}_i^{\mathrm{drag}} = 3\pi\nu d_i \mathbf{v}(\mathbf{x}_i)$ with ν the fluid viscosity. More details can be found in Ref. 7.

2.1 Overview of Iteration Methodology

The reaction-diffusion-advection Eq. 2 is solved on a uniform rectangular mesh by geometric multi-grid[8], cyclically implementing a single V-cycle *per* c^α until all converge simultaneously. Up-winding or line smoothing has not yet been included, which limits the strain rates for which the iteration converges. The delta functions in the reaction term in Eq. 2 are handled by (bi- or tri-) linearly interpolating the concentrations c^α at adjacent mesh points to the site of the particle $\mathbf{x}_i$, calculating the corresponding reaction rates $\{r_i^\alpha\}$, and distributing these back to the surrounding mesh nodes in a manner that conserves the total rate.

The mechanical equilibrium of the biomass is determined by one of two equivalent methods, selected according to their performance for the given problem: (i) *Overdamped molecular dynamics* in which the $\{\mathbf{x}_i\}$ are updated as per $\delta\mathbf{x}_i = A\mathbf{f}_i^{\mathrm{res}}\delta\tau$, with $\mathbf{f}_i^{\mathrm{res}}$ the residual (unbalanced) force on particle i and A a damping coefficient. The microscopic time step $\delta\tau$ is adaptive, increasing sub-linearly with the inverse of the maximum particle velocity at the previous time step. (ii) *Sparse matrix inversion* of the stiffness matrix constructed from the EPS-mediated interactions, with drag forces incorporated as a source term. The current implementation uses a non-linear conjugate gradient iteration with block-diagonal preconditioning. More details are given in Ref. 7.

3 Applications

3.1 Two-Species Plaque Model

Dental plaque is one of the most well-studied and accessible natural biofilms relevant to human health, and harbours many species interacting both intercellularly and with the environment, including the host[9]. The successful *ecological plaque hypothesis* regards this ecosystem as being potentially benign or pathogenic depending on the intrinsic population dynamics that can turn on environmental changes. Since indiscriminate removal of all oral bacteria can cause health problems such as fungal infections[9], alternative treatments target modulation of the plaque ecosystem into its benign state. A well-known problem is *supragingival* plaque that can lead to *caries* (tooth decay) due to the intake of carbohydrates, which shifts the population composition in the direction of acid-producing bacteria such as *S. mutans* at the expense of commensal species such as *S. gordonii*. The deleterious effects of *S. mutans* are primarily due to its *aciduricity* (ability to function at low pH), which is significantly reduced in the presence of even low concentrations of fluoride. Thus fluoride can help restore ecosystem balance.

To test this hypothesis, and make quantitative predictions for experimental verification, we have employed the biofilm model to include both of the *Streptococci* species mentioned above, which are both well characterised in the literature, including their glycolytic activity

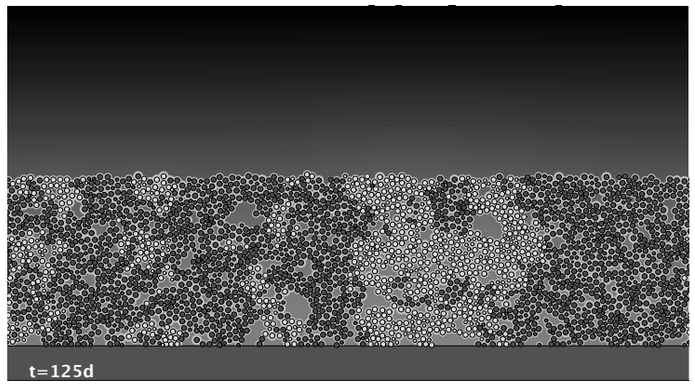

Figure 1. Example of the two-species plaque model with *S. mutans* (light discs) being outcompeted by *S. gordonii* (dark discs). The scalar field in the background (also visible through holes created by cell death) denotes lactic acid, with lighter shades corresponding to higher concentrations. This example corresponds to a feast-famine protocol in which 12 minutes of carbohydrate is added every 8 hours, and 1 mM of fluoride is continuously present. The flat upper surface at $150\mu m$ is imposed as a simple way to achieve a fixed film thickness.

rates (for the conversion of glucose to lactic acid) as a function of pH and fluoride[10]. This two-species system exhibits a benign, *S. gordonii* dominated state and a cariogenic *S. mutans* dominated state as stable solutions, depending on the duration and frequency of glucose intake and the presence of fluoride. As expected, fluoride acts to bias the system dynamics towards the *S. gordonii* dominated state. An example is shown in Fig. 1. More detailed analysis is ongoing and will be presented elsewhere[11].

3.2 Fractal Surface Growth

Fractal surface growth is an established field in statistical physics, with a range of canonical models typifying universal classes sharing invariant properties (symmetries, conserved quantities, locality *etc.*) in their growth rules[12]. Recent attempts to interpret two-dimensional growing IbM biofilms within this context suggested potentially non-canonical behaviour[13]. Simulations of the version of the IbM discussed here in three-dimensions suggests a possible explanation - that the non-local surface-surface coupling mediated by long-range variations in the nutrient (scalar) field drive anomalous roughening, where both the roughness and horizontal height-height correlation length scale *linearly* with time (this after taking the mean height to be a surrogate time variable, to reduce the gap to the canonical models). Introducing shear flow does not change this scaling, but does reduce the prefactor, thus shear flow is found to *smoothen* the film, in contrast to experiments with high Reynold's number flow[5]. The cause of this discrepancy is not yet apparent, but may result from the different flow regimes considered, or the lack of two-way fluid-structure coupling in the current model. A snapshot is given in Fig. 2 and further results are available[7].

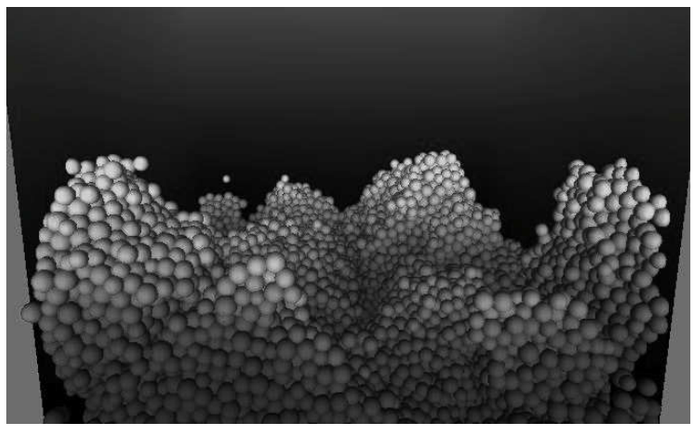

Figure 2. Surface roughening in a three-dimensional single species model, with slices through the single nutrient field displayed on the back and side walls. Particles have a brightness that is proportional to their growth rate, so the particles far from the peaks (which have low local concentrations of nutrient due to mass transfer limitation) grow only very slowly.

4 Discussion

Although the current model is still some way short of its intended goal of a fully-mechanistic IbM biofilm model with fluid-structure coupling, the early results presented here demonstrate the power of this approach, both in aiding the elucidation of potentially universal mechanisms governing biofilms as in §3.2, and its use as an *in silico* modelling tool to predict and, eventually, restrict experimental trials as in §3.1. In the latter case, the intention is to incrementally extend and validate this system to incorporate more species until matching one of the 10-species *in vitro* models that represent full dental plaque, both both supra- and subgingival. Once validated, it will then be employed as a rapid prescreening tool to reduce the number of lengthy and costly experiments that need to be performed when developing new treatments, accelerating the translational pipeline to novel clinical products.

Acknowledgements

The authors would like to thank D. Devine, A. Mighell and P. Marsh for many informative discussions relating to biofilms, and C. Goodyer and M. Walkley for useful discussions about multi-level algorithms. This work was funded by the Biomedical Health Research Centre (BHRC) in the University of Leeds through its Senior Translation Research Fellow (STRF) scheme.

References

1. D. G. Allison, P. Gilbert, H. M. Lappin-Scott and M. Wilson, *Community structure and co-operation in biofilms* (Cambridge University Press, Cambridge, 2000).
2. A. Seminara, T. E. Angelini, H. Vlamakis, S. Ebrahim, D. A. Weitz, R. Kolter, and M. P. Brenner, *Osmotic spreading of Bacillus subtilis biofilms driven by an extracellular matrix*, PNAS **109**, 1116–1121, 2012.
3. J.-U. Kreft, C. Picioreanu, J. Wimpenny, and M. van Loosdrecht, *Individual-based modelling of biofilms*, Microbiology **147**, 2897, 2001.
4. S. Hogg, *Essential Microbiology* (Wiley, Chichester, 2005).
5. P. Stoodley, B. Z. Lewandowski, J. D. Boyle, and H. M. Lappin-Scott, *The formation of migratory ripples in a mixed species bacterial biofilm growing in turbulent flow*, Environ. Microbiol **1**, 447–455, 1999; P. Stoodley, Z. Lewandowski, J. D. Boyle, and H. M. Lappin-Scott, *Structural deformation of bacterial biofilms caused by short-term fluctuations in fluid shear: an in situ investigation of biofilm rheology*, Biotech. Bioeng. **65**, 83–92, 1999.
6. E. Alpkvist and I. Klapper, *Description of mechanical response including detachment using a novel particle model of biofilm/flow interaction*, Water Sci. Tech. **55**, 265–273, 2007.
7. D. A. Head, *Linear surface roughness growth and flow smoothening in a three-dimensional biofilm model*, submitted; also `http://arxiv.org/abs/1210.8103`.
8. U. Trottenberg, *Multigrid* (Academic Press, 2001).
9. P. D. Marsh and M. V. Martin, *Oral microbiology* (Churchill-Livingstone, 2009).
10. I. R. Hamilton, P. J. Phipps, and D. C. Ellwood, *Effect of Growth Rate and Glucose Concentration on the Biochemical Properties of Streptococcus mutans Ingbritt in Continuous Culture*, Infec. Immun. **26**, 861, 1979; [1] P. D. Marsh, A. S. McDermid, C. W. Keevil, and D. C. Ellwood, *Environmental Regulation of Carbohydrate Metabolism by Streptococcus sanguis NCTC 7865 Grown in a Chemostat*, J. Gen. Microbiol. **131**, 2505–2514, 1985.
11. D. A. Head, D. Devine and P. Marsh, *in preparation*.
12. A.-L. Barabási and H. E. Stanley, *Fractal concepts in surface growth* (Cambridge University Press, 1995).
13. J. A. Bonachela, C. D. Nadell, J. B. Xavier, and S. A. Levin, *Universality in Bacterial Colonies*, J. Stat. Phys. **144**, 303–315, 2011.

Massively Parallel Molecular-Continuum Simulations with the Macro-Micro-Coupling Tool

Philipp Neumann[1] **and Jens Harting**[2]

[1] Department of Informatics, Technische Universität München, Germany
E-mail: neumanph@in.tum.de

[2] Department of Applied Physics, Technische Universiteit Eindhoven, The Netherlands
E-mail: j.harting@tue.nl

Efficient implementations of hybrid molecular-continuum flow solvers are required to allow for fast and massively parallel simulations of large complex systems. Several coupling strategies have been proposed over the last years for 2D/ 3D, time-dependent/ steady-state or compressible/ incompressible scenarios. Despite their different application areas, most of these schemes comprise the same or similar building blocks. Still, to the authors' knowledge, no common implementation of these building blocks is available yet. In this contribution, the Macro-Micro-Coupling tool is presented which is meant to support developers in coupling mesh-based methods with molecular dynamics. It is written in C++ and supports two- and three-dimensional scenarios. Its design is reviewed, and aspects for massively parallel coupled scenarios are addressed. Afterwards, scaling results are presented for a hybrid simulation which couples a molecular dynamics code to the Lattice Boltzmann application of the Peano framework.

1 Introduction

Hybrid molecular-continuum flow simulations allow to bridge the gap between purely molecular fluid descriptions and coarse-grained flow models such as mesoscopic or continuum models. The typical approach in concurrent molecular-continuum simulations is based on the decomposition of the computational domain into a continuum[a] and a molecular dynamics (MD) region. Within the molecular dynamics region, the fluid is resolved on the atomistic level. This yields a physically accurate description on the one hand, but implies high computational costs on the other hand since every molecule's trajectory needs to be computed. In contrast, a computationally fast, but less accurate flow simulation is carried out in the continuum region based on either particle- or mesh-based simulation methods. Examples for the latter comprise (in-) compressible Navier-Stokes or Lattice Boltzmann methods.

Several strategies for various flow problems have been proposed throughout the last years to coupled MD and mesh-based continuum solvers such as strategies for steady-state coupling of incompressible Navier-Stokes[1] or Lattice Boltzmann methods[2] and MD or compressible flux-based coupling schemes[3] for unsteady flow.

Despite their different application areas, most of these schemes comprise the same or similar building blocks. For example, the sampling of average velocities or fluxes is needed in nearly all coupling schemes; the same holds for particle insertion and removal. Depending on the similarity of two coupling schemes, the same algorithms or slightly modified versions or completely different approaches are required for each building block.

[a] In the following, the term "continuum" shall generally denote the coarse-grained flow description.

Besides, in order to handle large-scale problems from nanoscale engineering or biotechnnology, the simulation on massively parallel systems is of essential importance. Parallel solvers for the continuum and the MD region *as well as* a parallel implementation of the coupling mechanisms are hence necessary.

Within this context, we designed the Macro-Micro-Coupling tool[4,5] which is meant to support developers of new hybrid molecular-continuum schemes and allows for massively parallel coupled simulations. We recently described the parallel USHER-based[6] particle insertion implementation of the tool[4] and the software development of the coupling tool[5] in detail. In the following, the parallel performance of the coupling tool in a hybrid molecular dynamics-Lattice Boltzmann simulation is discussed. The software design with emphasis on the parallel extensions of the coupling tool is reviewed in Sec. 2. We report scaling results on different platforms in Sec. 3 and draw a short conclusion in Sec. 4.

2 Software Design

2.1 General Concept and Modularity Aspects

The design of the Macro-Micro-Coupling tool[4,5] is shown in Fig. 1 (a). The modules for momentum and particle insertion can be used, extended or modified by the developer to implement mass and momentum transfer on the MD solver side. In order to use these mechanisms, three interface implementations (`MoleculeWrapper`, `MoleculeIterator`, `MDSolverInterface`) need to be provided by the MD simulation. The `MacroscopicSolverInterface` represents the only required interface on the continuum solver side. All four interface implementations are used by the internal mechanisms of the coupling tool. A direct call to each interface is accomplished via the respective services, cf. the `CouplingMDSolverService` or the `CouplingMacroscopicSolverService`. In order to consistently describe the mapping of flow quantities be-

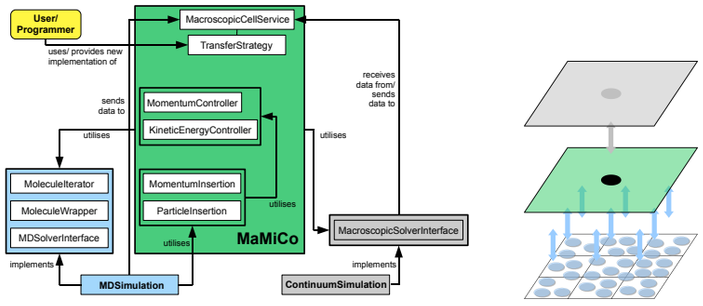

Figure 1. Design and general concept of the Macro-Micro-Coupling tool. (a) Interfaces and module separation. (b) Macroscopic cell-concept: macroscopic cells (green) build a geometrical interface between the mesh-based continuum solver (grey cell) and molecular dynamics (blue-coloured molecules).

tween the continuum and the MD solver, macroscopic cells are introduced, cf. Fig. 1 (b). They represent the discrete control volumes for sampling and exchange of mass and momentum; both two- and three-dimensional scenarios are supported.

2.2 Parallel Extensions

In distributed parallel simulations, the macroscopic cells are always stored on the same process as the respective volume in the MD simulation. Since the cells are strictly tied to the MD simulation, it is only the continuum solver which is left to be linked to the topology of the coupling tool (or the MD solver, respectively). For this purpose, the interface implementation of the `MacroscopicSolverInterface` needs to be provided. The method `accumulateSendReceiveInformation()` is called during the initialisation phase of the coupling. It loops over all continuum cells and calls `addSendReceiveInformation(cellPosition)` of the `CouplingMacroscopicSolverService` on each cell. The latter method uses the two methods `receiveMacroscopicQuantityFromMDSolver(...)` and `sendMacroscopicQuantityToMDSolver(...)` of the `MacroscopicSolverInterface` to determine if the flow data of a particular grid cell are received/ sent from/ to the MD solver. Depending on the coupling strategy and the respective implementation of the `MacroscopicSolverInterface`, an arbitrary subset of the macroscopic cells can thus be chosen in the initialisation phase for the quantity transfer mechanisms. As a consequence, the coupling tool has full knowledge of all required macroscopic cell-based communications after this phase.

In order to exchange quantities between the continuum and the MD solver during the coupled simulation, local macroscopic cell buffers are filled with respective mass and momentum contributions. A call to `receiveMacroscopicQuantitiesFromMacroscopicSolver()` or `sendMacroscopicQuantitiesToMacroscopicSolver()` of the `MacroscopicCellService` triggers the MPI-based communication between the processes.

3 Results

We recently investigated the sequential performance of the coupling tool as well as its parallel performance with respect to the parallel USHER-based particle insertion scheme[4]. In the following, the parallel performance of the tool in molecular dynamics-Lattice Boltzmann simulations of plane channel flow is measured. For this purpose, a single-centred Lennard-Jones MD simulation is coupled to the Lattice Boltzmann solver of the Peano framework[7].

The coupling is established following the principles of the steady-state based coupling approach by Dupuis *et al.*[2]. In our scenario, a fully three-dimensional domain is considered which consists of $54 \times 54 \times 54$ Lattice Boltzmann cells; each Lattice Boltzmann cell corresponds to one macroscopic cell of the coupling tool. In the middle, the molecular dynamics domain is embedded, cf. Fig. 2. The number density in the MD simulation is chosen as $n = 0.6$, and the Lennard-Jones parameters are scaled to unity. One coupling cycle consists of two Lattice Boltzmann time steps and 100 concurrent molecular dynamics time steps; though significantly more time steps are required to reach steady-state in each

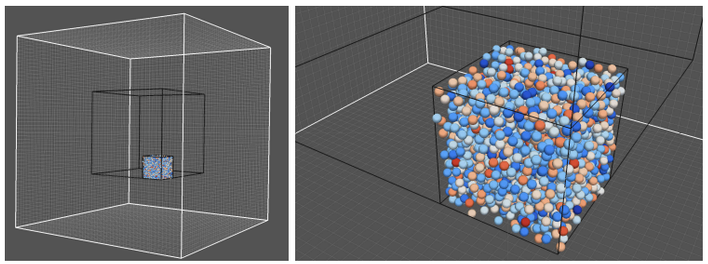

Figure 2. Parallel molecular dynamics-Lattice Boltzmann simulation executed on 64 cores. (a) Complete simulation domain consisting of $54 \times 54 \times 54$ Lattice Boltzmann cells. The molecules that are handled by the process on rank 0 are shown as coloured spheres. (b) Zoom into the molecular sub-domain on rank 0.

cycle, this choice is found to be sufficient for the scaling experiments. It further represents a suitable measure in case of unsteady flow simulations. Within a boundary strip of two Lattice Boltzmann cells, the flow velocity of the Lattice Boltzmann simulation is sent to the MD simulation. The molecules are relaxed towards this target average velocity in each macroscopic cell. In the outermost cell strip, the mass of the molecular system is relaxed towards the reference mass. For this purpose, the average mass is measured over one coupling cycle, and the mass difference between this average and the reference mass $m^{ref} = n \cdot dx^3$ is imposed over the next coupling cycle where dx denotes the cell size of one macroscopic, i.e. Lattice Boltzmann, cell. The removal of molecules is accomplished using a random removal technique whereas the particle insertion is based on the USHER scheme[4]. In the macroscopic cells which are located in the inner region of the molecular dynamics domain, the average velocity is sampled and sent to the Lattice Boltzmann solver.

Two scenarios are evaluated: in scenario A, the cell size is chosen as $dx = 2.5$ using $1.3 \cdot 10^5$ molecules. The scenario B applies cells of size $dx = 5.0$ and holds $1.0 \cdot 10^6$ molecules. This corresponds to a MD simulation which is eight times bigger than in scenario A and yields the same macroscopic cell topology in both scenarios. The strong scaling of a single coupling cycle has been measured on two IBM systems – Shaheen[b] (IBM BlueGene/P) and Huygens[c] (IBM pSeries 575). The computationally intensive MD simulation is executed in parallel mode using a standard domain decomposition to distribute the computational load among the processes. The Lattice Boltzmann simulation is executed in sequential mode on rank 0. The initialisation phase including the setup phase for the parallel topology between the solvers is negligible for both scenarios A and B; its contribution to the overall runtime has been found to be of the order of seconds.

The speed-up factors for one coupling cycle are shown in Tab. 1 and 2 for scenarios A and B. Besides the speed-ups for the hybrid molecular dynamics-Lattice Boltzmann simulations, the speed-ups for a pure MD simulation of the same MD setting are depicted

[b] See `http://www.hpc.kaust.edu.sa/documentation/user_guide/resources/shaheen/` for details.
[c] See `http://sara.nl/systems/huygens/description` for details.

Proc.	Shaheen		Huygens	
	MD-LB	MD	MD-LB	MD
1	1.0	1.0	1.0	1.0
8	6.6	6.8	6.5	6.4
64	36.0	44.0	34.6	37.6
512	105.4	206.6	98.0	122.5

Table 1. Strong scaling for scenario A. The first column shows the number of processor cores. The speed-ups obtained on Shaheen and Huygens are listed in the second and third major column. For both machines, the speed-up of the hybrid molecular dynamics-Lattice Boltzmann (MD-LB) simulation is compared to a pure MD simulation.

Proc.	Shaheen		Huygens	
	MD-LB	MD	MD-LB	MD
1	1.0	1.0	1.0	1.0
8	7.2	7.3	7.3	6.9
64	46.0	49.6	45.7	45.3
512	244.0	321.0	235.5	249.7
1728	484.4	814.5	456.7	494.7

Table 2. Strong scaling for scenario B.

for each scenario and platform. Especially for the lower core counts, the sequential Lattice Boltzmann simulation plays a negligible role, and similar speed-ups as in the pure MD simulations can be reached.

4 Conclusion

We presented the parallel extension of our Macro-Micro-Coupling tool which is meant to support developers of massively parallel molecular-continuum simulations. The strong scaling measurements indicate good scaling behaviour on moderate core counts. In these scenarios, a parallelisation of the computationally intensive MD simulation was found to be sufficient whereas the Lattice Boltzmann simulation was executed sequentially. In order to obtain speed-ups on bigger core counts, a parallel continuum solver is required as well. First steps towards a spatially adaptive parallel Lattice Boltzmann solver within the Peano framework are already taken. The realisation of a fully parallel molecular dynamics-Lattice Boltzmann simulation is therefore expected in near future.

Acknowledgements

This publication is based on work supported by the HPC-EUROPA2 project (project number: 228398) with the support of the European Commission Capacities Area - Research Infrastructures Initiative and by Award No. UK-C0020, made by King Abdullah University of Science and Technology (KAUST). We further gratefully acknowledge the support of the Faculty Graduate Center CeDoSIA at the Technische Universität München.

References

1. T. Werder, J. H. Walther, and P. Koumoutsakos, Hybrid atomistic-continuum method for the simulation of dense fluid flows, J. Comput. Phys. 205, 373–390, 2005.
2. A. Dupuis, E. M. Kotsalis, and P. Koumoutsakos, Coupling lattice Boltzmann and molecular dynamics models for dense fluids, Phys. Rev. E 75(046704), 2007.
3. R. Delgado-Buscalioni and P. V. Coveney, Continuum-particle hybrid coupling for mass,momentum and energy transfers in unsteady flows, Phys. Rev. E 67(046704), 2003.
4. P. Neumann and N. Tchipev, A Coupling Tool for Parallel Molecular Dynamics–Continuum Simulations, Proceedings of the International Symposium on Distributed an Parallel Computing 2012, 2012.
5. P. Neumann, W. Eckhardt. and H.-J. Bungartz, Hybrid Molecular-Continuum Methods: From Prototypes to Coupling Software, submitted.
6. R. Delgado-Buscalioni and P. V. Coveney, USHER: An algorithm for particle insertion in dense fluids, J. Chem. Phys. 119(2), 2003.
7. P. Neumann and T. Neckel, A Dynamic Mesh Refinement Technique for Lattice Boltzmann Simulations on Octree-Like Grids, Computational Mechanics, DOI 10.1007/s00466-012-0721-y, 2012. published online.

Molecular Dynamics Meets Finite Elements: An Approach for Coupled Simulations of Nanocomposites

Sebastian Pfaller[1], Gunnar Possart[1], Paul Steinmann[1], Mohammad Rahimi[2], Michael C. Böhm[2], and Florian Müller-Plathe[2]

[1] Chair of Applied Mechanics, Friedrich-Alexander-University Erlangen-Nuremberg, Egerlandstr. 5, 91058 Erlangen, Germany
E-mail: {s.pfaller, g.possart, p.steinmann}@ltm.uni-erlangen.de

[2] Eduard-Zintl-Institut für Anorganische und Physikalische Chemie and Centre of Smart Interfaces, Technische Universität Darmstadt, Petersenstr. 20, 64287 Darmstadt, Germany
E-mail: {m.rahimi, boehm, f.mueller-plathe}@theo.chemie.tu-darmstadt.de

In contrast to field-based continuum mechanics, particle-based methods can take into account the specific atomistic structure of the material under consideration. In our approach the system consists of a particle region that is coupled to a continuum by introducing a bridging domain where both regions overlap. The particle domain is computed by Molecular Dynamics (MD) at finite temperature, while the continuum is discretized and solved using the Finite Element Method (FEM). In addition to existing coupling schemes, the particles are tethered to anchor points which transfer displacements and forces between the different domains.

1 Introduction and Motivation

In continuum mechanics, a field-based approach is used to describe the mechanical behaviour of e.g. solids. The resulting equations can be solved by the Finite Element Method (FEM). In contrast, particle-based approaches may offer a deeper insight into the material since molecular or atomistic effects can be taken into account in order to capture relevant processes taking place in the material. In this field, e.g. Monte Carlo (MC) or Molecular Dynamics (MD) simulations are employed. However, these techniques do not allow for simulations at the macroscale due to the huge number of particles that would have to be considered.

Hybrid techniques bring together the advantages of particle-based and continuum-based tools by coupling the different domains. In our approach, we aim to combine the efficiency of continuum mechanics with the accuracy of MD simulations by applying the particle-based approach only in regions of interest, e.g. in the vicinity of solid-polymer interfaces. The remaining parts are treated by continuum mechanics at a much coarser resolution. Thus, a spatial decomposition into a particle region and into a continuum is necessary.

Here, we will focus on a hybrid scheme to solve structural mechanics problems. In the recent years, an increasing number of approaches have been published in that field, mainly focused on the failure of crystalline solids. A well-known example in this context is the Quasicontinuum method by Tadmor and co-workers[1].

However, applications to amorphous systems are still rare and often restricted to zero temperature. In our contribution we refer to the “Arlequin” method introduced by Ben Dhia and Rateau[2], which can be used for hybrid simulations of particle models and continuum mechanics.

In this method, a so-called “hand-shake” region is introduced where the continuum and the particle domain overlap. The particle domain does not require any underlying FE mesh, thus, the particles do not have to be arranged in a lattice.

In our approach, we use an extension of the Arlequin method that allows for a coupling between a continuum and an MD domain at finite temperature. Therefore, we only treat the particle domain dynamically while the continuum remains quasi-static. Due to the big gap between the timescales on the atomistic and the continuum level, any time-dependent processes taking place in the continuum seem to be almost static compared to the dynamics on the particle level.

In this contribution, we will highlight the most important requirements and features of our coupling scheme without going too much into detail. For deeper insight, we would like to refer to the literature and other publications.

2 System Setup and Mathematical Foundations

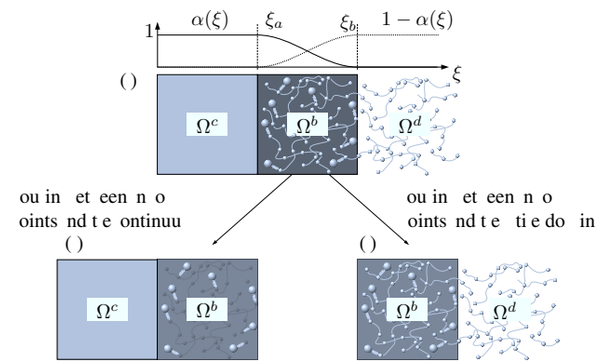

Figure 1. Spatial coupling: continuum Ω^c, bridging domain Ω^b, and particle domain Ω^d; small spheres: MD particles, large spheres: anchor points; weighting factor $\alpha(\xi)$; the complete spatial setup (a) is separated into a coupling between the anchor points and the continuum (b) and into a coupling between the anchor points and the particle domain (c).

The system to be considered consists of a particle region Ω^d that is embedded into a continuum Ω^c and which is large compared to the dimensions usually encountered in atomistic simulations. Thus, it is modelled by a coarse grained (CG) technique that treats groups of atoms as superatoms, cf. e.g. the publications by Müller-Plathe[3,4]. In order to couple the particle system to the continuum, stochastic boundary conditions (SBC) are used rather than more common periodic boundary conditions (PBC). For a more detailed description we refer to a previous publication of our groups[5].

The overlapping region between the continuum and the particle domain is called the bridging domain Ω^b, cf. Fig. 1[6]. In this region, a set of auxiliary particles is defined as

"anchor points" which serve as transmitter units. They do not interact within each other and are coupled to the remaining MD particles via a harmonic interaction potential. Thus, the coupling procedure (a) can be subdivided into a (static) coupling (b) between the anchor points and the continuum and into a (dynamic) coupling (c) between the anchor points and the MD domain.

In case of the coupling between anchor points and MD particles, the anchor points form a rigid frame that prevents the MD particles from leaving the simulation box and pretends the existence of particles outside the box. Within this boundary, the movement of the MD particles can be computed by employing the conventional MD procedures.

On the other hand, when the coupling of the continuum to the anchor points is considered, the MD particles appear to the continuum as static particles at fixed positions. The anchor points can be coupled to the continuum by the Arlequin method as mentioned above. Therefore, a weighting factor $\alpha(\xi)$ is introduced to couple the energy of the continuum and that of the anchor points. In the continuum, the weighted total energy can be written as

$$\hat{E}_c^{tot} = \int_{\Omega_0^c} \alpha(\xi(\mathbf{X}))\ \Psi(\mathbf{F})\ \mathrm{d}V - \int_{\partial_\sigma \Omega_0^c} \alpha(\xi(\mathbf{X}))\ \mathbf{u} \cdot \mathbf{T}\ \mathrm{d}A - \int_{\Omega_0^c} \alpha(\xi(\mathbf{X}))\ \rho_0\ \mathbf{u} \cdot \mathbf{b}\ \mathrm{d}V, \quad (1)$$

with the scalar function $\Psi = \Psi(\mathbf{F})$ denoting the strain or stored energy density, the deformation gradient $\mathbf{F}$, the displacement field $\mathbf{u}$, the surface tractions $\mathbf{T}$, and the density ρ_0 in the initial configuration. Furthermore, V is the volume of the body, A the area in the initial configuration, while $\partial_\sigma \Omega_0^c$ denotes the Neumann boundary with prescribed surface tractions.

Accordingly, the weighted energy of the particle domain can be formulated. It has to be remarked that within our investigations no external forces acting on anchor points shall be considered. Thus, the weighted total energy follows as

$$\hat{E}_d^{tot} = \hat{E}_{MD}^{int} + \frac{1}{2} \sum_{I=1}^{n^{MS}} \left[1 - \alpha(\xi(\mathbf{R}_I^{MS}))\right]\ E_{MS\,I}^{int}, \quad (2)$$

with the internal energy contribution $E_{MS\,I}^{int}$ of the bond between anchor point I and its associated MD particle. Furthermore, the total number of anchor points is given as n^{MS}, while the energy contribution of the remaining MD particles is denoted by $\hat{E}_{MD}^{int}$. Here, it is not necessary to know the exact formulation of $\hat{E}_{MD}^{int}$ since a change of MD particle positions is not possible during the continuum equilibration. Consequently, $\hat{E}_{MD}^{int}$ remains constant.

Thus, the total energy of the system can be written as $\hat{E}^{tot} = \hat{E}_c^{tot} + \hat{E}_d^{tot}$ and has to be minimized in order to obtain equilibrium. Additionally, the mismatch between the displacement field $\mathbf{u}$ of the continuum and the displacements of the anchor points has to be minimized in the coupled system. This is realized by introducing a coupling constraint that is incorporated by employing Lagrange multipliers $\boldsymbol{\lambda}$, which renders the following problem:

$$L(\boldsymbol{\lambda}, \mathbf{u}, \mathbf{w}^*) = \hat{E}_{tot} + \int_{\Omega^b} \boldsymbol{\lambda} \cdot [\mathbf{u} - \mathbf{w}^*]\ \mathrm{d}V \quad \rightarrow \quad \min \quad (3)$$

The artificial displacement field $\mathbf{w}^*$ of the anchor points is computed from the discrete anchor point displacements using an MLS approximation[7].

Eventually, after discretization using linear shape functions and with restriction to a linear elastic continuum, a linear system of equations is obtained and solved by standard algorithms.

3 Coupling Algorithm

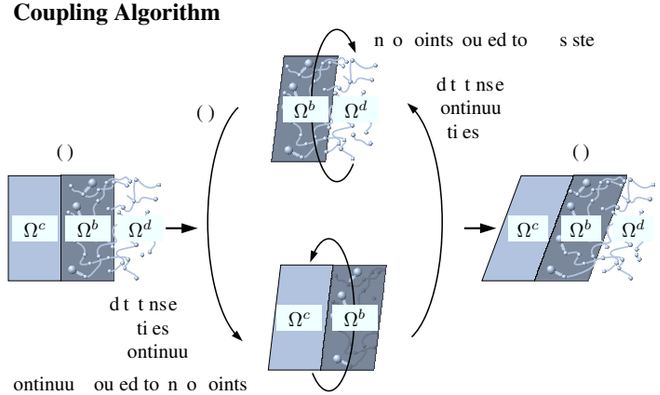

Figure 2. Concept of the staggered coupling scheme, small spheres: MD particles, large spheres: anchor points.

In Fig. 2 (taken from Ref. 6), the staggered coupling scheme employed here is depicted: starting from an initial configuration (a), the coupling procedure (b) is carried out. This consists of an equilibration run of the continuum coupled to anchor points (bottom, merely the anchor points are "visible" to the continuum, the MD particles are fixed), which renders modified anchor point positions as a result of the boundary conditions and of the forces exerted to the anchor points by the pure MD particles. Next, an equilibration run of the particle system is required (top, fixed anchor points represent the continuum enclosing the particles), which delivers updated forces on the anchor points. Consequently, the continuum has to be equilibrated again. After a sufficient number of MD–FE iteration steps, the coupled system reaches equilibrium (c).

4 Numerical Results

In order to demonstrate the coupling scheme described above, a polystyrene system in 3d is considered under uniaxial tension, cf. Fig. 3[6]. It consists of a cubic particle system, enclosed by the bridging domain and a cubic continuum, discretized by finite elements, with an edge length of 30 nm. The FE system is subjected to prescribed displacements u_y at the top and bottom xz-surfaces. In total, the MD domain contains 300 polymer chains, each of them consisting of 200 superatoms, which amounts to 60,000 superatoms.

In the boundary region, approximately 29,000 superatoms are located, 9004 of them being tethered to the same number of anchor points. Furthermore, the FE domain is represented by 936 FE nodes, 448 of them located in the bridging domain. The material parameters, i.e. the Young's modulus E and Poisson's ration ν, of the FE system are chosen based on a parameter identification of the pure MD system.

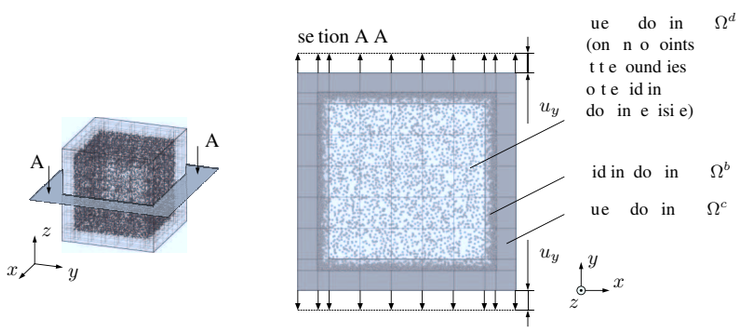

Figure 3. Coupled system subjected to prescribed displacements u_y at the top and bottom xz-surfaces, 3d view (left) and sectional view A–A (right).

In order to evaluate the coupling scheme, the results are compared to those obtained from a pure FE system with the same material parameters. Among others, the mean value of the normal stresses $\bar{\sigma}_{yy}$ in load direction is investigated as a function of MD–FE iteration steps, cf. Fig. 4[6]. As an example, the results for $E = 800$ MPa and $\nu = 0.3$ at a strain of 1% in y-direction are discussed here.

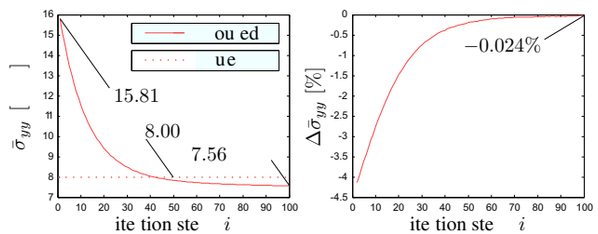

Figure 4. Uniaxial tension test, $E = 800$ MPa, $\varepsilon_{yy} = 1\%$: mean value of normal stress $\bar{\sigma}_{yy}$ (coupled and pure FE simulation) and convergence behaviour of $\Delta\bar{\sigma}_{yy}$ versus MD–FE iteration step i.

It is obvious that $\bar{\sigma}_{yy}$ converges to a value of 7.56 MPa, which is slightly lower than the analytic value of 8.00 MPa that is obtained from the pure FE simulation as well. Fur-

thermore, the change $\Delta\bar{\sigma}_{yy}$ in each MD–FE iteration step is very close to zero after 100 steps. Thus, the methodology described here seems to be reasonable, although adaptions and improvements are still necessary and currently in progress. Meanwhile, the scheme has been applied to nanocomposites which delivers reasonable results as well.

5 Concluding Remarks

We have described a staggered algorithm to couple a continuum discretized by finite elements to an amorphous particle domain solved by an MD procedure under stochastic boundary conditions. In contrast to many methods already available, this scheme allows for a coupling at finite temperature. Furthermore, the MD procedure can be carried out at highly specified machines employing specialised algorithms. Our numerical findings have proven that the coupling scheme produces reasonable results, although there is still effort required to improve the methodology. This is still work in progress.

Acknowledgements

We are indebted to Azadeh Ghanbari, Tinashe Ndoro, and Enrico Riccardi for useful discussions. Financial support by the German Research Foundation (DFG) within the DFG-priority programme 1369 "Polymer-Solid Contacts: Interfaces and Interphases" (`www.dfg-spp1369.de`) is gratefully acknowledged.

References

1. E. B. Tadmor, M. Ortiz, and R. Phillips, *Quasicontinuum analysis of defects in solids*, Philosophical Magazine A, **73**, no. 6, 1529–1563, 1996.
2. H. Ben Dhia and G. Rateau, *The Arlequin method as a flexible engineering design tool*, International Journal for Numerical Methods in Engineering, **62**, 1442–1462, 2005.
3. F. Müller-Plathe, *Scale-Hopping in Computer Simulations of Polymers*, Soft Materials, **1**, no. 1, 1–31, 2003.
4. F. Müller-Plathe, *Coarse-Graining in Polymer Simulation: From the Atomistic to the Mesoscopic Scale and Back*, ChemPhysChem, **3**, no. 9, 754–769, 2002.
5. M. Rahimi, H. A. Karimi-Varzaneh, M. C. Böhm, F. Müller-Plathe, S. Pfaller, G. Possart, and P. Steinmann, *Nonperiodic stochastic boundary conditions for molecular dynamics simulations of materials embedded into a continuum domain*, Journal of Physical Chemistry, **134**, 154108, 2011.
6. S. Pfaller, M. Rahimi, G. Possart, P. Steinmann, F. Müller-Plathe, and M. C. Böhm, *An Arlequin-based method to couple molecular dynamics and finite element simulations of amorphous polymers and nanocomposites*, Computer Methods in Applied Mechanics and Engineering, **submitted**, 2012.
7. T. Belytschko, Y. Krongauz, D. Organ, M. Fleming, and P. Krysl, *Meshless methods: An overview and recent developments*, Computer Methods in Applied Mechanics and Engineering, **139**, 3–47, 1996.

Coarse Graining: From Particles to a Continuum

Jens Boberski, Alexander Ries, Lothar Brendel, and Dietrich E. Wolf

Department of Physics, University of Duisburg-Essen,
Lotharstr.1, 47057 Duisburg, Germany
E-mail: jens.boberski@uni-due.de

After a brief summary of the coarse-graining formalism we present two applications with regard to particle continuum hybrid simulations of disordered systems. First we discuss the possibility to calculate local elastic fields and, in a second part, coarse graining close to interfaces between continuum and discrete particle system is discussed.

1 Introduction to Coarse Graining

Coarse graining is a way to derive a continuum description for a particle system. In granular systems, which lack a clear scale separation (unlike simple fluids)[1,2], it must be applied with care. As a first example, we will discuss how microscopic expressions for elastic constants of a granular packing can be calculated unambiguously. Second, the problem will be briefly addressed how to implement coarse-graining procedures in order to treat the interface between continuum and particles in hybrid simulations.

Recent publications by Goldhirsch[3,4] provide a comprehensive description of the coarse-graining formalism. Here we give only a short guide. In the following, Latin indices like i and j are used for different particles. Greek indices indicate the spatial coordinates, and summation convention is implied. The mass, centre of mass position and velocity of the i-th particle are given by m_i, $\mathbf{r}_i$ and $\mathbf{v}_i$ respectively. The contact between the particles i and j is characterized by the contact point $\mathbf{r}^{\mathrm{c}}_{ij}$ and the branch vectors $\boldsymbol{\ell}_{ij} = \mathbf{r}^{\mathrm{c}}_{ij} - \mathbf{r}_i$ and $\boldsymbol{\ell}_{ji} = \mathbf{r}^{\mathrm{c}}_{ij} - \mathbf{r}_j$. The force acting on particle i due to a contact with particle j is given by $\mathbf{f}_{ij}$.

Microscopic quantities that can be attributed to an individual particle i, like the mass m_i and momentum $\mathbf{p}_i$ are assigned to its centre of mass. The mass and momentum density fields are then defined as weighted averages of the microscopic quantities:

$$\rho(\mathbf{r},t) \equiv \sum_i m_i \phi(\mathbf{r} - \mathbf{r}_i(t))\,, \qquad \mathbf{p}(\mathbf{r},t) \equiv \sum_i m_i \mathbf{v}_i(t) \phi(\mathbf{r} - \mathbf{r}_i(t))\,, \tag{1}$$

where the weighting (coarse-graining) function $\phi(\mathbf{r})$ is positive semidefinite, normalized and localized around $\mathbf{r} = 0$ with the width w (the coarse-graining scale).

Defining the coarse-grained velocity field as $\mathbf{V}(\mathbf{r},t) \equiv \mathbf{p}(\mathbf{r},t)/\rho(\mathbf{r},t)$, it can be shown[3] that the coarse-grained fields satisfy the continuity equation

$$\frac{\partial \rho(\mathbf{r},t)}{\partial t} = -\frac{\partial}{\partial r_\beta}(\rho V_\beta)\,. \tag{2}$$

According to the equation of momentum conservation with the body forces $\mathbf{b}(\mathbf{r})$,

$$\frac{\partial p_\alpha(\mathbf{r},t)}{\partial t} = -\frac{\partial}{\partial r_\beta}\left[\rho(\mathbf{r},t) V_\alpha(\mathbf{r},t) V_\beta(\mathbf{r},t) - \sigma_{\alpha\beta}(\mathbf{r},t)\right] + b_\alpha(\mathbf{r})\,, \tag{3}$$

a stress tensor field $\sigma_{\alpha\beta}(\mathbf{r},t)$ is defined, consisting of a kinetic part

$$\sigma^{\text{kin}}_{\alpha\beta}(\mathbf{r},t) = -\sum_i \left(v_{i\alpha}(t) - V_\alpha(\mathbf{r},t)\right)\,\left(v_{i\beta}(t) - V_\beta(\mathbf{r},t)\right) m_i \phi(\mathbf{r}-\mathbf{r}_i) \tag{4}$$

and a contact-force-dependent part, the contact-stress tensor field, which is given by

$$\sigma^{\text{cont}}_{\alpha\beta}(\mathbf{r},t) = \sum_{ij} f_{ij\alpha}\,\ell_{ij\beta} \int_0^1 \phi(\mathbf{r}-\mathbf{r}_i(t) - s\,\boldsymbol{\ell}_{ij})\mathrm{d}s\,. \tag{5}$$

In frictional granular materials, the conservation of angular momentum introduces the couple-stress tensor[5]. In the quasistatic limit and without taking rolling friction into account, this reads[3]

$$\mu_{\alpha\delta}(\mathbf{r},t) \equiv \sum_{ij} \left(\left(\mathbf{r}^{\text{c}}_{ij} - \mathbf{r}\right) \times \mathbf{f}_{ij}\right)_\alpha \ell_{ij\delta} \int_0^1 \phi(\mathbf{r}-\mathbf{r}_i(t) - s\,\boldsymbol{\ell}_{ij})\mathrm{d}s\,. \tag{6}$$

This tensor appears in the equilibrium condition for frictional materials (in absence of external torques), which is given by

$$\epsilon_{\alpha\beta\gamma}\sigma_{\beta\gamma} = \partial_\delta \mu_{\alpha\delta}\,, \tag{7}$$

and is a generalization of the classical symmetric stress tensor ($\epsilon_{\alpha\beta\gamma}$ is the Levi-Civita symbol).

So far, we have not specified a coarse-graining function ϕ, because the basic structure of the resulting continuum description does not depend on it. In the following we use a Gaussian, $\phi(\mathbf{r}-\mathbf{r}_i) = \frac{1}{(\pi w^2)^{d/2}} \exp\left(|\mathbf{r}-\mathbf{r}_i|^2/w^2\right)$, where d is the number of spatial dimensions.

2 Coarse-Grained Elastic Tensor

The microscopic foundation of elasticity theory for disordered materials (like glasses, granular or amorphous solids) is hampered by the fact that for those materials the uniform strain assumption does not hold, due to non-affine deformations[6]. The aim of this section is to show how elastic constants for these materials can be defined. Calligraphic letters are used for matrices, generalized vectors are underlined. The derivation is given for the two-dimensional case, but the generalization to three dimensions is straightforward.

Consider a two-dimensional assembly of granular particles that is in equilibrium, i.e. the net force and torque on each particle are zero. When deformed by displacing the boundaries, the particles will move form their initial equilibrium positions $\{\mathbf{r}^0_i\}$ to new positions, so that the system is in equilibrium again. In general this behaviour is not reversible, since contacts may be created, opened or slide, which in a generalized sense can be regarded as plastic deformations of the granular packing. In any finite system, these plastic events (numbered by k) occur at certain discrete deformations ε_k. Generically, one can therefore choose a pre-deformed configuration as reference state in between the ε_k, and keep its perturbation small enough as to probe only the elastic response. Generically, one can therefore choose a small enough perturbation of the pre-deformed configuration (reference state) such that it only probes the elastic response. The interaction between the particles can then be linearized around the reference state[7] $\{\mathbf{r}^0_i\}$. In a two-dimensional

system with N particles this leads to a system of $3N$ coupled linear equations (force and torque equilibrium) for the $3N$ unknowns $\{\mathbf{u}_i, \varphi_i\}$ (displacements and rotations). In matrix form, this set of equilibrium equations can be written as $\mathcal{M}\underline{U} + \underline{F}^{\text{ext}} = 0$, where $\underline{U}$ is the generalized displacement vector containing all $3N$ components of the displacements and rotations in the system. $\underline{F}^{\text{ext}}$ contains the external forces and torques on the particles. They are determined by displacements of the boundary particles, $\underline{U}_B$. Hence, in linear order $\underline{F}^{\text{ext}} = -\mathcal{A}\underline{U}_B$, and the equilibrium equations can be written with the discrete Green's function $\mathcal{G} = \mathcal{M}^{-1}\mathcal{A}$ as:

$$\underline{U} = \mathcal{G}\underline{U}_B \,. \tag{8}$$

The vector $\underline{U}$ gives all displacements and rotations of the particles and enables one to calculate local displacement and stress fields[4]. For small deformations (to linear order in $\mathbf{u}_i$) and small pre-strain the incremental stress field is given by (cf. Eq. 5)

$$\delta\sigma^{\text{lin}}_{\alpha\beta}(\mathbf{r}) = \sum_{ij} \delta f^{\text{lin}}_{ij\alpha} \ell^0_{ij\beta} \int_0^1 \mathrm{d}s \phi(\mathbf{r} - \mathbf{r}^0_i + s\boldsymbol{\ell}^0_{ij}) \,, \tag{9}$$

where $\delta\mathbf{f}^{\text{lin}}_{ij}$ is the change of the contact force between particles i and j due to the deformation to linear order in the relative displacements and rotations. The displacement field for small deformations is given by $u^{\text{lin}}_\alpha(\mathbf{r}) = \frac{1}{\rho}\sum_i m_i u_{i\alpha}\phi(\mathbf{r} - \mathbf{r}^0_i)$, which leads to the displacement gradient field:

$$\frac{\partial u^{\text{lin}}_\alpha(\mathbf{r})}{\partial r_\beta} = \frac{1}{\rho^2}\sum_{ij} m_i m_j (u_{i\alpha} - u_{j\alpha}) \frac{\partial\phi(\mathbf{r} - \mathbf{r}^0_i)}{\partial r_\beta}\phi(\mathbf{r} - \mathbf{r}^0_j) \,. \tag{10}$$

Using the fields to linear order in the relative displacements allows one to write the coarse-graining procedures as linear functions of the generalized displacement vector $\underline{U}$,

$$\underline{\delta\sigma}^{\text{lin}}(\mathbf{r}) = \mathcal{S}(\mathbf{r})\underline{U} \,, \qquad\qquad \underline{\Delta}^{\text{lin}}(\mathbf{r}) = \mathcal{D}(\mathbf{r})\underline{U} \,, \tag{11}$$

where the stress and displacement gradient vectors in two dimensions are defined as $\underline{\delta\sigma}^{\text{lin}} = (\delta\sigma^{\text{lin}}_{11}, \delta\sigma^{\text{lin}}_{12}, \delta\sigma^{\text{lin}}_{21}, \delta\sigma^{\text{lin}}_{22})^T$ and $\underline{\Delta}^{\text{lin}} = (\partial_1 u^{\text{lin}}_1, \partial_2 u^{\text{lin}}_1, \partial_1 u^{\text{lin}}_2, \partial_2 u^{\text{lin}}_2)^T$. The $4 \times 3N$ matrices $\mathcal{S}$ and $\mathcal{D}$ are defined by Eqs. 9 and 10.

The local 4×4 elastic matrix, $\mathcal{C}$ (see right panel of Fig. 1), is usually defined as

$$\underline{\delta\sigma}^{\text{lin}}(\mathbf{r}) = \mathcal{C}(\mathbf{r})\underline{\Delta}^{\text{lin}}(\mathbf{r}) \,. \tag{12}$$

The trouble is that such a unique linear relation between $\underline{\delta\sigma}^{\text{lin}}$ and $\underline{\Delta}^{\text{lin}}$ does not exist. The fact that $\mathcal{D}$ and $\mathcal{S}$ in two dimensions are $4 \times 3N$ matrices shows, that there are many microscopic displacements $\underline{U}$ that lead to the same coarse-grained displacement gradient but different stress fields. We solve this dilemma by restricting ourselves to deformations that are caused by *affine displacements of the boundary particles*, determined by a fixed four component boundary displacement gradient $\underline{\Delta}_B$ (analogous to $\underline{\Delta}^{\text{lin}}$), $\underline{U}_B = \mathcal{H}\underline{\Delta}_B$. The $4 \times 3M$ matrix $\mathcal{H}$ contains the unstrained coordinates of the M boundary particles. For any such affine boundary deformation, the elastic matrix field throughout the whole system is uniquely given by

$$\mathcal{C}(\mathbf{r}) = \mathcal{S}(\mathbf{r})\mathcal{G}\mathcal{H}\left[\mathcal{D}(\mathbf{r})\mathcal{G}\mathcal{H}\right]^{-1} \,. \tag{13}$$

We calculated $\mathcal{C}(\mathbf{r})$ for a pre-strained packing of 4000 frictional disks generated by a Discrete Element Method (DEM) simulation. The interaction is harmonic in normal and tangential direction, with $k_t/k_n = 0.5$ and the mean radius of the particles is $\bar{r}$.

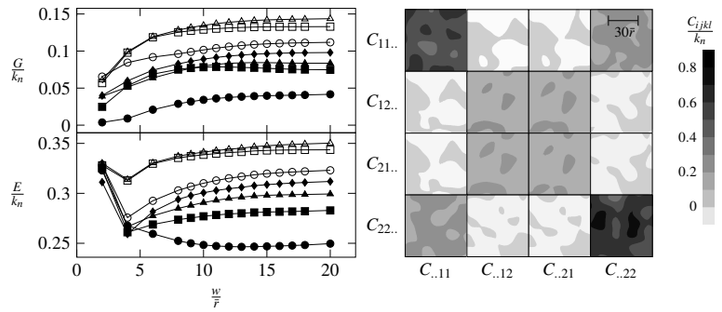

Figure 1. (left) The coarse-graining length dependence of the shear and bulk moduli for different configurations with increasing z from bottom to top.
(right) The spatial dependence of the 16 components of the elastic tensor. Each square shows the same segment at the centre of a system with coordination number $z = 3.56$, calculated with a coarse-graining length of $w = 8\bar{r}$.

The left panel of Fig. 1 shows that the shear modulus, $G = C_{1111} + C_{2222} - C_{1122} - C_{2211}$, and bulk modulus, $E = C_{1111} + C_{2222} + C_{1122} + C_{2211}$, become almost independent of the coarse-graining scale for $w > 14\bar{r}$ (with deviations less than 5%)[8]. Plateaus like these have also been observed experimentally in the stress fields of granular systems[9] and allow a scale-independent definition of physical quantities.

The right panel of Fig. 1 shows spatial maps of the local elastic constants for a fixed coarse-graining length. One notices that the components C_{1111} and C_{2222} have the largest values, and the elastic constants that are relating off-diagonal elements of the strain (stress) to diagonal elements of the stress (strain) are close to zero. Calculating these maps enables one to see local structures in the system and study correlations between the elastic constants and other fields. Fig. 1 confirms that the elastic tensor field violates the classical symmetries, but the deviations are small (below 5% of the norm of the elastic tensor). The stress tensor of a frictional material is in general not symmetric due to its micropolar nature[3], so the symmetry in the first two indices is not present. Rotational degrees of freedom and fluctuations of the microscopic displacements (non-affine motion) lead to a coarse-grained energy-density field that is not given[4] by $\sigma_{\alpha\beta} \frac{\partial u_\alpha}{\partial r_\beta}$, so the symmetry in a pairwise exchange of indices is broken. The fact that classically only the symmetric strain tensor is needed to describe the deformation of a material is a consequence of the first two symmetries and thus can not be expected in a material where either of them is broken.

3 Coarse Graining at Boundaries of the Discrete System

We turn to the question of how to coarse grain near a planar boundary, e.g. the interface between regions with a continuous and a particle based description in a hybrid simulation. We imagine the planar boundary as the surface of an infinitely big particle (the “wall”).

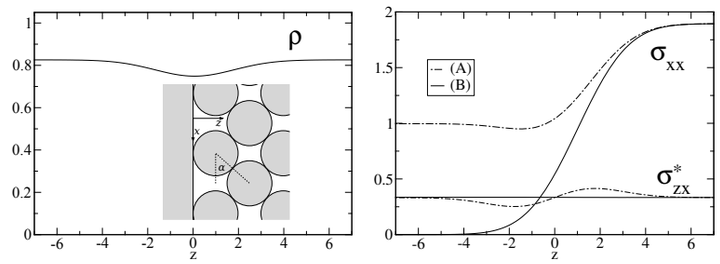

Figure 2. (left) The coarse-grained mass density ρ. (right) The stress components σ_{zx}, $\sigma^*_{zx} = \sigma_{zx} - \partial_z \mu_{yz} - \partial_x \mu_{yx}$ close to the wall for the different models (A) and (B), done with $w = 2.5$, $f_x/f_z = 1/3$ and $\alpha = \pi/5$.

As a first model (A), we may regard the wall as an elastic continuum. A particle in contact with it at the origin, and exerting a force $\mathbf{f}_\mathrm{w}$, provides the following contribution to the stress field within the wall[10,11]:

$$\sigma^{\mathrm{w,mic}}_{\alpha\beta}(\mathbf{r}, \mathbf{f}_\mathrm{w}) = -c_d \, \frac{\mathbf{f}_\mathrm{w} \cdot \mathbf{r}}{r^{d+2}} \, r_\alpha r_\beta \tag{14}$$

with $c_2 = 2/\pi$ and $c_3 = 3/(2\pi)$. Coarse graining (by convoluting with $\phi(\mathbf{r})$) removes the singularity at the contact point, but of course does not influence the long-range behaviour. Coarse graining (by convoluting with $\phi(\mathbf{r})$) removes the singularity at the contact point, but of course does not influence the long range behaviour of the resulting $\sigma^\mathrm{w}_{\alpha\beta}$. The latter appears in the total coarse grained stress tensor

$$\tilde{\sigma}_{\alpha\beta}(\mathbf{r}) = \sigma^c_{\alpha\beta}(\mathbf{r}) + \sum_i \sigma^\mathrm{w}_{\alpha\beta}(\mathbf{r} - \mathbf{r}^c_{i\mathrm{w}}, \mathbf{f}_{i\mathrm{w}}), \tag{15}$$

as an addition to Eq. 5 in form of contributions from the contacts between particles and the wall, which are located at $\mathbf{r}^c_{i\mathrm{w}}$.

As a second model (B), we can generalize Eq. 5 by extending the wall branch vectors $\boldsymbol{\ell}_{i\mathrm{w}}$ infinitely far into the (infinite) particle representing the wall. Denoting their unit vectors as $\mathbf{n}_{i\mathrm{w}}$, the additional terms are of the form (cf. also Weinhart et al.[12])

$$f_{i\mathrm{w}\alpha} n_{i\mathrm{w}\beta} \int_0^\infty \phi(\mathbf{r} - \mathbf{r}_i - r' \mathbf{n}_{i\mathrm{w}}) \mathrm{d}r' \, . \tag{16}$$

Note that the generalization Eq. 16, can as well be applied to the couple stress in Eq. 6.

We illustrate the two models by means of a semi-infinite rhombic array (see inset of Fig. 2) of identical frictional disks, terminated by a wall at $z = 0$ which exerts the same force $f_x \mathbf{e}_x + f_z \mathbf{e}_z$ on each boundary particle. For a large enough coarse-graining width ($w = 2.5$ turns out to be sufficient), the fields like density and stress are constant far from the interface. They agree with the asymptotic bulk quantities, which can be calculated analytically.

The behaviour in the vicinity of the interface is displayed in Fig. 2, where the left panel shows the density for the case that the wall density agrees with the bulk density of the particle array. The dip at the interface is due to the increased pores caused by the planar

wall. For the stress tensor, equilibrium requires that σ_{zz} and σ_{xz} are constant throughout the whole system (bulk, interface, wall), which is fulfilled by both models. Rotational equilibrium further demands that

$$\sigma^*_{zx} = \sigma_{zx} - \partial_z \mu_{yz} - \partial_x \mu_{yx} \tag{17}$$

is equal to σ_{xz} (cf. Eq. 7). This only holds true for model (B), but not for the elastic wall. Though the latter fulfills equilibrium far beyond the wall, it is violated at the interface. The reason is the elastic medium's lack of micropolar character.

σ_{xx} drops to $\sigma_{zz} = 1$ for model (A) and to 0 for model (B). Due to translational symmetry in x-direction, the equilibrium condition derived from Eq. 3 is fulfilled, no matter how σ_{xx} continues beyond the wall. Therefore, its value could be adjusted to match the bulk field, just as done with the density ρ.

Acknowledgements

We gratefully acknowledge stimulating discussions with Isaac Goldhirsch and Thorsten Pöschel and support by the DFG-grant WO 577/9-1.

References

1. B. J. Glasser and I. Goldhirsch, *Scale dependence, correlations, and fluctuations of stresses in rapid granular flows*, Phys. Fluids, **13**, 407, 2001.
2. C. Goldenberg, *Scale Separation in Granular Packings: Stress Plateaus and Fluctuations*, Phys. Rev. Lett., **96**, 168001, 2006.
3. I. Goldhirsch, *Stress, stress asymmetry and couple stress: from discrete particles to continuous fields*, Granular Matter, **12**, no. 3, 239–252, Mar. 2010.
4. I. Goldhirsch and C. Goldenberg, *On the microscopic foundations of elasticity.*, The European physical journal. E, Soft matter, **9**, no. 3, 245–51, Dec. 2002.
5. H. Schaefer, *Das Cosserat-Kontinuum*, Z. angew. Math. und Mech., **47**, no. 8, 485–498, 1967.
6. M. van Hecke, *Jamming of soft particles: geometry, mechanics, scaling and isostaticity.*, J. Phys.: Condens. Matter, **22**, no. 3, 033101, Jan. 2010.
7. W. Ellenbroek, E. Somfai, M. van Hecke, and W. van Saarloos, *Critical Scaling in Linear Response of Frictionless Granular Packings near Jamming*, Phys. Rev. Lett., **97**, no. 25, 1–4, Dec. 2006.
8. M. Reza Shaebani, J. Boberski, and D. E. Wolf, *Unilateral interactions in granular packings: a model for the anisotropy modulus*, Granular Matter, **14**, no. 2, 265–270, Feb. 2012.
9. J. Zhang, R. P. Behringer, and I. Goldhirsch, *Coarse-Graining of a Physical Granular System*, Progress of Theoretical Physics Supplement, **184**, no. 184, 16–30, 2010.
10. E. Melan, *Der Spannungszustand der durch eine Einzelkraft im Innern beanspruchten Halbscheibe*, Z. angew. Math. und Mech., **12**, 343–346, 1932.
11. L. Landau and E. Lifschitz, *Elastizitätstheorie*, chapter 1.8, Akademie-Verlag, 1975.
12. T. Weinhart, A. R. Thornton, S. Luding, and O. Bokhove, *From discrete particles to continuum fields near a boundary*, Granular Matter, **14**, 289–294, 2012.

First-Principles and Tight-Binding Quantum Chemical Molecular Dynamics Simulations on Chemical Mechanical Polishing Processes

Momoji Kubo

Fracture and Reliability Research Institute, Graduate School of Engineering, Tohoku University,
Aoba, Aramaki, Aoba-ku, Sendai 980-8579, Japan
E-mail: momoji@rift.mech.tohoku.ac.jp

Miniaturized and multi-stratified semiconductor devices require high-precision planarization of their copper (Cu) wiring layers. Chemical mechanical polishing (CMP) by abrasive silica grains in aqueous H_2O_2 solution is a popular technique to reach this goal, owing to high polishing rates and good planarity[1]. However, Cu-CMP has critical problems of dishing, erosion, the persistence of residual copper, and wiring corrosion. Such effects can cause a rise of the wiring resistance, an increased dielectric constant of the dielectric film as well as short circuits. Recently, the demands on CMP accuracy have increased to further improve 32 nm and 22 nm process technologies. The development of more precise Cu-CMP techniques requires a better understanding of the atomic-scale mechanism of the mechano-chemical reactions by the abrasive grain and the oxidizer on the substrate. However, the polishing mechanism with chemical reactions has not been clear, because it is very difficult to obtain atomic-scale information directly by experiments.

Computer simulations have accumulated useful information for many different aspects of the mechanical processing of semiconductors. Yet, simulations of CMP have remained challenging, because both chemical reactions and mechanical polishing need to be simulated at the same time. While force-field based molecular dynamics can be used to simulate the mechanical polishing process, it is not sufficiently predictive to model chemical reactions. Conversely, a static first-principles calculation can address the chemical reactions, although it can not be applied to the mechanical polishing processes. A first-principles molecular dynamics method cannot be used for the simulation of systems containing sufficiently many atoms to represent the polishing process.

To simulate both, the chemical reaction and mechanical polishing dynamics in the CMP process, we developed a CMP process simulator based on our tight-binding quantum chemical molecular dynamics method[2]. Our CMP process simulator was successfully applied to a CMP process of a Si surface by a SiO_2 particle[2] and of a SiO_2 surface by CeO_2 particle[3]. For the present study, we used our tight-binding quantum chemical molecular dynamics CMP process simulator to elucidate the CMP mechanism of a Cu surface by a SiO_2 particle in an aqueous 20% H_2O_2 solution. We performed the polishing simulation of a Cu(111) surface by an OH-terminated SiO_2 particle in an aqueous 20 % H_2O_2 solution and in a pure water environment. In our simulations, a constant normal force of 4.5×10^{-10} N was applied to the polishing particle, which was slid in lateral direction at a constant velocity of 50 m/s. Temperature was maintained at 330 K by through the scaling of atomic velocities. The adopted model is shown in Fig. 1(a) and 2(a). First-principles calculations were also

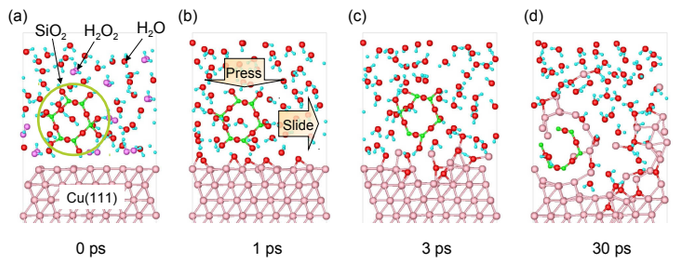

Figure 1. Snapshots of the polishing simulation in a aqueous 20 % H_2O_2 solution.

performed to estimate the activation barrier of the chemical reactions using the Accelrys DMol^3 code[4].

Snapshots of the polishing process of the Cu(111) surface in an aqueous 20 % H_2O_2 solution are shown in Fig. 1. During picosecond long equilibrium calculation, some H_2O_2 molecules adsorbed onto the Cu(111) surface and dissociated into two OH radicals. The subsequent oxidation reaction of the Cu surface occurred through these OH radical as shown in Fig. 1(b). After 1 ps equilibration, we applied the pressure on the SiO_2 particle and imposed the sliding motion. We observed that oxygen atoms coming from the oxidized Cu surface diffused into the bulk area due to the friction of the SiO_2 particle as shown in Fig. 1(c). Then, copper oxide was generated and the SiO_2 particle easily polished the copper oxide as shown in Fig. 1(d). From these observations, we conclude that the friction of the SiO_2 particle promotes the oxidation and the softening of the Cu surface under aqueous H_2O_2 solution environment. This is why the CMP process of the Cu surface can proceed efficiently.

We also performed the polishing simulation under a pure H_2O environment (Fig. 2). The oxidation of the Cu surface no longer occurred. Instead, the SiO_2 particle polished the pure copper surface as shown in Fig. 2 (a)-(d). Under a pure H_2O environment, fewer Cu atoms were removed from the Cu surface as compared to an aqueous H_2O_2 solution environment. This result is in good agreement with the experiments. The above analysis indicates that the oxidation of the Cu(111) surface by H_2O_2 molecules is essential for the efficient CMP process of the Cu surface. Softening of the Cu surface by the oxidation was identified to be a key step for the Cu CMP processes.

In order to evaluate the activation barriers for the oxidation of the Cu(111) surface by H_2O_2 molecule, we employed density-functional-theory based first-principles calculations. First, we investigated the activation barrier for the dissociative adsorption of the H_2O_2 molecule to two OH species. The calculated activation barrier for the above process is only 8.0 kcal/mol. Such a low activation barrier indicates that the process easily

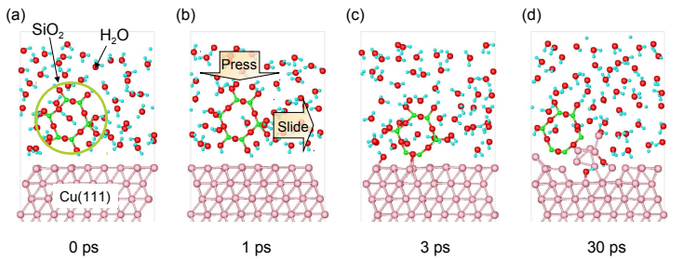

Figure 2. Snapshots of the polishing simulation in 100 % H_2O environment.

occurs on the Cu(111) surface in the aqueous H_2O_2 solution. This is in good agreement with our tight-binding quantum chemical molecular dynamics simulations. Next, we investigated the formation process of the adsorbed O atom on the Cu(111) surface by the chemical reaction of the adsorbed OH species and an H_2O_2 molecule. The final product of this process is the adsorbed O atom, the adsorbed OH group and an H_2O molecule. The calculated activation barrier for the above process is only 8.2 kcal/mol. This low activation barrier indicates that this process also easily occurs on the Cu(111) surface in the aqueous H_2O_2 solution. This is also in good agreement with our tight-binding quantum chemical molecular dynamics simulations. Finally we investigated the intrusion process of the adsorbed O atom into the Cu surface. The activation barrier for this copper oxide formation process is 35.1 kcal/mol. Such a high activation barrier indicates that this process needs the enhancement of the chemical reactions by the mechanical polishing. This result is also in good agreement with our tight-binding quantum chemical molecular dynamics simulations. In the tight-binding quantum chemical molecular dynamics simulation, the formation of copper oxide was not observed before the friction of the SiO_2 particle against the substrate.

In summary, we applied our chemical-mechanical-polishing-process simulator based on the tight-binding quantum chemical molecular dynamics method to the chemical mechanical polishing processes of Cu surface by SiO_2 particles. Under aqueous H_2O_2 solution, a Cu surface was oxidized by H_2O_2 and SiO_2 particles. The resulting Cu surface was softened by the oxidation and then easily polished. We clarified that the friction force of SiO_2 particle accelerates the chemical oxidation of Cu surface by H_2O_2. The activation barrier for the oxidation reaction processes of the Cu surface obtained by density-functional-theory based calculations supports the above results. We also performed the polishing simulation of a Cu surface in a pure H_2O environment. Fewer Cu atoms were removed from the Cu surface as compared to an aqueous H_2O_2 solution environment. This result is in good agreement with experiments. Overall, the study confirms the effective-

ness of our chemical mechanical polishing simulator based on the tight-binding quantum chemical molecular dynamics method.

References

1. Y. Ein-Eli and D. Starosvetsky, Electrochimica Acta, 52 (2007) 1825.
2. T. Yokosuka, H. Kurokawa, S. Takami, M. Kubo, A. Miyamoto, and A. Imamura, Jpn. J. Appl. Phys., 41 (2002) 2410.
3. A. Rajendran, Y. Takahashi, M. Koyama, M. Kubo, and A. Miyamoto, Appl. Surf. Sci., 244 (2005) 34.
4. B. Delley, J. Chem. Phys., 113 (2000) 7756.

NIC Series Volume 32
NIC Symposium 2006 - Proceedings
1 - 2 March 2006, Jülich, Germany
edited by G. Münster, D. Wolf, M. Kremer (2006), iv, 365 pages
ISBN: 3-00-017351-X

NIC Series Volume 33
Parallel Computing: Current & Future Issues of High-End Computing
Proceedings of the International Conference ParCo 2005
edited by G.R. Joubert, W.E. Nagel, F.J. Peters, O. Plata, P. Tirado, E. Zapata (2006), xiv, 930 pages
ISBN: 3-00-017352-8

NIC Series Volume 34
From Computational Biophysics to Systems Biology 2006 Proceedings
edited by U.H.E. Hansmann, J. Meinke, S. Mohanty, O. Zimmermann (2006), iv, 214 pages
ISBN-10: 3-9810843-0-6, ISBN-13: 978-3-9810843-0-6

NIC Series Volume 35
Dreistufig parallele Software zur Parameteroptimierung von Support-Vektor-Maschinen mit kostensensitiven Gütemaßen
by T. Eitrich (2007), xiv, 231 pages
ISBN: 978-3-9810843-1-3

NIC Series Volume 36
From Computational Biophysics to Systems Biology (CBSB07) Proceedings
edited by U.H.E. Hansmann, J. Meinke, S. Mohanty, O. Zimmermann (2007), vi, 312 pages
ISBN: 978-3-9810843-2-0

NIC Series Volume 37
Parallel Computing: Architectures, Algorithms and Applications - Book of Abstracts of the International Conference ParCo 2007
ParCo 2007 Conference, 4 - 7 September 2007
edited by G.R. Joubert, C. Bischof, F.J. Peters, T. Lippert, M. Bücker, P. Gibbon, B. Mohr (2007), xiv, 195 pages
ISBN: 978-3-9810843-3-7

NIC Series Volume 38
Parallel Computing: Architectures, Algorithms and Applications - Proceedings of the International Conference ParCo 2007
edited by C. Bischof, M. Bücker, P. Gibbon, G.R. Joubert, T. Lippert, B. Mohr, F. Peters (2007), xx, 810 pages
ISBN: 978-3-9810843-4-4

John von Neumann Institute for Computing
NIC Series

NIC Series Volume 39
NIC Symposium 2008 - Proceedings
20 - 21 February 2008, Jülich, Germany
edited by G. Münster, D. Wolf, M. Kremer (2008), iv, 358 pages
ISBN: 978-3-9810843-5-1

NIC Series Volume 40
From Computational Biophysics to Systems Biology (CBSB08)
Proceedings
edited by U.H.E. Hansmann, J.H. Meinke, S. Mohanty, W. Nadler,
O. Zimmermann (2008), viii, 430 pages
ISBN: 978-3-9810843-6-8

NIC Series Volume 41
Multigrid methods for structured grids and their application in particle simulation
by M. Bolten (2008), viii, 132 pages
ISBN: 978-3-9810843-7-5

NIC Series Volume 42
Multiscale Simulation Methods in Molecular Sciences - Lecture Notes
Winter School, 2 - 6 March 2009, Forschungszentrum Jülich
edited by J. Grotendorst, N. Attig, S. Blügel, D. Marx (2009), vi, 576 pages
ISBN: 978-3-9810843-8-2

NIC Series Volume 43
Towards the Confirmation of QCD on the Lattice
Improved Actions and Algorithms
by S. F. Krieg (2008), vi, 89 pages
ISBN: 978-3-9810843-9-9

NIC Series Volume 44
NIC Symposium 2010 – Proceedings
24 - 25 February 2010 | Jülich, Germany
edited by G. Münster, D. Wolf, M. Kremer (2012), v, 395 pages
ISBN: 978-3-89336-757-3

NIC Series Volume 45
NIC Symposium 2012 – Proceedings
25 Years HLRZ / NIC
7 - 8 February 2012 | Jülich, Germany
edited by K. Binder, G. Münster, M. Kremer (2012), v, 400 pages
ISBN: 978-3-89336-758-0

John von Neumann Institute for Computing
NIC Series

NIC Series Volume 46
Hybrid Particle-Continuum Methods in Computational Materials Physics Proceedings
4 - 7 March 2013 | Jülich, Germany
edited by M. H. Müser, G. Sutmann, R. G. Winkler (2013), ii, 232 pages
ISBN: 978-3-89336-849-5

The John von Neumann Institute for Computing (NIC) was established in 1998 by Forschungszentrum Jülich and Deutsches Elektronen-Synchrotron DESY to support the supercomputer-oriented simulation sciences. In 2006, GSI Helmholtzzentrum für Schwerionenforschung joined NIC as a contract partner.

The core task of NIC is the peer-reviewed allocation of supercomputing resources to computational science projects in Germany and Europe. The NIC partners also support supercomputer-aided research in science and engineering through a three-way strategy:

- Provision of supercomputing resources for projects in science, research, and industry.
- Supercomputer-oriented research and development by research groups in selected fields of physics and natural sciences.
- Education and training in all areas of supercomputing by symposia, workshops, summer schools, seminars, courses, and guest programmes for scientists and students.

The research groups of the John von Neumann Institute for Computing (NIC) regularly conduct workshops on leading-edge subjects in computational physics. In this tradition, the Computational Materials Physics Group organized a workshop on Hybrid Particle-Continuum Methods jointly with the Institute of Advanced Simulation on March 4 - 7, 2013 at the Forschungszentrum Jülich. The goal of the workshop was to foster the exchange of ideas between the communities working on complex fluids and complex solids. Particular emphasis was placed on continuum-mediated interactions between particles as well as on the adaptive and non-adaptive coupling between particle-based and continuum-based descriptions of materials.

JÜLICH FORSCHUNGSZENTRUM

GSI

Deutsches Elektronen-Synchrotron DESY

HYBRID 2013

M. H. Müser, G. Sutmann, R. G. Winkler (Editors)

Hybrid Particle-Continuum Methods in Computational Materials Physics

4 - 7 March 2013 | Jülich, Germany

Martin H. Müser, Godehard Sutmann, Roland G. Winkler (Editors)

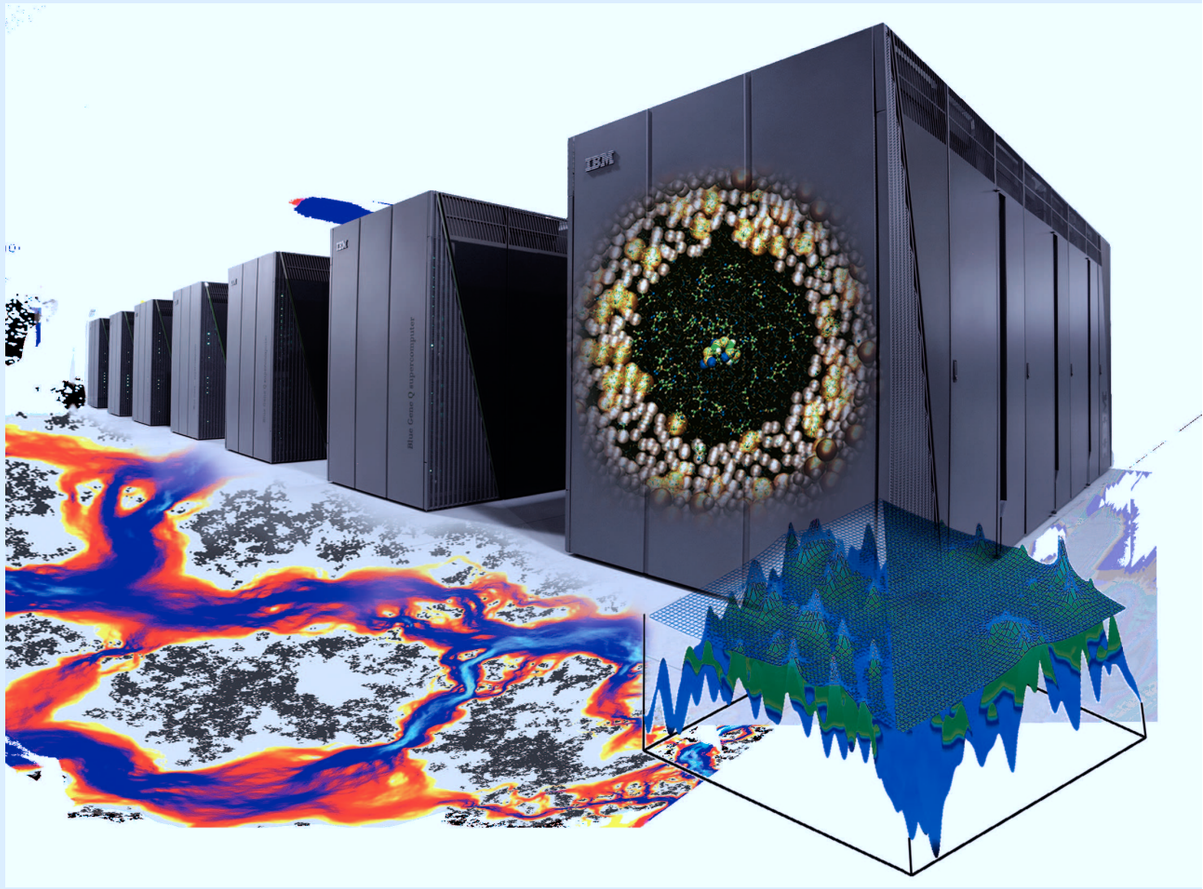

NIC Series Volume 46

ISBN 978-3-89336-849-5